NUMERICAL INVESTIGATION OF NATURE INSPIRED FOG HARVESTING FOR WATER COLLECTION

AHMAD SHAKEEL

PhD

The Hong Kong Polytechnic University

2019

The Hong Kong Polytechnic University

Department of Mechanical Engineering

NUMERICAL INVESTIGATION OF NATURE INSPIRED FOG HARVESTING FOR WATER COLLECTION

AHMAD Shakeel

A thesis submitted in partial fulfilment of the requirements for the degree of Doctor of Philosophy

July 2018

CERTIFICATE OF ORIGINALITY

I hereby declare that this thesis is my own work and that, to the best of my knowledge and belief, it reproduces no material previously published or written, nor material that has been accepted for the award of any other degree or diploma, except where due acknowledgement has been made in the text.

__________________ (Signed)

AHMAD Shakeel (Name of Student)

ABSTRACT

Fresh water scarcity has become a major problem especially in arid environments. Although water is abundant on earth, only 0.36% freshwater is available for human use that arises from frozen glaciers and polar ice caps. This has triggered the need for search of alternative sources of fresh water. Harvesting fresh water present in the form of fog can be a viable solution to this issue. Traditionally, a simple device, known as fog collector, consisting of mesh net is used to harvest water from air. The mesh net has a lower water collection efficiency though, which can be improved five-folds by optimum tuning of mesh wetting characteristics and topography. Recently, surfaces inspired from Namib dessert beetle's wing topographical and wettability features have shown higher water collection rates. The fog harvesting is essentially the collection of small fog droplets intercepting on the surface, which signifies the need to understand the dynamics of droplet impact on beetle inspired surfaces in order to achieve higher water collection rates. In literature, some studies have also investigated fog collection due to condensation on surfaces at lower temperature. Therefore, the present work aims to study this nature inspired fog harvesting phenomenon, with the focus placed on the two key physical processes, namely droplet impact and condensation on beetle inspired bumps and surfaces. To tackle these complex multiphase problems, a lattice Boltzmann method (LBM) based simulation framework has been developed for this research.

Four major issued were addressed in this research. First, droplet impact on beetle inspired hemispherical bumps was investigated. The bumps were nanotextured and superhydrophobic in nature. The effects of several key parameters, including the interpost spacing, post height, bump radius and Weber number, were investigated. The results showed that droplets impacting on bumps with higher posts and larger radius were generally in the Cassie state and hence favorable for water collection, whereas droplets impacting on bumps with higher posts and smaller radius were easy to rebound which are difficult to collect.

Secondly, the influence of surface slope on impact of two successive droplets was investigated. The effects of surface inclination, lateral/longitudinal offset, the impact dynamics of the two droplets and subsequent dynamics of the combined droplet were studied. It was observed that oblique impact causes asymmetric droplet spreading, with the downward spreading dominant over the lateral spreading. Furthermore, it was highlighted that the coalescence of the two droplets can result in abrupt changes in the evolution of the back and left/right contact edges, which is attributed to the partial landing of the trailing droplet on the leading droplet.

Thirdly, inspired from beetle's bump structure, shedding of condensing droplet from hydrophilic/superhydrophobic bump was studied. Bumps of two different shapes, i.e., cylindrical and hemispherical, were studied. It was found that water droplet condenses on the top hydrophilic area of a bump until it reaches a critical volume and sheds from the bump due to the gravity. The critical volume was found to be strongly dependent on the bump height.

Fourth, to study fog condensation on cold surfaces, the impact of droplets at saturation condition on a cold superhydrophobic surface was investigated. The effects of several key parameters, including the Jakob number, the Prandtl number, Weber number and surface slope, were investigated. It was revealed that the maximum spreading factor increases in non-isothermal impact compared to isothermal impact for both level and slanted surfaces. Furthermore, the Jakob number and the Prandtl number have strong influence on motion of the back contact edge in the case of droplet impacting on inclined surfaces.

The research presented in this thesis reveals the effects of dessert beetle inspired bump topographical features and surface inclination on droplet impact dynamics and condensing droplet shedding, which are useful in improving the future design and implementation of such bio-inspired water collectors.

LIST OF PUBLICATIONS

Journal Papers

1. **Ahmad**, S., Tang, H., and Yao, H.M., 2018, Oblique Impact of Two Successive Droplets on a Flat Surface, International Journal of Heat and Mass Transfer, Vol. 119, pp. 433-445.

2. **Ahmad**, S., Tang, H., and Yao, H.M., Droplet impact dynamics on Namib beetle inspired superhydrophobic hemispherical textured bumps, Submitted.

3. **Ahmad**, S., Tang, H., and Yao, H.M., On the critical volume of a condensing droplet shed from Namib beetle inspired bumps, Submitted.

4. **Ahmad**, S., Tang, H., and Yao, H.M., Dynamics of droplet impacting on cold surface in presence of saturated vapor, To be submitted soon.

Conference Papers

1. **Ahmad, S.**, Tang, H. and Yao, H.M., Effect of Wettability and Topological Features of Namib Beetle Inspired Bumps on Dropwise Condensation, 70th Annual Meeting of the APS Division of Fluid Dynamics, Denver, Colorado, USA, Nov 2017.

2. **Ahmad, S.**, Tang, H. and Yao, H.M., Droplet impact dynamics on convex nanotextured bumps, 22nd Annual Conference of Hong Kong Society of Theoretical and Applied Mechanics, Hong Kong, APR 2018. (Best presentation award)

3. **Ahmad, S.**, Tang, H. and Yao, H.M., LBM Simulation of Successive Impingement of Two Droplets on an Inclined Surface, 21st Annual Conference of Hong Kong Society of Theoretical and Applied Mechanics, Hong Kong, Apr 2017.

ACKNOWLEDGEMENTS

Praise and glory be to Allah, the Almighty with whose gracious help it was possible to complete this Doctoral research.

First, I would like to express heartiest gratitude to my supervisor, Dr. Hui Tang, for his valuable assistance, guidance and encouragement during this research work. His optimistic attitude, constructive criticism and continuous support enabled the timely completion of this work. Thank you for the thoughtful conversations regarding the nature and goals of this thesis work.

I am indebted to my co-supervisor, Dr. Haimin Yao, who has been a source of encouragement, motivation and inspiration. I am exceedingly thankful for the support and knowledge I have received from him. I would also like to express my gratitude for administrative supporting staff of our department's general office especially Ms Lily Tam and Ms Michelle Lai for their guidance, support and listening our queries.

I would like to thank my friends and colleagues at The Hong Kong Polytechnic University for their friendship and motivation over the period of my Doctoral research-particularly Dr. Nafees Qadri, Dr. Gholamreza Kefayati, Mr. Zhao Fuwang, Mr. Wang Zhaokun, Dr. Hafiz Zahoor, Mr. Ahmadighadikolaei Meisam, Mr. Khawaja Mateen, Mr. Waleed Umer, Mr. Engineer Saad Shakeel Chugtai, Mr. Faisal Khurshid, Mr. Talha Qasim Ansari and Mr. Sana Ullah.

Finally, I would like to thank my parents and siblings for their love, constant support and prayers. Without their support completion of this study would be impossible.

TABLE OF CONTENTS

LIST OF FIGURES

LIST OF TABLES

LIST OF SYMBOLS

ρ	density
σ	surface tension
μ	dynamic viscosity
λ	thermal conductivity
λ_x	lateral offset
λ_y	longitudinal offset
λ_{CL}	modified capillary length
θ	surface wettability
g	acceleration due to gravity
α	surface slope
U	droplet impact velocity
Re	Reynolds number
We	Weber number
Oh	Ohnesorge number
Bo	Bond number
Pr	Prandtl number
Ja	Jakob number
$\mathrm{S}^*_{\mathrm{max}}$	maximum spreading factor
$\mathrm{S}^*_{\mathrm{x}}$	lateral spreading factor
$\mathrm{S}^*_{\mathrm{y}}$	longitudinal spreading factor
C_v	specific heat at constant volume

T	temperature
w	post width
s	inter-post spacing
h	post height
D	droplet diameter
R	bump radius
t^*	nondimensional time
V_c	critical volume of shedding droplet
h_{fg}	specific latent heat of condensation

CHAPTER 1

INTRODUCTION

1.1 BACKGROUND

The demand for clean water is ever increasing in arid areas. In the recent Global Risks report, the water crisis has been listed as an environmental risk [1]. Besides, the World Economic Forum expressed that two-thirds of the world population may face water shortage problems by 2025. Water is also needed for basic human necessities, for example, drinking, cooking, sanitation, hygiene, productive and commercial activities, but at present the accessibility of freshwater is rising as an extremely challenging global issue [2,3]. In rural areas of African, Asian and Latin American countries, there are approximately one billion people who have lack clean water access [4–6]. Though water is abundantly available natural resource on the earth, most of the water is salty comprising around 96.54% of the total water. The freshwater available for human is only 0.36%, which largely comes from the frozen glaciers and polar ice caps, while the remainder of water is the unfrozen groundwater available in small proportion above the ground or in the air [7,8]. Obtaining fresh water has become a hot issue required to be solved urgently.

Fog water has been given less attention in past. However, previous studies [9,10] show that fog harvesting can be used as a viable option for water collection in some arid and semiarid regions. Besides, fog harvesting provides a low cost, easily maintainable and sustainable water source augmenting to rainfall. Traditional fog harvester is a very simple device, known as fog collector, consisting of a mesh net supported by a strong frame. As fog passes through the mesh, the fog droplets are intercepted on mesh ribbon or wire of the mesh and get deposited. These droplets coalesce, become bigger and then run down into gutters from which they are collected into collection reservoir. Fog water collection has been widely studied in past, spanning more than 20 countries across the globe [11]. Mostly the water collection range varies from 1 to 10 L/m^2 per day but can reach as high as 40 L/m^2 per day [12]. Though the design and implementation of fog collector may vary according to location but for the evaluation of site the standard fog collector (SFC), introduced by Schemenauer and Cereceda [12], is used. The SFC consists of a 1 m x 1 m frame supported on a 2 m high sturdy base. The frame is covered with mesh. The geometrical details of SFC are shown in Fig. 1.1. To achieve the optimal performance the SFC should be oriented perpendicular to wind direction [12].

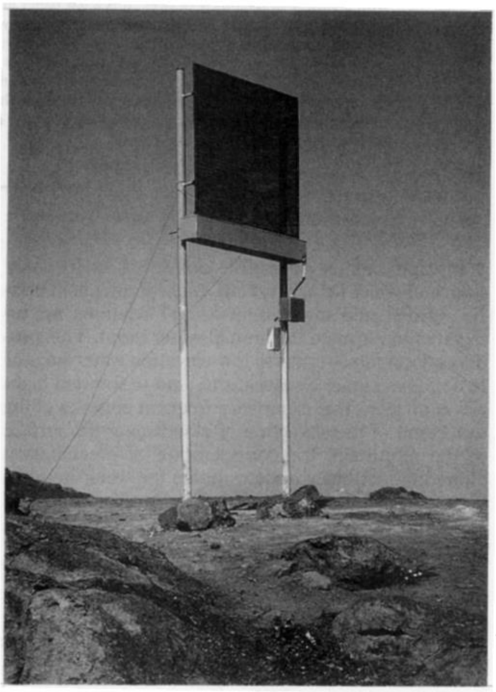

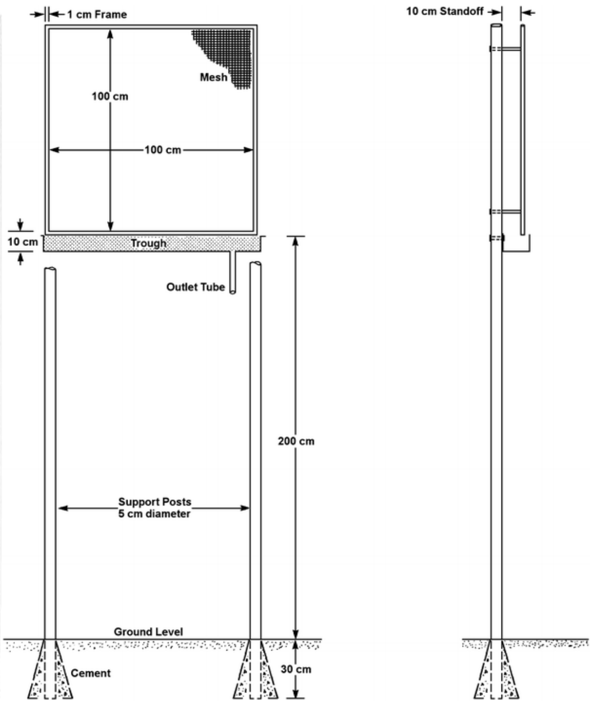

Figure 1. 1 Standard fog collector [12].

The generally used mesh, for the fog collectors, consists of flat fibers with various widths ranging from 0.5 mm to 1.5 mm and pore sizes of 1.0-1.3 cm, called Raschel mesh. The mesh features triangular links of fibers to reduce damages because of tears or wind [13,14]. Rivera [15] developed a model to predict maximum percentage of fog that can be captured by a fog collector, called the aerodynamic collection efficiency. Their model showed the maximum aerodynamic collection efficiency of the order of 20–24.5% for shade coefficients between 0.5 and 0.6, where the shade coefficient of a mesh is defined as ratio of mesh material surface area to the total area covered by the mesh. While this model only approximates shade coefficient in order to maximize the flow of fog through the mesh, fog collection efficiency may be further increased by tuning the wettability and mesh ribbon topography. Park et al. [16] investigated the effects of the several important parameters, including surface wettability, length scale, and mesh wire weave density, on fog collection rate. They also developed a model to predict overall fog-collection efficiency of the mesh, and found that appropriate tuning of the wettability characteristics and topography of the mesh can enhance fog-collection efficiency by five-folds compared to the conventional Raschel mesh. Thus research on wettability contrast of patterns and topography is required to achieve further higher water collection rates.

1.2 NAMIB BEETLE INSPIRED SURFACES

Recently biomimetic surfaces have got popularity for their topographical and chemical properties, which allow higher water collection rates. In nature some plants and animals have skilled the survival abilities to collect water from fog. For example, Namib dessert beetles can live in area with very little rainfall [17]. Among Namib dessert beetles, the Stenocara beetle's body contains randomly spaced bumps with hydrophilic peaks surrounded by superhydrophobic areas [18] (Fig. 1.2). The bumps are about 0.5 mm in diameter with random separation of about 0.5 – 1.5 mm from each other. Furthermore, the apparent smooth superhydrophobic regions are also made up of flattened hemispherical bumps of micrometer size (Fig. 1.2 (c)).

Parker and Lawrence [18] suggested the fog basking mechanism of water collection for Stanocare beetle. In fog basking beetle tilts its body into the wind. The fog droplets incident on the wing surface, then coalesce into bigger droplets and roll down into the beetle's mouth. This idea of fog collection by hydrophilic/superhydrophobic nature of bumpy surface has received much appreciation. Following Parker and Lawrence [18] many studies have been conducted to understand moisture harvesting on beetle inspired surfaces [19–22]. On the contrary, Nørgaard and Dacke [23] argued about the fog basking nature and the presence of hydrophilic areas on beetle's body. Their investigation, which included the study of four different Namib dessert beetles, showed that elytra of all beetles were completely hydrophobic. Furthermore, they only observed small differences in fog harvesting efficiencies of beetles with very different elytra surfaces, questioning the importance of structural adaptations. However, it has been confirmed by recent studies that water collection rates for hydrophilic/hydrophobic patterned surfaces are higher than that of completely hydrophilic or hydrophobic surfaces [24–26]. Besides, a number of past reports have also investigated innovative and facile methods to replicate the beetle's hydrophilic/superhydrophobic pattern owing to potential water collection applications [24–30].

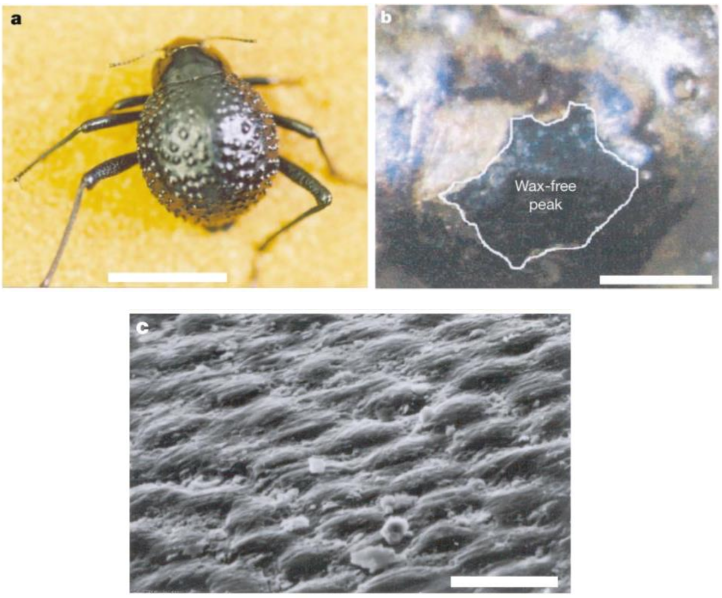

Figure 1. 2 (a) desert beetle Stenocara, (b) hydrophilic bumps (wax-free), (c) Scanning electron micro- graph of the textured surface valley. Scale bars (a) 10 mm, (b) 0.2 mm, (c) 10 µm [18].

1.3 RESEARCH AIMS AND OBJECTIVES

The aim of this work is to investigate the roles of beetle surface topography and wettability characteristics in fog water collection. Fog consists of airborne droplets of size 1 - 50 µm [31]. In fog harvesting water is largely collected by direct droplet impact, coalescence and then gravity assisted removal. Besides, in literature condensation studies have also been conducted on beetle inspired surfaces [32]. Therefore, the focus of the present work is placed on investigating the effects of both condensation and droplet impact on fog harvesting over beetle inspired surfaces. Keeping in view the background and importance of beetle inspired surfaces for higher water collection rates, the following four issues are to be addressed in the present research:

1. Since the beetle surface contains two types of bumps, i.e., larger hydrophilic bumps and small hemispherical bumps of micrometer size that make up the superhydrophobic valleys. Both of these bumps are convex in shape. Therefore, **to understand the role of convex bumps in water collection, we will study the droplet impact on hemispherical bumps**.

2. In fog basking multiple droplets may successively impact on a normal or inclined surface, then coalesce into bigger droplets, and finally get dislodged from the surface. Similarly, in case of traditional fog collectors positioned with an inclined angle, successive droplets may also impact on mesh wire/ribbon. The offsets of successively impacting droplets both in lateral and longitudinal direction can affect the water collection owing to small width of the mesh wire/ribbon. Furthermore, the offsets can also influence the impact dynamics due to surface inclination. Accordingly, **we will investigate the dynamics of multiple droplet impacting on an inclined surface**.

3. The condensation water collection efficiency of a surface depends on two criteria; one is the droplet growth, and the other is its facile removal. The early removal of the growing droplet creates the space for new droplets, and therefore increases the water collection rate. A condensing droplet on the bump grows till a critical volume at which gravity becomes dominant causing the droplet to shed off the bump. The bump shape and other geometrical parameters such as bump height and diameter can influence the shedding time and critical volume of droplets. Accordingly, **we will investigate the critical volume of condensing droplets shedding from desert beetle inspired bumps**.

4. Consider the impingement of a fog droplet on a cold surface. Droplet and surrounding vapors are at saturated temperature, which mimics a 100% humidity case. As soon as the droplet hits the surface, its temperature decreases, resulting in the condensation of surrounding vapors. The condensation may change the impact dynamics. Furthermore, if the surface is inclined (such as in case of fog basking), the downward motion of droplet during the impact may also be affected by condensation. Hence, **we will study the effects of surface temperature on droplet impact dynamics in presence of saturated vapor**.

The above four issues will be addressed using a systematic numerical study using the lattice Boltzmann method (LBM). Challenges, such as quantification of contact line motion on nanostructures, impacting droplets intermixing and high experimental cost has prompted the use of numerical simulations. Over the years, conventional methods, including the finite difference method (FDM), finite volume method (FVM) and finite element method (FEM) are being used frequently in computational fluid dynamics (CFD). In the last two decades, a different type of numerical method, which is based on mesoscopic kinetic equations, and known as the lattice Boltzmann Method has emerged. The LBM acts as a bridge between micro scale and macro scale phenomena. It becomes a powerful and alternative CFD tool, and has achieved substantial success in the fields of both fluid flow and heat transfer. In addition, it is easy to implement in complex domains, and is easy to model multiphase and multicomponent problems without the need to track the interface movement. Furthermore, it can be naturally extended to parallel process computing.

1.4 ORGANIZATION OF THESIS

This dissertation is composed of eight chapters and is organized as follows: In Chapter 2, the existing literature on droplet impact, condensation and dessert beetle inspired surfaces is presented. This chapter also provides systematic reviews of studies related to the aforementioned four issues, leading to the identification and understanding of the research gaps. In Chapter 3, the methodology, i.e., the LBM, is introduced. The details of single-relaxation-time, multiple-relaxation-time (MRT) and phase-change LBM models are introduced. In Chapter 4, droplet impact on beetle inspired hemispherical nanotextured bumps is studied. The different bump geometrical features are explored for the Cassie suspended state, which is known to be favorable for water collection compared to the sticky Wenzel state and droplet rebound. In Chapter 5, two successive droplets impact is simulated on inclined surfaces. The dynamics of droplet impacts with different lateral/longitudinal offsets, and surface inclination are studied. In Chapter 6, the shedding volume of condensing droplets on beetle inspired bumps is studied. The results revealed the critical volume of shedding droplets and the critical height of bumps. In Chapter 7, fog droplet impacting on cold surfaces in the presence of saturated vapor is investigated. This chapter highlights the comparison of droplet spreading and contact line motion between isothermal and nonisothermal impacts. In Chapter 8, conclusions, main findings, and suggestions for future work are presented.

CHAPTER 2

LITERATURE REVIEW

In this chapter a review of previous studies regarding condensation and droplet impact is presented. First, droplet impact on dry surfaces is generally discussed. The possible outcomes of droplet impact, such as deposition, splashing and rebound are briefly explained. Then the past studies on objective 1 and 2 are reviewed, and the research gaps are highlighted. The objective 1 and 2 are titled as "droplet impact dynamics on nanotextured bumps: topology effects" and "oblique impact of two successive droplets on a flat surface", respectively. Thereafter, condensation of vapor is discussed. The literature surveys on objective 3 titled as "critical volume of a condensing droplet shedding from beetle inspired bumps" and objective 4 titled as "droplet impact in presence of saturated vapor" with related research gaps are presented. A survey on past studies discussing droplet impact and phase-change phenomena using LBM is presented. Finally, the summary of the chapter is presented.

2.1 DROPLET IMPACT

Droplet impact has ubiquitous applications, such as ink-jet printing, plasma spraying, spray cooling, internal combustion engine, microfluidics, spray painting and coating, and atomization and cleaning. Droplet impact on dry surfaces and pools or films can have entirely different outcomes. In the present work, only impingement on dry surfaces is discussed. Furthermore, surface topology (flat, curved, hardness), surface roughness, wettability, fluid properties (Newtonian or non-Newtonian), surface temperature also have significant influence on impact dynamics.

The important parameters generally used in droplet impact investigations include density ρ, surface tension σ, viscosity μ, impact angle, impact velocity U, droplet size D and surface roughness. Some of these parameters can be grouped into dimensionless numbers in order to facilitate impingement study.

$$\mathrm{Re} = \rho UD/\mu \tag{2.1}$$

$$\mathrm{We} = \rho U^2 D/\sigma \tag{2.2}$$

$$Oh = \mu/(\rho\sigma D)^{½} \quad (2.3)$$

$$Bo = \Delta\rho g D^2/\sigma \quad (2.4)$$

Reynolds number Re describes the relative importance of the fluid inertia compared to the viscosity force in the droplets, the Weber number We describes the relative importance of the fluid inertia compared to the surface tension of the droplets. Bond number Bo describes relative importance of gravitational force relative to surface tension. In some work the Ohnesorge number Oh = $\mu/(\rho\sigma D)^{½}$ is used to describe droplet dynamics, which can be related to Re and We through Oh = $(We)^{½}/Re$.

2.1.1 DROPLET IMPACT ON DRY SURFACE

Outcome of the droplet impact on dry surfaces is largely influenced by fluid and surface properties. Rioboo et al. [33] conducting an experimental study of droplet impact classified the six possible outcomes as shown in Fig. 2.1.

In deposition scenario droplet impacts, spreads but remains attached to the surface all the time. Actually, in deposition case droplet spreads in two stages. The first stage is called Kinematic spreading, which lasts for $t^*<0.1$, where t^* is nondimentional time defined as $t^*=tU/D$ [34]. In kinematic phase, spreading is independent of physical properties of liquid and surface. The spreading factor is given as $S^* \sim t^{1/2}$. Actual deposition or spreading starts after kinematic spreading phase. The liquid and surface parameters begin to play roles in actual deposition. The spreading is influenced by inertial forces, capillary forces and viscous dissipation and surface wettability. The ratio of maximum value of diameter of lamella at bottom surface to droplet initial diameter is called maximum spreading factor and is given as

$$S_{max}^* = \frac{S_{max}}{D} \quad (2.5)$$

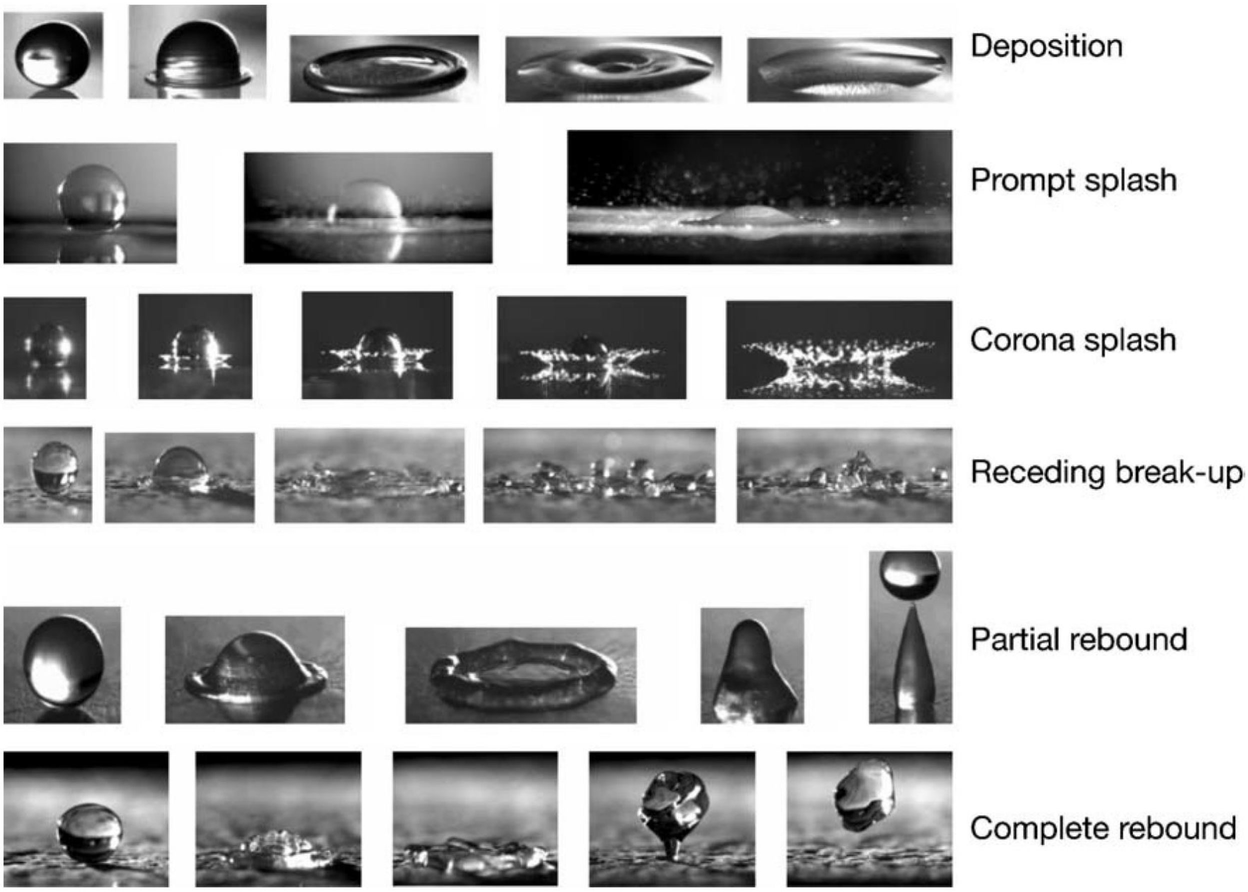

Figure 2.1 Six possible outcomes of droplet impact on a dry surface [33].

A number of relations between maximum spreading factor and other impact parameters have been proposed. Chandra and Avedisian [35], Mao et al. [36], Pasandideh-Fard et al. [37] used energy balance method to derive semi-empirical maximum spreading factor relation. Clanet et al. [38] proposed a simple scaling law $S^* \sim We^{1/4}$ that gives good quantitative agreement with experimental results for hydrophobic surfaces. Yeong et al. [39] investigated droplet impact on inclined surface and proposed a relation $S^* = 0.9\mathrm{We}_N{}^{1/4} + C\ \mathrm{We}_T,$ which can be reverted back to Clanet et al.'s [38] relation for normal impact case. Table. 2.1 shows the summary of important relations of maximum spreading factor. Though the apparent formulations of these relations are quite different from each other but they show reasonable agreement with experimental and simulation results.

Table 2. 1 Summary of maximum spreading factor relations. All relations are applicable to perpendicular impact except the last one, which is applicable to impact on inclined surfaces.

Chandra and Avedisian (1991) [35]	$\frac{3\mathrm{We}}{2\mathrm{Re}} {S_{max}^{*}}^{4} + (1 - cos\theta){S_{max}^{*}}^{2} - \left(\frac{1}{3}\mathrm{We} + 4\right) \approx 0$
Asai et al. (1993) [40]	$S_{max}^{*} = 1 + 0.48\mathrm{We}^{0.5} \times \exp[-1.48\mathrm{We}^{0.22}\mathrm{Re}^{-0.21}]$
Scheller & Bousfield (1995) [41]	$S_{max}^{*} = 0.61(\mathrm{Re}^{2}\mathrm{Oh})^{0.166}$
Pasandideh-Fard et al. (1996) [37]	$S_{max}^{*} = \sqrt{\frac{\mathrm{We} + 12}{3(1 - cos\theta_{a}) + 4(\mathrm{We}/\sqrt{\mathrm{Re}})}}$ θ_{a} is advancing contact angle
Mao et al. (1997) [36]	$\left[\frac{1}{4}(1 - cos\theta) + 0.2\frac{\mathrm{We}^{0.83}}{\mathrm{Re}^{0.33}}\right]{S_{max}^{*}}^{3} - \left(\frac{\mathrm{We}}{12} + 1\right)S_{max}^{*} + \frac{2}{3} = 0$
Clanet et al. (2004) [38]	$S^{*} \propto \mathrm{We}^{1/4}$
Ukiwe & Kwok (2005) [42]	$(\mathrm{We} + 12)S_{max}^{*} = 8 + {S_{max}^{*}}^{3}(3(1 - cos\theta_{d}) + 4\frac{\mathrm{We}}{\sqrt{\mathrm{Re}}})$
Roisman (2009) [43]	$S_{max}^{*} \sim 0.87\ \mathrm{Re}^{1/5} - 0.4\ \mathrm{Re}^{2/5}\mathrm{We}^{-1/2}$
Yeong et al. (2014) [39]	$S_{max}^{*} = 0.9{\mathrm{We}_{\mathrm{N}}}^{1/4} + C\ \mathrm{We}_{\mathrm{T}}$ $\mathrm{We}_{\mathrm{N}} < 60$ Inclined surface relation. *N* represent normal component and *T* tangential component. *C* is a constant.

Higher impact velocities can produce droplet splash (Fig. 2.1). Stow and Hadfield [44] and Mundo et al. [45] proposed a splashing parameter related to splashing threshold.

$$K = \mathrm{We}\sqrt{\mathrm{Re}} \tag{2.6}$$

Where the splashing parameter K depends on inertia, surface tension and viscosity. A splash can be produced if $K \gtrsim 3000$. A splash can be categorized into two forms; prompt splash and corona splash as shown in Fig 2.1 [33]. Xu et al. [46] using high speed photography, discovered that decreasing the surrounding gas pressure without changing other parameters can suppress the splashing. Later, Xu et al. [47] also investigated the interplay between surface roughness and surrounding gas pressure. It was proposed that surface roughness is responsible for prompt splash, whereas corona splash is produced due to instabilities caused by surrounding gas. On the contrary, Thoroddsen et al. [48] has observed prompt splash for droplet hitting on a smooth glass. To date there are still debates on how to distinguish between prompt and corona splash based on impact parameters. For contemporary studies on this topic on can refer to review papers [49,50].

Droplets post the impact can leave fingers type patterns (Figs. 2.1 and 2.2). Previously this was related to Rayleigh-Taylor instability of lamella edge, which was also supported by some recent reports [51,52]. Thoroddsen and Sakakibara [53] showed the evolution of fingering pattern during impact. They showed that fingers can widen, split and merge during spreading. Some researcher also proposed fingers number scaling. Marmanis and Thoroddsen [54] showed that number of fingers can scale with impact Reynolds number as

$$N \propto \frac{U(\pi^2 \rho D^3)^{\frac{1}{4}}}{16\sigma^{1/4}\nu^{1/2}} \tag{2.7}$$

Aziz and Chandra [55] and Mehdizdhe et al. [56] also studied impingement of droplets and proposed relations. Fassmann et al. [57] studied droplet impact at high velocity and investigated sizes of splashed droplets .

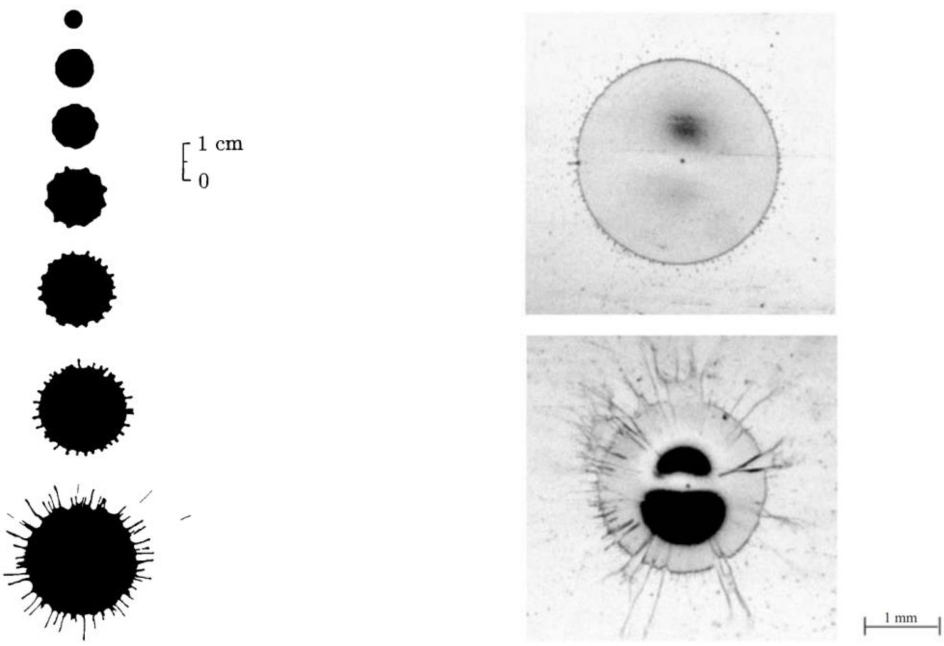

(a) (b)

Figure 2.2 (a) Change in splatter shape and numbers of fingering [54] (b) Splashing at higher velocities; 30 m/s (top), 40 m/s (bottom) [56].

A droplet impacting on the surface spreads, achieves maximum spreading, and then starts to recede. In some cases the surface energy and remaining kinetic energy are enough to squeeze the receding lamella liquid upward from the surface forming a rising column of liquid. In partial rebound liquid column partly remains at surface and detaches one or more droplets at top due to capillary instability. In complete rebound, the liquid column detaches from the surface as a droplet (Fig. 2.1). Droplet rebound on superhydrophobic surfaces has a number of potential applications, such as self-cleaning surfaces, anti-icing, water collection, and enhanced heat transfer. Superhydrophobic surface consists of hydrophobic micro or nano textures. Droplet rebound on textured surface is further reviewed in next section.

2.1.2 DROPLET IMPACT DYNAMICS ON NANO TEXTURED BUMPS: TOPOLOGY EFFECTS

As discussed in Chapter 1, beetle’s back is composed of bumpy hydrophilic/superhydrophobic patterns. That is, hydrophilic bumps are surrounded by superhydrophobic valleys featuring microstructures of flattened hemisphere, which assist in collection of passing by fog water [18]. Inspired from beetle, several surfaces have been mimicked and investigated for condensation process of water collection [32,58–60]. However in fog harvesting process, droplet impaction is the leading phenomenon for water collection [61]. Therefore, a surface should perform better for both condensation and impaction processes for best overall water collection efficiency. For simplicity in the present work only droplet impaction is considered.

In literature droplet impact has been widely investigated on smooth as well as textured surfaces. Normal impact of droplets has been well reviewed by Yarin [49]. In addition to level surfaces, several works on single as well as multiple droplets impact on inclined surfaces have also been conducted in past [62–64].

Recently, droplet impact on smooth convex surfaces has also been studied [65–68]. Shen et al. [65] found that droplets impinging on a convex superhydrophobic surfaces can quickly rebound compared to flat surfaces. The reduction of 28.5% in the contact time, which was mainly connected to faster retraction process of impacting droplet, was determined (Fig. 2.3). Similarly, Liu et al. [67] studied droplet impact on Echevaria leaves, which have convex/concave architecture. This showed an asymmetric bouncing phenomenon with different spreading and recoiling processes along two orthogonal directions (Fig. 2.4). Nearly 40% reductions in contact time was determined owing to asymmetric bounce off. Khojasteh et al. [68] studied droplet impact on hydrophobic and superhydrophobic hemispherical surfaces and focused on Weber number, surface curvature and contact angle. They found higher area of liquid in contact with surface compared to flat surfaces. Chen et al. [69] investigated water droplet impact on soft hemispherical surfaces.

Apart from smooth surfaces droplet impact on level surfaces with micro-nano structures has also been investigated. Jung and Bhushan [70] studied the dynamic impact behavior of water droplets on superhydrophobic surfaces. The surfaces were micropatterned with pillars of two different diameters and heights and with various pitch values. They developed a correlation for the transition from the Cassie state to the Wenzel state by studying the relationship between velocity and geometrical parameters of micropatterned surface. The impact velocity for the Cassie state should be less than the critical velocity, which is given as

$$U_c < \sqrt{\frac{32\sigma h}{\rho(\sqrt{2}P-D)^2}} \tag{2.8}$$

where σ, ρ, U_c, D, h, and P are surface tension, density and the critical impact velocity of droplet, and diameter, height and pitch of circular cylinder, respectively.

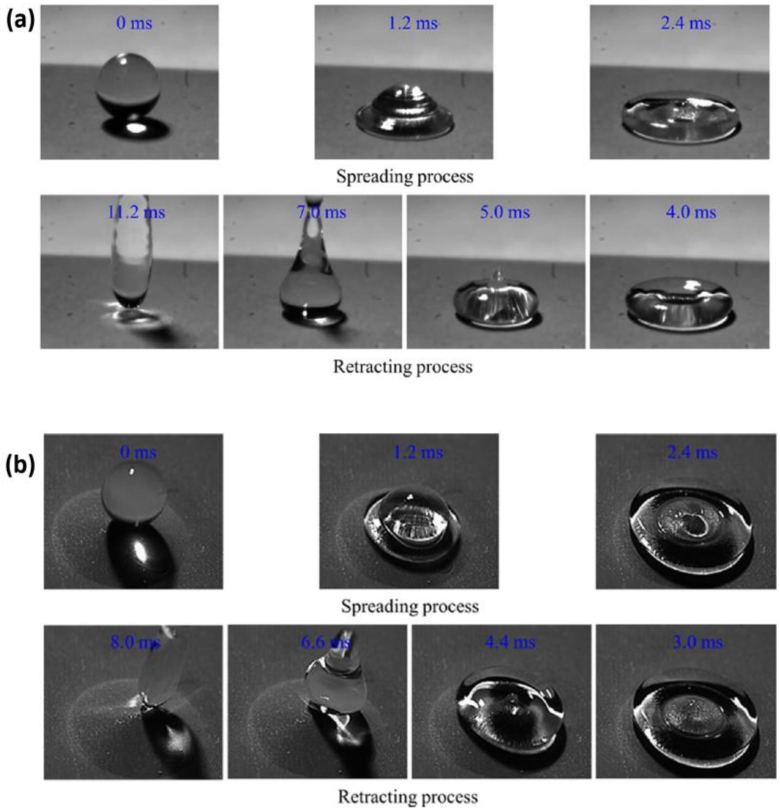

Figure 2.3 Droplet impact on (a) the flat superhydrophobic surface showing contact time is 11.2 ms and (b) on convex superhydrophobic surface revealing small contact time of 8.0 ms [65].

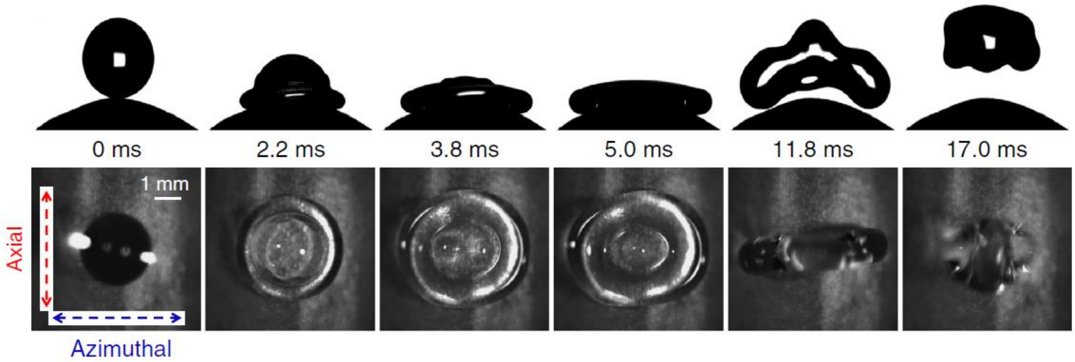

Figure 2.4 Asymmetric impact on an Echeveria leaf at We=7.9. The top row shows the cross-sectional view parallel to the azimuthal direction and bottom row shows plan view from above the droplet [67].

Hao et al. [71] experimentally studied the effects critical impact velocity of droplets impinging onto superhydrophobic surfaces. They observed a strong dependence of critical impact velocity induced wetting transition on geometrical parameters and contact angle of micropillars. The quantitative relation between the critical impact velocity of droplet and geometry parameters of microstructure is given as

$$U_c < \sqrt{\frac{-2\sigma\, cos\theta_a}{\rho} \cdot \frac{L_{cp}}{A_{cp}}} \tag{2.9}$$

where θ_a, L_{cp} and A_{cp} are the advancing contact angle, the perimeter of single pillar and area of air space between pillars, respectively.

Wang et al. [72] reported the impact outcomes of water droplets impacting on superhydrophobic carbon nanotube arrays. They varied the wetting properties of arrays and found droplet rebound at contact angle 163° and no rebound at contact angle 140°. Aria and Gharib [73] described droplet impact dynamics on superhydrophobic carbon nanotube arrays. The key parameters in their study were critical Weber number, coefficient of restitution, spreading factor and contact time. Analyzing the effects of these parameters, they observed that superhydrophobic carbon nanotube arrays show excellent water repellency.

Kwak et al. [74] studied the effects of droplet impact velocity as well as intrinsic wettability of nanowires array surfaces. They also focused on Weber number and the surface free energy, and produced the relationship for transitions from rebound to wetting and rebound to splashing (Fig. 2.5). They introduced the critical Weber number (We_c), which is the minimum Weber number required for droplet rebound given as

$$\mathrm{We_c} = 12\left[cos\theta_r\left\{1-(1+cos\theta_r)^3-3sin^2\theta_r(1+cos\theta_r)^{\frac{2}{3}}\right\} - cos\theta_a\left\{1-(1+cos\theta_a)^3-3sin^2\theta_a(1+cos\theta_a)^{\frac{2}{3}}\right\}\right] \tag{2.10}$$

where θ_a and θ_r are advancing and receding contact angles, respectively. The open red circles in Figure 2.5 represent the droplet rebound.

Tsai et al. [75] experimentally investigated droplet impingement on superhydrophobic surfaces. The surfaces had similar contact angles but different roughness, i.e., one surface with regular polymeric micropatterns and the other with rough carbon nanofibers. They observed that at small Weber numbers, the droplet impact outcomes are similar for both types of surfaces, which included the Cassie state, complete rebound, partial rebound, trapping of an air bubble, jetting, and sticky vibrating water balls. However, at large Weber numbers, the splashing impacts forming several satellite droplets arose, which was more favorable for rough carbon nanofiber surfaces.

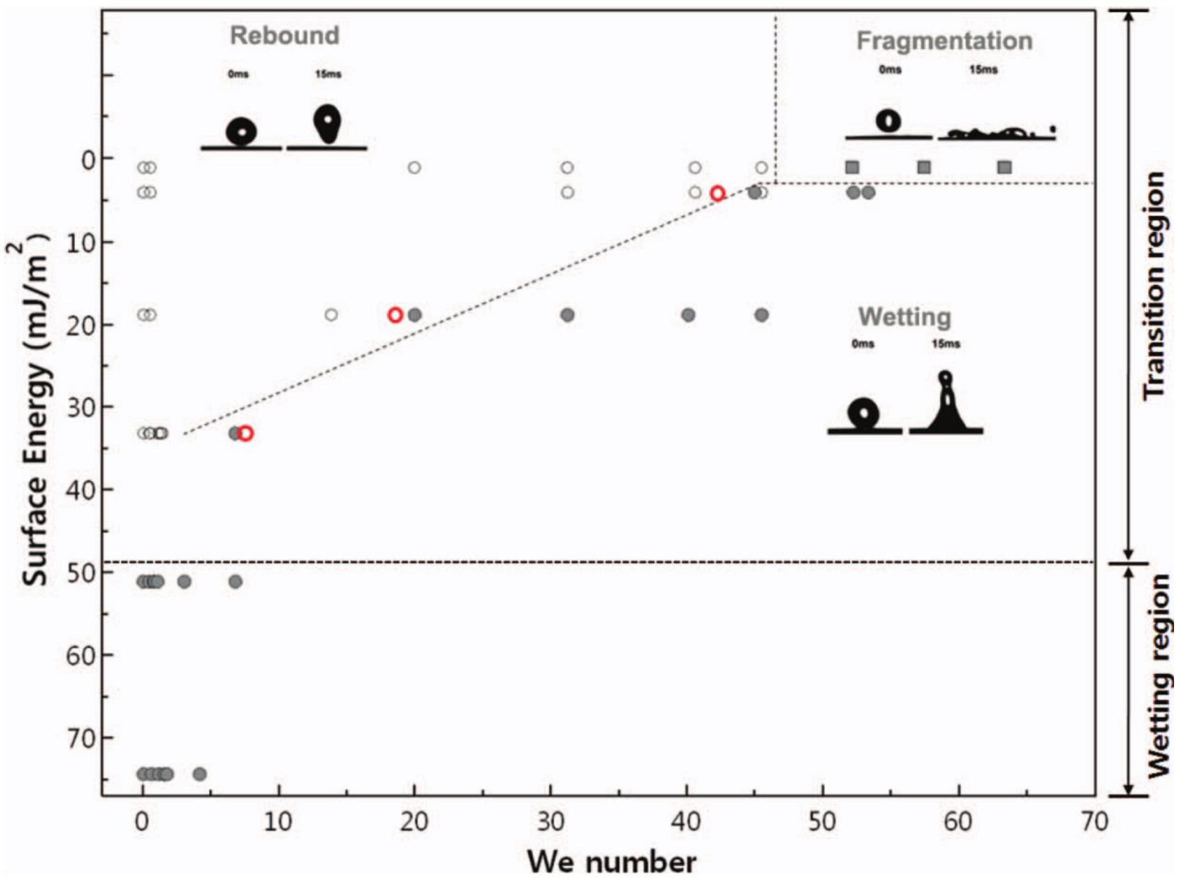

Figure 2.5 The relationship of wetting characteristics of droplet impacting with different Weber number on nanostructures composed with different surface energies that are represented by filled circles for wetting, open circles for rebound and filled rectangles for fragmentation. The critical Weber numbers of rebound/wetting transition are represented by open red circles [74].

Lee et al. [76] explained water droplet bouncing on the multiscale hierarchical nanostructures by employing free energy barrier (FEB) analysis. They found that multiscale hierarchical nanostructures show low FEBs, which induce higher contact angle and droplet rebound. McCarthy et al. [77] studied the roles micro and nano scale components of hierarchical superhydrophobic surfaces on droplet impingement. They found that droplet rebounds on the hierarchical surfaces with impact velocities larger than 4.3 m/s, whereas droplet experiences wetting transition on nanostructured surfaces at an impact velocity of 2.7 m/s. Kim et al. [78] reported the droplet impact dynamics on different hydrophobic surfaces with various length scale structures, including smooth, micro, nano, and hierarchical micro/nano structures. They found that the microstructures provide resistance on droplet spreading and retraction. The nanostructures feature extreme water-repellency, whereas the micro/nano structures produce droplet fragmentation.

Different from previous works, the current work focuses on fog droplet impact dynamics on micro-scale nanotextured bumps inspired from dessert beetle superhydrophobic surface area's micrometer scale flatten hemispherical bumps. The state of fog droplet subsequent to impact can be crucial to water collection. As a droplet hitting on nanotextured bump can either rebound or deposit. The rebounding droplet jumps back to atmosphere, and hence is lost, which reduces the water collection rate. On the other hand, the deposited droplet can have two possible states; the Cassie–Baxter state (droplet remains suspended on the nanostructures) or the Wenzel state (droplet penetrates into the structure). Droplet in the Cassie state can easily be removed from the surface and thus more favorable for water collection. On the contrary, the wetting and rebounding droplets may degrade the water collection efficiency of the surface. The outcome of droplet impact depends on geometrical parameters of the nanotextured bump and impact velocity. Therefore, focus is placed on effects of Weber number (which represent the impact velocity), post height, interpost spacing and bump radius. The relationships between bump geometrical parameters and Weber number are established to determine range of the parameters that can promote Cassie state, which in turn can be helpful to improve the water collection ability of the surface.

2.1.3 OBLIQUE IMPACT OF TWO SUCCESSIVE DROPLETS ON A FLAT SURFACE

Impact of droplets on solid surfaces is a commonly observed phenomenon both in nature and in industrial applications, such as ink-jet printing [79,80] , plasma spraying, spray cooling [81], droplet fuel mixtures in internal combustion engines and microfluidics [82], and hence it is of fundamental and practical importance. In the past century the dynamics of droplet normally impacting on surfaces has been extensively investigated [34–37,40,83–86], which has been well reviewed by Yarin [49]. Apart from normal impact, works are also available in which oblique impact of single droplet is studied. Šikalo et al. [62] investigated droplet impact and spreading on dry walls and liquid films with low impact angles by looking at the effects of impact angle (Fig 2.6 (a)), Weber number and surface properties on the occurrence of droplet rebound. Lunkad et al. [63] studied the effects of surface inclination, surface properties, liquid properties and impact velocity on the dynamics in different regimes of droplet spreading: spreading and sliding, splash, and rebound and deformation. Particularly, they focused on surface wetting characteristics by using the static contact angle (SCA) and dynamic contact angle (DCA) models. They found that the DCA model performed better in predicting the spreading behavior. Shen et al. [64] used the lattice Boltzmann method (LBM) to study complex asymmetric spreading on slanted surfaces by investigating droplet spreading, contact line motion and topological evolution. They observed asymmetric spreading coupled with sliding motion. Furthermore, increasing hydrophobicity reduces the wetted area with faster droplet motion.

Impact of successive droplets further encompasses the dynamics of collision and coalescence of one droplet with another that is stationary or has hit the surface slightly earlier. The coalescence of a moving droplet with a stationary droplet on a surface has been studied both experimentally and numerically [87–89] (Fig. 2.6 (b)). Li et al. [87] focused on the spreading length and identified three different coalescence mechanisms. To define these mechanism, the term spreading length is used. The spreading length is the ratio of actual spreading of two impacting droplets to the sum of spreading diameter of single droplet and center to center spacing between two droplets. When the sum of spreading diameter of single droplet and center to center spacing between two droplets is equal to actual spreading, the ratio is equal to one and spreading is called ideal spreading. If the maximum spreading length is larger while minimum spreading length is smaller than the ideal spreading length, the coalescence is called drawback due to retraction. When maximum and minimum spreading lengths are both larger than ideal spreading length, the coalescence is called additional spread. Finally, if both spreading lengths are smaller than ideal spreading length, the coalescence is called drawback not due to retraction. Graham et al. [88] carried out a combined experimental and numerical study on coalescence of two droplets with various wettability and offsets. It was found that the maximum spreading length decreased with increasing the hydrophobicity and offset, but increased with the droplet inertia. The dynamics and intermixing of two similar-sized droplets normally impacting on a flat surface was studied by Castrejón-Pita et al. [89]. They did not see the occurrence of mixing during the impact and coalescence. Roisman et al. [90] experimentally and theoretically studied the velocity, thickness and height of the uprising liquid sheet formed from the impact of two droplets. Raman et al. [91] reported the formation of crown and central uprising jet during the impact and subsequent coalescence of two droplets simultaneously impinging on a liquid film. Air bubbles entrapment and segment detachment from the surface depending on the Bond number and Weber number for two droplets impacting on a dry surface was investigated by Wu et al. [92]. Zhou et al. [93] applied an improved lattice Boltzmann method to investigate multiple droplet impact and subsequent interactions. Fujimoto et al. [94] also experimentally investigated the normal impact of two successive droplets (Fig. 2.6 (c)), and looked at the influence of impact interval between the droplets on the evolution of the diameter of resulting liquid film. It was shown that, although the non-dimensional diameter of the liquid film is larger than that in the single droplet case, they share a similar variation trend. Tong et al. [95] observed two modes of interaction, namely in-phase and out-of-phase, depending on the interdroplet spacing. Their results indicated an increase in maximum spread factor with increasing trailing droplet velocity. Recently, Raman et al. [96] also studied the modes of droplet impact depending on the velocity ratio of the leading and trailing droplets. In addition, they investigated the droplet offset and observed asymmetric coalescence. By fixing the offset between two droplets, the same group [97] also studied simultaneous impact of the two droplets on a surface with one droplet having an oblique velocity, and observed the formation of asymmetric ridge.

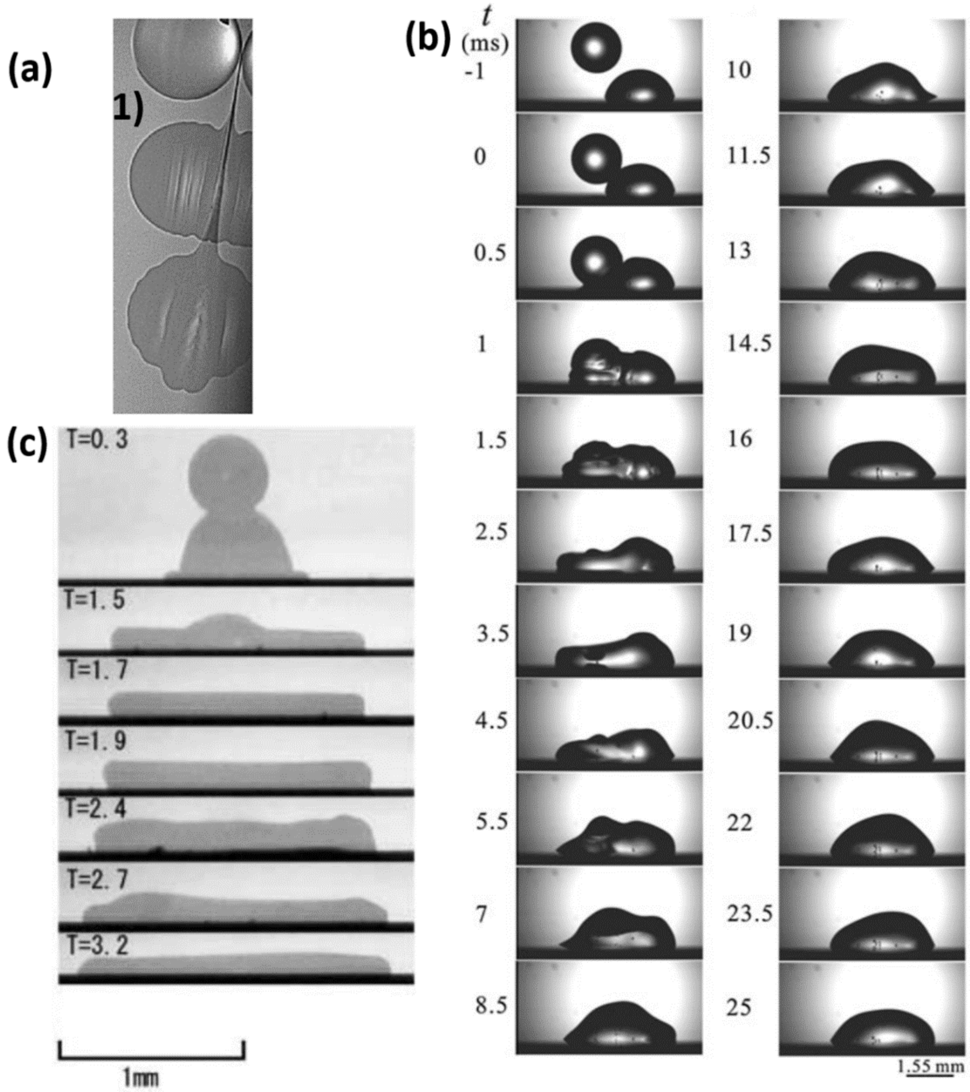

Figure 2.6 The spreading of (a) a single droplet on inclined surface at inclination α=10º [62] (b) two droplets and following coalescence with overlap ratio = 0.35 on a level surface [87] and (c) two droplets successive impact on level surface [94].

Different from all the previous studies, in the present study we aim to investigate the dynamics of two successive droplets obliquely impacting on a flat surface, including both the impact process and the subsequent coalescence. The focus is placed on the effects of impact obliqueness (equivalently the surface inclination if the droplet velocity is fixed) and lateral/longitudinal offset between the two droplets. This study is directly motivated by fog harvesting, in which tiny fog droplets successively impinge on an inclined mesh, coalesce, grow in size, and roll off the mesh surface due to gravity [61]. Recently, bio-inspired meshes are being prepared for efficient fog collection. Such mesh wires can have a diameter (or width in case of flat ribbons) of micrometers [16], where the role of droplet offset also becomes important for determining minimum mesh wire diameter (or ribbon width). This study is also important for the understanding of some natural phenomena, such as rain droplets impacting on car windscreen, spray coating where the droplet impact angle is a key for uniform deposition, and spray on plant leaves in agriculture herbicide applications [98].

2.2 CONDENSATION

In condensation a phase change from the gas or vapor phase to the liquid or solid phase occurs when the temperature of the gas is lowered below its saturation temperature. Condensation occurs when vapor come into contact with surface having temperature under the saturation temperature of the vapor.

2.2.1 DROPWISE AND FILMWISE CONDENSATION

Broadly condensation can be categorized into two groups namely, bulk condensation and the surface condensation. The example of bulk condensation is fog formation where condensation vapor condense in a gas. On the other hand, in surface condensation the surface temperature is below the saturation temperature of vapor and vapor impinge on the surface. The surface condensation can be classified into two groups; filmwise condensation and dropwise condensation (Fig. 2.7).

In filmwise condensation a liquid film is formed on surface while in dropwise condensation the droplets are formed, when vapor come into contact with surface. Generally, filmwise condensation is more favorable on hydrophilic surfaces. In the presence of gravity the condensed liquid film slides downward. The thickness of film grows with time in the flow direction, which increases the thermal resistance to heat transfer. The thickness, mass flow rate, velocity distribution of condensing film are explained in detail in the references [99–101].

Different from filmwise condensation, the vapor condenses over the surface forming several droplets of various sizes in case of dropwise condensation. The droplets originate at nucleation sites. These small droplets grow bigger in size owing to condensation, coalesce into larger droplets, and then get removed from the surface. Thus, clearing space for formation of new droplet. So, there is not continuous liquid film resisting the heat transfer. That is why larger heat transfer coefficients can be achieved in dropwise condensation compared to filmwise condensation. However, maintaining dropwise condensation over longer periods of time itself is an extremely challenging task.

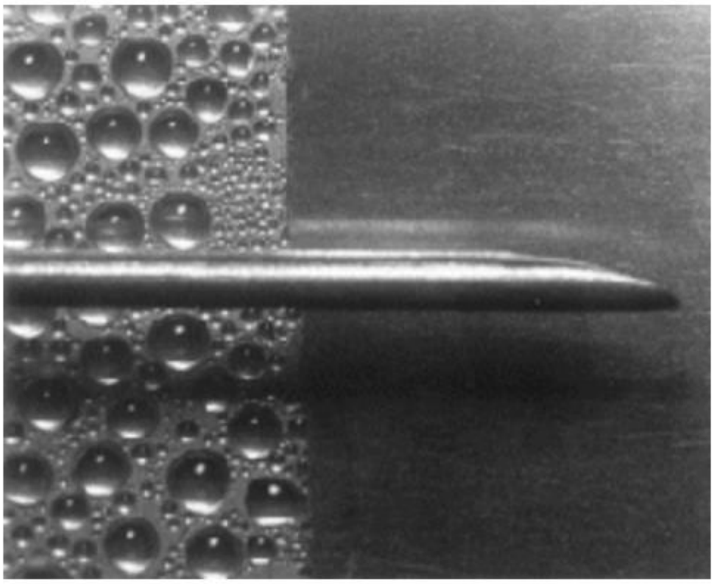

(a) (b)

Figure 2.7 Condensation (a) dropwise (b) filmwise [102].

2.2.2 CRITICAL VOLUME OF A CONDENSING DROPLET SHEDDING FROM BEETLE INSPIRED BUMPS.

Dessert beetle inspired surfaces have been widely mimicked for water collection purposes. Recently, water collection rates of beetle inspired hydrophilic/superhydrophobic patterned surfaces have been found higher than that of completely hydrophilic or hydrophobic surfaces [24–26]. Yin et al. [25] prepared the surface by combining a femtosecond-laser fabricated polytetrafluoroethylene nanoparticles deposited mesh and a hydrophilic copper sheet. The as-prepared sample surface had shown enhanced fog collection efficiency compared with the uniform superhydrophobic or superhydrophilic surface (Fig. 2.8). Wang et al. [28] proposed an efficient water collecting fabric with a superhydrophobic surface combined with TiO_2 bumps. TiO_2 bumps show superhydrophilic behavior when exposed to sunlight. Such fabric can lead to the development of smart water collection devices. Zhang et al. [24] developed a direct method to produce superhydrophilic/superhydrophobic pattern using inkjet printing technology. They also showed enhanced water collection efficiency of micropatterned superhydrophobic surfaces prepared by this inkjet printing method (Fig. 2.9). Hou et al. [32] prepared a hybrid surface that contains hydrophilic patches confined to the top of pillars surrounded by superhydrophobic nanograss. The resulting surface was able to synergistically combine filmwise and dropwise condensation, which helped in achieving higher water collection rate.

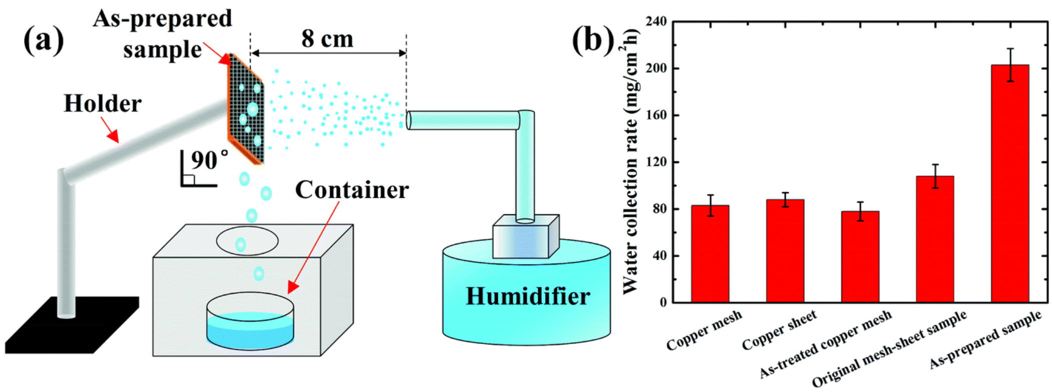

Figure 2.8 (a) Schematic of the fog-harvesting system. (b) Water collection rates of the different samples [25].

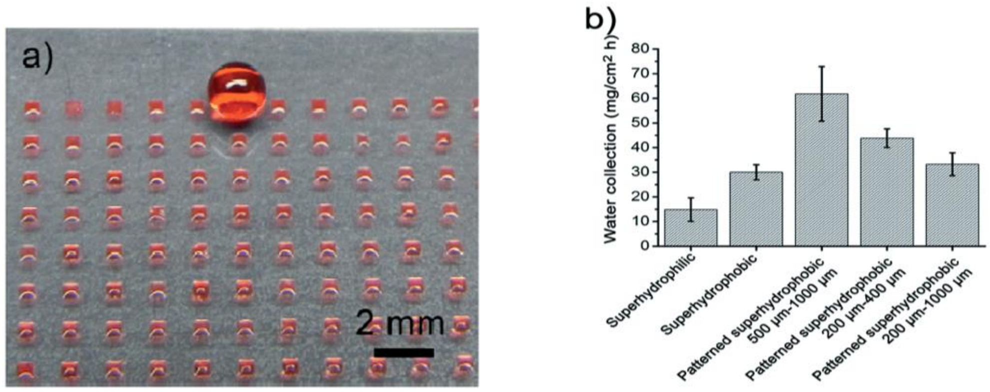

Figure 2.9 Small water droplets attached on hydrophilic patterns on the superhydrophobic background surface after removal of the substrate from water. The water is stained with red ink to help in observation. A large water droplet (6 µL) is suspended on pattern. (b) Water collection efficiency of different patterned and unpatterned surfaces [24].

Furthermore, Garrod et al. [20] studied micro-condensation efficiency of microcondensers produced by fabricating hydrophilic pixels onto superhydrophobic background. They investigated chemical nature and dimensions of hydrophilic pixels and obtained optimum (500 µm / 1000 µm) hydrophilic pixel size / center to center distance by comparing condensation results with Stenocara beetle's elytra pattern. Lee et al. [103] investigated water harvesting via vapor condensation for different surfaces, including hydrophilic/hydrophobic surface, uniform hydrophilic surface and uniform hydrophobic surface. Their results showed higher rates of water condensation for uniformly hydrophilic surface than other surfaces. White et al. [60] studied fog harvesting for a number of patterned surfaces, including hydrophobic, channel patterned, hydrophobic patch patterned, hydrophilic patch patterned, and hydrophilic, made from different materials. Analysing the amount of collected water they found that wind and thermal convection are more influencing parameter rather than wettability and pattern. Furthermore they observed different water removal mechanisms based on different surface materials and patterns. Dorrer and Rühe [21] prepared hydrophilic/superhydrophobic samples to mimic Stenocara beetle pattern. They have investigated the critical volumes for various wettability contrasts, patch diameters and surface inclinations at which droplet is rolled off the circular hydrophilic patched surface. Hong et al. [22] studied pinning and dewetting mechanism of a droplet from a designed patch on the superhydrophobic background surface. They investigated the influence of patch shape and size experimentally, theoretically and through simulation. They found that the critical inclined angle of the slanted surface, at which pinned droplet dewets the patch, increases linearly with pinning length. The pinning length is equal to the side length normal to sliding direction for square and rectangular patches.

Different from previous studies, in this work we aim to investigate the droplet shedding from dessert beetle inspired bumps of different heights. Furthermore, the droplet dewetting from the milimeter-scale bump is compared with the micro-scale bump. Other key parameters of investigation include droplet critical volume, bump shape, bump diameter, surface inclination and wettability. A scaling law is developed for estimation of the critical bump height at the end.

2.3 DROPLET IMPACT IN PRESENCE OF SATURATED VAPOR

Water collection through fog harvesting majorly incorporates the droplet impact process. Fog consists of small airborne droplets that impact on surface, coalesce into bigger droplets and get removed from surface with the help of gravity. Besides, water can also be collected by condensation of fog droplets on the surface. Recently, condensation on nature inspired surfaces has also been investigated in literature [32,104,105]. The combination of both droplet impact and condensation processes can be articulated as the droplet impact simultaneous with condensation.

A number of studies are available in literature on droplet impact on heated walls [106–108]. Liang and Mudawar [109] presented a comprehensive review on dynamics of droplet impact on heated walls. One the other hand, many previous studies discussed the droplet impact on lower temperature surfaces, most of them focused on droplet freezing effects under icing conditions though [110–112]. Some reports have also focused on droplet impact on surface at lower temperature compared to droplet temperature. Siavoshani [113] studied effects of surface properties on molten metal droplets. They maintained droplet temperature higher than surface temperature. Using single shot photographic technique they studied droplet spreading and final outcomes. Shiri [114] studied the heat transfer for droplet impact as well as rebound on superhydrophobic surfaces, and compared it with the case where droplet sticks to the surface instead of rebound. They also investigated heat transfer for both cold and hot droplets compared to surface temperature. However, effects of humidity were not investigated in their work. Alizadeh et al. [115] studied temperature dependent droplet impingement on hydrophilic as well as hydrophobic surfaces. They kept droplet temperature constant while surface temperature was varied in range from below freezing point to boiling point. They observed slow droplet retraction at lower temperature, which was slowest for hydrophilic surfaces.

In the present work, the surface temperature variation effects on fog harvesting are investigated. If humidity is fixed at 100% then this problem can be articulated as the impact of droplet at saturated temperature in the presence of saturated vapor on a surface set at lower temperature. The focus is placed on parameters, including the Jakob number, the Prandtl number, surface inclination and Weber number.

2.4 LBM SIMULATIONS ON DROPLET IMPACT AND CONDENSATION

In computational fluid dynamics, single phase fluid flow problems are modeled by solving the Navier Stokes equations. To solve multiphase problems, additional calculations to track interface motion must be carried out. The commonly used traditional multiphase methods include, front tracking [116] method, the volume of fluid (VOF) [117] method, and the level set [118] method. The front tracking method is usually unable to simulate problems involving interface tortuous and break up, such as interface coalescence [119,120]. Volume of fluid method and level set method have been widely used to model droplet impacting on surface problems [63,121–123]. They have also been used to study phase-change problems [124,125]. However, volume of fluid method can introduce some numerical diffusion, which needs very complex algorithms to be solved, rendering it inconvenient for three dimensional problems [117]. The level set method has a severe drawback of lack of mass conservation [126]. In the last few decades, LBM has emerged as a powerful and efficient tool for simulating both single phase and multiphase fluid flow problems [127–131]. Furthermore, one does not need to explicitly track interface movement [132,133].

In this thesis, LBM is used to study droplet impact and phase-change condensation problem. A number of studies have been published discussing the droplet impact on level, inclined, smooth and rough surfaces. A summary of important works related to droplet impact using LBM is presented in Table. 2.2, where information related to number of impacting droplets, surface properties and key investigation parameters is presented. The phase-change problem is important for stream generator, and the condensation heat exchanger and water collection. The phase-change lattice Boltzmann (LB) models, generally solve two evolution equations, one for the density and the other for temperature. In literature, LBM has been used to model film condensation [134–137], droplet condensation [138–140] and boiling problem [141–151]. The important LB phase change models have been reviewed, recently, in a monograph by Li et al. [152]

2.5 SUMMARY

In this chapter literature surveys on droplet impact and condensation were presented. The literature review on objectives with corresponding knowledge gaps are summarized as follows;

The droplet impact phenomenon has been well studied for single droplet impacts on level and inclined surfaces. Many reports are also available on droplet impact on micro-nano textured surfaces, including surface inclination effects. However, only few reports have been published on convex surfaces, which are limited to smooth convex surfaces. Different from the previous reports, droplet impact on hemispherical nano-textured bumps will be focused in this work.

In addition to single droplet impact, multiple droplets impact has also become an extensively studied topic. Dynamics of the falling droplet impacting on an already deposited droplet on a level surface, and successive droplets impact have been comprehensively studied in literature. Nevertheless, effects surface inclination together with lateral/longitudinal offsets for successively impacting droplets have not been discussed to date. Therefore, in this work we will focus on surface inclination and lateral/longitudinal offsets.

Inspired from beetle surface, many hydrophilic/hydrophobic surfaces investigating the condensation rates have been published in past. In these reports, the water collection rates of hydrophilic/hydrophobic patterned surfaces were compared to fully hydrophilic or hydrophobic surfaces. Some reports also considered the droplet shedding from a patch surrounding by superhydrophobic background, where the focus was placed on patch size, surface inclination and wettability contrast. However, the effects height and convex shape of beetle bumps on droplet shedding are still unclear. Therefore, in this work focus will be placed on critical volume of a condensing droplet shedding from beetle inspired bumps of different heights and shapes.

The droplet impact on hot and cold surfaces has been investigated in literature. Droplet impact on cold surfaces has mostly been studied previously under icing conditions. Furthermore, the effects of saturated vapor on droplet impact dynamics are not clearly understood. Therefore, in this study the droplet impact dynamics in the presence of saturated vapor will be revealed.

All of aforementioned problems include multiphase flow phenomenon. In multiphase flow problems interface capturing is a challenging issue. The traditional numerical models, including front tracking method, VOF, level set method require additional calculations to track the interface. Although, these methods are still being used, but the tracking of interface becomes extremely challenging in complex problems. Additionally, there can be drawbacks of numerical diffusion and mass conservation issues. On the other hand, in LBM interface in not needed to be tracked explicitly. A literature survey on previous studies on droplet impact and phase change problems using LBM was also conducted, which confirms its ability to successfully handle multiphase flow problems. Therefore, in this work LBM is used to simulate the multiphase problems.

Table 2.2 A survey of LBM studies on droplet impact on dry surfaces

S/N	Authors	2D study or 3D study	Droplets number	Surface topography/orientation	Key parameters
1	Castrejón-Pita et al. (2013) [89]	3D	two (falling droplet impact on stationary droplet)	level	contact angle hysteresis, droplet size, intermixing, surface wettability, Re, We
2	Chang and Alexander (2006) [153]	3D	one	level	gravity, wettability of striped surface, width of strips
3	Cheng et al. (2017) [154]	3D	multiple	level	contact angle, impact velocity, droplet spacing, impingement and coalescence
4	Ebrahim et al. (2017) [155]	3D	one	level	contact, angle, Re, We, ambient air and stagnation gas flow effects
5	Gupta and Kumar (2010) [83]	3D	one	level	Re, We, Oh, droplet break up

Table 2.2 A survey of LBM studies on droplet impact on dry surfaces

S/N	Authors	2D study or 3D study	Droplets number	Surface topography/orientation	Key parameters
6	Gupta et al. (2011) [84]	2D	one	level	Re, We, low density ratio, droplet break up
7	Lee and Liu (2010) [156]	3D	one	level	We, Re, Oh, contact angle, large density ratio
8	Raman et al. (2016) [96]	3D	Two (successive impact)	level	contact angle hysteresis, trailing droplet velocity, surface wettability, droplet viscosity tension, offset ratio
9	Raman et al. (2016) [157]	3D	One	level	impact velocity, impact angle, receding contact angle
10	Raman et al. (2017) [97]	3D	Two	level	one droplet has different impact angle, impact velocity, surrounding gas density, contact angle

Table 2.2. A survey of LBM studies on droplet impact on dry surfaces

S/N	**Authors**	**2D study or 3D study**	**Droplets number**	**Surface topography/orientation**	**Key parameters**
11	Shen et al. (2012) [158]	2D	one	curved surface (spherical)	We, surface wettability
12	Shen et al. (2016) [64]	3D	one	inclined	surface inclination, surface wettability
13	Tanaka et al. (2011) [159]	2D	two (falling droplet impact on stationary droplet)	level	We, contact angle, intermixing
14	Taghilou and Rahimian (2014) [160]	2D	one	level	Re, We, Pr
15	Yuan and Zhang [161]	2D	one	level	randomly structured surface, contact angle, kurtosis, skewness, We

Table 2.2. A survey of LBM studies on droplet impact on dry surfaces

S/N	Authors	2D study or 3D study	Droplets number	Surface topography/orientation	Key parameters
16	Zhang et al. (2014) [85]	3D	one	level and spherical	Bo, Oh, Re, We, post impact droplet film thickness, spreading factor
17	Zhang et al. (2014) [162]	2D	one	curved surface	Galilei number Ga, Re, We, high density ratio
18	Zhang et al. (2014)[163]	3D	one	level	We, Re, Oh, large density ratio
19	Zhou et al. (2014) [93]	3D	multiple	level	Oh, We, multiple droplet interactions
20	Zu et al. (2011) [164]	3D	one	level	chemically heterogeneous and microstructured surfaces

CHAPTER 3

MULTIPHASE LATTICE BOLTZMANN METHOD

This chapter describes the methodologies used in this work. The introduction of traditional computational fluid dynamics (CFD) methods along with multiphase models, such as front tracking method, volume of fluid method (VOF) and level set method is presented. Then, the basics of lattice Boltzmann (LB) multiphase Shan-Chen model are described. The important boundary conditions are briefly elaborated. Thereafter, the mathematical formations of LB multiphase models, including multiple-relaxation-time (MRT) pseudopotential model and He–Chen–Zhang model, and phase-change model are presented.

3.1 NUMERICAL METHODS FOR MULTIPHASE FLOW

The continuous advancement of computational power has stimulated the use of CFD for numerical solutions of fluid flow problems. Generally, CFD employs mathematical models, which are basically ordinary or partial differential equations, consisting of convective and diffusive transport terms. The examples of such model equations, in fluid flow problems, are Navier–Stokes equations that lack analytical solutions. These equations contain nonlinear terms making them challenging to solve. To approximate Navier–Stokes equations one has to use numerical methods.

Over the years, traditional numerical methods, including the finite difference method (FDM), finite volume method (FVM) and finite element method (FEM) are being used to approximate Navier-Stokes equations. FDM is basically performed by creating a uniform grid, then discretizing the governing equations on it. In these equations the derivatives are basically replaced with the equivalent finite difference approximations, and then the resulting algebraic equations are solved using appropriate numerical tools. FVM, on the other hand, solves the governing equations that are integrated over control volumes. In FEM, governing equations are multiplied with a weight function and integrated over an element.

Multiphase flow problems are more challenging to model, as additional care is needed to track the dynamics of movement of interface compared to single phase flow problem. Most widely used traditional multiphase methods include front tracking (FT), volume of fluid method (VOF) and level set method. FT method is based on Lagrangian approach, an easy approach to track moving interface, but the difficulties arise in coalescence and break up cases [119,120]. VOF employs the marker and cell methods [117,165], in which a fraction function is used. The fraction function can have values in range from 0 to 1. When fraction function value is 0, it is completely filled with gas, and 1 when occupied by liquid. If value of fraction function is in between 0 and 1, the interface lies within the cell. The shortcoming of volume of fluid method is introduction some numerical diffusion [117]. In the level set method [118] the interface is determined by closed curve using level set function. The boundary or interface has zero level set on curve, positive inside the curve and negative outside the curve. However, level set method suffers from mass conservation problems [126], which become noticeable in complex geometry cases.

Over last few decades, a different type of method, namely, the Lattice Boltzmann Method (LBM) has emerged as robust numerical tool to model fluid flow problems. The LBM provides an alternative of CFD in simulating complex multiphase, phase-change and heat transfer problems [127–131,166–168]. The fundamental procedure of LBM is to solve the kinetic equation for the particle distribution function [169]. The macroscopic variables, such as velocity and density are determined from the moments of these distribution functions. In order to recover the Navier–Stokes equations in the low Mach number limit one can use Chapman–Enskog analysis [170].

LBM due to its kinetic nature provides many advantages such as, simple boundary conditions and natural adoption of parallelization. Moreover, the interface does not need to be tracked explicitly [132,133]. The fluid-solid interactions and surface wetting properties can be easily realized without implementation of the additional complex formulations [171,172]. In single phase LB models, there is no need to solve Laplace equation at each time step in order to satisfy continuity equation as it is required in solving Navier–Stokes equations in CFD, and this is also true for many multiphase models [128,133].

3.2 LATTICE BOLTZMANN MULTIPHASE FLOW MODELS

The LBM has achieved considerable success as an alternative approach of simulating multiphase flow problems [127]. The comprehensive introduction of fundamentals of the LBM can be found in recent monographs [173,174] as well as in review articles [127,175].

Over last two decades, several LB models have been developed to simulate multiphase flow problems [128–131,133,176–178]. In single component Shan-Chen LB model [131,133] the phase segregation is achieved by incorporating an interparticle interaction force that realizes the non-ideal gas behavior of the single chemical component. Rothman and Keller's color LB model [176,177] employs two distribution functions to related to two components, one fluid component is represented by red color and the other component by blue color. A recoloring step is used to implement the phase segregation. Swift et al. [128] free energy model uses a free energy based lattice model. This model is able to simulate both the static and the dynamic properties of a liquid-vapor system . Inamuro et al. [178] developed a model based on the free energy method for stable simulations at large density ratio. However, this employs Poisson equation that reduces the simplicity of the LBM. In He et al. [129] model two distribution functions, i.e., one for pressure and the second for an index function, are introduced. The LB equations for the pressure and index function are able to recover the Navier–Stokes equations and the Cahn-Hilliard type interface-tracking equation, respectively. Lee and Lin [130] further developed the He et al.'s [129] model and achieved high density ratio using a stable discretization of directional derivatives.

3.3 SHAN-CHEN MULTIPHASE MODEL

In the Shan-Chen (SC) [131,133] multiphase flow model the phase segregation is mainly determined by microscopic molecular interactions. The SC model, also known as pseudo-potential model, is the widely used due to its simplicity and efficiency. The important feature of this model is the pseudopotential which is often called effective mass, and it depends on the local density and basically represents the microscopic molecular interactions. The single component fluid spontaneously segregates, when the temperature is under the critical temperature, into two phases corresponding to high and low densities. Furthermore, in this model the interface is not needed to be tracked explicitly as it is done in CFD. The fluid density changes smoothly across the interface from one bulk value to another, and it spans the width of several lattice nodes. In spite of the simplicity, this model has become promising method for simulating the multiphase problems, especially those incorporating complicated interface changes, such as breakup, coalescence, deformation, etc.

The temporal evolution equation of particle distribution function is written as

$$f_i\left(\mathbf{x}+\mathbf{e}_i\delta_t, t+\delta_t\right)-f_i\left(\mathbf{x},t\right)=-\frac{1}{\tau}\left(f_i\left(\mathbf{x},t\right)-f_i^{(eq)}\left(\mathbf{x},t\right)\right) \tag{3.1}$$

where $f_i\left(\mathbf{x},t\right)$ and $f_i^{(eq)}\left(\mathbf{x},t\right)$ are the particle and equilibrium distribution functions at $\left(\mathbf{x},t\right)$, $\mathbf{e}_i$ is the particle velocity along the i[th] direction and τ is the single-relaxation time parameter that controls the rate of approach to equilibrium. In LBM simulations, the Eq. (3.1) is evolved in the following two steps:

$$\text{Collision step}: \qquad f_i^*\left(\mathbf{x},t\right)=f_i\left(\mathbf{x},t\right)--\frac{1}{\tau}\left(f_i\left(\mathbf{x},t\right)-f_i^{(eq)}\left(\mathbf{x},t\right)\right) \tag{3.2}$$

$$\text{Streaming step}: \quad f_i\left(\mathbf{x}+\mathbf{e}_i\delta_t, t+\delta_t\right)=f_i^*\left(\mathbf{x},t\right) \tag{3.3}$$

where f_i and f_i^* denote the pre- and post-collision states of the distribution function, respectively.

The lattice models in LBM follow a notation of D_xQ_y reference system, where x denotes the number of dimensions and y denotes the number of particle velocities. Most commonly used lattice models are D2Q9 and D3Q19 in two-dimensions and three-dimensions respectively (Fig. 3.1).

The equilibrium distribution function is defined as

$$f_i^{(eq)}=\omega_i\rho\left[1+\frac{\mathbf{e}_i\cdot\mathbf{u}}{c_s^2}+\frac{\left(\mathbf{e}_i\cdot\mathbf{u}\right)^2}{2c_s^4}-\frac{\mathbf{u}^2}{2c_s^2}\right] \tag{3.4}$$

where ω_i are the weight coefficients, c_s^2 is the lattice sound speed, and c is the lattice speed, which is defined as $c=\delta_x/\delta_t$.

For two-dimensional lattice (D2Q9) [179], the weight coefficients are $\omega_0 = 4/9, \omega_{1-4} = 1/9,$ and $\omega_{5-8} = 1/36$ and lattice speed of sound is $c_s = c/\sqrt{3}$. The discrete lattice velocity vectors $\mathbf{e}_i$ are given as

$$\left[\mathbf{e}_0, \mathbf{e}_1, \mathbf{e}_2, \mathbf{e}_3, \mathbf{e}_4, \mathbf{e}_5, \mathbf{e}_6, \mathbf{e}_7, \mathbf{e}_8\right] = c\begin{bmatrix} 0 & 1 & 0 & -1 & 0 & 1 & -1 & -1 & 1 \\ 0 & 0 & 1 & -1 & -1 & 1 & 1 & -1 & -1 \end{bmatrix} \tag{3.5}$$

For three-dimensional lattice (D3Q19) [180], the weight coefficients are $\omega_0 = 1/3, \omega_{1-6} = 1/8,$ and $\omega_{7-18} = 1/36$ and lattice speed of sound is $c_s = c/\sqrt{3}$. The discrete lattice velocity vectors $\mathbf{e}_i$ are given as

$$\begin{aligned} &\left[\mathbf{e}_0, \mathbf{e}_1, \mathbf{e}_2, \mathbf{e}_3, \mathbf{e}_4, \mathbf{e}_5, \mathbf{e}_6, \mathbf{e}_7, \mathbf{e}_8, \mathbf{e}_9, \mathbf{e}_{10}, \mathbf{e}_{11}, \mathbf{e}_{12}, \mathbf{e}_{13}, \mathbf{e}_{14}, \mathbf{e}_{15}, \mathbf{e}_{16}, \mathbf{e}_{17}, \mathbf{e}_{18}\right] \\ &= c\begin{bmatrix} 0 & 1 & -1 & 0 & 0 & 0 & 0 & 1 & -1 & 1 & -1 & 1 & -1 & 1 & -1 & 0 & 0 & 0 & 0 \\ 0 & 0 & 0 & 1 & -1 & 0 & 0 & 1 & 1 & -1 & -1 & 0 & 0 & 0 & 0 & 1 & -1 & 1 & -1 \\ 0 & 0 & 0 & 0 & 0 & 1 & -1 & 0 & 0 & 0 & 0 & 1 & 1 & -1 & -1 & 1 & 1 & -1 & -1 \end{bmatrix} \end{aligned} \tag{3.6}$$

The macroscopic quantities, such as density ρ and momentum density $\rho\mathbf{u}$ are obtained as moments of the distribution function f_i as follows:

$$\rho = \sum_i f_i \tag{3.7}$$

$$\rho\mathbf{u} = \sum_i \mathbf{e}_i f_i \tag{3.8}$$

The kinematic viscosity is calculated as,

$$\nu = c_s^2 \left(\tau - 0.5\right) \delta t \tag{3.9}$$

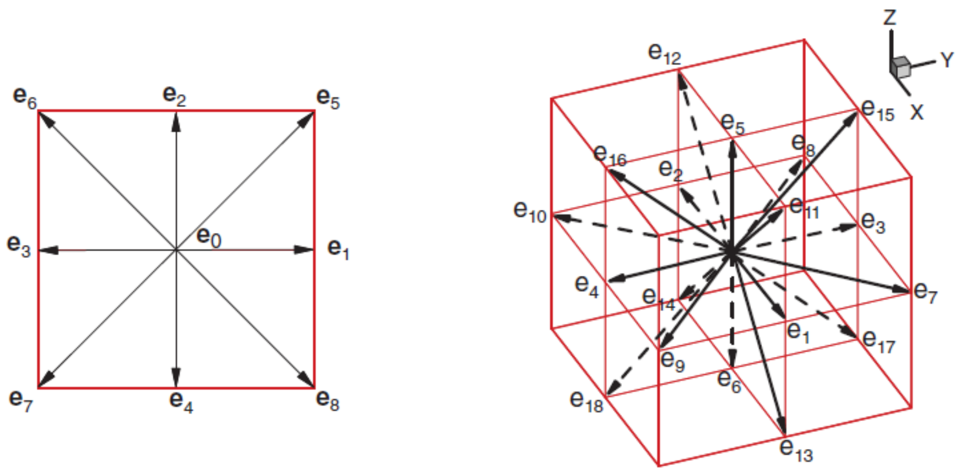

Figure 3.1 (a) Two dimensional D2Q9 Lattice (b) three dimensional D3Q19 Lattice [181]**.**

In the original D2Q9 SC model, the interparticle force responsible for phase segregation is given as [171]

$$\mathbf{F}_{\text{int}}(\mathbf{x},t) = -G\psi(\mathbf{x},t)\sum_i w_i \psi(\mathbf{x}+\mathbf{e}_i\Delta t, t)\mathbf{e}_i \tag{3.10}$$

where G is a parameter that controls the strength of the interparticle force, and ψ is called the effective mass and it depends on the local density. The effective mass can be related to equation of state [182] as

$$p = \frac{\rho}{3} + \frac{G}{6}\psi^2 \tag{3.11}$$

Solving for pressure p for a given equation of state (EOS), and substituting p into Eq. (3.11), the corresponding ''effective mass'' given as

$$\psi(\rho) = \sqrt{\frac{2(p-\rho c_s^2)}{c_s^2 G}} \tag{3.12}$$

Thus, the Eq. (3.11) allows use of any arbitrary equation of state to implement the interparticle interactions. The EOS relates the density of gas and liquid phases to the given pressure and temperature. The choice of suitable EOS is curial, as the attractive force which causes the phase separation is characterized by non- ideal EOS. The selection of EOS depends on several key points, such as density ratio of gas and liquid phases, reduction of spurious currents at interface, the agreement between mechanical stability solution and thermodynamic stability. The details of these criteria can be found in reference [182] . Yuan and Schaefer [182] studied various equation of states in a single component multiphase LB model. They found Carnahan Starling EOS can produce smaller spurious currents and can also be applied to wide range of density ratios. Carnahan and Starling equation of state is given as

$$p = \rho R_g T \frac{1 + b\rho/4 + (b\rho/4)^2 - (b\rho/4)^3}{(1 - b\rho/4)^3} - a\rho^2 \tag{3.13}$$

In this thesis, Carnahan and Starling equation of state (as it produces smaller spurious currents [182]) is used for all works apart from the phase-change method, which employs Peng-Robinson EOS. Peng-Robinson equation of state , when used with Gong and Chen [183] improved model, also produces smaller spurious currents. This EOS is described in section 3.7.

Velocity shifting method is used to incorporate the body force term through equilibrium particle distribution function (Eq. (3.4))

$$\mathbf{u}^{eq} = \mathbf{u} + \frac{\mathbf{F}\tau}{\rho}\delta t \tag{3.14}$$

where **F** is total body force, which is given as

$$\mathbf{F} = \mathbf{F}_{\text{int}} + \mathbf{F}_{ads} + \mathbf{F}_g \tag{3.15}$$

where, $\mathbf{F}_{\text{int}}$ is interparticle interaction force responsible for phase segregation, $\mathbf{F}_{ads}$ is the adhesion force between solid surface and fluid and $\mathbf{F}_g$ is the gravitational force.

The wetting characteristics of the surface are achieved by computing a specific adhesion force between the gas/liquid phase and solid walls, which is given as

$$F_{ads}(\mathbf{x},t) = -G\psi\left(\rho(\mathbf{x},t)\right)\sum_a w_a \psi\left(\rho_w\right) s\left(\mathbf{x} + \mathbf{e}_a \Delta t, t\right)\mathbf{e}_a \tag{3.16}$$

To achieve the desired contact angle the parameter ρ_w is accordingly tuned. This parameter actually represents a fluid density (virtual density) on the wall that has the sole purpose of setting the contact angle [172]. The whole fluid velocity, which is also the real velocity, is calculated by the following equation

$$\rho\mathbf{U} = \rho\mathbf{u} + \frac{\delta t}{2}\mathbf{F} \tag{3.17}$$

3.4 BOUNDARY CONDITIONS

In LBM, different boundary conditions can be easily implemented. The periodic, bounce back and pressure boundary conditions are introduced below.

3.4.1 PERIODIC BOUNDARY CONDITIONS

Periodic boundary conditions are the simplest one, and they arise from flow symmetry. They are used to isolate repeating flow pattern. In periodic boundary conditions, fluid leaving from one side re-enters from the opposite side. In other words, the systems becomes closed by considering the edges as if they are attached to opposite edges.

Figure 3.2 Illustration of distribution function for periodic boundary conditions on left and right walls.

Consider a two dimensional domain in which the left wall is at x = 1 and right wall is at x = nx (Fig 3.2). In periodic boundary conditions the distribution functions leaving the right wall are the same that are entering the left wall. The distribution functions for periodic boundary conditions on left and right walls are determined as

Left wall

$$f_1(1, y) = f_1(nx, y)$$

$$f_5(1, y) = f_5(nx, y)$$

$f_8(1, y) = f_8(nx, y)$

Right wall

$f_3(nx, y) = f_3(1, y)$

$f_6(nx, y) = f_6(1, y)$

$f_7(nx, y) = f_7(1, y)$

3.4.2 BOUNCE-BACK BOUNDARY CONDITION

In LBM simulations, bounce-back boundary condition is most commonly used solid wall boundary condition. By the so-called bounce-back, it means that when fluid particles reach a boundary node, they scatter back along the incoming direction of particles. Generally, two kinds of bounce-back boundary conditions are widely used; fullway bounce-back and halfway bounce-back. In fullway bounce-back [184], particles travel all the way to solid nodes and return back in the next collision step (Fig. 3.3 (a)). It can be noticed that particles need two time steps to go forth and return back. In halfway bounce-back [185], particles travel only half of the link distance and return back in streaming step. It take only one time step for particles to return.

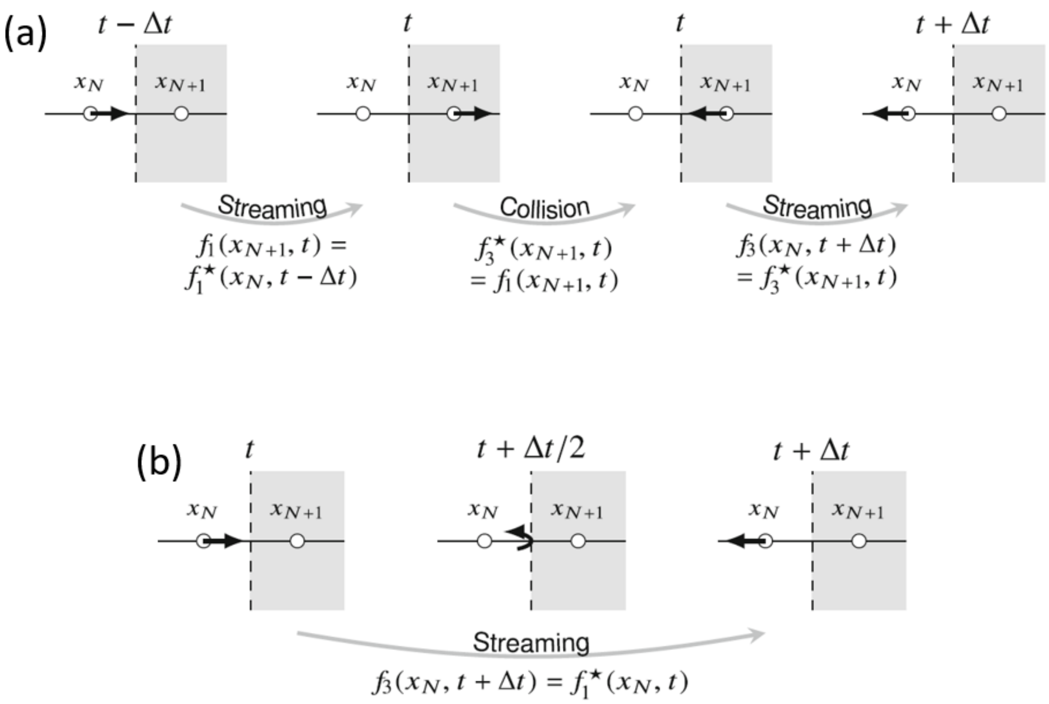

Figure 3.3 The evolution of distribution function for (a) fullway bounce-back and (b) halfway bounce-back. The particle's direction is represented by arrow, and the wall is represented by dashed line [186]**.**

3.4.3 INLET/OUTLET BOUNDARY CONDITIONS (PRESSURE/VELOCITY BOUNDARY CONDITION)

In LBM, the pressure or velocity boundary conditions are used at inlet or outlet boundaries. For condensation the vapor are introduced in domain using Zou-He [184,187] pressure or velocity boundary conditions. The three dimensional extension can be found in reference [188]. These boundary conditions are based on the idea of bounce-back of non-equilibrium part. If velocity boundary conditions are defined on the left wall then after streaming step the known distributions functions are f_0, f_2, f_3, f_4, f_6 and f_7, whereas f_1, f_5 and f_8 are unknown. Consider the velocity at wall is known and is given as $\mathbf{u} = (u_x, u_y)$. Further assume that the velocity component u_y is zero. Then, substituting the velocity and known distribution functions in Eqs. (3.7) and (3.8), we have

$$f_1 + f_5 + f_8 = \rho - f_0 - f_2 - f_3 - f_4 - f_6 - f_7 \tag{3.18}$$

$$f_1 + f_5 + f_8 = \rho u_x + (f_3 + f_4 + f_6 + f_7) \tag{3.19}$$

$$\begin{aligned} f_5 - f_8 &= \rho u_y - f_2 + f_4 - f_6 + f_7 \\ &= - f_2 + f_4 - f_6 + f_7 \end{aligned} \tag{3.20}$$

Since the density value is still not known, more constrains are needed to solve these equations. Using non-equilibrium part of bounce back rule in normal direction to boundary, we have

$$f_1 - f_1^{eq} = f_3 - f_3^{eq} \tag{3.21}$$

Using Eqs. (3.4) and (3.5) into Eq. (3.20), the unknown distribution functions can be written as

$$f_1 = f_3 + \frac{2}{3}\rho u_x \tag{3.22}$$

$$f_5 = f_7 - \frac{1}{2}(f_2 - f_4) + \frac{1}{6}\rho u_x \tag{3.23}$$

$$f_8 = f_6 - \frac{1}{2}(f_2 - f_4) + \frac{1}{6}\rho u_x \tag{3.24}$$

If pressure boundary condition is applied then density value is specified and velocity is determined from Eq.(3.18-3.20) as

$$u_x = 1 - \frac{f_0 + f_2 + f_4 + 2(f_3 + f_6 + f_7)}{\rho} \tag{3.25}$$

If velocity boundary condition is applied then velocity value is specified and density is determined from Eq.(3.18-3.20) as

$$\rho = \frac{f_0 + f_2 + f_4 + 2(f_3 + f_6 + f_7)}{1 - u_x} \tag{3.26}$$

3.5 MULTIPLE-RELAXATION-TIME PSEUDOPOTENTIAL LBM

The pseudopotential LBM suffers from numerical stability problem at large density ratios. The numerical stability was improved by incorporating MRT collision model [189]. Furthermore, an improved forcing scheme was adopted based on the findings of Li et at. [190]. Li et at. [190] suggested that one can realize the thermodynamic consistency in the pseudopotential LB model by tuning the mechanical stability condition. Using the new forcing term, stable numerical simulations can be carried out at a density ratio as large as 500 and Reynolds number of 40-1000. Using the MRT collision operator [191] the evolution equation of the density distribution function can be written as [192,193]

$$f_\alpha\left(\mathbf{x}+\mathbf{e}_\alpha\delta_t, t+\delta_t\right) = f_\alpha\left(\mathbf{x},t\right) - \bar{\Lambda}_{\alpha\beta}\left(f_\beta - f_\beta^{eq}\right)\Big|_{(x,t)} + \delta_t\left(S_\alpha - 0.5\bar{\Lambda}_{\alpha\beta}S_\beta\right)\Big|_{(x,t)} \tag{3.27}$$

where f_α is the density distribution function, f_α^{eq} is its equilibrium distribution, t is the time, $\mathbf{x}$ is the spatial position, $\mathbf{e}_\alpha$ is the discrete velocity along the αth direction, δ_t is the time step, S_α is the forcing term in the velocity space. The collision matrix is $\bar{\mathbf{\Lambda}} = \mathbf{M}^{-1}\mathbf{\Lambda}\mathbf{M}$, where $\mathbf{M}$ is an orthogonal transformation matrix and $\mathbf{\Lambda}$ is the diagonal matrix given as (for the D2Q9 lattice)

$$\mathbf{\Lambda} = diag\left(\tau_\rho^{-1}, \tau_e^{-1}, \tau_\varsigma^{-1}, \tau_j^{-1}, \tau_q^{-1}, \tau_j^{-1}, \tau_q^{-1}, \tau_\upsilon^{-1}, \tau_\upsilon^{-1}\right) \tag{3.28}$$

The transformation matrix $\mathbf{M}$ can be used to map the density distribution function f_α and its equilibrium distribution function f_α^{eq} onto the moment space as $\mathbf{m} = \mathbf{M}\mathbf{f}$ and $\mathbf{m^{eq}} = \mathbf{M}\mathbf{f}^{\mathbf{eq}}$, respectively. For the D2Q9 lattice, the equilibrium of the moment $\mathbf{m^{eq}}$ is given as

$$\mathbf{m^{eq}} = \rho\left(1, -2+3|\mathbf{V}|^2, 1-3|\mathbf{V}|^2, v_x, -v_x, v_y, -v_y, v_x^2 - v_y^2, v_x v_y\right)^T \tag{3.29}$$

The right hand side of Eq. (3.27) can be simplified using Eqs. (3.28) and (3.29) as [194]

$$\mathbf{m}^* = \mathbf{m} - \mathbf{\Lambda}\left(\mathbf{m} - \mathbf{m}^{eq}\right) + \delta_t\left(\mathbf{I} - \frac{\mathbf{\Lambda}}{\mathbf{2}}\right)\bar{\mathbf{S}} \tag{3.30}$$

where $\mathbf{I}$ denotes the unit tensor and $\bar{\mathbf{S}} = \mathbf{M}\mathbf{S}$ the forcing term in the moment space with $\mathbf{S}$ given as

$$\mathbf{S} = \left(S_0, S_1, \ldots, S_8\right)^T \tag{3.31}$$

The streaming process is given as

$$f_\alpha\left(\mathbf{x} + \mathbf{e}_\alpha \delta_t, t + \delta_t\right) = f_\alpha^*\left(\mathbf{x}, t\right) \tag{3.32}$$

where $f^* = \mathbf{M}^{-1}\mathbf{m}$. The macroscopic density is computed by Eq.(3.7) and velocity is calculated as

$$\rho\mathbf{v} = \sum_\alpha \mathbf{e}_\alpha f_\alpha + \frac{\mathbf{F}\delta t}{2} \tag{3.33}$$

where $\mathbf{F} = \left(F_x, F_y\right)$ is the interparticle interaction force which is used to obtain phase separation, and is given by Eq.(3.10).

In the MRT LB methods the interparticle force is incorporated through a forcing scheme. The generally used forcing scheme is given as [192,193]

$$\bar{\mathbf{S}} = \begin{bmatrix} 0 \\ 6\left(v_x F_x + v_y F_y\right) \\ -6\left(v_x F_x + v_y F_y\right) \\ F_x \\ -F_x \\ F_y \\ -F_y \\ 2\left(v_x F_x + v_y F_y\right) \\ \left(v_x F_y + v_y F_x\right) \end{bmatrix} \tag{3.34}$$

However, in the present model an improved force scheme, which is given below, was used. The main feature of this force scheme is that the numerical stability can be tuned by changing the value of σ.

$$\bar{\mathbf{S}} = \begin{bmatrix} 0 \\ 6\left(v_x F_x + v_y F_y\right) + \dfrac{12\sigma\left|\mathbf{F}\right|^2}{\psi^2 \delta t\left(\tau_e - 0.5\right)} \\ -6\left(v_x F_x + v_y F_y\right) + \dfrac{12\sigma\left|\mathbf{F}\right|^2}{\psi^2 \delta t\left(\tau_e - 0.5\right)} \\ F_x \\ -F_x \\ F_y \\ -F_y \\ 2\left(v_x F_x + v_y F_y\right) \\ \left(v_x F_y + v_y F_x\right) \end{bmatrix} \tag{3.35}$$

where $\left|\mathbf{F}\right|^2 = \left(F_x^2 + F_y^2\right)$.

3.6 HE–CHEN–ZHANG MULTIPHASE LBM

He at al. [129] proposed a model in which phase segregation and interfacial dynamics are achieved by the incorporation of the molecular interactions. Two sets of distribution functions, namely pressure distribution function and distribution function for index function are introduced in this model. LB equations for these distribution functions are able to recover the Navier-Stokes equations and Cahn-Hilliard type equation. The LB evolution equations of pressure distribution function $\bar{f}$ and distribution function of index function $\bar{g}$ can be written as

$$\begin{aligned}&\bar{f}_\alpha\left(\mathbf{x}+\mathbf{e}_\alpha\delta_t,t+\delta_t\right)-\bar{f}_\alpha\left(\mathbf{x},t\right)=-\frac{1}{\tau}\left(\bar{f}_\alpha\left(\mathbf{x},t\right)-f^{eq}{}_\alpha\left(\mathbf{x},t\right)\right)\\&-\frac{\left(2\tau-1\right)}{2\tau}\frac{\left(e_\alpha-\mathbf{u}\right)\cdot\nabla\psi\left(\phi\right)}{RT}\Gamma_\alpha\left(\mathbf{u}\right)\delta_t\end{aligned}\tag{3.36}$$

$$\begin{aligned}&\bar{g}_\alpha\left(\mathbf{x}+\mathbf{e}_\alpha\delta_t,t+\delta_t\right)-\bar{g}_\alpha\left(\mathbf{x},t\right)=-\frac{1}{\tau}\left(\bar{g}_\alpha\left(\mathbf{x},t\right)-g^{eq}{}_\alpha\left(\mathbf{x},t\right)\right)-\\&\frac{\left(2\tau-1\right)}{2\tau}\left(e_\alpha-\mathbf{u}\right)\cdot\left[\Gamma_\alpha\left(\mathbf{u}\right)\left(\mathbf{F}_s+\mathbf{G}\right)-\left(\Gamma_\alpha\left(\mathbf{u}\right)-\Gamma_\alpha\left(0\right)\right)\nabla\psi\left(\rho\right)\right]\delta_t\end{aligned}\tag{3.37}$$

where $\mathbf{e}_\alpha$ is the discrete velocity. τ represents the non-dimensional time and is related to viscosity as $\nu=c_s^2\left(\tau-0.5\right)\delta t$. $\mathbf{G}$ represents the body force. $\mathbf{F}_s$ represents the force responsible for surface tension, which is given as

$$\mathbf{F}_s=\kappa\rho\nabla\nabla^2\rho\tag{3.38}$$

where ρ is fluid density and κ is parameter that controls the magnitude of surface tension. The equilibrium distribution functions $f_\alpha^{(eq)}$ and $g_\alpha^{(eq)}$ are given as

$$f_\alpha^{(eq)}=\omega_\alpha\phi\left[1+\frac{3\mathbf{e}_\alpha\cdot\mathbf{u}}{c^2}+\frac{9\left(\mathbf{e}_\alpha\cdot\mathbf{u}\right)^2}{2c^4}-\frac{3\mathbf{u}^2}{2c^2}\right]\tag{3.39}$$

$$g_\alpha^{(eq)}=\omega_\alpha\left[p+\rho\left(\frac{3\mathbf{e}_\alpha\cdot\mathbf{u}}{c^2}+\frac{9\left(\mathbf{e}_\alpha\cdot\mathbf{u}\right)^2}{2c^4}-\frac{3\mathbf{u}^2}{2c^2}\right)\right]\tag{3.40}$$

where ϕ is the index function and p is the pressure.

In Eq. (3.37) $\Gamma_\alpha(\mathbf{u})$ is given as

$$\Gamma_\alpha(\mathbf{u}) = \omega_\alpha \left[1 + \frac{3\mathbf{e}_\alpha \cdot \mathbf{u}}{c^2} + \frac{9(\mathbf{e}_\alpha \cdot \mathbf{u})^2}{2c^4} - \frac{3\mathbf{u}^2}{2c^2}\right] \tag{3.41}$$

Both $\psi(\rho)$ and $\psi(\phi)$ are related to hydrodynamic and thermodynamic pressure [195] as follows

$$\psi(\rho) = p - \rho RT \tag{3.42}$$

$$\psi(\phi) = p_{th} - \phi RT \tag{3.43}$$

The thermodynamic pressure can be calculated by Carnaharn-Starling equation of state [196,197] as

$$p_{th} = \phi RT \frac{1 + b\phi/4 + (b\phi/4)^2 - (b\phi/4)^3}{(1 - b\phi/4)^3} - a\phi^2 \tag{3.44}$$

The macroscopic variables can be calculated from moments of distribution functions as

$$\phi = \sum \bar{f}_\alpha \tag{3.45}$$

$$p = \sum \bar{g}_\alpha - \frac{1}{2}\mathbf{u} \cdot \nabla \psi(\rho)\delta_t \tag{3.46}$$

$$\rho RT\mathbf{u} = \sum e_\alpha \bar{g}_\alpha + \frac{RT}{2}(\mathbf{F}_s + \mathbf{G})\delta_t \tag{3.47}$$

Once the index function is calculated, density $\rho(\phi)$, kinematic viscosity $\nu(\phi)$ and relaxation factor $\tau(\phi)$ can be found using the following relations,

$$\rho(\phi) = \rho_l + \frac{\phi - \phi_l}{\phi_h - \phi_l}(\rho_h - \rho_l) \tag{3.48}$$

$$\nu(\phi) = \nu_l + \frac{\phi - \phi_l}{\phi_h - \phi_l}(\nu_h - \nu_l) \tag{3.49}$$

$$\tau(\phi) = \tau_l + \frac{\phi - \phi_l}{\phi_h - \phi_l}(\tau_h - \tau_l) \tag{3.50}$$

where ρ_h, ν_h and τ_h denote the density, kinematic viscosity and non-dimensional relaxation time of liquid phase, respectively , whereas ρ_l, ν_l and τ_l denote the density, kinematic viscosity and non-dimensional relaxation time of gas phase, respectively. ϕ_h and ϕ_l represent the maximal and the minimum values of the index function.

3.7 PHASE-CHANGE LBM

Hazi and Markus [198] proposed a phase-change lattice Boltzmann method to study bubble departure dynamics. However, they used an equation of state which is not applicable to real gases. Then Gong and Cheng [168] proposed a liquid vapor phase-change model. They improved the energy equation source term. Latter, this model was also used for condensation work [138]. The model consist of two distribution functions; one is density distribution function and the other is temperature distributions function. Both distribution functions are coupled through temperature term.

The LB evolution equation of density distribution function can be written as

$$f_i(\mathbf{x} + \mathbf{e}_i\delta_t, t + \delta_t) - f_i(\mathbf{x}, t) = -\frac{1}{\tau}\left(f_i(\mathbf{x}, t) - f_i^{(eq)}(\mathbf{x}, t)\right) + \Delta f_i(\mathbf{x}, t) \tag{3.51}$$

where $f_i(\mathbf{x}, t)$ is the discrete density distribution function. $\Delta f_i(\mathbf{x}, t)$ is the force term. $f_i^{(eq)}(\mathbf{x}, t)$ is the equilibrium distribution function, which is defined by Eq.(3.4).

The density and velocity of the fluid are computed by Eqs.(3.7) and (3.8), respectively, and Kinematic viscosity is computed by Eq.(3.9)

To incorporate the force term in LBM, they chose the exact difference method (EDM) [199], since it offers independence of relaxation time and higher accuracy. The force term in EDM can be incorporated as

$$\Delta f_i(\mathbf{x}, t) = f_i^{(eq)}\left(\rho(\mathbf{x}, t), \mathbf{u} + \Delta\mathbf{u}\right) - f_i^{(eq)}\left(\rho(\mathbf{x}, t), \mathbf{u}\right) \tag{3.52}$$

where $\Delta\mathbf{u} = \delta t/\rho\,\mathbf{F}$ is the velocity change due to force term $\mathbf{F}$. The force term $\mathbf{F}$ (see Eq.(3.15)) is the sum of interparticle interaction force $\mathbf{F}_{\text{int}}$,gravitational force $\mathbf{F}_g$, and the interaction force between fluid and solid $\mathbf{F}_s$.

They used an improved scheme [183] to compute the interparticle interaction force given as

$$\begin{aligned}\mathbf{F}_{\text{int}}(\mathbf{x},t) = -\beta\psi(\mathbf{x},t)\sum_i G(\mathbf{x}+\mathbf{e}_i)\psi(\mathbf{x}+\mathbf{e}_i)\mathbf{e}_i \\ -\frac{1-\beta}{2}\sum_i G(\mathbf{x}+\mathbf{e}_i)\psi^2(\mathbf{x}+\mathbf{e}_i)\mathbf{e}_i\end{aligned} \tag{3.53}$$

Where β is the weighing factor and its value depends on the equation of state. $G(\mathbf{x}+\mathbf{e}_i)$ is the interaction strength and is given as

$$G(\mathbf{x}+\mathbf{e}_i) = \begin{cases} \{\ g_1, & |\mathbf{e}_i| = 1 \\ \{\ g_2, & |\mathbf{e}_i| = \sqrt{2} \\ \ 0\ , & otherwise \end{cases} \tag{3.54}$$

$\psi(x)$ is the interaction potential and this also depends on the equation of state (see Eq.(3.12)).

In this model the Peng–Robinson (P–R) EOS is used, since it produces small spurious currents

$$p = \frac{\rho R_g T}{1-b\rho} - \frac{a\rho^2\alpha(T)}{1+2b\rho-b^2\rho^2} \tag{3.55}$$

where $\alpha(T) = [1+(0.37464+1.54226\omega-0.26992\omega^2)(1-\sqrt{T/T_c})]^2$. The values of constants a, b and ω can be found in references [144,183].

Upon calculating the force term **F**, the real fluid velocity ($\mathbf{U}$) is computed by Eq.(3.17).

To determine the temperature field the evolution of second set of distribution function g_i is to computed as

$$g_i\left(\mathbf{x}+\mathbf{e}_i\delta_t, t+\delta_t\right)-g_i\left(\mathbf{x},t\right)=-\frac{1}{\tau_g}\left(g_i\left(\mathbf{x},t\right)-g_i^{(eq)}\left(\mathbf{x},t\right)\right)+\omega_i\delta t\, q_s \tag{3.56}$$

where τ_g is the relaxation time and q_s is the a source term derived from the phase-change process given by [168]

$$q_s = T\left[1-\frac{1}{\rho C_v}\left(\frac{\partial p}{\partial T}\right)_\rho\right]\nabla\cdot\mathbf{U} \tag{3.57}$$

where the equilibrium distribution g^{eq} is determined as

$$g_i^{eq}=\omega_i\left[T+3T\mathbf{e}_i\cdot\mathbf{U}-3D_T\mathbf{e}_i\cdot\nabla T\right] \tag{3.58}$$

The temperature T is defined as

$$T=\sum_i g_i \tag{3.59}$$

The parameter D_T in Eq.(3.58) is related to the thermal diffusion coefficient and is defined as

$$\frac{\lambda}{\rho C_v}=D_T+c_s^2\left(\tau_g-0.5\right)\delta t \tag{3.60}$$

where C_v is the specific heat at constant volume and λ is the thermal conductivity.

The simulation process carried out as follows: once the EOS has been applied on temperature filed of the previous time step, the hydrodynamic equations are evaluated to determine density and velocity. Then, employing the values of these variables the temperature equation of phase-change process is solved. The process is reiterated at each time step.

Furthermore, the Lattice Boltzmann models presented in this Chapter have some limitations; for example, in case of MRT model the density ratio of liquid/gas should not be much higher than 500 because increasing density ratio introduces larger spurious currents, which in turn cause stability issues [182,189], and Reynolds number should smaller than 2000 [182,189]. The Prandtl number for phase-change model should not much higher than unity [137]. Keeping in view these limitations, generally density ratio is kept smaller and Prandtl is not allowed to exceed unity.

All of these multiphase models are used in Chapters 4 to 7. MRT [190] model is used in Chapter 4. He–Chen–Zhang [129], Shan-Chen [131,133] and Phase-Change [168] models are used employed in Chapters 5, 6 and 7 respectively.

CHAPTER 4

DROPLET IMPACT DYNAMICS ON NANOTEXTURED BUMPS: TOPOLOGY EFFECTS

4.1 INTRODUCTION

In this work the impact of fog droplets on dessert beetle inspired nanotextured superhydrophobic bumps was investigated using multiple-relaxation-time (MRT) lattice Boltzmann method. Effects of nanopost height, interpost spacing, and bump radius of curvature were studied for a range of Weber number which represents the impact velocity. Three different outcomes of droplet impact simulations were captured; the suspended Cassie state, droplet rebound and the sticky Wenzel state. The droplets in the Cassie state can be easily removed from the surface and thus favorable for water collection. The conditions satisfied by the geometrical parameters and the Weber number for the Cassie state were explored.

4.2 PROBLEM DESCRIPTION

Fog droplets vary in size (1 - 50 μm) [31] with mean volume diameter ranging from 10.8 μm to 15 μm [13]. Though the previously studied wind speeds for fog harvesting range from 1 to 9 m/s [13,200], it can be even higher depending on location. Fig. 4.1 shows the schematic diagram of the problem. A fog droplet is allowed to impact on bump with impact velocity *U*. The surface is made of nanoposts. The dynamics of droplet impact are determined by following key parameters: the surrounding gas density ρ_g and viscosity μ_g, the liquid droplet diameter *D*, density ρ, viscosity μ, surface tension σ, contact angle θ_o, impact velocity *U*, height *h* and width *w* of nanopost and bump radius of curvature *R*.

Effects of velocity are studied by Weber number (We) which is defined as relative importance of the fluid inertia compared to the surface tension of the droplets.

$$\mathrm{We}=\rho U^2 D/\sigma \tag{4.1}$$

The effect of gravitational force relative to surface tension force is described by Bond number as

$$\mathrm{Bo}=\Delta\rho g D^2/\ \sigma\ \sim\ 0.12\ \times 10^{-6} \quad (4.2)$$

where g is gravitational force. As the Bond number is small, so the effect of gravity can be neglected in the present study.

In this Chapter the liquid-to-gas density and viscosity ratios are fixed at ρ/ρ_g = 114.5 and μ/μ_g = 114.5, respectively. This density ratio was determined using Maxwell construction for Carnaharn-Starling equation of state. The readers are referred to Huang et al. [188] for more details. Droplet diameter is fixed at D = 10 μm. Impact velocity is varied from U=1.0 m/s (We=0.13) to U=15 m/s (We=30.6). Considering the previous reports [104,201,202] nanopost's dimensions are selected as follows: maximum height h = 5000 nm and interpost spacing s = 400 nm - 2000 nm. For simplicity post width is fixed at w = 400 nm and is used for nondimensionalization purpose. The bump radius of curvature is varied from w/R=1/15 to w/R=1/180 μm. The conversion factor between physical length unit to lattice unit is 1.0 lu = 20 nm. The intrinsic contact angle θ_o is taken as 110°.

To describe the dynamics of impacting droplets, non-dimensional spreading factor is defined as

$$S_x^* = S_x/D \quad (4.3)$$

where S_x is dimensional spreading length (see Fig. 4.1) along x-axis and D is original diameter of droplet. In addition, a non-dimensional time t* is used to describe the temporal events

$$t^* = Ut/D \quad (4.4)$$

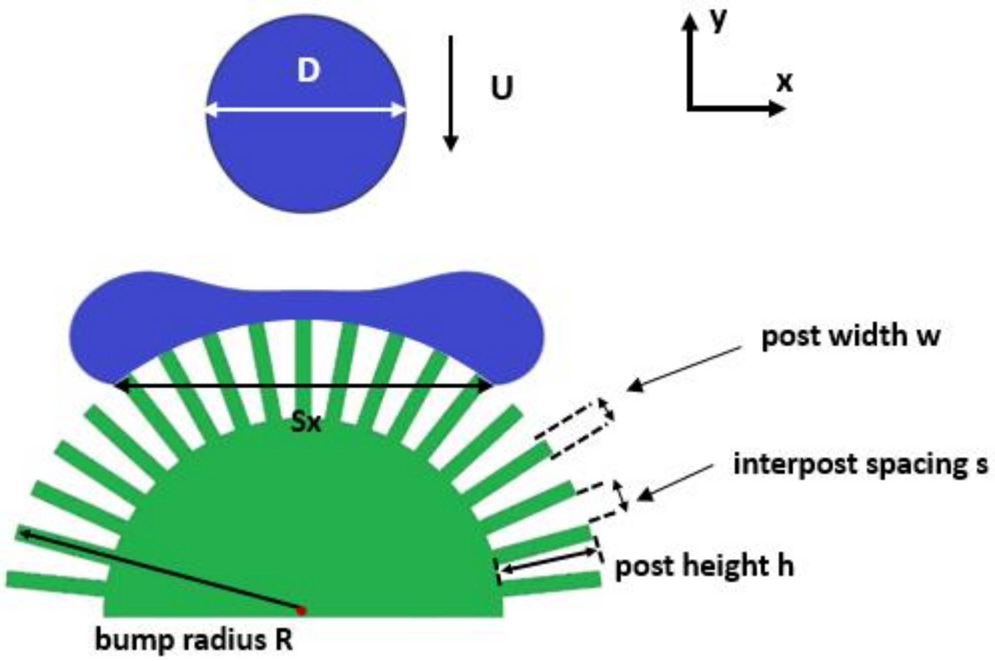

Figure 4.1 Droplet impact on hemispherical nanotextured bump.

4.3 METHODOLOGY

In the present study MRT pseudopotential lattice Boltzmann model based on Li et al. [189] model is used. This model uses an improved forcing scheme in order to achieve thermodynamic consistency and large density ratio at relatively higher Reynolds number. The details of MRT LBM are presented in section 3.5. The wetting characteristics of the surface are incorporated by specifying fluid-solid interactions. These interactions are introduced by an adhesion force between the gas/liquid phase and solid walls, details of which are provided in section 3.3.

4.3.1 COMPUTATIONAL DOMAIN AND BOUNDARY CONDITIONS

The computational domain is a two-dimensional rectangular box. Periodic boundary conditions are applied on the right and left sides of the domain. The bounce back boundary conditions are employed on the top and bottom boundaries as well as on the walls of the nanoposts to implement no-slip boundary condition. A grid independence test has been conducted using four sets of conversion factors between lattice units and physical units. Changing conversion factor alters the size of the geometry, which in turn can affect the simulation outcome. Consider the impact of a droplet with diameter D = 10 μm on the bump with interpost spacing s = 800 nm and post height h = 3000 nm. Now if the conversion factor is too large it will make interpost spacing too small and this can impede the fluid penetration into interpost spacings at all. On the other hand, for smaller conversion factor overall grid size will increase that will make simulation computationally expensive. In table. 4.1 maximum spreading factors of droplets impacting on nanotextured bumps with different unit conversion factors are compared. It can be seen that conversion factor 1.0 lu = 20nm has the error less than 0.5%, so it was selected for simulations.

Table 4.1 Grid independence test

Lattice unit to physical unit conversion factor	1.0 lu = 40nm	1.0 lu = 25nm	1.0 lu=20nm	1.0 lu=12.5nm
$S_x^*(max)$	1.96	1.765	1.748	1.74
Error (%)	12.64	1.43	0.45	-

4.3.2 VALIDATION

The droplet contact angle in the Cassie state is validated with the Cassie and Baxter equation [203]. For a structure with inter-post spacing s and post width w, the apparent contact angle can be determined as

$$cos\theta = \varphi(cos\theta_o + 1) - 1 \tag{4.5}$$

where θ is the apparent contact angle, θ_o is the intrinsic contact angle and φ is the ratio of solid area in contact with droplet to projected area, and can be determined as

$$\varphi = w/(w + s) \tag{4.6}$$

A droplet is placed on the nanostructure with fixed post width w = 400 nm and post height h = 4000 nm. Two different inter-post spacings are considered, i.e., s = 400 nm and s = 800 nm. The intrinsic contact angle is 110^o. The apparent contact angle is compared in Fig. 4.2, which shows a good agreement between simulation and results of Eq.(4.5).

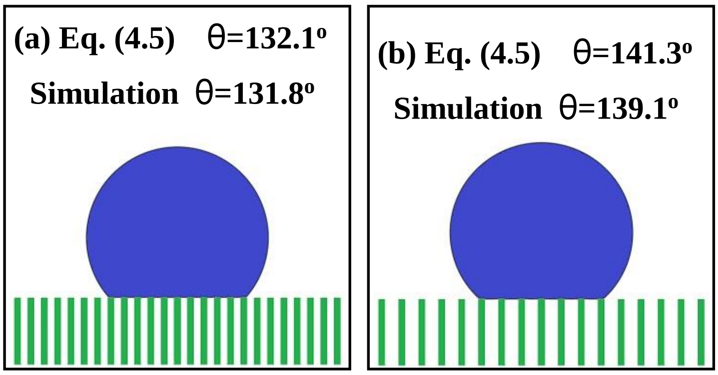

Figure 4.2 Droplet contact angle on nanostructure with post height 4000 nm and interpost spacing (a) *s* = 400 nm (b) *s* = 800 nm.

Next droplet impact and subsequent rebound on a microtextured surface is compared with experimental results. Bobinski et al. [204] studied droplet rebound on a microtextured surface. They investigated droplet (diameter D = 0.6 mm) impact with Weber number 2.6 on a structure having post height h = 10 μm, post width w = 8 μm and interpost spacing s = 22 μm. For comparison purpose, LBM simulations are conducted with droplet size D = 600 lu. The conversion factor is selected as 1.0 lu = 1.0 μm. The contact angle is 151° [204,205]. The droplet is allowed to hit on the surface with Weber number 2.6 and time resolved images are compared with experimental results in Fig.4.3. Though some over prediction of spreading is observed at time instants t = 0.56 ms and t = 0.93 ms, a good agreement of droplet retraction and droplet rebound can be seen at later stages.

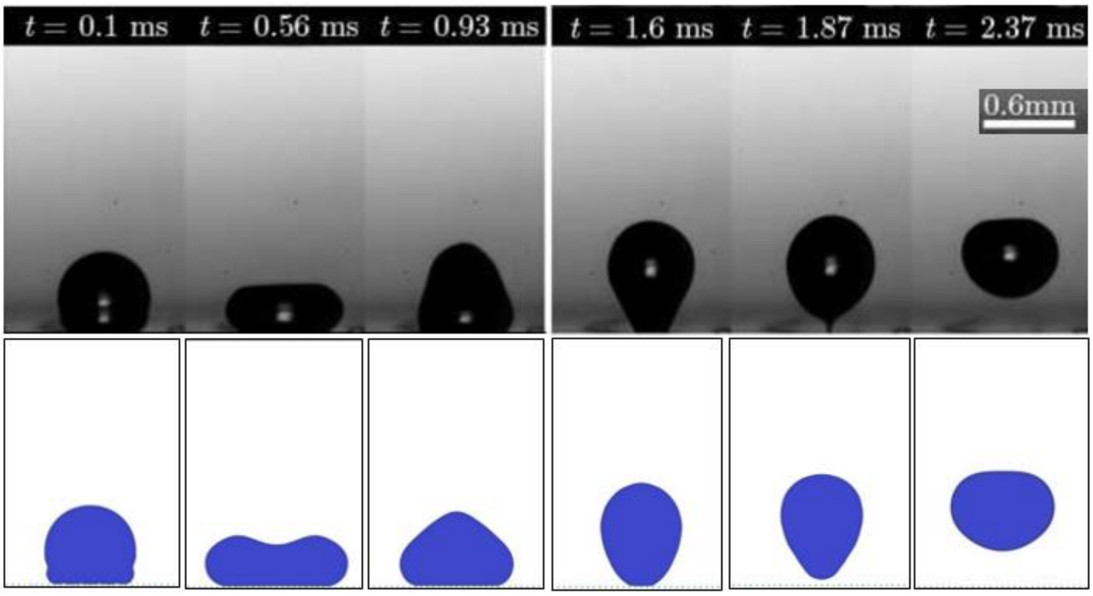

Figure 4.3 Time resolved images of droplet impact on microtextured surface. Top row: experimental results [204]**,bottom row: simulation results.**

4.4 RESULTS AND DISCUSSION

First, the droplet impact dynamics are explained for the base case, which will later be used for comparison purpose. The Weber number of the base case is selected such that only variation of geometrical parameters of the bump can capture all three impact outcomes, including the Cassie state, the Wenzel state and droplet rebound. Weber number, post height, interpost spacing and bump radius of curvature are fixed at We = 19.6, h/w=7.5, s/w=2.0, and *w/R*=2/225, respectively. The evolution of droplet impact is shown by time resolved images in Fig. 4.4. Figure 4.5 serves to quantify the spreading. It can be seen in Fig. 4.4(a), upon impact some of droplet liquid penetrates into interpost spacings (voids) while the lamella film spreads on top of nanostructure. In the start droplet has higher impact kinetic energy that results penetration of droplet liquid. There are air pockets in the voids, if the kinetic energy of droplet is high enough to collapse these air pockets then the penetrating droop will touch down the bottom surface inside voids leading to the transition to the Sticky Wenzel state, which is not observed in this case. Meanwhile, the upper liquid film spreads on the bump (Fig. 4.4 (a, b)) till the maximum spreading factor is achieved (Fig. 4.4(c)) ,which is represented by peak value near t*=1.9 in the spreading factor evolution curve in Fig. 4.5. Afterwards, surface tension effects come into play and droplet starts to retract. Figure 4.5 shows that spreading factor decreases in retraction phase, however, the decrease of spreading factor is rather stepwise instead of smooth manner. It can be understood by investigating the motion of contact line on the tops of nanoposts. Figure 4.4(d and e) show when the contact line recedes from top face of a nanopost into void space the contact edge lifts off in order to achieve higher contact angle. This process causes immediate decrease in spreading factor (marked as abrupt change, see Fig. 4.5) and is responsible for a stepwise type retraction. Furthermore, during this retraction phase droplet surface energy converts back into kinetic energy and droplet endeavors to bounce off the bump. However, in the present case droplet kinetic energy is not high enough to lift off the droplet (Fig. 4.4(f, g)). Besides, it can be noticed that as the time passes beyond t*=9.5, the droplet oscillates again by spreading and retraction, however this peak value, which is near *t**=11, is less than maximum spreading factor value (first peak value near *t**=1.9). This oscillation process will repeat few times till the equilibrium phase is reached (not captured by present simulations). The droplet is also in the Cassie state as seen in Fig. 4.4(h). In the present study main focus is placed on first cycle of spreading and retraction, as liquid droop that is majorly responsible for the transition to Wenzel state, occurs immediately after the impact (Fig4.4 (a, b)).

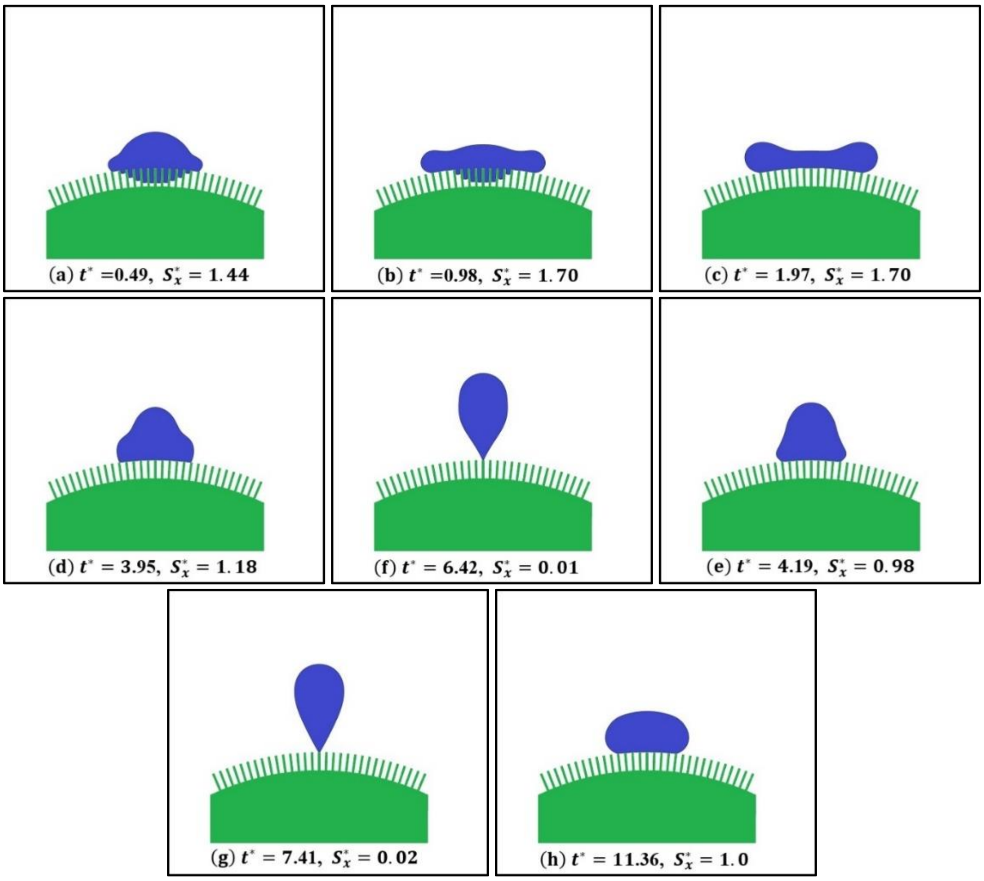

Figure 4.4 Droplet impact evolution on nanotextured bump. Post height *h/w*=7.5, interpost spacing *s/w*=2.0, bump radius of curvature *w/R*=2/225, We=19.6.

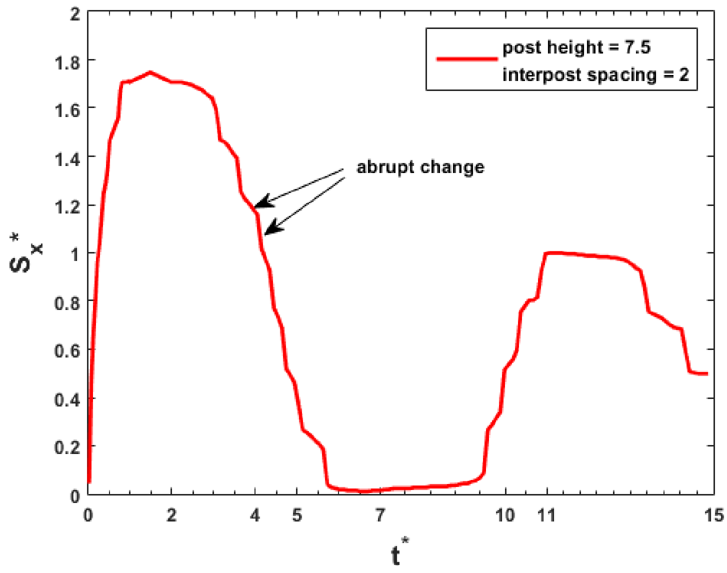

Figure 4.5 Evolution of spreading factor. Post height *h/w*=7.5, interpost spacing *s/w*=2.0, bump radius of curvature *w/R*=2/225, We=19.6.

4.4.1 EFFECTS OF POST HEIGHT

Figure 4.6 shows the droplet impact on bumps with three different post heights, i.e., *h/w*=0 (smooth bump), 2.5 and 7.5. The interpost spacing, Weber number and bump curvature are fixed at *s/w*=2.0, We=19.6 and *w/R*=2/225, respectively. It can be seen in Fig. 4.6 (a3, b3, c3), the spreading for smooth bump is larger compared to textured bump. This is due to the fact that for the textured bump the droplet liquid penetrates into interpost spacings, and this limits the spreading. Furthermore, as seen from Fig. 4.6(b,c), for same Weber number air pockets for smaller posts *h/w*=2.5 are collapsed and the liquid droop has touched down the bottom surface, whereas it does not reach bottom in case of higher posts *h/w*=7.5. Therefore, transition to the Wenzel state occurs for smaller posts, whereas droplet assumes the Cassie state for higher posts (Fig. 4.6 (b6, c6)). Besides, it is interesting to compare the droplet retraction time of smooth bump to textured bump for taller posts case (*h/w*=7.5). It is known that droplet retraction is faster for smooth convex surfaces as compared to level surfaces [206]. In the present case, droplet retraction for textured bump is found to be even faster than smooth bumps (see Fig. 4.6(a4, c4)). The spreading factor evolution curve also confirms this (see Fig. 4.7, from t^*=2.0 to t^*=7.0). Moreover, the spreading factor evolution is smooth for the smooth bump, whereas in stepwise manner for nanotextured bump, which is due interpost spacings.

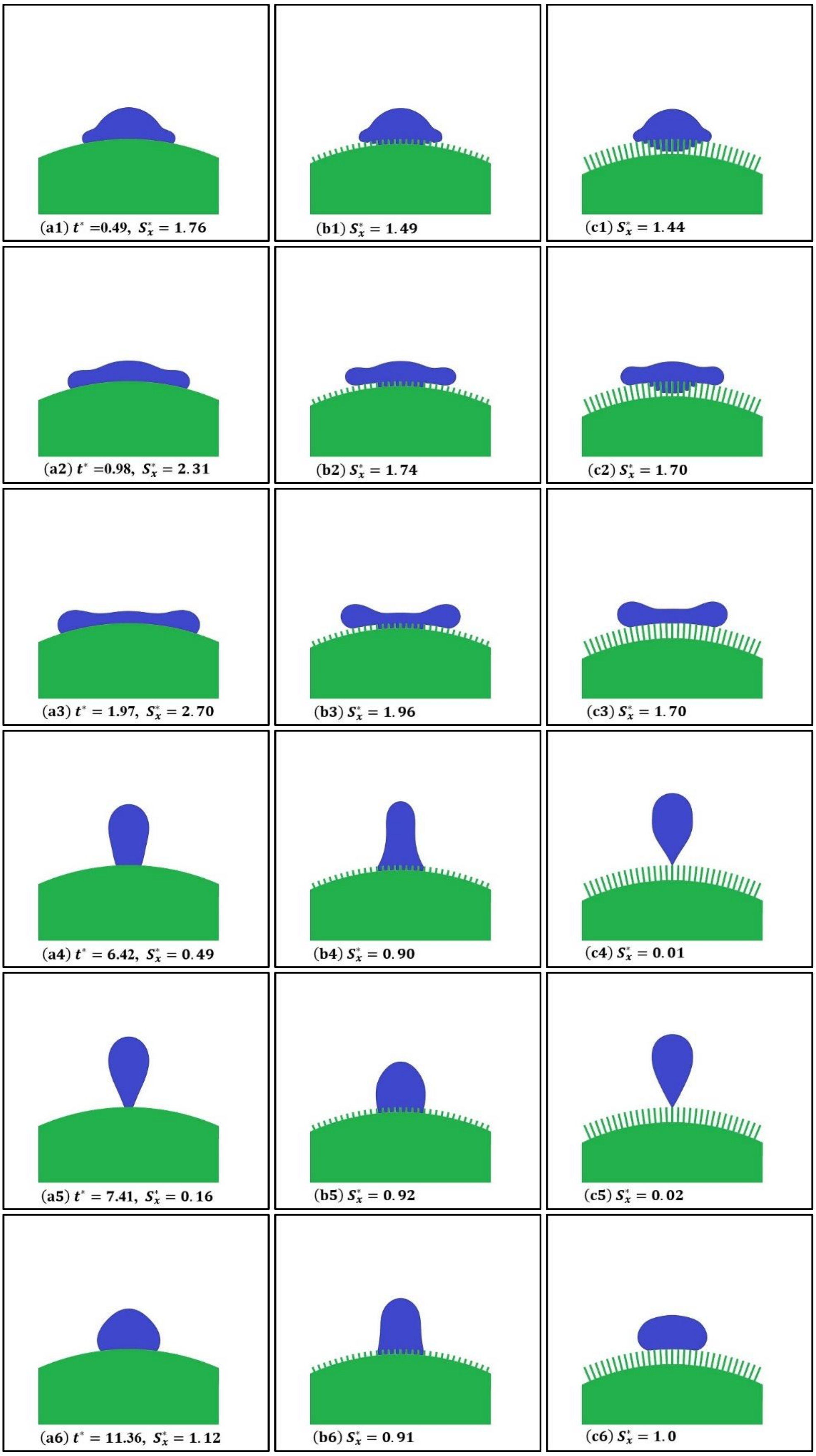

Figure 4.6 Evolution of droplet impact on nanotextured bumps with different post heights: (a) smooth surface, (b) post height *h/w*=2.5, (c) post height *h/w*=7.5.

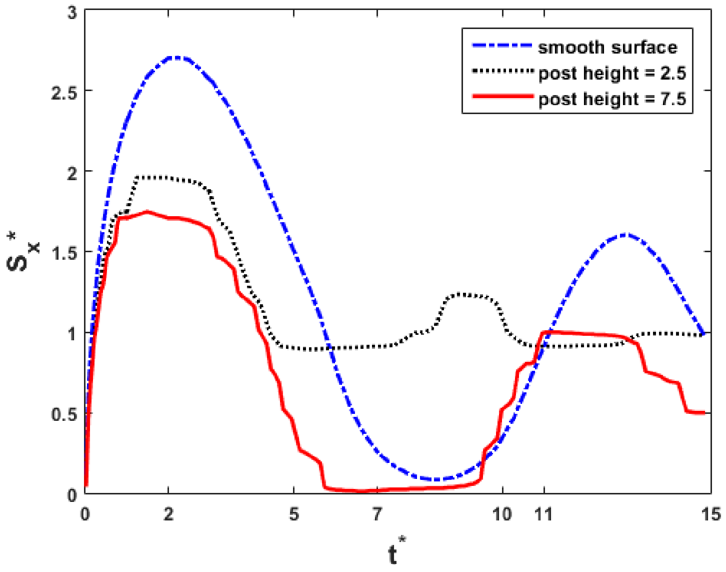

Figure 4.7 Evolution of spreading factor of droplet impact on nanotextured bumps with different post heights: smooth surface, post height *h/w*=2.5, post height *h/w*=7.5.

4.4.2 EFFECTS OF INTERPOST SPACING

Figure 4.8 shows the evolution of droplet impact on nanotextured bumps with different interpost spacings, i.e., *s/w*=1.0, 2.0 and 3.0. Post height, bump curvature and Weber are fixed at *h/w*=7.5, *w/R*=2/225 and We=19.6, respectively. It can be seen from Figs.4.8 (a1, b1, c1) to (a3, b3, c3) that with increasing interpost spacing the droplet spreading reduces, and more liquid penetrates into interpost spacings. This is also observed from maximum spreading factor values of all three surfaces near t*=1.9 (see, Fig.4.10). The maximum spreading factor deceases with increasing interpost spacing. For larger interpost spacing (*s/w*=3) transition to the sticky Wenzel state occurs (Fig. 4.8 (c6)), whereas for smaller interpost (spacing *s/w*=1) droplet rebound occurs while for interpost spacing *s/w*=2 the Cassie state is captured. This can be understood by assuming two sources of kinetic energy driving the droplet rebound during the retraction phase. Shen et al. [206] pointed out that during the retraction phase of droplet on smooth convex surfaces, higher velocities are generated at internal and external rims of the droplet causing faster retraction. One contribution to retraction kinetic energy arises from these higher rim velocities. The second contribution comes from the initial kinetic energy that was stored in the form of surface energy due to liquid penetration into interpost spacings and then converted back into kinetic energy during the retraction phase.

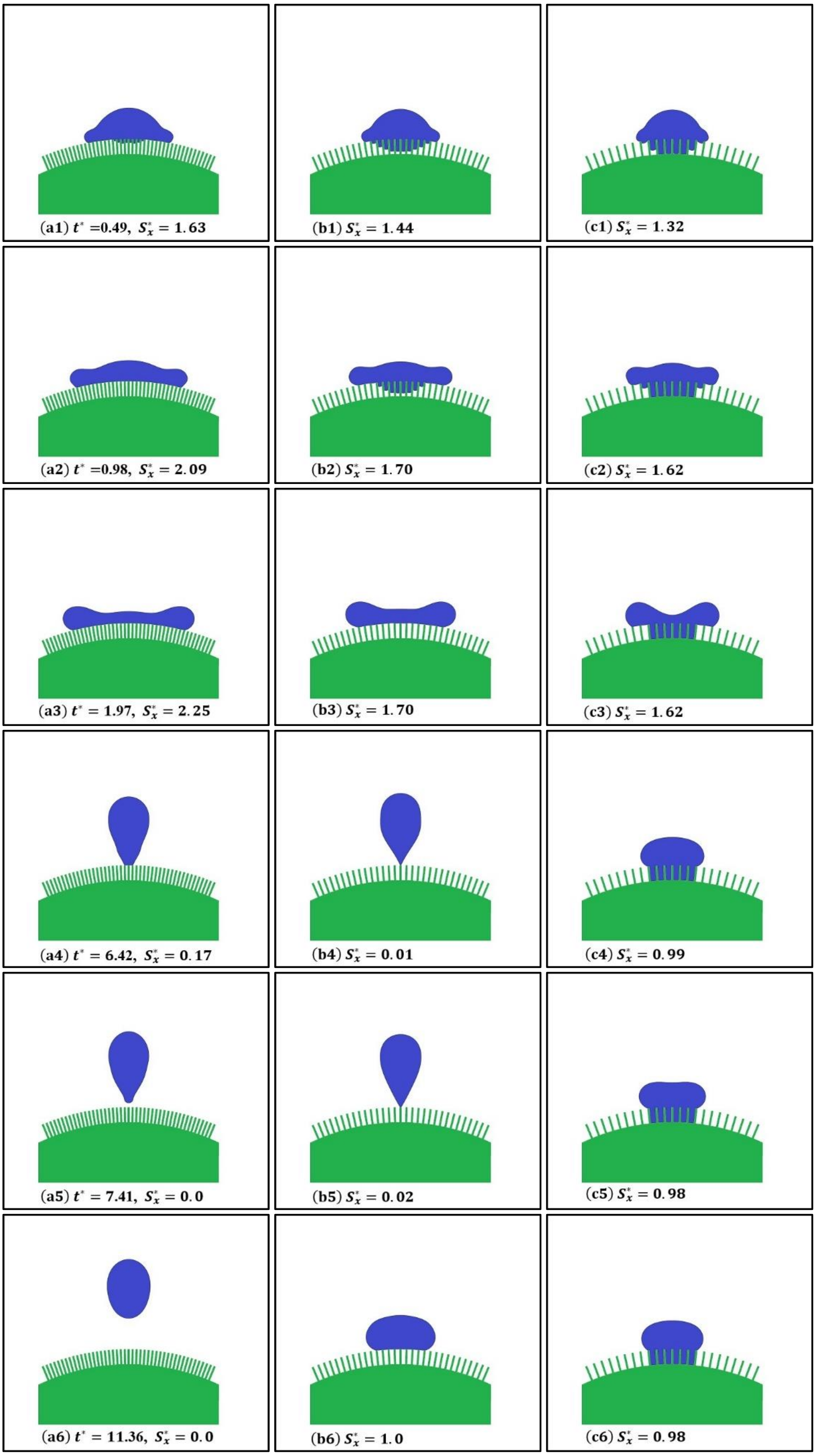

Figure 4.8 Evolution of droplet impact on nanotextured bumps with different interpost sapcing: (a) *s/w* =1.0, (b) *s/w* =2.0, (c) *s/w* =3.0.

It can be hypothesized that because of smaller spreading for inerpost spacing (*s/w*=2.0) (Fig. 4.8(b3)), the energy contribution during retraction phase from rim velocities is smaller. Therefore droplet rebound does not occur for interpost spacing *s/w*=2.0. This can also be seen from velocity vectors near droplet lift off time (t^*= 6.42) (Fig. 4.9(a,b)), the droplet upward velocities are larger for interpost spacing ((*s/w*=1.0)), whereas smaller for interpost spacing (*s/w*=2.0).

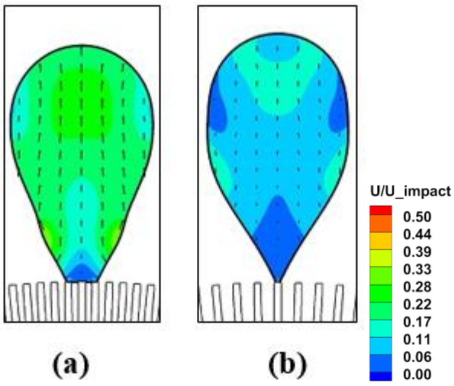

Figure 4.9 Velocity vectors during retraction phase at t^*= 6.42 (a) interpost spacing *s/w*=1.0, (b) inter post spacing *s/w*=2.0.

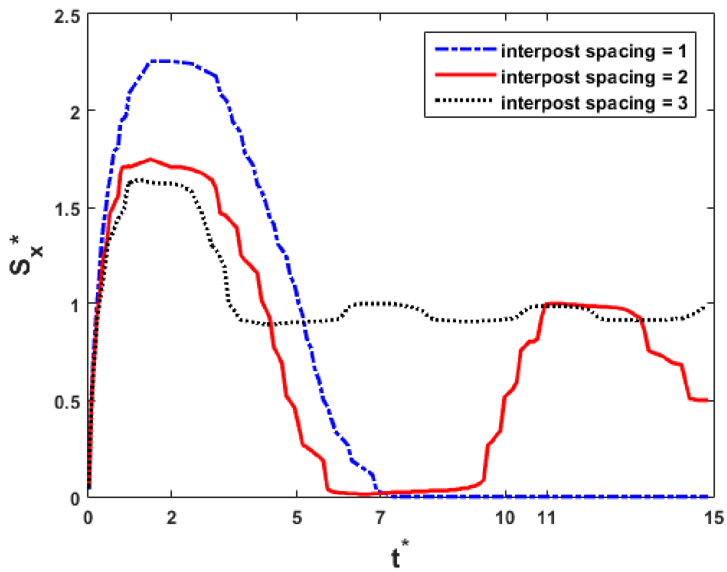

Figure 4.10 Evolution of spreading factor of droplet impact on nanotextured bumps with different interpost sapcing: *s/w* =1.0, *s/w* =2.0, *s/w* =3.0.

4.4.3 EFFECTS OF BUMP RADIUS

Three different values of bump curvature, i.e., *w/R*= 2/75, 2/225 and 2/900 for fixed Weber number We = 19.6 are studied by time resolved images. Interpost spacing and post height are fixed at s/w=2.0 and h/w=7.5, respectively. It can be seen from Fig.4.11 that for larger bump curvature droplet rebounds (Fig. 12(a5)), whereas for smaller radius of curvature droplet does not. Evolution of spreading factor is shown in Fig. 4.12. It can be seen maximum spreading factor is slightly larger for larger bump curvature.

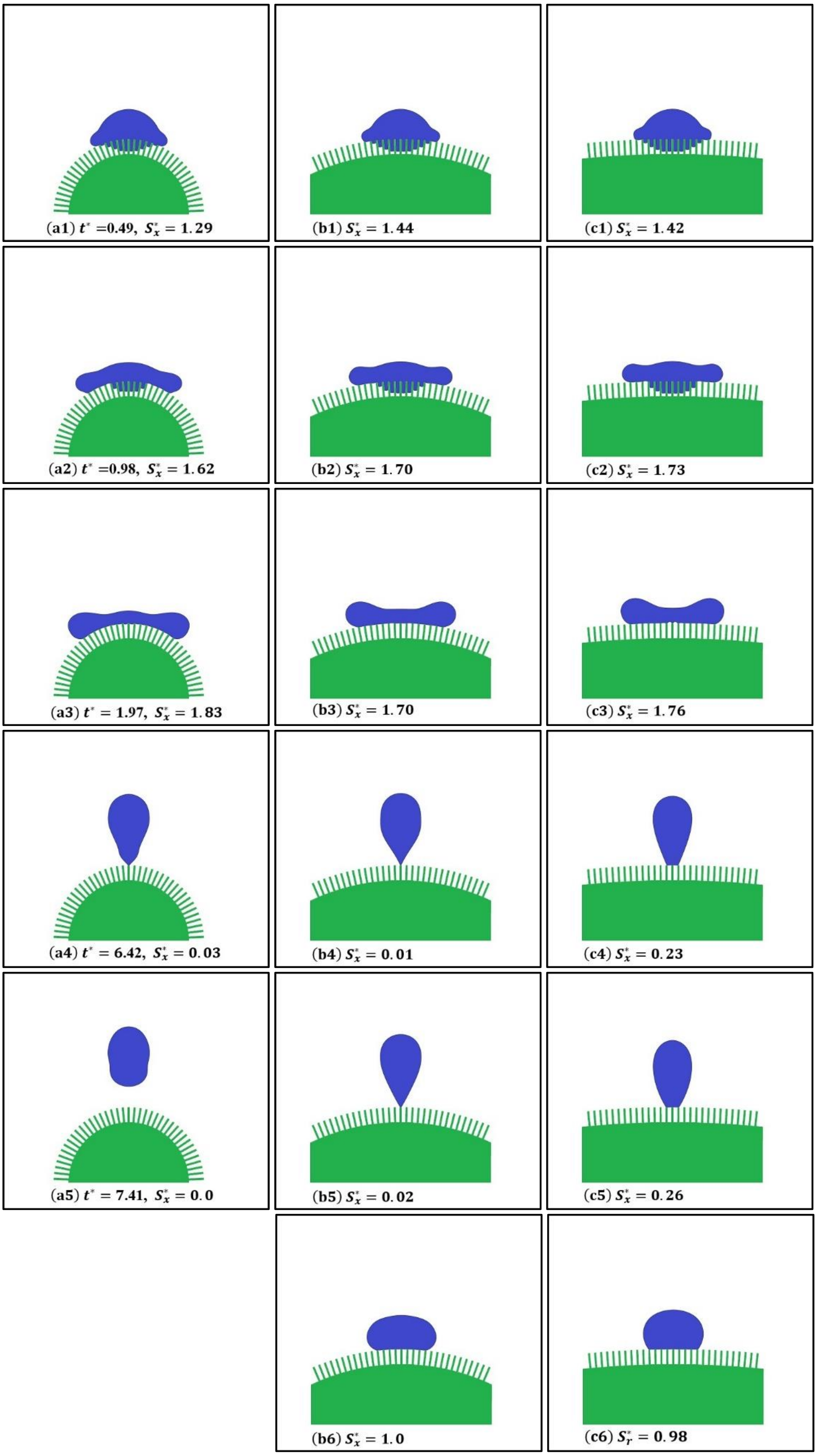

Figure 4.11 Evolution of droplet impact on nanotextured bumps with different bump curvature: (a) w/R =2/75, (b) w/R =2/225, (c) w/R =2/900.

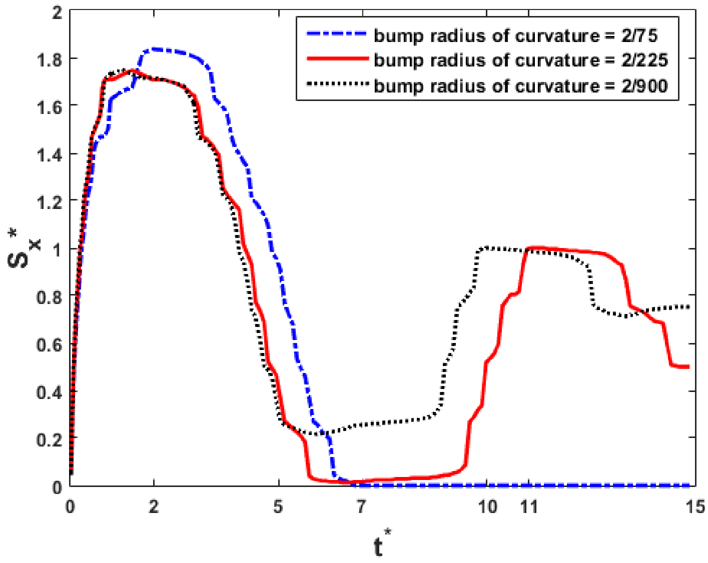

Figure 4.12 Evolution of droplet impact spreading factor for nanotextured bumps with different bump curvature: w/R =2/75, w/R =2/225, w/R =2/900.

4.4.4 EFFECTS OF IMPACT SPEED

Figure 4.13 shows the final outcomes of droplet impact for various post heights and Weber numbers. Post height is varied from *h/w*=1.25 to 12.5 and Weber number (which mainly represents the impact velocity) is varied from We=0.13 to 30.6, while interpost spacing and bump curvature are fixed at *s/w*=2.0 and *w/R*=2/225, respectively. It is seen from Fig. 4.13, droplet impact outcome is the Cassie state for Weber number less than 4.9 corresponding to velocity 6 m/s for all post heights. However a transition from the Cassie state to the Wenzel state is observed for higher Weber numbers and smaller post heights. Furthermore, for taller posts, larger than or equal to *h/w*=8.75, droplet rebound occurs at Weber number We = 30.6 and below this value droplet occupies the Cassie state.

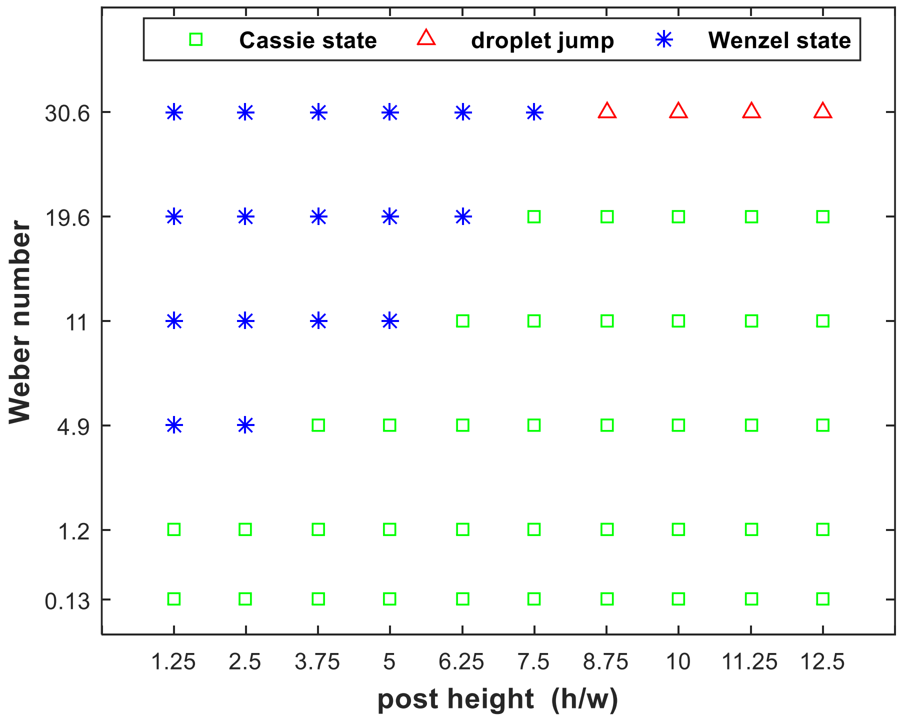

Figure 4.13 Effects of interpost spacing and Weber number on droplet impact. Bump curvature *w/R*=2/225, post height *w/h*=7.5.

Next, interpost spacing is varied from *s/w*= 1 to 5. Post height and bump radius of curvature are fixed to *h/w*=7.5 and *w/R*=2/225, respectively. It can be seen that subsequent to impact droplet assumes the Cassie state at smaller Weber number (less than 4.9) for all values of interpost spacing (Fig. 4.14). Transition to the Wenzel state occurs with increasing Weber number for higher values of interpost spacing. Besides droplet rebound occurs only for *s/w*=1 at We= 19.6 and 30.6.

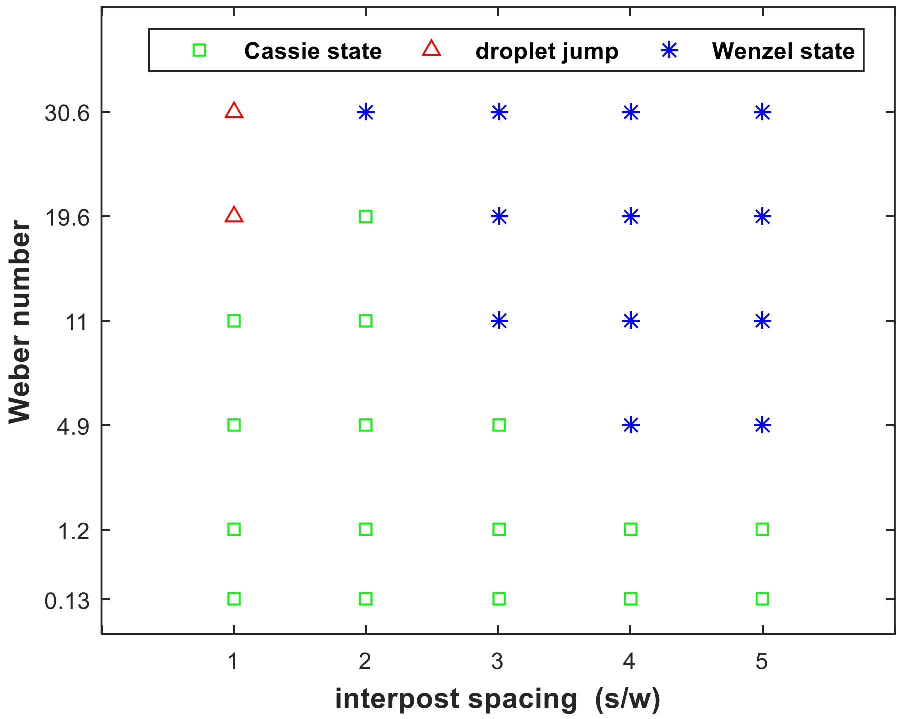

Figure 4.14 Effects of post height and Weber number on droplet impact. Bump curvature *w/R*=2/225, interpost spacing *s/w*=2.0.

Next, bump curvature is varied from w/R = 2/75 to 2/900. Interpost spacing and post height are fixed at s/w = 2.0 and h/w = 7.5, respectively. It can be seen from Fig. 4.15, transition to the Wenzel state occurs for all bump curvature values at Weber number 30.6. Droplet bounces off at larger values of bump curvature at Weber number We = 19.6 and We = 11. For all other values of bump curvature droplet is in the Cassie state provided that Weber number is less than 30.6.

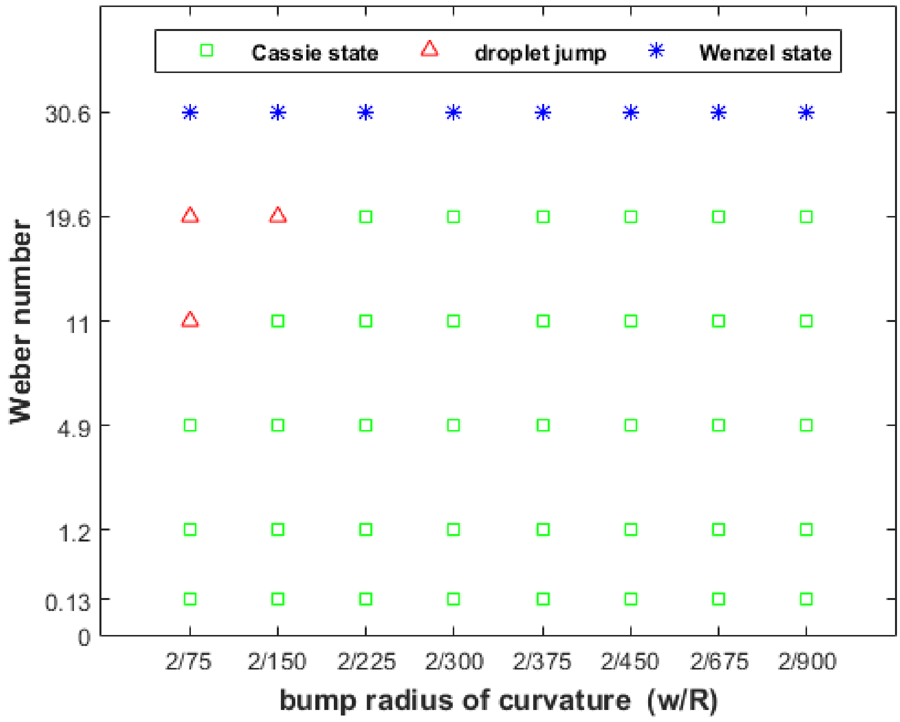

Figure 4.15 Effects radius of curvature and Weber number. Post height *h/w*=7.5, interpost spacing *s/w*=2.0.

4.4.5 RELATIONSHIP BETWEEN DROPLET IMPACT OUTCOME AND BUMP GEOMETRICAL PARAMETERS

Figure 4.16 shows a three-dimensional relationship between outcomes of droplet impact and parameters, including Weber number, post height and interpost spacing. Interpost spacing is varied from *s/w*=1 to 5, post height is varied from *h/w*=1.25 to 12.5 and Weber number is varied from We=0.13 to 30.6. Radius of curvature is fixed at *w/R*=2/225. The values of all these parameters are plotted in Fig. 4.16 to obtain a surface. The droplet impact final outcome is the Cassie state for all values of these parameters below this surface (Fig. 4.16). This whole surface is then divided into three sub-surfaces, namely surface 1, surface 2 and surface 3. Surface 1 represents transition from the Cassie to the Wenzel regime, which is, for all parameters values at and above surface 1 droplet is in Wenzel state, while below in Cassie state. Surface 2 represents region at and above which droplet rebound occurs. Surface 3 is a small region above surface 2, and shows that the droplet rebounds at surface 2, but if the Weber number is increased to surface 3 then transition to the Wenzel state occurs. It can be observed that for larger interpost spacing and smaller post heights droplet is in Wenzel state even at smallest Weber number of 0.13.

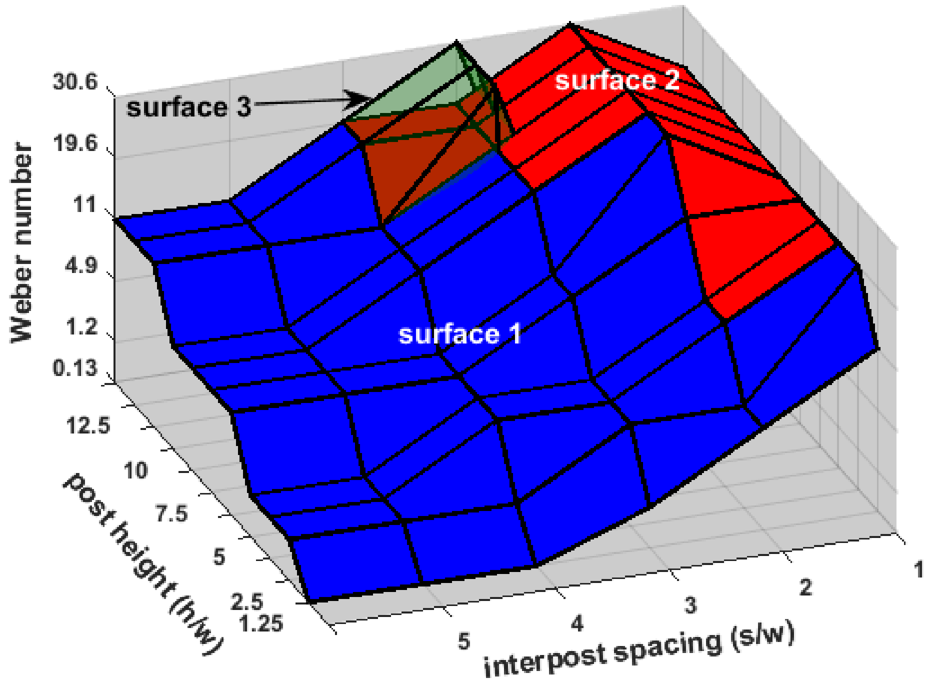

Figure 4.16 3D relationship among interpost spacing, post height and Weber number. Surface 1: transition from Cassie to Wenzel state, surface 2: transition from Cassie to droplet rebound, surface 3: transition from droplet rebound to Wenzel state.

Next, the post height is varied from *h/w*=1.25 to 12.5. Bump curvature is varied from *w/R*=2/75 to 2/900. Interpost spacing is fixed at *s/w*=2.0. The surface is divided into four sub-surfaces (Fig. 4.17). Underneath all surfaces, the droplet is in the Cassie state. Surface 1 represents the transition region at and above which droplet is in the Wenzel state. Surface 2 features a region at which droplet bounces off. At surface 3 droplet is in the Wenzel state. Surface 4 shows that till upper bound of Weber number droplet impact outcome is the Cassie state. It can be seen the surface 4 region representing higher posts and smaller bump curvature is optimum for Cassie state.

As discussed in Chapter 2, droplet impacts may have six possible outcomes (Fig 2.1). However, only deposition, Cassie sate and rebound are observed in the present study. Droplet splash and break-up are more pronounced for larger droplets impacting at higher velocities, which are not overserved here.

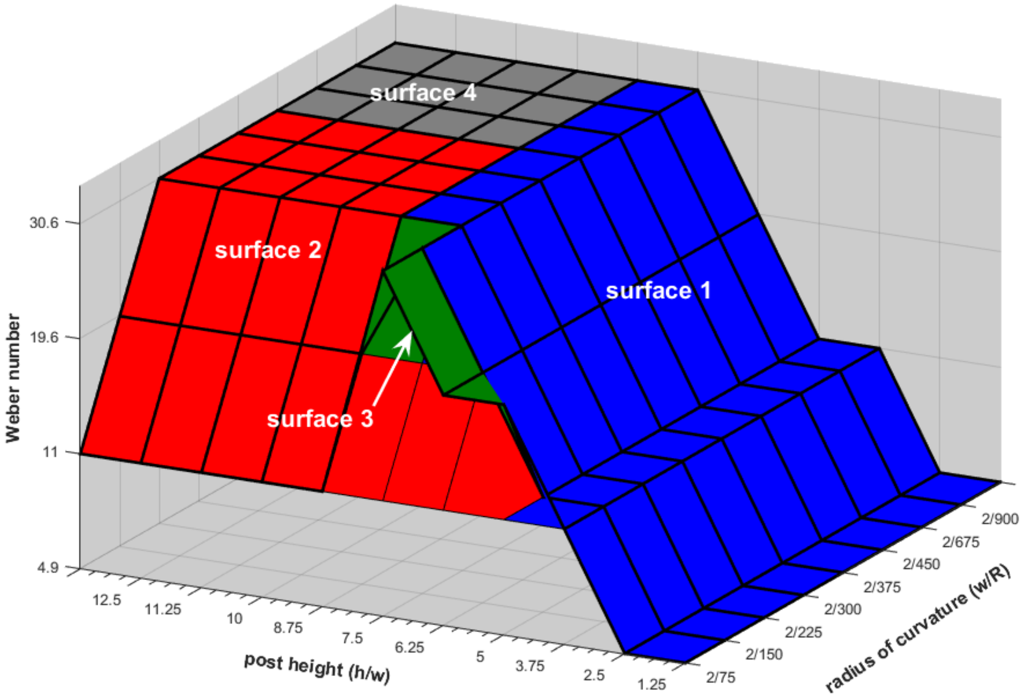

Figure 4.17 Relationship among bump radius of curvature, post height and Weber number. Surface 1: transition from Cassie to Wenzel state, surface 2: transition from Cassie to droplet rebound, surface 3: transition from droplet rebound to Wenzel state, surface 4: no transition.

4.5 SUMMARY

In this work a MRT lattice Boltzmann method was used to study fog droplet impact on dessert beetle inspired nanotextured bumps. Investigation parameters included post height, interpost spacing, bump radius of curvature and Weber number. The outcome of droplet impact was found to be one of three different states, i.e., the Cassie state, droplet rebound and the Wenzel state, depending on bump geometrical parameters and Weber number. As well known, droplet in the Cassie state remains suspended on the nanostructure, hence easy to collect compared to the Wenzel state (in which droplet wets the nanostructure) and droplet rebound (droplet is lost to atmosphere). Two graphical relationships were drawn representing relation between the droplet impact outcomes and bump geometrical parameters and Weber number. Following is a brief summary of interesting findings of this work.

1. Upon impact on nanotextured bumps the droplet liquid penetrate into interpost spacings and limit the maximum spreading factor value compared to the

smooth bumps. The faster retraction of droplet in case of nanotextured bumps was observed.

2. The penetrating droop of impacting droplet can easily collapse the airpockets for smaller posts compred the higher posts, which causes transition to the Wenzel state.
3. Increasing the interpost spacing allows the high momentum liquid of droplet to easily enter into interpost spacings inducing the Wenzel state, whereas smaller interpost spacings induce higher retraction velocities leading to droplet rebound.
4. The droplet rebound is observed on bumps with larger curvature and Cassie state on bumps with smaller curvature.

Overall, droplets impacting on nanotextured bumps with higher posts and smaller bump curvature are in the Cassie state, which is favorable water collection. The bumps with taller posts and smaller radius of curvature lead to droplet rebound. Weber number is more important for droplet impacts on bumps with smaller posts and larger interpost spacings, where transition to the Wenzel state can occur even at very small Weber number.

In this Chapter, we mainly investigated roles bump geometrical properties on single droplet impact. However, slope of surface was not investigated. Next Chapter discusses the roles of surface slope on two droplets impact.

CHAPTER 5

OBLIQUE IMPACT OF TWO SUCCESSIVE DROPLETS ON A FLAT SURFACE

5.1 INTRODUCTION

Using the lattice Boltzmann method, a numerical study was conducted to investigate the oblique impact of two successive droplets on a flat surface. The focus was placed on the effects of surface inclination, lateral/longitudinal offset, the impact dynamics of the two droplets and the subsequent dynamics of the combined droplet. The evolution of the topology, contact lines and spreading factor of the two droplets under various conditions was compared and analyzed. Furthermore, the intermixing between the two droplets during the oblique impact was also examined.

5.2 PROBLEM DEFINITION AND DIMENSIONAL ANALYSIS

Figure 5.1 shows a schematic of the present problem. With the same velocities two identical droplets make successive impact on a slanted surface along the vertical direction. The two droplets are separated with a vertical distance and, in some cases, a lateral/longitudinal distance during the impact. To help facilitate the study, a Cartesian coordinate system is defined in such a way that its origin is located at the impact point of the leading droplet on the surface, and its *x* and *y* axes point to the lateral and longitudinal (slope) directions over the slanted surface, respectively.

This chapter is based on a published study and being reproduced with the permission of Elsevier.
Ahmad, S., Tang, H., and Yao, H.M., 2018, Oblique Impact of Two Successive Droplets on a Flat Surface, International Journal of Heat and Mass Transfer, Vol. 119, pp. 433-445

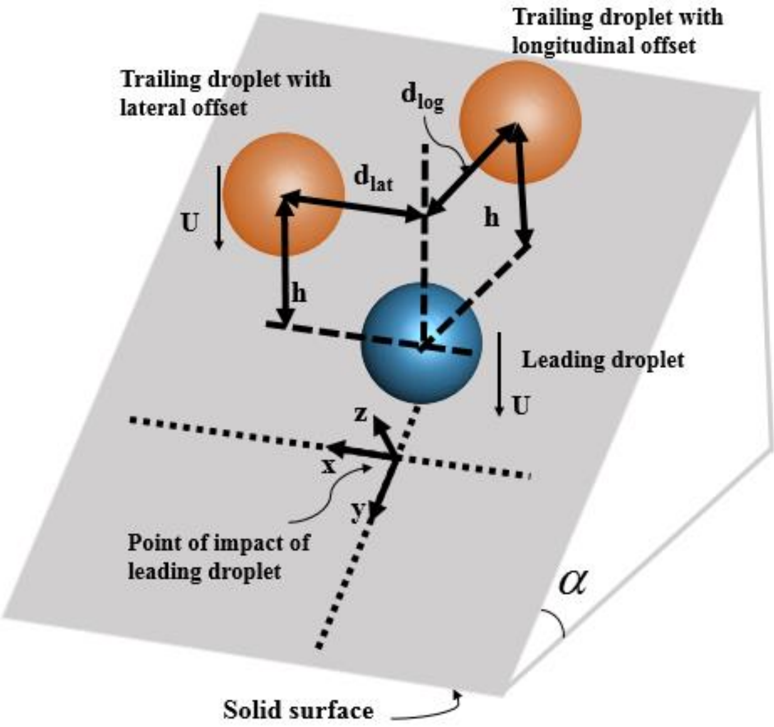

Figure 5.1 Schematic of two successive droplets impacting on an inclined surface.

Assume there is no gravitational force. The dynamics of the two droplets are determined by twelve key parameters: the surface inclination angle α, the surrounding gas density ρ_g and viscosity μ_g, the liquid droplet diameter D, density ρ, viscosity μ, surface tension σ, contact angle θ and impact velocity U, and the center-to-center distance of the two droplets in the lateral direction d_{lat}, in the longitudinal direction d_{long}, and in the vertical direction h (see Fig. 5.1). According to the Buckingham-Pi theorem, these parameters can be condensed into following nine independent non-dimensional parameters:

$$\alpha,\ \rho/\rho_g,\ \mu/\mu_g,\ \mathrm{Re} = \rho UD/\mu,\ \mathrm{We} = \rho U^2 D/\sigma,\ \theta,\ \lambda_x = d_{lat}/D,\ \lambda_y = d_{long}/D,\ h/D \quad (5.1)$$

where ρ/ρ_g and μ/μ_g are liquid-to-gas density ratio and viscosity ratio, respectively. The Reynolds number Re describes the relative importance of the fluid inertia compared to the viscosity force in the droplets, the Weber number We describes the relative importance of the fluid inertia compared to the surface tension of the droplets, and λ_x, λ_y and h/D describe the offsets between the two droplets along the x (lateral), y (longitudinal) and vertical directions, respectively. In literature the Ohnesorge number $\mathrm{Oh} = \mu/(\rho\sigma D)^{1/2}$ is also used to describe droplet dynamics [41,85], which can be related to Re and We through $\mathrm{Oh} = (\mathrm{We})^{1/2}/\mathrm{Re}$.

In this Chapter, the properties of the two droplets and surrounding gas are fixed. That is, the density ratio ρ/ρ_g = 10.46, viscosity ratio μ/μ_g = 10.46, Reynolds number Re = 80, and Weber number We = 40 are all constants. It should be noted that density and viscosity ratio are different from Chapter 4. In addition, among the three offsets of the two droplets, the vertical distance is fixed at h/D = 1.15. The contact angle of the droplets on the slanted surface is fixed at θ = 90°, a moderate value between hydrophobicity and hydrophilicity. Hence the focus is placed on the remaining three non-dimensional parameters, i.e., the inclination angle of the surface α, the lateral and longitudinal offsets between the two droplets λ_x and λ_y.

To describe the dynamics of the two successive impacting droplets, non-dimensional spreading factors along the lateral and longitudinal directions are defined, respectively, as

$$S_x^* = S_x/D,\ S_y^* = S_y/D \tag{5.2}$$

where S_x and S_y are dimensional spreading lengths defined as the largest distances of the contact edges of the two droplet system over the slanted surface in the x and y directions, respectively, as denoted in Fig. 5.2. In addition, a non-dimensional time t^* is used throughout this study to describe the temporal events

$$t^* = Ut/D \tag{5.3}$$

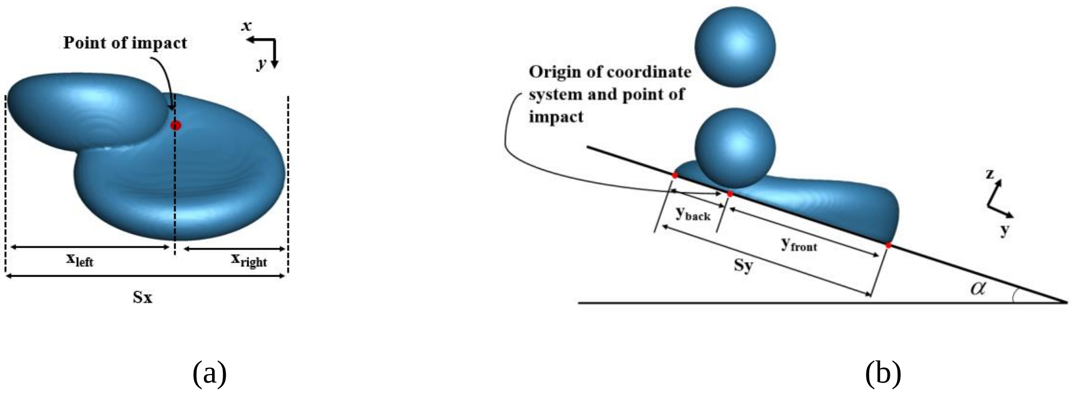

Figure 5.2 (a) Lateral and (b) longitudinal spread lengths and motion of contact edges defined for the two droplet system.

5.3 METHODOLOGY

In this study, the lattice-Boltzmann method (LBM) was adopted to simulate the two-phase fluid flow since handling the liquid-gas interface using this method is relatively easier [127]. The fundamentals of this method can be found in many review articles [127,175] and monographs [173,174], and hence are only briefly introduced here. In this study we used the LBM based on He et al.'s model [129]. In this method, two sets of distribution function, namely a pressure distribution function and a distribution function for index function, are used, and the phase segregation and interfacial dynamics are achieved by incorporating molecular interactions. The Navier-Stokes equation and interface-tracking equation can be recovered from the LBM equations of pressure distribution and index function, respectively [129,207]. The present LBM framework can achieve the second order accuracy in both space and time [207].

5.3.1 COMPUTATIONAL DOMAIN AND BOUNDARY CONDITIONS

The computational domain is a three-dimensional rectangular box. Its lower boundary is set as the slanted surface. The two droplets are placed inside the domain with preset offsets. Instead of redefining the surface, the change of impact obliqueness or surface inclination angle α is realized by relocating the two droplets such that the angle between the line connecting their centers and the surface's normal direction is equal to α. The periodic boundary condition is applied on the domain's four side boundaries, and the bounce back boundary condition is employed on the top and bottom boundaries to implement the no-slip boundary condition.

A grid dependence test has been conducted using four sets of grids as listed in Table 5.1. The maximum spread factors (S_x^* and S_y^*) for successive droplet impact on a surface of inclination 45° were calculated. It was found that relative errors in both the spread factors for a droplet having a diameter of 40 lattice units is less than 0.5% compared to that having a diameter of 60 lattice units. Therefore, by considering the trade-off between the accuracy and the computational cost, 40 lattice units per droplet diameter was chosen for the present study. During the simulations, the two droplets are firstly equilibrated for 15,000 time steps and are then allowed to move and impact on the slanted surface. The spurious current was found to be in the order of 10^{-5} lattice unit per time step, about three orders of magnitude less than the droplet impact velocity. Hence the effect of spurious current can be neglected.

As mentioned in Section 5.2, in this study the liquid-gas density ratio is fixed at only ρ/ρ_g = 10.46. The use of this low density ratio is mainly determined by the limitation of the current LBM code. The simulation became unstable when the density ratio is higher than this value. However, since the Reynolds number and Weber number used in the present study are not high, so that the inertial effects in the surrounding gas are small, it is believed that the use of such a moderate density ratio is still able to capture the key dynamics of the two droplets successive impact problem.

Table 5.1 Grid independence test for droplet diameter at Re = 80 and We = 40

D (lattice units)	30	40	50	60
S_y^*(max)	2.446	2.469	2.473	2.479
Error	1.33%	0.40%	0.24%	-
S_x^*(max)	2.128	2.15	2.154	2.16
Error	1.48%	0.463%	0.27%	-

5.3.2 VALIDATION

As an important benchmark for validation, the Laplace law relates the pressure difference across the droplet interface ΔP to the surface tension σ

$$\Delta P = 2\sigma/R \tag{5.4}$$

where R is the droplet radius. A droplet is initialized and equilibrated in a periodic domain of 120×120×120. Fig. 5.3 plots the pressure difference against the inverse of droplet radius, where a good agreement between the simulation and analytical results has been achieved.

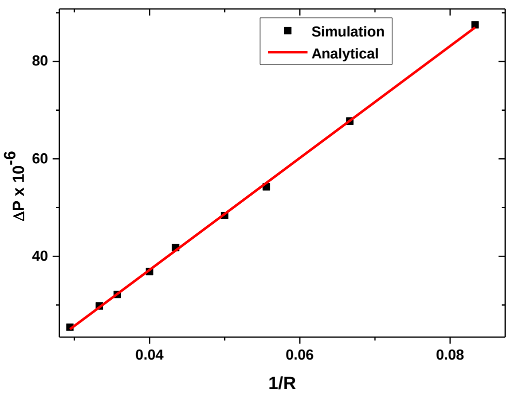

Figure 5.3 Validation of the current LBM framework using the Laplace law for a stationary droplet.

To further validate the present simulation framework, the dynamic process of single droplets normally impacting on a flat surface is simulated. Fig. 5.4 shows the typical evolution of the spread factor S^* of single, normally impacting droplets. This dynamic process generally consists of four consecutive phases, i.e., the kinematic phase, spreading phase, relaxation phase and equilibrium phase [34].

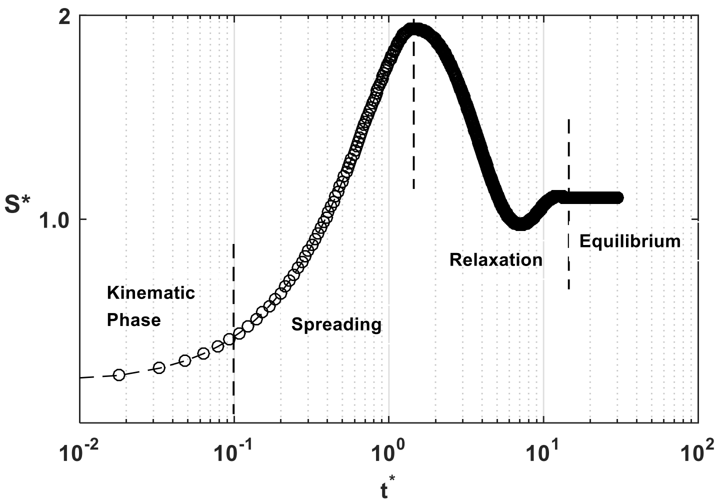

Figure 5.4 Typical evolution of spreading factor of a single droplet normally impacting on a flat surface.

The simulation results are firstly validated against existing experimental data. In the experiment [208], the normal impact of a droplet of diameter 2.45 mm was considered, which is a mixture of water and glycerin, with the density of 1,220 kg/m^3, surface tension of 0.063 N/m, and viscosity of 116 mPa·s. A wax surface, having contact angle hysteresis with advancing contact angle θ_a = 97° and receding contact angle θ_r = 90°, was used for the impact. Two cases with impact velocities of 1.04 m/s and 1.41 m/s were conducted, corresponding to Re = 27, We = 51 and Re = 36, We = 93, respectively. Simulations are performed accordingly, in which the contact angle hysteresis is modeled by following Wang et al. [209]. The spreading factor is obtained for the kinematic phase, the spreading phase and a part of the relaxation phase, as shown in Fig. 5.5. It can be seen that reasonable agreement between the experimental data and the simulation results is achieved.

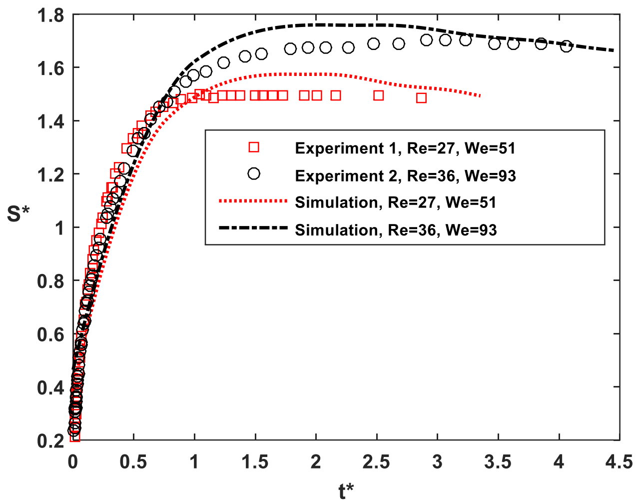

Figure 5.5 Evolution of spreading factor of single, normal impacting droplets in kinematic, spreading and part of relaxation phases.

Validation is then made by examining the droplet dynamics in the kinematic phase (t^* << 1) and the maximum spreading factor. In reference [34], it was reported that the spreading factor is proportional to $(t^*)^{½}$ in the kinematic phase with a coefficient of 2.8. Various numerical studies [83–85,160,210] were also carried out and obtained the coefficient varying from 1.35 to 2.5. Moreover, theoretical analysis predicted a value 2.0 for the coefficient [7, 12]. Using the present LBM framework, six cases are simulated at different Reynolds and Weber numbers. As shown in Fig. 5.6, a curve fitting gives $S^* = 1.9(t^*)^{½}$, where the coefficient value is close to the theoretically predicted value 2.0. Furthermore, the same set of data predicts that the maximum spreading factor of single, normal impacting droplets has a good power law with $\mathrm{Re}^2\mathrm{Oh}$ as revealed in Fig. 5.7, which agrees well with what have been reported in literature [36,40,85] and also with a more specific relation obtained experimentally by Scheller et al. [41]

$$S^*_{\max} = 0.61\left(\mathrm{Re}^2 Oh\right)^{0.166} \tag{5.5}$$

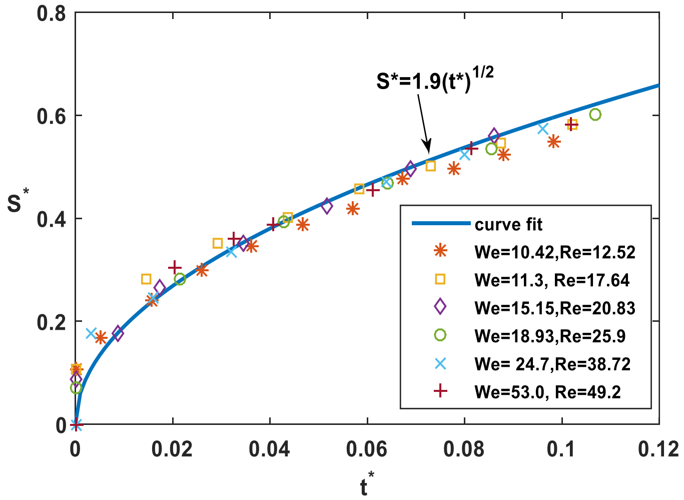

Figure 5.6 Evolution of spreading factor of single, normal impacting droplets in kinematic phase.

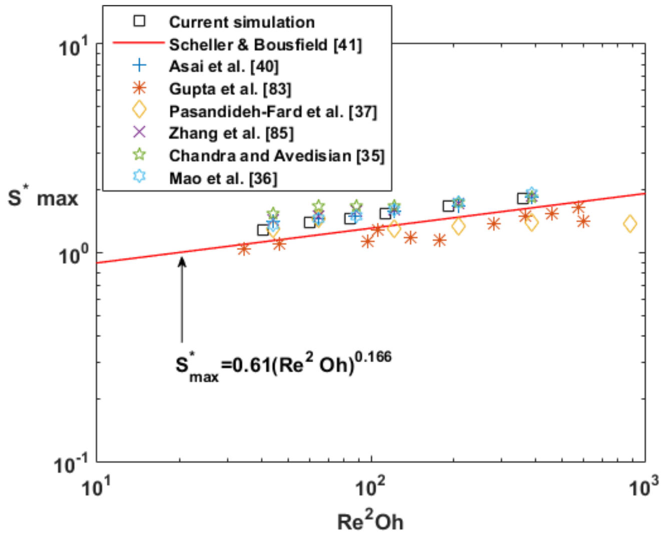

Figure 5.7 Correlation of the maximum spreading factor of single, normal impacting droplets with Re^2Oh.

Finally, the validation is conducted on the impact and coalescence of two droplets, where the position of the second droplet can significantly affect the maximum spreading factor. Graham et al. [88] investigated the impact of a falling droplet with a stationary droplet, and proposed empirical correlations for the maximum spreading factor over different surfaces.

$$S^* = S / (D + d) \tag{5.6}$$

$$S^*_{max} = 1.322(1 + d/D)^{-0.9220}\,\mathrm{We}^{0.1943} \tag{5.7}$$

where d is the offset. Simulations are performed over a surface having contact angle hysteresis with an advancing contact angle θ_a = 108° ± 5 and a receding contact angle θ_r = 71° ± 5, and a static contact angle of θ = 93° ± 3. The dimensionless number are chosen the same as in the single droplet validation cases, i.e., Re = 38.72 and We = 24.7. The simulated maximum spreading factors are compared with those given by an empirical correlation Eq. (5.7) as listed in Table 5.2. The maximum error is found to be about 4%.

Table 5.2 Maximum spreading factor results for coalescence of two droplets at Re = 38.72 and We = 24.7

Offset ratio (d/D)	0	0.25	0.50	1.0
S^*_{max} (Eq. 5.7)	2.46	2.0	1.69	1.30
S^*_{max}(Simulation)	2.5	1.92	1.63	1.35
Error	1.66%	-4.0%	-3.5%	3.7%

5.4 RESULTS AND DISCUSSION

5.4.1 EFFECT OF TWO SUCCESSIVE IMPACTS

Figure 5.8 shows the evolution of the simulated two droplets successively impacting on a surface with an inclination angle of α = 45°. The corresponding velocity fields inside and around the droplets in the mid-span plane are shown in Fig. 5.9. At an instant before the trailing droplet hits the surface (e.g., t^* = 1.0, shown in Fig. 5.8(a)), the leading droplet starts its spreading process. Instead of axisymmetric spreading in normal impact events, the presence of surface inclination results in different spreading along the two major directions, i.e., the lateral spreading along x direction and the longitudinal spreading along y direction. In addition, the centroid of the leading droplet moves downward along the inclined surface due to the relative fluid motion inside the droplet and the surface friction, as depicted in the velocity field in Fig. 5.9(a). At t^* = 1.66, the trailing droplet hits the spreading leading droplet which does not fully slide away, and the two droplets start coalescing. During the early stage of the coalescence (e.g., at t^* = 3.0 as shown in Fig. 5.8(b)), the two droplets merge and generate a combined, larger droplet, causing significant increase of both lateral and longitudinal spreading as compared to the spreading of each individual droplet (as quantified in Fig. 5.10). It is also seen from the velocity field shown in Fig. 5.9(c) that the trailing droplet injects high momentum fluid into the leading droplet through the coalescence, further enhancing the spreading. After the spreading in both directions reaches their respective maximum, the combined droplet starts its recoiling process due to the surface tension, as revealed in Figs. 5.8(d) to 5.8(f), at t^* = 6.0, 9.0 and 13.0, respectively. In this recoiling process, the velocity near the front contact edge of the combined droplet becomes small and even reverses to form a vortex, while the velocity near the back contact edge is large, as revealed in Figs. 5.9(d) to 5.9(f). As such, the longitudinal spreading of the combined droplet reduces, and the height increases.

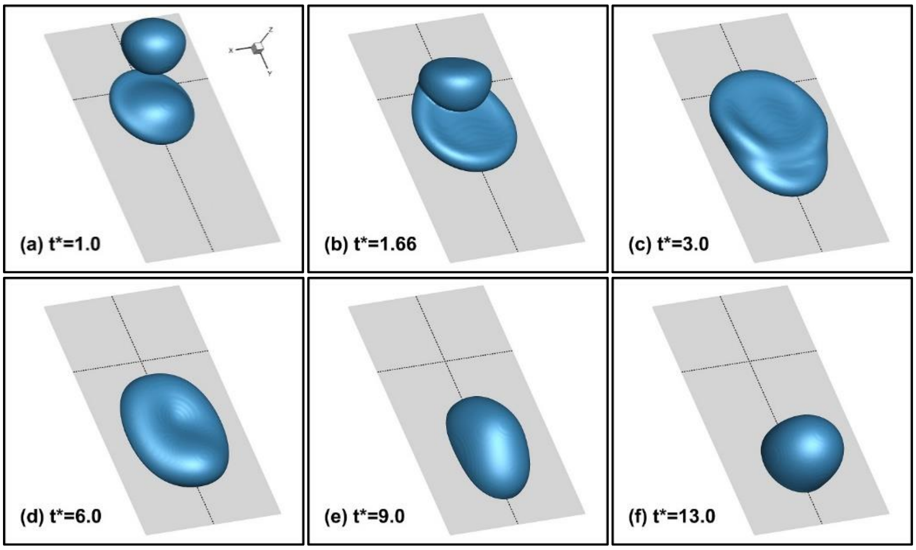

Figure 5.8 Evolution of two droplets successively impacting on a surface with an inclination angle of α = 45°. The intersection point of the two dashed lines on the surface indicates the point of impact for the leading droplet.

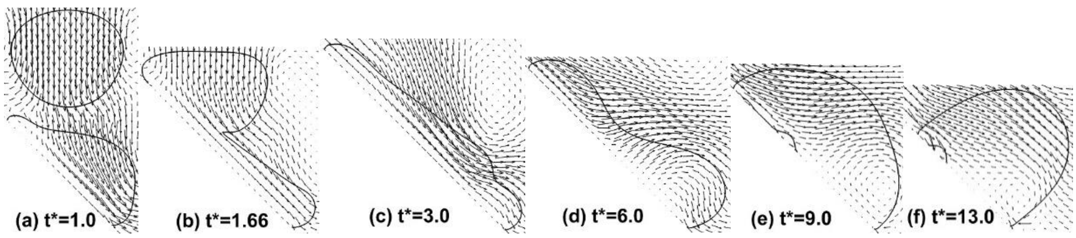

Figure 5.9 Evolution of the velocity field inside and around the two droplets in the mid-span plane (i.e., the x = 0 plane).

Figure 5.10 further compares the evolution of spreading factors of the two successively impacting droplets and of a single droplet. It is observed that, in the present case of two successively impacting droplets, the coalescence occurs when the leading droplet is in its spreading phase. After the coalescence, abrupt jumps in both the lateral and longitudinal spreading factors occur, which, as having been explained above, is attributed to the injection of high momentum fluid from the trailing droplet. Note that the two spreading factors reach their respective maximum at different timings. That is, the longitudinal spreading reaches its maximum value first at about $t^* = 2.8$, which is very close to $t^* = 2.66$ for the single droplet, while the lateral spreading reaches its maximum at about $t^* = 3.92$, significantly delayed from $t^* = 2.01$ for the single droplet. It is also observed that a small plateau appears in the curve of two-droplet longitudinal spreading factor during about $t^* = 5.0$ to 7.0, which defers the decrease of spreading factor. Detailed inspection of Figs. 5.8 and 5.9 reveals that this plateau corresponds to the arrival of the trailing droplet front to the combined droplet front. Although the simulation time is not long enough to show the final trend, it is seen that, as time advances, both the spreading factors of the two droplets gradually approach those for the single droplet.

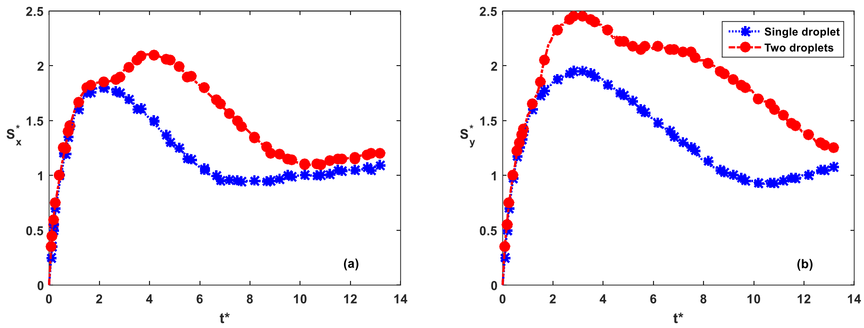

Figure 5.10 Comparison of the evolution of (a) lateral and (b) longitudinal spreading factors between a single impacting droplet and two successively impacting droplets.

5.4.2 EFFECT OF SURFACE INCLINATION ANGLE

The evolution of the two droplets successively impacting on surfaces with three different inclination angles, i.e., α = 30°, 45° and 60°, is presented in Fig. 5.11. It is seen that with the increase of the inclination angle, the leading droplet slides faster, and hence the longitudinal distance between the two droplets increases when the trailing droplet hits the surface. As such, in the α = 30° and 45° cases the trailing droplet can still entirely fall on the leading droplet, but in the α = 60° case it only partially falls on the leading droplet. For this reason, the droplet dynamics in the α =

60° case is quite different from that in the other two cases, especially during the spreading and relaxation phases.

The evolution of laterally left/right contact edges and longitudinally front/back contact edges of the combined droplet for the three cases is compared in Fig. 5.12, and the evolution of their respective distances, i.e., the lateral and longitudinal spreading factors, are plotted in Fig. 5.13. It is seen from Fig. 5.12(a) that the left/right contact edges are symmetric about the mid-span plane (x = 0) in all the cases. During the spreading and relaxation phases (about $t^* < 10$), the distance between the left and right edges, i.e., the lateral spreading factor, slightly decreases with the increase of the surface inclination angle, which is also confirmed in Fig. 5.13(a).

As for the motions of the front and back contact edges, as shown in Fig. 5.12(b), both edges move downward (along the positive y direction) faster with the increase of inclination angle, confirming the sliding trend observed in Fig. 5.11. The back contact edges in all the cases experience a short upward motion (along the negative y direction) before moving downward, which is the result of spreading. For the α = 60° case, an upward jump in the back contact edge is observed, starting at about $t^* = 1.66$. This is due to the partial contact of the trailing droplet with the already-on-surface leading droplet as revealed in Fig. 5.11(c1). This abrupt jump is also observed in the evolution of longitudinal spreading factors in Fig. 5.13(b).

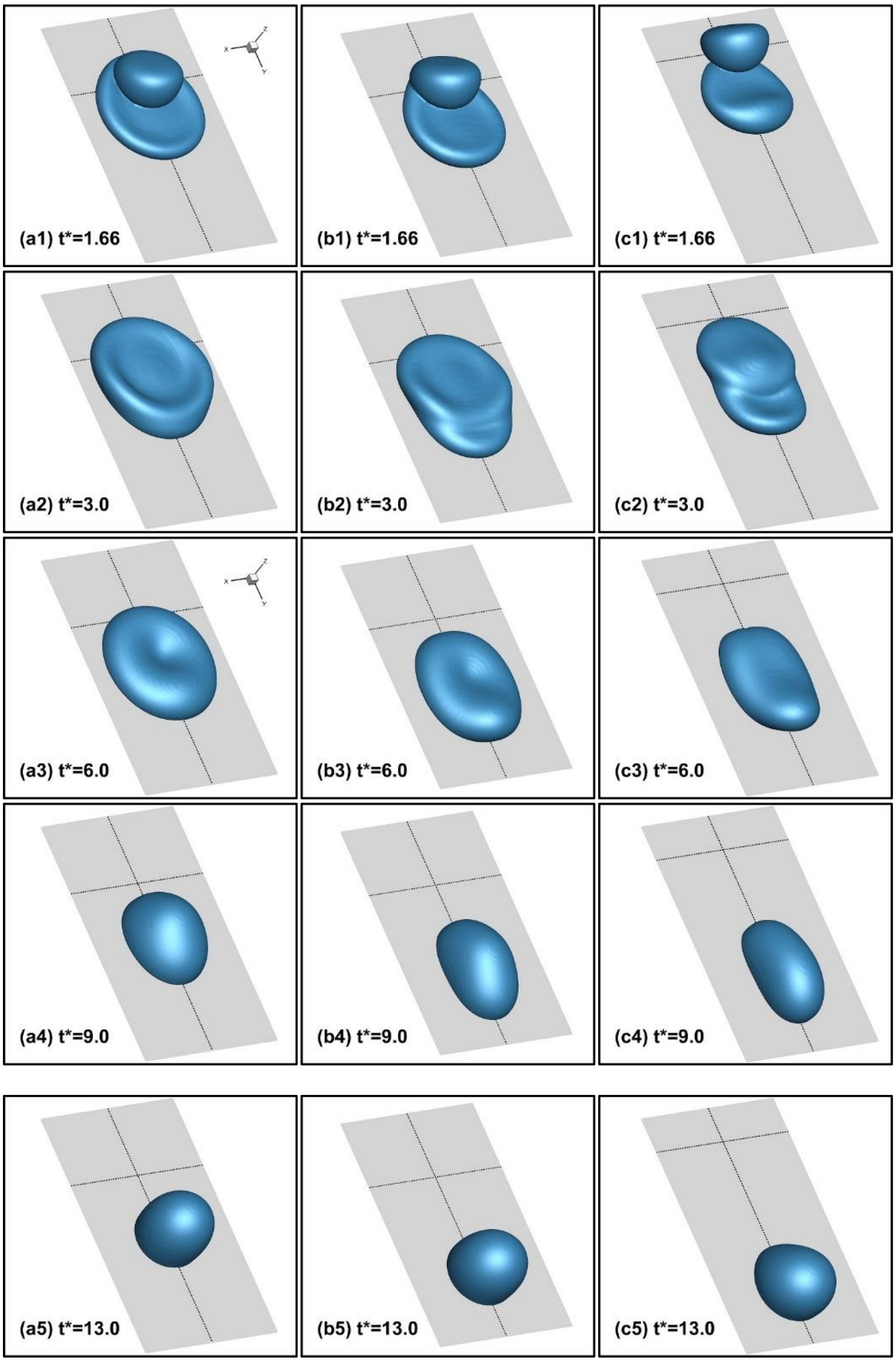

Figure 5.11 Evolution of two droplets successively impacting on surfaces of different inclination angles: (a) α = 30°, (b) α = 45°, and (c) α = 60°. The intersection point of the two dashed lines on the surface indicates the point of impact for the leading droplet.

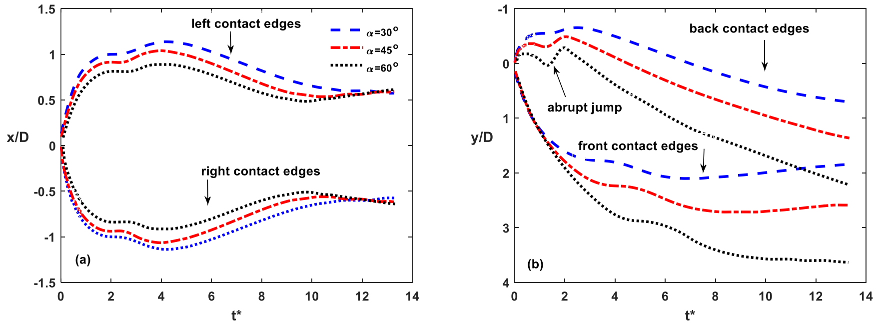

Figure 5.12 Evolution of (a) left and right edges and (b) front and back edges of the combined droplet at different surface inclination angles.

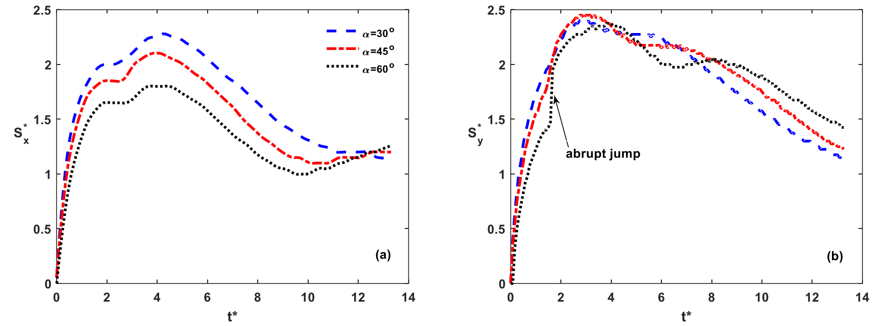

Figure 5.13 Evolution of (a) lateral and (b) longitudinal spreading factors at different surface inclination angles.

5.4.3 EFFECT OF LATERAL OFFSET

The evolution of the two droplets successively impacting on a surface of an inclination angle α = 45° with various lateral offsets, i.e., λ_x = 0.50, 0.75, 1.0 and 1.5, is presented in Fig. 5.14. It is seen that, due to the non-zero lateral offset, the coalescence of the two droplets in all the cases becomes asymmetric about the mid-span plane (x = 0). When the trailing droplet hits the surface, the overlap between the two droplets becomes smaller with the increase of lateral offset, and the subsequent coalescence process lasts for a longer time. Note that the two droplets will never merge if the lateral offset is greater than about 1.5. In the λ_x = 0.50, 0.75 and 1.0 cases, clear capillary wave propagation is observed during the coalescence process at t^* = 3.0. When this wave front reaches the front contact edge of the leading droplet at t^* = 6.0, a bulge appears at the front. At this instant, a slight corner shape is observed at the back contact edge of the combined droplet in the λ_x = 0.75 and 1.0 cases (see Figs. 5.14(b3) and 5.14(c3)), which is attributed to the intermediate lateral offset. As for the λ_x = 1.5 case, since the lateral offset is large, a combined droplet of dumbbell shape is observed at t^*

= 6.0 as shown in Fig. 5.14(d3). After t^* = 6.0, the surface tension force dominates in all the cases and the droplet retraction begins. At t^* = 13.0, the combined droplets in the λ_x = 0.50, 0.75 and 1.0 cases share a similar shape, while the droplet in the λ_x = 1.5 case is elongated in the lateral direction.

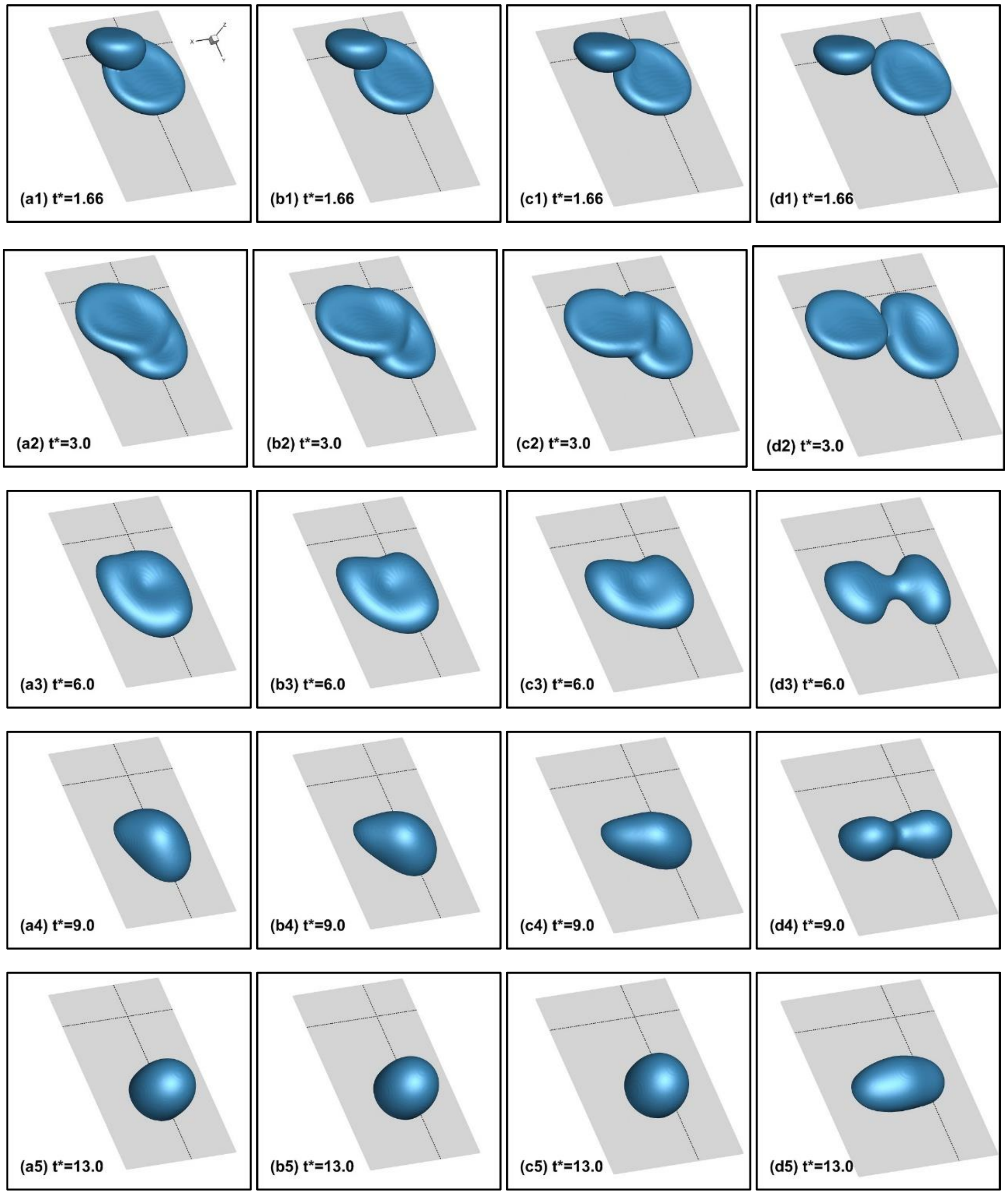

Figure 5.14 Evolution of two droplets successively impacting on a surface of inclination α = 45° with various lateral offsets. From left to right: λ_x = 0.5, 0.75, 1.0 and 1.5. The intersection point of the two dashed lines on the surface indicates the point of impact for the leading droplet.

The evolution of the left/right and front/back contact edges of the combined droplets for these four cases is shown in Fig. 5.15. The data from the zero-offset case is also plotted as a reference. It can be seen from Fig. 5.15(a) that, with the increase of lateral offset, the abrupt increase of the left contact edge at about $t^* = 1.66$ becomes more obvious, and the subsequent peak gets higher. For the right contact edge, however, the introduction of non-zero lateral offset makes it slightly retreat. As a result, the lateral spreading factor, i.e., the distance between the left and right contact edges, increases with the increase of lateral offset, as revealed in Fig. 5.15(c).

As for the front contact edges, it is seen from Fig. 5.15(b) that in the beginning they all spread very similarly. Starting from $t^* = 4.5$, an abrupt change is observed, which is a clear sign of the arrival of high-momentum fluid from the trailing droplet. This sudden change is largest in the zero-offset case and decreases with the lateral offset. In the largest offset case where $\lambda_x = 1.5$, however, such a sudden change is not observed owing to the bare coalescence of the two droplets. This abrupt change also appears in the spreading of the back contact edge at around $t^* = 1.6$. After this instant, the back-edge spreading decreases with the increase of the offset. Due to the less interaction, this sudden change is not obvious for the largest two offset cases where $\lambda_x = 1.0$ and 1.5. Different from its lateral counterpart, the longitudinal spreading factor decreases with the increase of lateral offset, as depicted in Fig. 5.15(d).

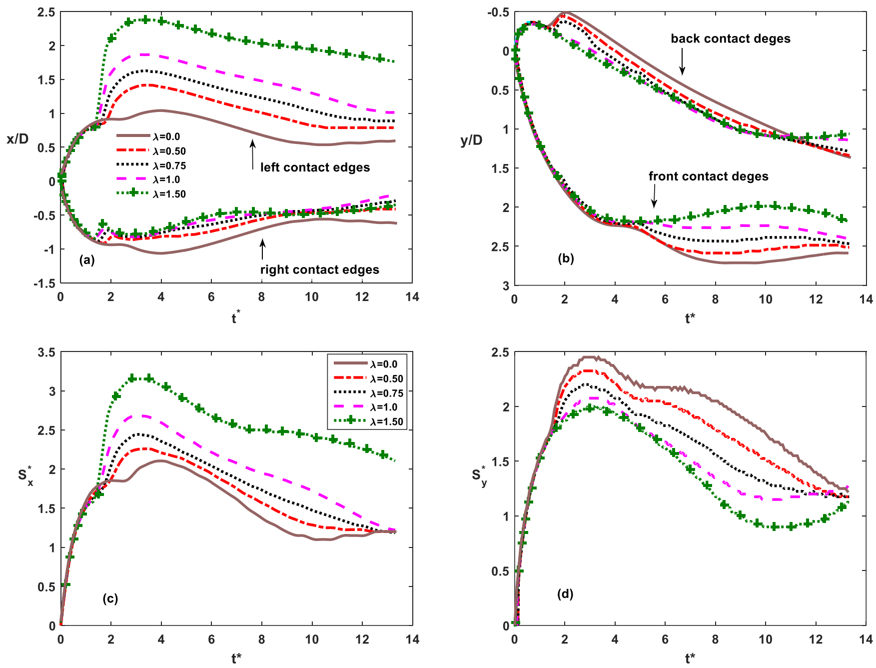

Figure 5.15 Evolution of (a) left and right contact edges, (b) front and back contact edges, (c) lateral spreading factor and (d) longitudinal spreading factor of the combined droplet on a surface of inclination α = 45° with various lateral offsets.

5.4.4 EFFECT OF LONGITUDINAL OFFSET

The dynamics of the combined droplet also changes if the two droplets are offset in the longitudinal direction, i.e., in y direction. In the present study, three non-zero longitudinal offsets are considered, i.e., λ_y = 0.25, 0.5 and 0.75. It was found that the two droplets do not merge if λ_y is greater than about 0.75.

The topological evolution of the two droplets with different longitudinal offsets is shown in Fig. 5.16. It is seen that, due to the offset, at t^* = 1.0 the trailing droplet partially hits the leading droplet in the λ_y = 0.25 and 0.5 cases, whereas it completely hits the dry surface in the λ_y = 0.75 case. Comparison of the coalescence process in these three cases reveals that the increase of longitudinal offset increases the longitudinal spreading of the combined droplet. This is also confirmed by the evolution of the droplet's front and back contact edges and the resulting longitudinal spreading factor shown in Fig. 5.17. From Fig. 5.17(b), it is seen that the increase of longitudinal spreading is mainly attributed to the abrupt change of the back contact edge due to the landing of the trailing droplet. As for the evolution of the left and right contact edges of the combined droplet, it is seen from Fig. 5.17(a) that both edges are symmetric about the mid-span plane, and shift inwards with the increase of longitudinal offset. As such, the lateral spreading factor reduces with the increase of the longitudinal offset as revealed in Fig. 5.17(c)

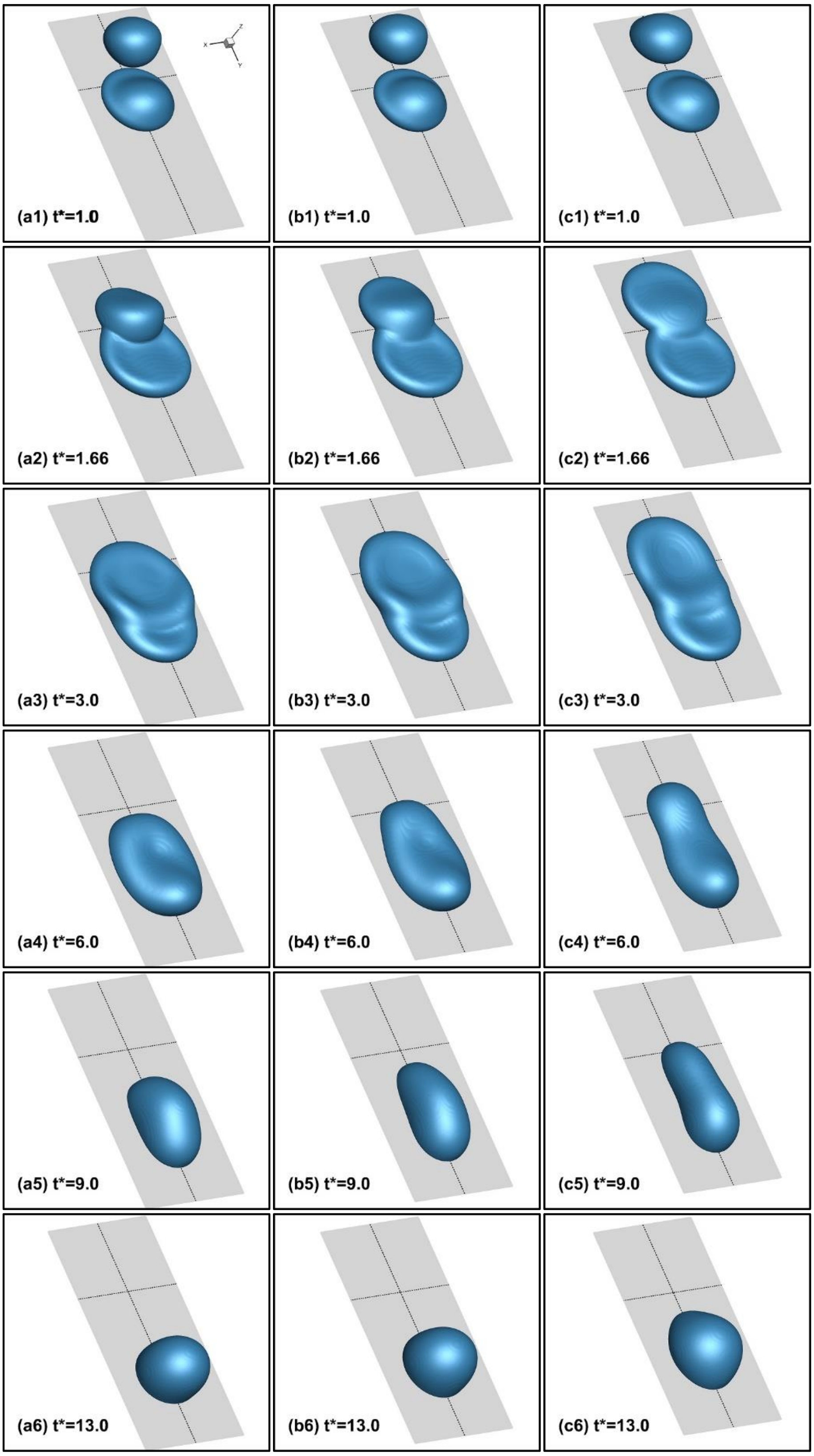

Figure 5. 16 Evolution of two droplets successively impacting on a surface of inclination $\alpha = 45°$ with various longitudinal offsets. From left to right: $\lambda_y = 0.25$, 0.5 and 0.75. The intersection point of the two dashed lines on the surface indicates the point of impact for the leading droplet.

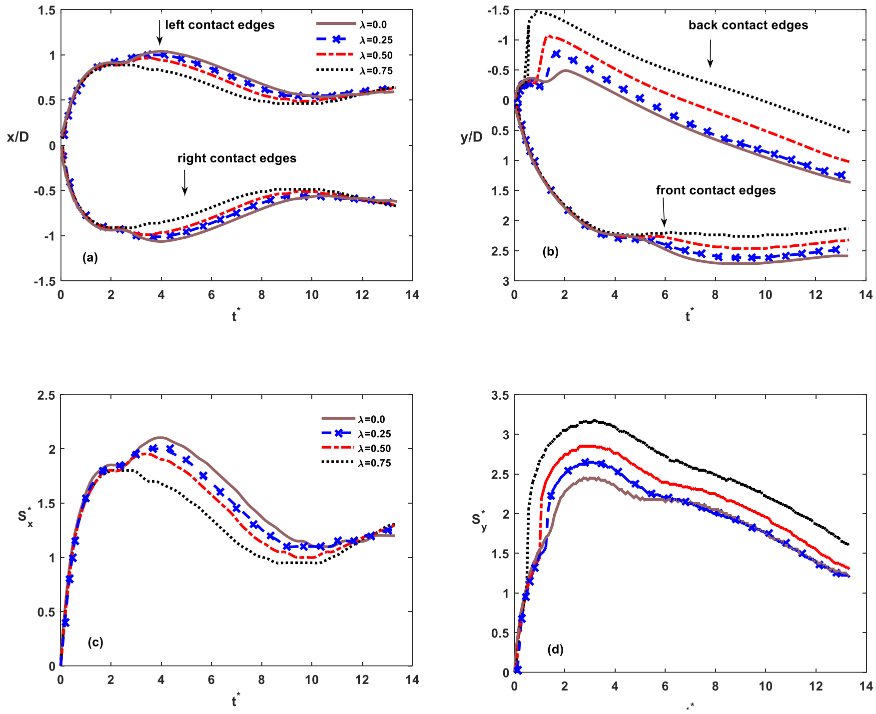

Figure 5. 17 Evolution of (a) left and right contact edges, (b) front and back contact edges, (c) lateral spreading factor and (d) longitudinal spreading factor of the combined droplet on a surface of inclination α = 45° with various longitudinal offsets.

5.4.5 DROPLET INTERMIXING

The intermixing of the two droplets during the impact and coalescence process is also investigated. To visualize the mixing process, tracer particles of two different colors are seeded inside the two droplets, whose trajectories are computed during the simulations. Fig. 5.18 shows the intermixing of the two zero-offset droplets successively impacting on surfaces of different slopes from two views, i.e., the mid-length view along the *y* axis as shown in the upper row and the mid-span view along the *x* axis as shown in the lower row. The leading droplet is filled with red tracer particles, whereas the trailing droplet is filled with green tracer particles. Evolution of the green particles clearly shows that upon collision the trailing droplet first penetrates the rear portion of the leading droplet, and then slides over the leading droplet to reach its front. With the increase of surface inclination angle, the green particles become less in the rear portion of the combined droplet and more in the front, indicating the change of mass distribution of the two droplets.

When the non-zero lateral offsets are introduced, the two droplets gradually become distinguishable in the lateral direction with a clear interface between them, as shown in the first row of Fig. 5.19. In the λ_x = 1.5 case where the lateral offset is the largest, this interface becomes vertical and coincides with the mid-span plane. Accordingly, the green particles observed from the mid-span become less and less, as shown in the lower row of Fig. 5.19. All these observations indicate that the intermixing is reduced with the increase of lateral offset.

When the non-zero longitudinal offsets are introduced, the trailing droplet is left further behind the leading droplet. Hence, with the increase of longitudinal offset, more green particles are accumulated in the rear portion of the combined droplet, and less are scattered in the front portion, as shown in Fig. 5.20, indicating the reduced intermixing.

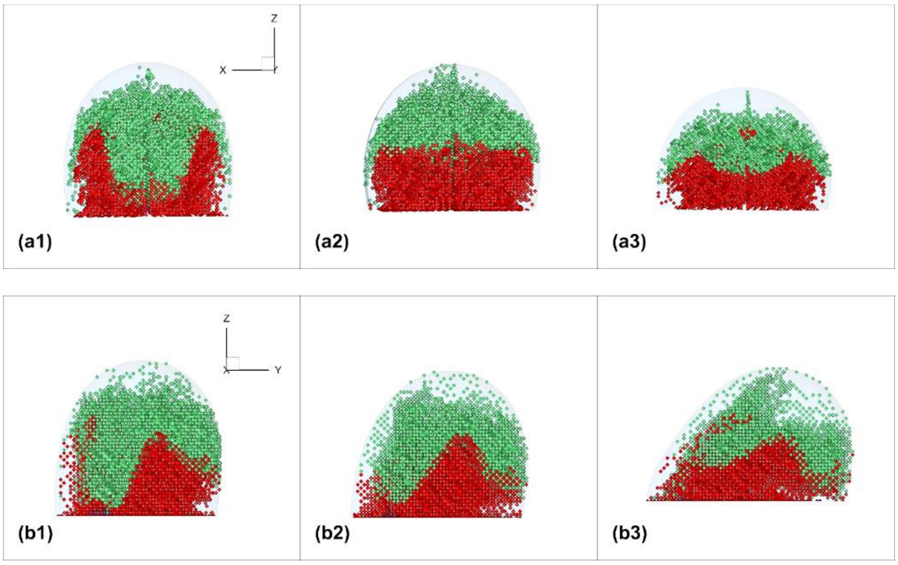

Figure 5.18 Snapshots at t^* = 13 showing the intermixing of the two zero-offset droplets successively impacting on surfaces of different inclination angles. From left to right: α = 30°, 45° and 60°; Top row: the mid-length view along the y axis; Bottom row: the mid-span view along the x axis.

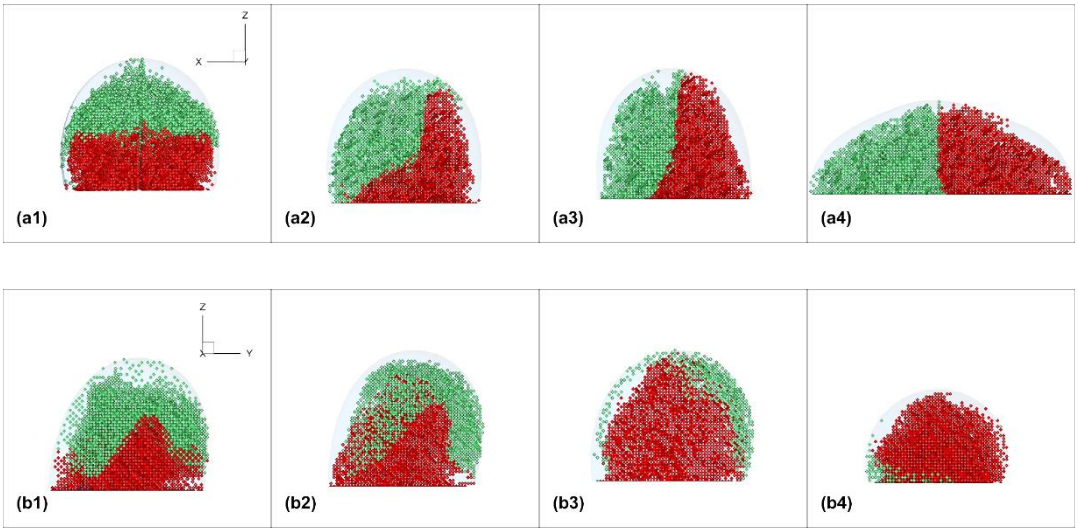

Figure 5.19 Snapshots at t^* = 13 showing intermixing of the two droplets successively impacting on a surface of inclination α = 45° with various lateral offsets. From left to right: λ_x = 0, 0.5, 1.0 and 1.5; Top row: the mid-length view along the y axis; Bottom row: the mid-span view along the x axis.

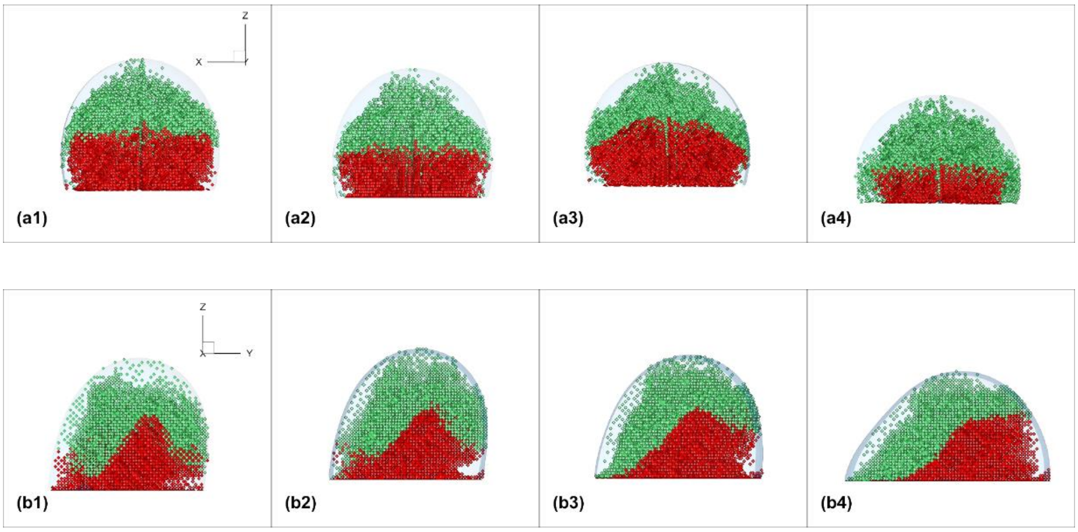

Figure 5.20 Snapshots at t^* = 13 showing intermixing of the two droplets successively impacting on a surface of inclination α = 45° with various longitudinal offsets. From left to right: λ_y = 0, 0.25, 0.5 and 0.75; Top row: the mid-length view along the y axis; Bottom row: the mid-span view along the x axis.

5.4.6 EFFECTS OF WEBER NUMBER, SURFACE WETTABILITY AND DROPLET SIZE ON INTERMIXING

In this section, only lateral and longitudinal offsets are discussed for brevity purpose. The Weber number is varied from We=20 to 80 by changing surface tension. Figure 5.21 shows the temporal snapshots of droplets impact process, and it evolution is quantified in Fig. 5.22. It is noticed from Fig. 5.22 that increasing Weber number lateral and longitudinal spreading factor retraction rates of combined droplet decrease, which are also evident from Figs. 5.21(a5)-5.21(c5).

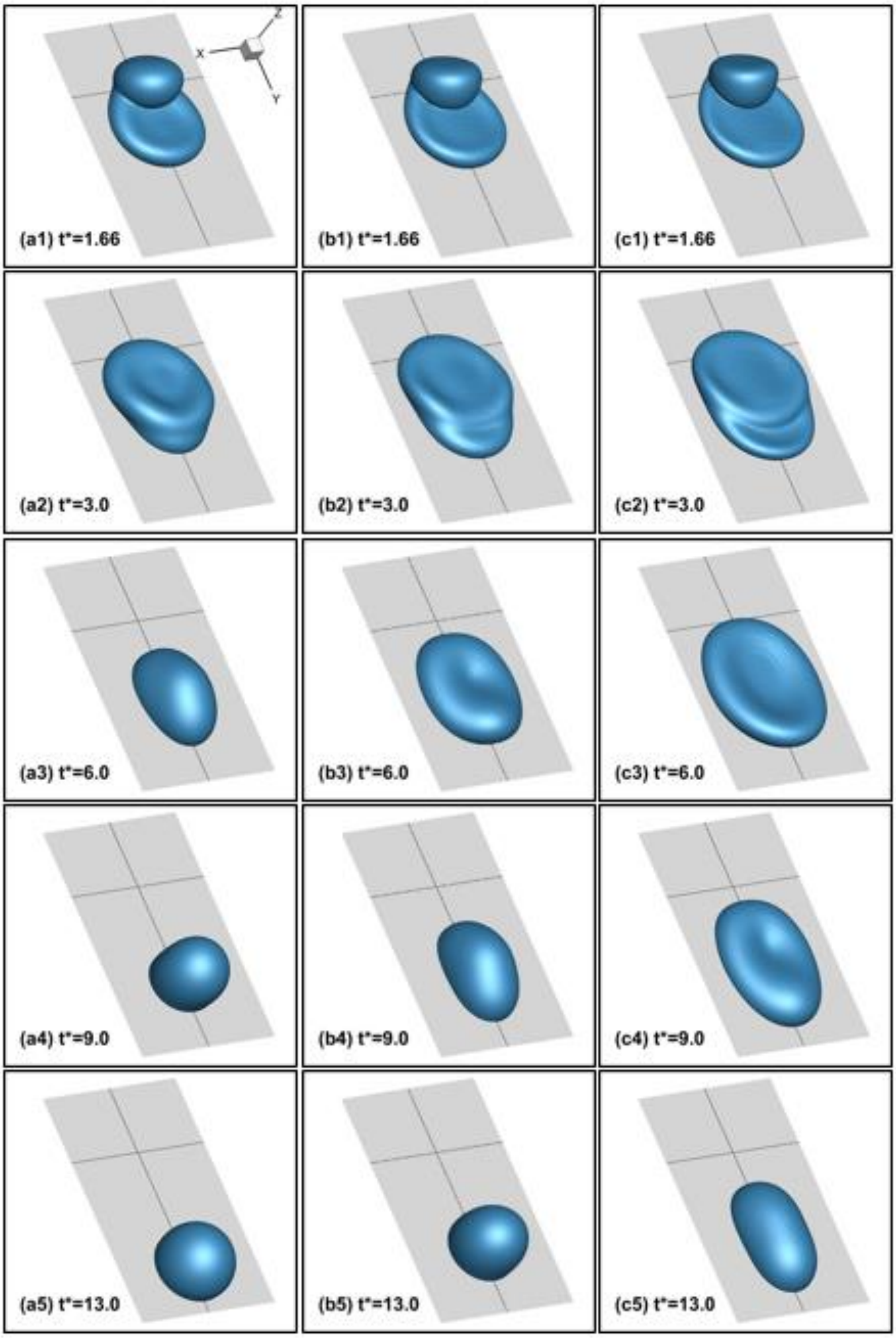

Figure 5.21 Evolution of two droplets successively impacting with different Weber numbers: (a) We=20, (b) We=40, and (c) We=80. The intersection point of the two dashed lines on the surface indicates the point of impact for the leading droplet.

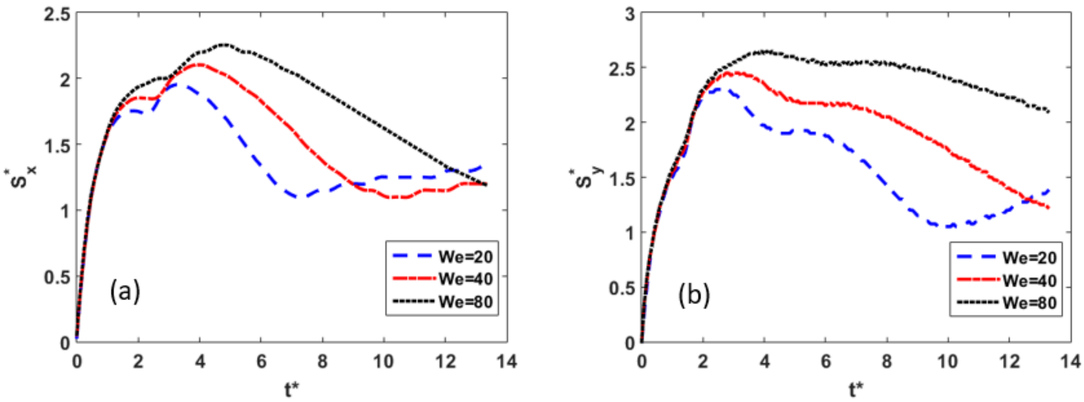

Figure 5.22 Evolution of (a) lateral and (b) longitudinal spreading factors at different Weber numbers.

Next, the effects of surface wettability are investigated. Surface wettability is changed hydrophilic to super-hydrophobic corresponding to contact angles to θ=50° to θ=140°, respectively. It is observed from temporal snapshots (Fig. 5.23) that droplet spreading area is larger for hydrophilic surface (θ=50°) as compared to super-hydrophobic surface (θ=140°). Furthermore, on super-hydrophobic surface droplet retraction rate is faster (Fig. 5.24). However, jumping is not observed in this case.

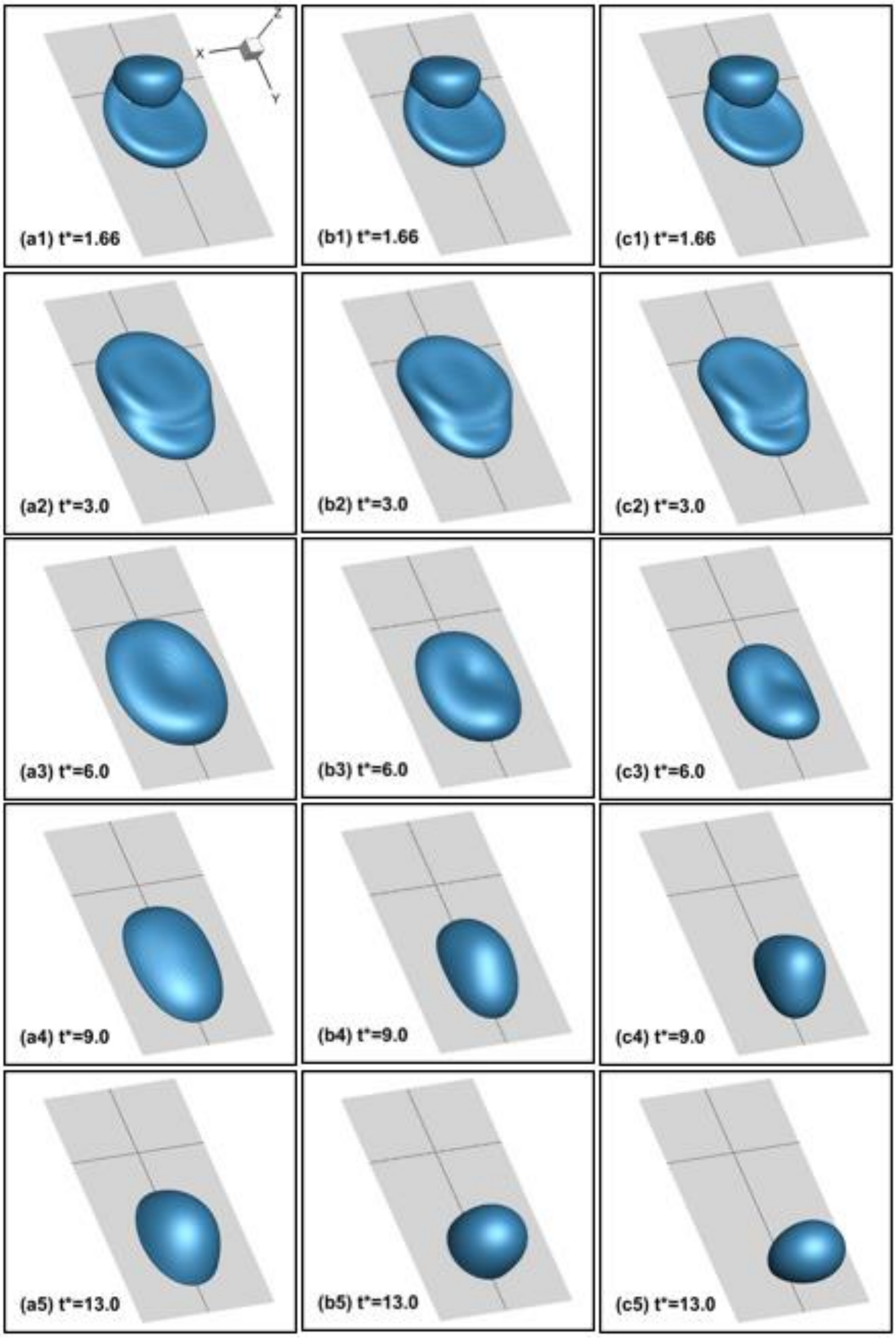

Figure 5. 23 Evolution of two droplets successively impacting on surfaces with different wettability: (a) θ=50°, (b) θ=90°, and (c) θ=140°. The intersection point of the two dashed lines on the surface indicates the point of impact for the leading droplet.

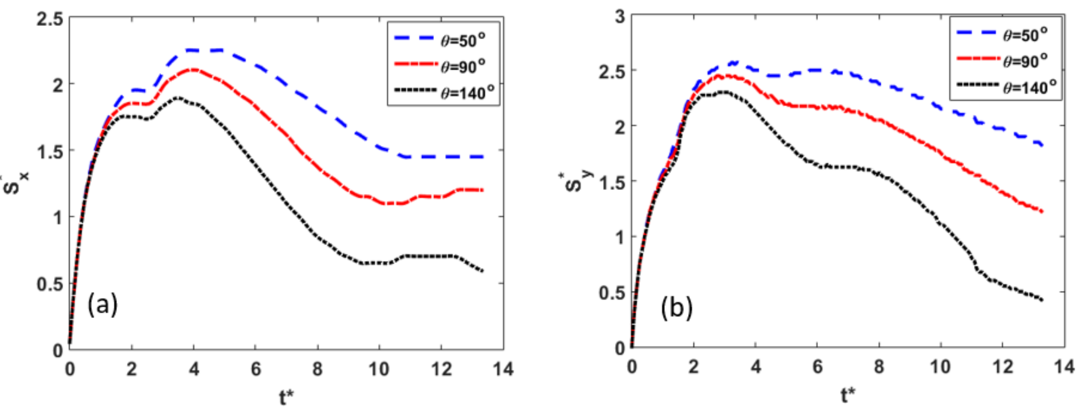

Figure 5.24 Evolution of (a) lateral and (b) longitudinal spreading factors at surfaces with different wettability.

Next, the effects of droplet size are studied. Three cases are considered; in first case, leading droplet is of half size (diameter D/2) as compared to trailing droplet, in second case both droplets are of equal size and in third case trailing droplet is of half size. The temporal snapshots are shown in Fig. 5.25 It is seen from Figs. 5.25(a3) - 5.25(c3) that droplets coalesce and recoil earlier for cases where one droplet has smaller size. Moreover, Fig. 5.26 do not show the abrupt increase of lateral and longitudinal spreading factors when trailing droplet is smaller due to reduced impart of high momentum from trailing to leading droplet.

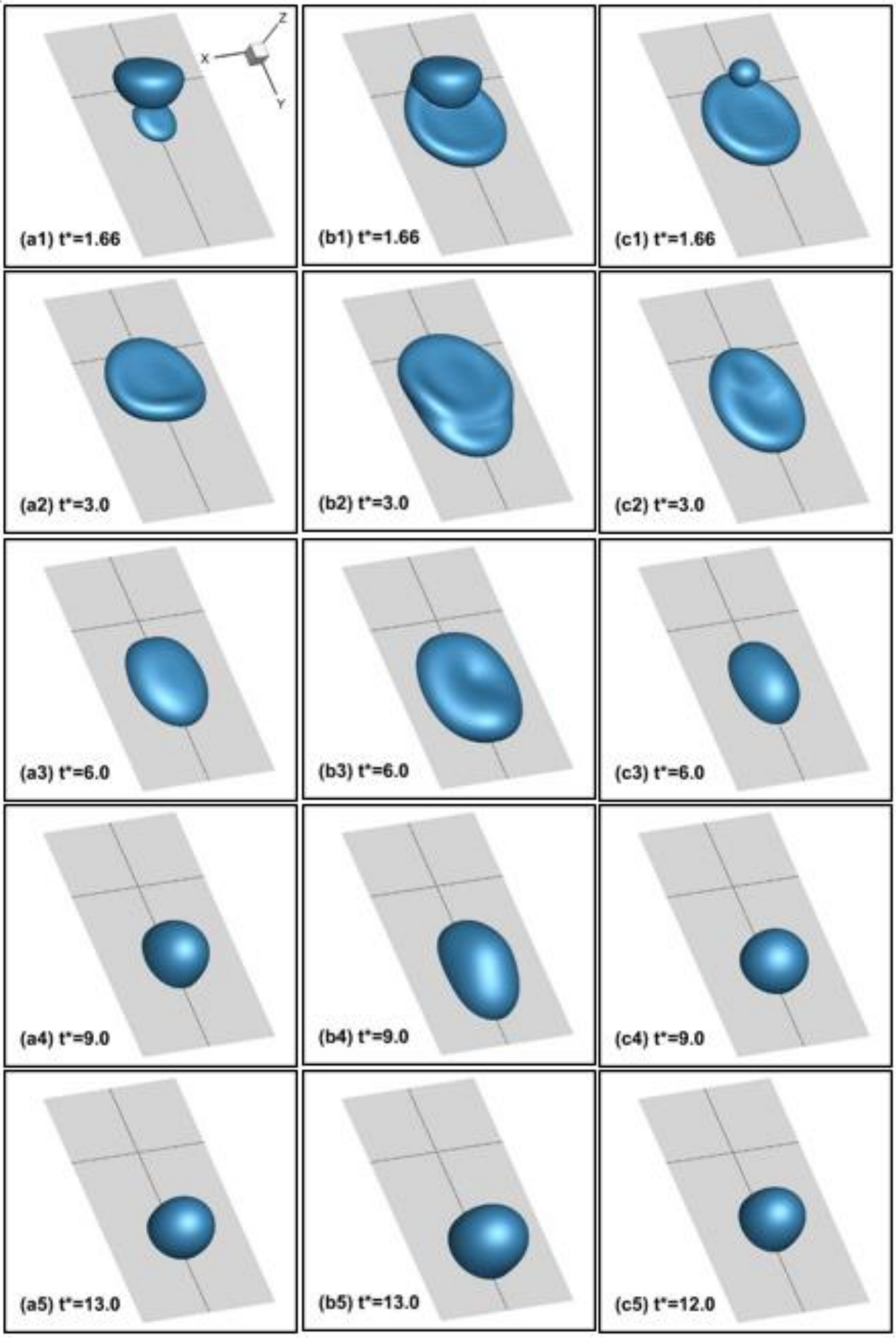

Figure 5. 25 Evolution of two droplets of different sizes impacting successively on surfaces: (a) $D_{leading}/D_{trailing}$=1/2, (b) $D_{leading}/D_{trailing}$=1, and (c) $D_{leading}/D_{trailing}$=2. The intersection point of the two dashed lines on the surface indicates the point of impact for the leading droplet.

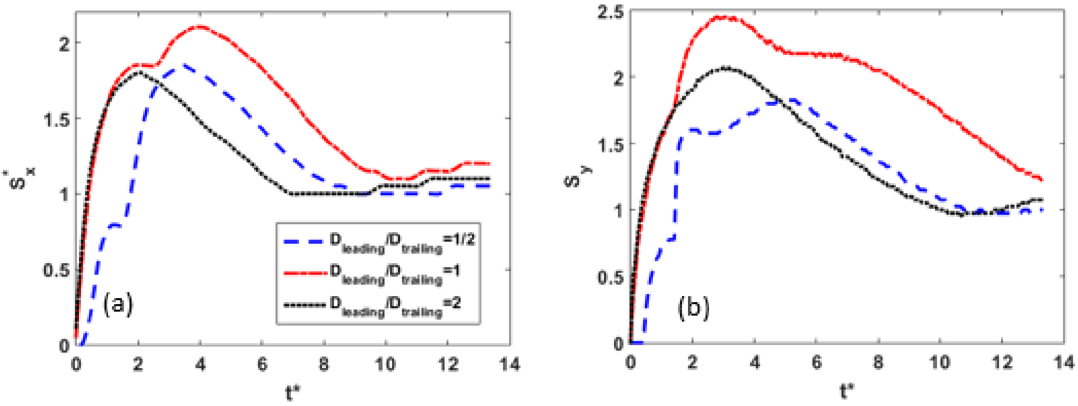

Figure 5. 26 Evolution of (a) lateral and (b) longitudinal spreading factors for different droplet sizes.

As for the droplets intermixing patterns, only snapshots for mid-span view along the x axis are shown. It is revealed from Figs. 5.27-5.29 that droplet size has more pronounced effects on intermixing as compared to Weber number and surface wettability. The intermixing is improved when trailing droplet has smaller size as shown in Fig. 5.29(c).

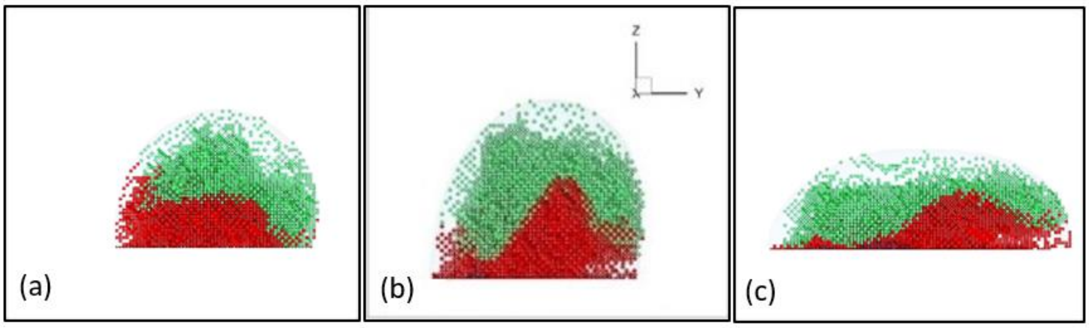

Figure 5.27 Snapshots at t* = 13 showing intermixing of the two droplets successively impacting with different Weber numbers. From left to right: (a) We=20, (b) We=40, and (c) We=80. The mid-span view along the x axis.

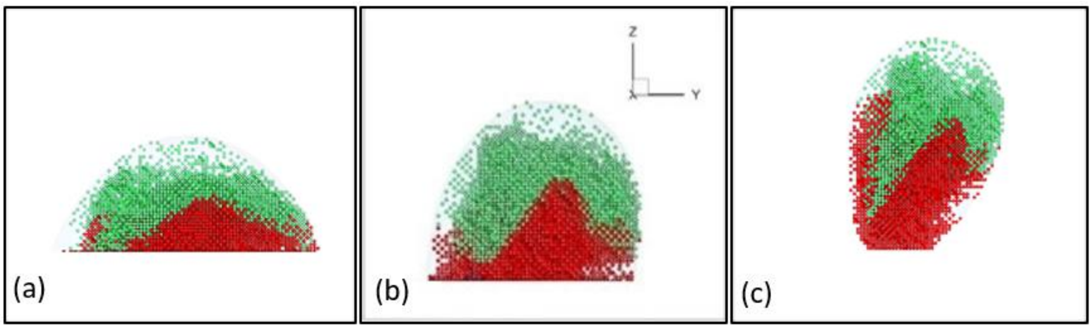

Figure 5.28 Snapshots at t* = 13 showing intermixing of the two droplets successively impacting on surfaces with different wettability. From left to right: (a) θ=50°, (b) θ=90°, and (c) θ=140°. The mid-span view along the x axis.

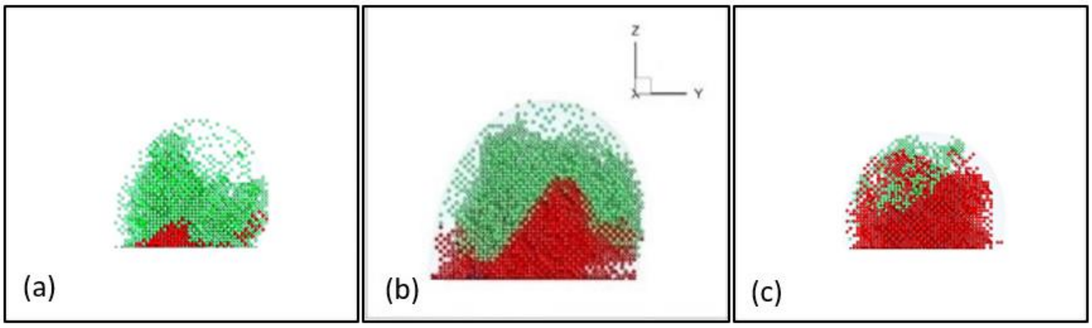

Figure 5.29 Snapshots at t* = 13 showing intermixing of the two droplets of different sizes. From left to right: (a) $D_{leading}/D_{trailing}$=1/2, (b) $D_{leading}/D_{trailing}$=1, and (c) $D_{leading}/D_{trailing}$=2. The mid-span view along the x axis.

5.5 SUMMARY

In this study, the dynamics of two identical droplets successively and obliquely impacting on a flat surface has been investigated using three-dimensional LBM simulations. It was first demonstrated that the interaction between two successively impinging droplets can result in quite different dynamics compared to that of single droplets. The focus was then placed on the effects of impact obliqueness (or surface inclination) and the lateral/longitudinal offsets on the two droplets' impact and coalescence processes. The major findings are summarized as follows:

1. Oblique impact causes asymmetric droplet spreading, with the downward spreading dominant over the lateral spreading. The increase in the surface slope leads to faster downward spreading and reduced lateral spreading.
2. The coalescence of the two droplets can result in abrupt changes in the evolution of the back and left/right contact edges, which is attributed to the partial landing of the trailing droplet on the leading droplet.
3. The offset between the two droplets further increases the asymmetry of the combined droplet's dynamics. The increase of lateral offset causes the increase of the maximum lateral spreading factor and the reduction of the maximum longitudinal spreading factor, whereas the increase of longitudinal offset results in the opposite change.
4. The impact obliqueness or inclination of the surface changes the intermixing of the two droplets and hence the mass distribution of the combined droplet. In addition, the introduction of lateral or longitudinal offsets reduces the intermixing.

This study furthers our understanding in oblique impact of two successive droplets on flat surfaces. In next two Chapters, condensation process on beetle inspired bumps and slanted surfaces will be discussed.

CHAPTER 6

CRITICAL VOLUME OF A CONDENSING DROPLET SHEDDING FROM BEETLE INSPIRED BUMPS

6.1 INTRODUCTION

Inspired by beetle's bumpy structure, condensation on hydrophilic/superhydrophobic bumps with two different shapes, i.e., cylindrical and hemispherical, using LBM was studied in the present work. Water droplets condensed on the top hydrophilic area of a bump till they reach a volume, called critical volume, and then shed down due to gravity. First, droplet shedding was studied for both cylindrical and hemispherical bumps, and then in order to do more detailed analysis only cylindrical bump case was focused. The critical volume of droplet was investigated for different bump diameters, heights, surface inclinations and hydrophilic/superhydrophobic contrasts. Finally a scaling law between the critical height of bump and these parameters was proposed.

6.2 PROBLEM DEFINITION

Figure 6.1 shows the schematic and computational domain of the problem. A seed droplet is placed on the bump with diameter '*d*' and height '*h*' (Fig. 6.1). The lattice length unit is related to physical unit by 1 lu= 50 μm. Water vapors are introduced from the top inlet with fixed inlet velocity, i.e V_{inlet} =0.008 lu/ts, where lu (length unit) and ts (time step) are lattice units in LBM. The water vapors condense and the seed droplet grows in size. The droplet continues to grow until the effect of gravity becomes dominant. At this point the droplet begins downward sliding and eventually shed down. This volume is called critical volume (V_c) of the droplet. The droplet critical volume is computed for different bump geometrical parameters such as bump shape, height, wettability contrasts and surface slopes.

In order to perform the comparison among different bump shapes, three kinds of bumps having same diameter are introduced, i.e., cylindrical (Fig. 6.2(a)), hemispherical 1 (Fig. 6.2(b)) and hemispherical 2 (Fig. 2 (c)). The patch and super-hydrophobic areas are represented by green and gray colors, respectively (Fig. 6.2). In cylindrical bump case, the patch area is limited to top face of radius d/2. However, in case of hemispherical 1 bump the patch area is equal to area of top segment of height hp=d/4 of hemisphere (Fig. 6.2(b)). At this value of patch segment height both cylindrical and hemispherical 1 bumps have the same patch areas, and therefore can be used to investigate the surface curvature effects on droplet shedding. The hemispherical 2 bump has larger patch area spanned by bump radius d/2 (Fig. 2 (c)), and it is used to investigate effects of surface curvature along with larger patch area on droplet shedding.

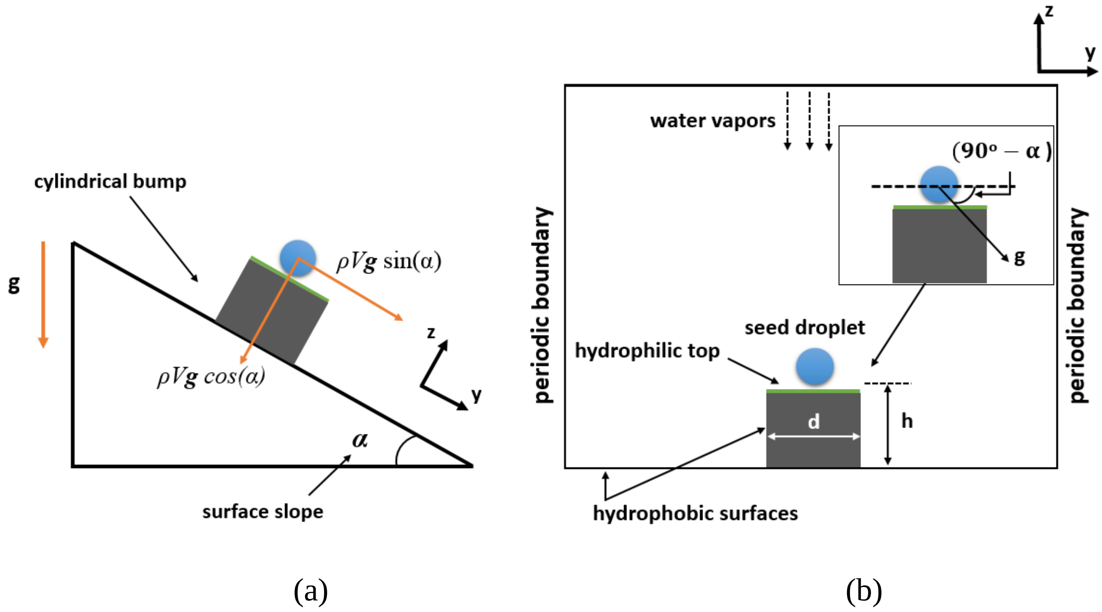

Figure 6.1 (a) Schematic of the problem and (b) computational domain.

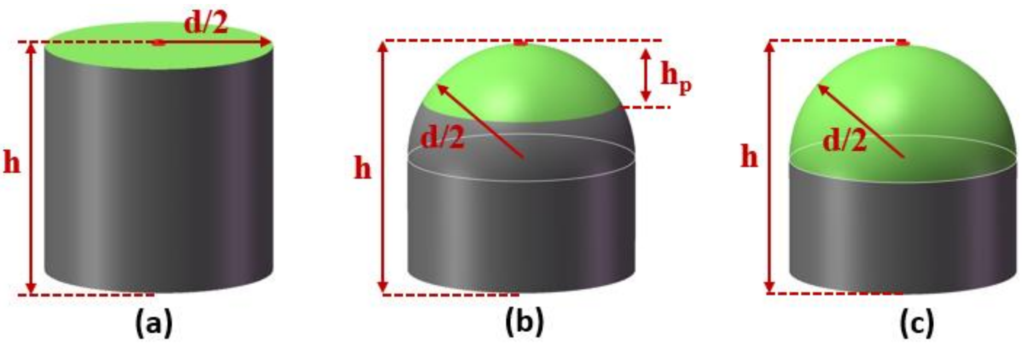

Figure 6.2 Different bump shapes (a) cylindrical bump with patch area on top (b) hemispherical 1 bump with top patch area equal to cylindrical bump patch area and (c) hemispherical 2 bump with largest patch area, green color represents patch area while gray the super-hydrophobic region.

The main parameter involved in this problem are as follows: the surface inclination angle α, the surrounding gas density ρ_g and viscosity μ_g, the liquid droplet diameter D, droplet density ρ, viscosity μ, surface tension σ, gravitational acceleration **g**, contact angle of hydrophilic patch θ_{patch} and contact angle of superhydrophobic background θ, bump height h and bump diameter d (see Fig. 6.1).

In present LBM framework liquid density ρ and viscosity are fixed at ρ =0.378 and μ =0.063, respectively. The liquid-to-gas density and viscosity ratios are fixed at ρ/ρ_g = 114.5 and μ/μ_g 114.5, respectively. The density ratio was limited to 114.5 because of the numerical stability issues at higher density ratios. The Bond number Bo describes the effect of gravitational force compared to surface tension force. Magnitude of gravitational acceleration is computed from Bond number, which is $\mathbf{g}$=1.53x10^{-5} lu / ts^2. Following Dorrer and Rühe [21] the contact angle of superhydrophobic surface is fixed at 176^o.

6.3 METHODOLOGY

In this work three-dimensional pseudopotential LBM is used to simulate the condensation on dessert beetle inspired bumps. The pseudopotential LBM is based on Shan-Chen scheme [131,133], and employs Carnahan-Starling equation of state for better stability at larger density ratio. Further implementation of this method can be found in reference [182] or in section 3.3. The wetting characteristics of the surface are incorporated by specifying the fluid solid interactions as explained in section 3.3.

In past, LBM has been successfully used for condensation related problems. Dupuis and Yeomans [211] employed LBM to investigate droplet condensation on Beetle inspired bumps. They found that chemical patterning on the beetle's back is important for water droplet formation. Zhang et al. [212] used multicomponent LBM model based on the Shan-Chen scheme to simulate dropwise condensation on nano-structured surfaces. Fu et al. [213] employed pseudopotential model to simulate condensation on structured surface to investigate preferential nucleation modes of condensate droplets.

6.3.1 COMPUTATIONAL DOMAIN AND BOUNDARY CONDITIONS

The computational domain is a three-dimensional rectangular box with a cylindrical or hemispherical bump on its lower wall. Periodic boundary conditions are used on side boundaries of the domain. Bounce back boundary conditions are employed on bottom surface and bump walls to implement no-slip boundary condition. To introduce the water vapor source, the velocity inlet boundary condition is applied on top wall [188,214].

To check the influence of velocity of inlet vapors, the critical volume of droplet is compared for different grid sizes in Table. 6.1. The cylindrical patch diameter is fixed at d = 40 lu (2mm). It is found that relative error for grid 180×220×220 is smaller than 1.0%. Therefore, by considering the trade-off between the accuracy and the computational cost, grid 180×220×220 was chosen for the present study (Table. 6.1).

Table 6.1 Grid independence test

Grid size(x y z)	Critical volume (μl) (Patch d=2mm)	Relative error (%)
160×220×220	33.57	4.54
180×220×220	34.92	0.71
200×220×220	35.04	0.36
180×180×220	33.54	4.63
180×200×220	34.91	0.73
180×240×220	34.93	0.90
180×220×150	34.913	0.73
180×220×300	34.915	0.73
200×240×300	35.17	--

6.3.2 VALIDATION

The LBM framework is validated for droplet shedding from a circular patch on a tilted surface. Consider a droplet on hydrophilic patch on a tilted superhydrophobic background surface. The droplet would roll off the surface once it volume is equal to critical volume. The criterion for droplet to remain attached to surface is such that pinning force must be equal to or greater than the gravitational pull exerted on the droplet [215,216]. Dorrer and Rühe [21] modified expression of critical volume of droplet as

$$V_c = \lambda_{CL}^2\, d \quad (\cos\theta_{patch} \; - \; \cos\theta \;) \tag{6.1}$$

where d is the width of the solid-liquid contact, which is equal to diameter of patch. Note that θ_{patch} and θ are equilibrium contact angles representing the receding contact angle of hydrophilic patch and advancing contact of superhydrophobic background, respectively. Dorrer and Rühe [21] found that only receding contact angle of hydrophilic patch and the advancing contact of superhydrophobic background play important role in droplet rolling off the surface. So, to simplify the problem, the contact angle hysteresis of patch and superhydrophobic surface is not taken into account. It should be noted that Eq. (6.1) only holds true for circular patch and cannot be used for bump with height.

Moreover, λ_{CL} is called modified capillary length, which is the modified expression of the capillary length expression by assuming that the gravity effects are influenced by surface inclination α as

$$\lambda_{CL}=(\sigma / \rho g \sin\alpha\,)^{0.5} \tag{6.2}$$

Simulations are conducted for two surface inclinations, i.e., α = 18° and 32°, and for three different wettabilities of the hydrophilic patch, i.e., θ_{patch} = 23°, 81° and 101°. The contact angle of the superhydrophobic surface is kept constant at θ = 176°. The simulation results are then compared to experimental [21] and analytical results of Eq. (6.1). Overall there is good agreement (Fig. 6.3). However at higher wettability contrast, i.e θ_{patch} = 23° and θ = 176°, there is some discrepancy between experimental and analytical results, which is due to droplet meniscus instability [21].

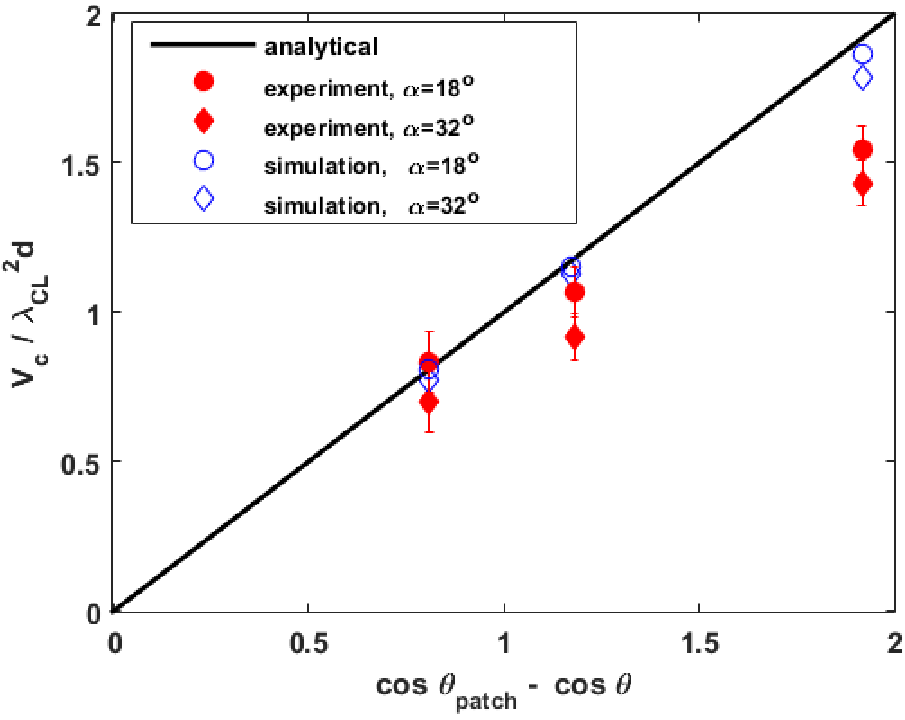

Figure 6.3 Normalized critical volume versus wettability contrast.

6.4 RESULTS AND DISCUSSION

6.4.1 DROPLET SHEDDING FROM CIRCULAR PATCH

Figure 6.4 shows a droplet being dislodged from a hydrophilic circular patch on a tilted plane. Droplet growth, necking and shedding is presented temporally by mid-span images along x-axis in Fig. 6.5. The patch diameter, surface slope and patch contact angle are fixed at d = 2mm, α = 45^{o} and θ_{patch} = 50^{o}, respectively. In start, seed droplet grows into bigger droplet by condensation till it occupy the whole hydrophilic patch. The component of force of gravity parallel to surface tries to pull the condensing droplet downward, however, the contact line remains pinned as the contact angle of the meniscus is less than the contact angle of superhydrophobic region (Fig 6.5(b)). Then by further increase in droplet size the downhill contact angle becomes equal to contact angel of superhydrophobic region and as a result it starts moving along y-axis, however the uphill contact angle still has not reached the contact angle of hydrophilic patch so uphill contact line remains pinned (Fig 6.5(c)). The droplet volume further enhances with time while the downhill part keep moving (Fig 6.5(d, e)). Because of this downhill motion of droplet into superhydrophobic region the uphill contact angle reduces, and once it has reached the contact angle of hydrophilic patch, it will lead to movement of uphill meniscus ((Fig 6.5(f))), Then rupture of necking film occurs and droplet rolls off the patch (Fig 6.5(g, h)).

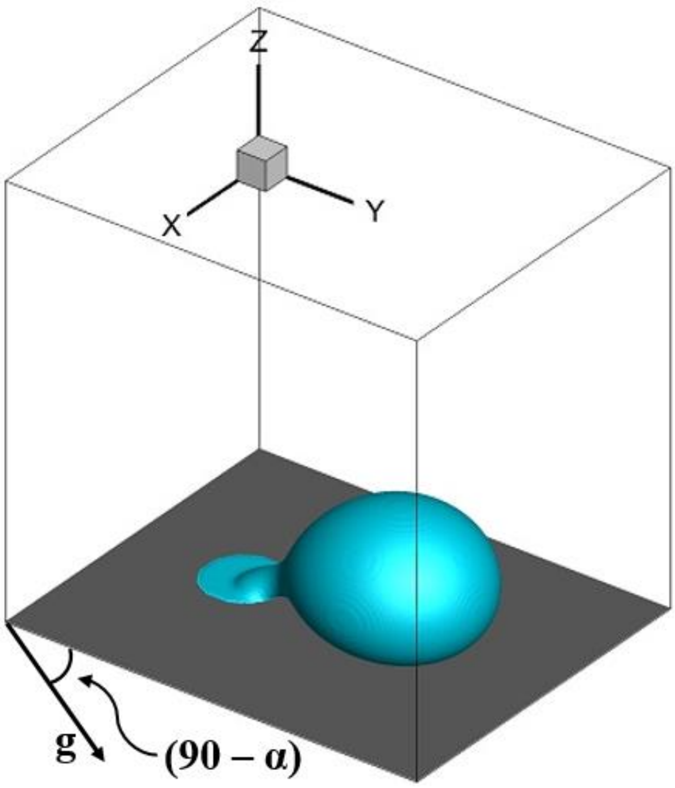

Figure 6.4 Droplet shedding from a circular patch at time *t* = 58000 (ts). *d* = 2mm, *h* = 0 mm, *α* = 45º and θ_{patch} = 50º.

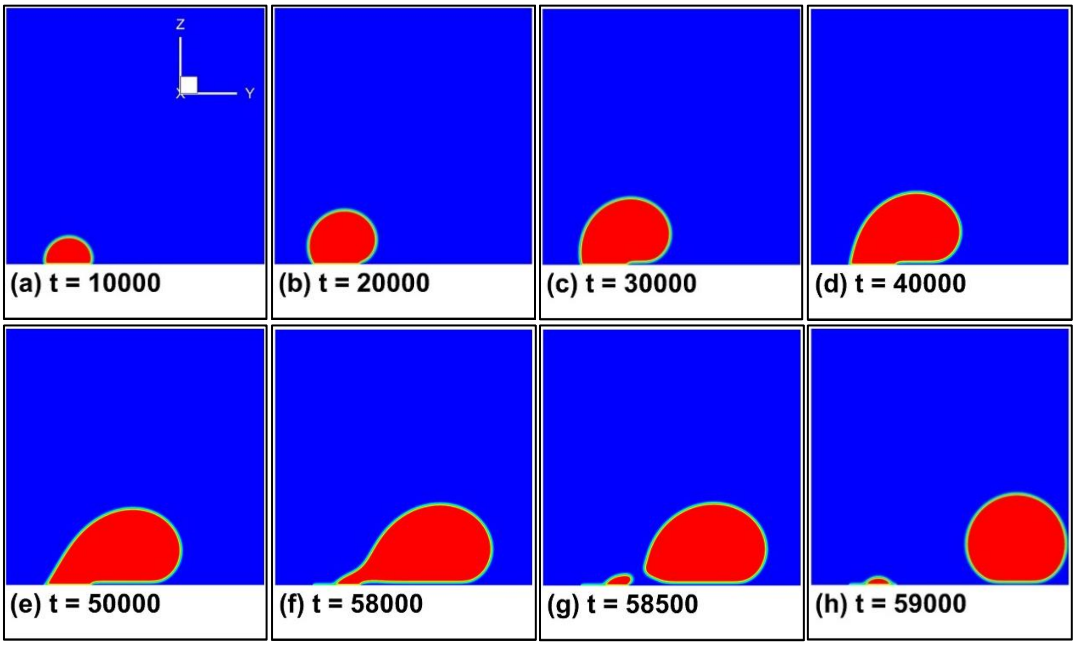

Figure 6.5 Mid-span images along x-axis of droplet growth and roll off a circular patch.

6.4.2 EFFECTS OF BUMP HEIGHT

Now, consider the case of cylindrical bump. Figure 6.6 shows the comparison of droplet shedding process of cylindrical bump with circular patch through time resolved images. The bump height is fixed at h = 1.5 mm. It can be seen that droplet growth is similar during the initial stage for both circular patch and cylindrical bump (Fig. 6.6 (a1, b1)). At time $t = 30000$, a bulge at droplet downhill side appears in case of circular patch, and suggest the movement of front part into superhydrophobic region (Fig. 6.6(a2)). However, in case of cylindrical bump the front bulging part also droops downward (Fig. 6.6(b2)). This is due to the action of perpendicular component of force of gravity. The simultaneous action of both parallel and perpendicular components of force of gravity induces the downhill drooping motion of droplet. This drooping part in turn quickly decreases the uphill contact angle for cylindrical bump case compared to circular patch. So the droplet necking and shedding occurs earlier for cylindrical bump (Fig. 6.6(a (3,4), b (3,4)). This early shedding of droplet, because of the bump height, affects the critical volume of droplet.

To further study the influence of bump height on critical volume, simulations are conducted with different bump heights. Figure 6.7 shows the critical volume plotted against the bump height. It can be seen that critical volume is maximum when bump height is zero (i.e circular patch), then decreases with increasing the bump height till the certain value of bump height. Thereafter, further increase in bump height do not affect significantly the critical volume. This value of bump height after which critical volume does not change significantly is called “critical bump height”. To determine critical bump height the critical volume values of the shedding droplets are interpolated between data points as can be seen in Fig. 6.7. Then the value with 1.5% percent change of critical volume compared to level off value is determined. This is indicated as red bar in Fig. 6.8 and represents the critical bump height in the present study.

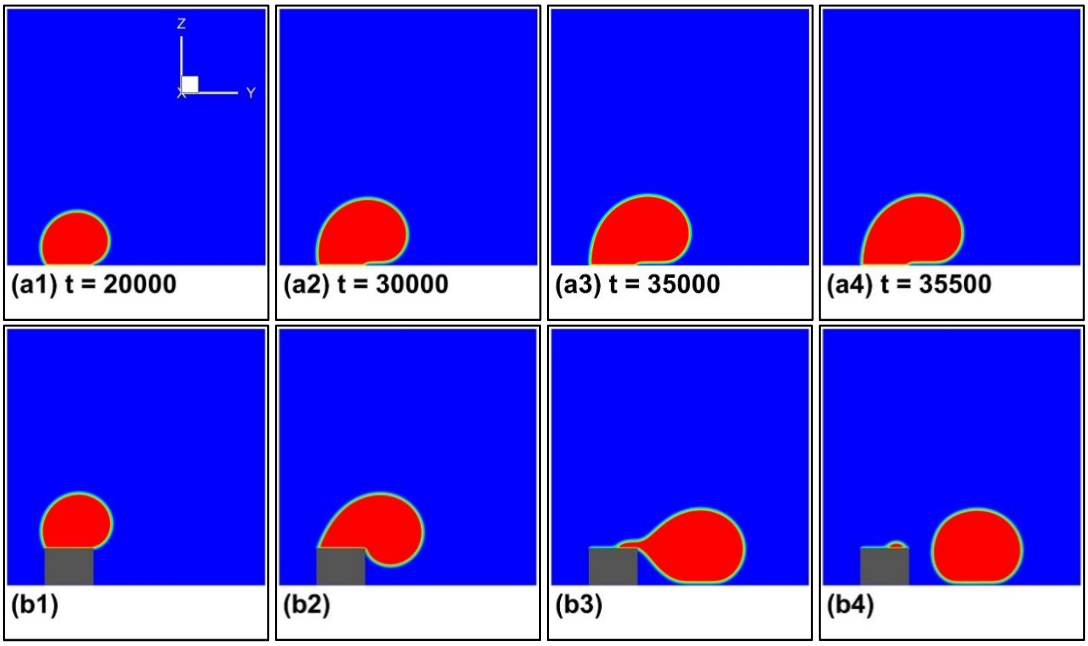

Figure 6.6 Mid-plan view of droplet growth on a cylindrical bump when *d* = 2mm, α = 45°, θ_{patch} = 50° and (a) *h* = 0 mm (b) *h* = 1.5mm

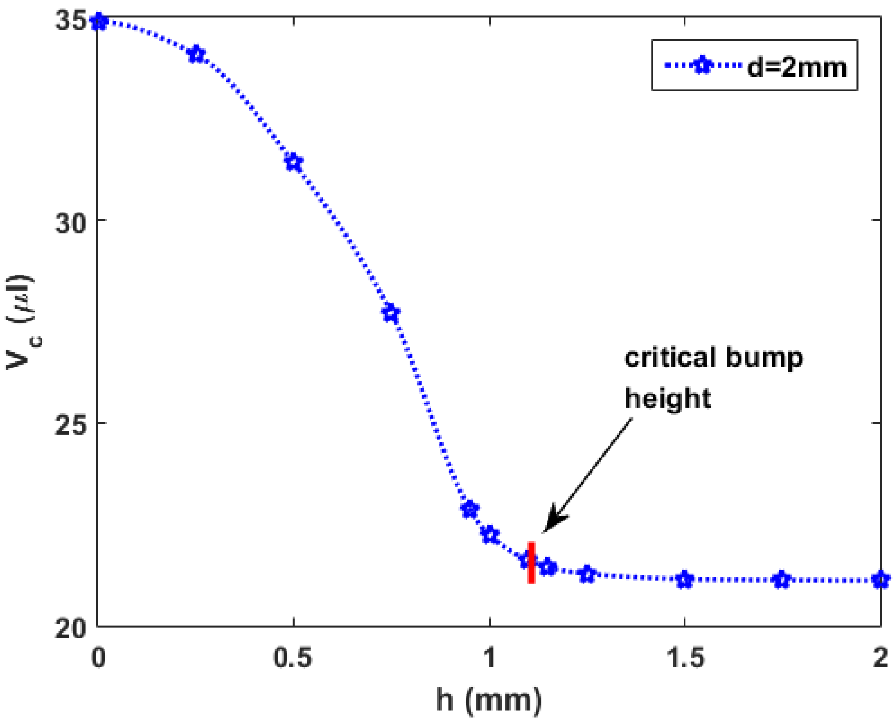

Figure 6.7 Variation of critical volume with bump height. Red bar represent the critical bump height, where *d*=2mm, α=45° and θ_{patch} =50°.

6.4.3 EFFECTS OF BUMP SHAPE

To investigate the influence of bump shape on droplet shedding two different bump shapes, i.e., cylindrical and hemispherical, are incorporated (Fig. 6.2). The cylindrical and hemispherical 1 bumps have the same areas of top hydrophilic patch, whereas the hemispherical 2 bump has larger hydrophilic area equal to hemisphere with radius *d/2*. The time resolved images of droplet shedding are shown in Fig. 6.8. The bump diameter, height, patch contact angle and surface slope are fixed at d = 2.0 mm, h = 1.5 mm, α = 45° and θ_{patch} = 50°, respectively. It is seen from Fig. 6.8 (a) that the droplet grows bigger on cylindrical bump, then a bulge appears on downhill side (Fig.6.8 (a2,a3)), and thereafter droplet dislodges from the bump (Fig.6.8 (a4)) at t=35500. In case of hemispherical 1bump, the downhill bugle is larger (Fig. 6.8 (b2)), and droplet slides down from the bump earlier (at t = 28000) compared to the cylindrical bump, which is due to curvature of bump. In case of hemispherical 2 bump the bulge is largest (Fig.6.8 (c2)). The droplet dislodges from the bump to surface at t = 27500 (Fig.6.8 (c3)), however it remains in contact with the bump because of larger hydrophilic patch area (Fig.6.8 (c4, c5)). This delays the droplet shedding time significantly (t = 56000) (Fig.6.8 (c6)). Figure 6.9 shows the plot of critical volume of shedding droplet against bump height. Due to hemispherical nature the minimum height of hemispherical 1 and hemispherical 2 bumps is *d/2*, which is 1.0 mm in this case. As the revealed in Fig. 6.8, the shedding time is smallest for hemispherical 1 (Fig.6.8 (b4)) bump, and then larger for cylindrical (Fig.6.8 (a5)) bump and largest for hemispherical 2 bump (Fig.6.8 (c6)). Therefore, the critical volume at h = 1.5 mm is smallest for hemispherical 1bump, and then increases from cylindrical bump to hemispherical 2 bump (Fig.6.9). Furthermore, it is seen from Fig.6.9, the critical bump height of cylindrical bump is smallest, and it increases from hemispherical 1 bump to hemispherical 2 bump. On the other hand, the critical volume of shedding droplet is smaller for both hemispherical bumps compared to cylindrical bump owing bump curvature that reduces the shedding time.

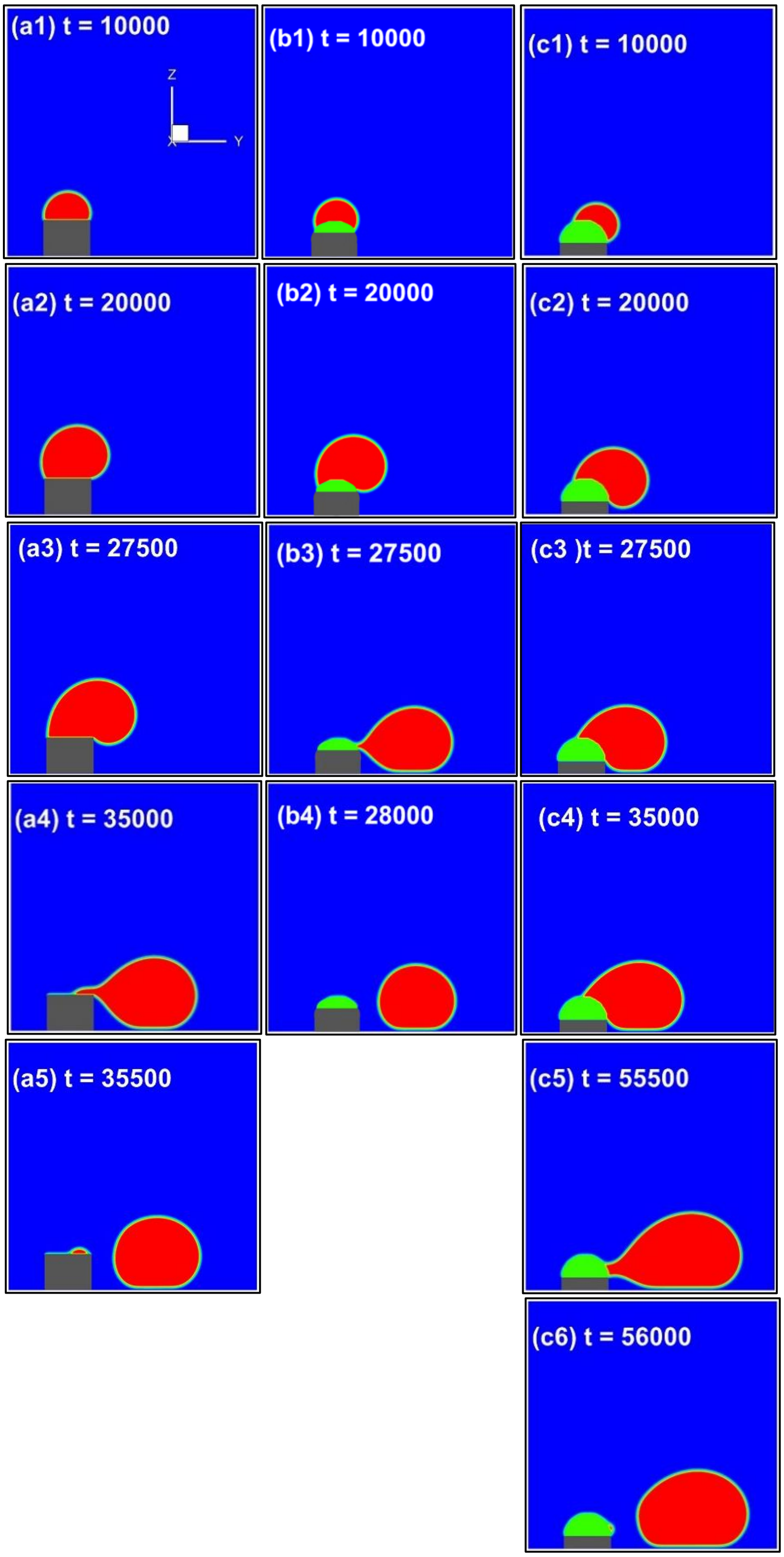

Figure 6.8 Mid-plan view of droplet shedding from (a) cylindrical bump (b) hemispherical 1 bump and (c) hemispherical 2 bump.

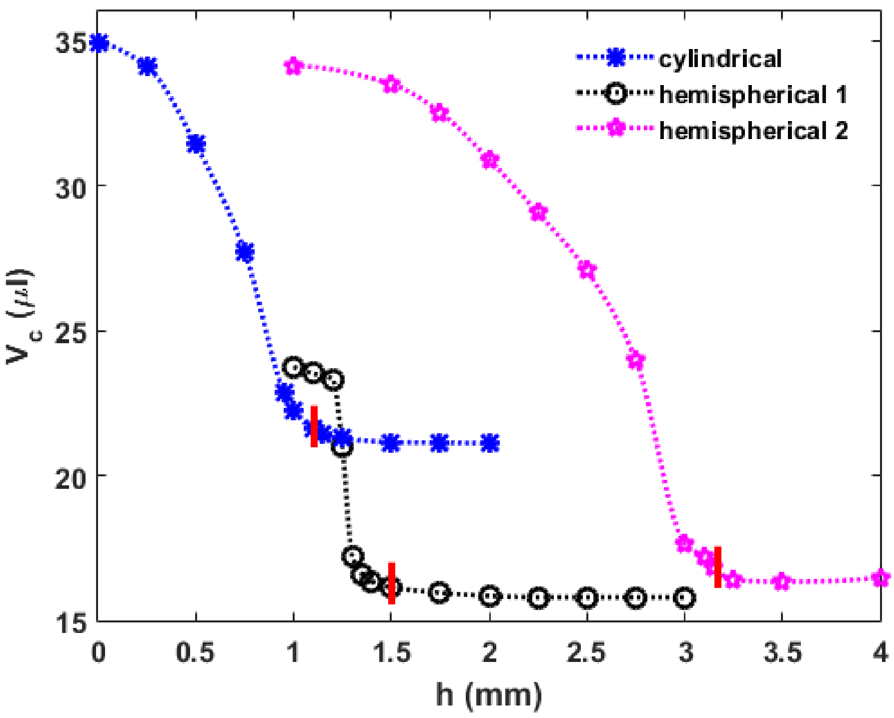

Figure 6.9 Variation of critical volume with bump height for different bump shapes: cylindrical, hemispherical 1 and hemispherical 2 bump.

6.4.4 EFFECTS OF BUMP SCALE

The efficient water collection requires two conditions: higher condensation rate and effective removal of condensing droplets from the surface. The latter condition is very important as the removal of condensing droplet creates space for new newer droplets. It can influence the water collection if bump scale is not properly chosen. To check the influence of bumps scale, two cylindrical bumps at different scales, i.e., micrometer scale and millimeter scale, are selected. The conversion factor for micrometer scale from lattice unit to physical unit is 1.0 lu = 10.0 µm. Micro-scale bump has diameter and height of d =100 µm and h = 400 µm, respectively, whereas millimeter scale bump has bump diameter and height of d = 1mm and h = 4 mm, respectively. The aspect ratio of both bumps is kept constant, that is h/d=4. Although not shown here, the heights of both bumps are ensured to be higher than the critical bump height. Figure 6.10 shows time resolved images of droplet removal from both bumps. It can be seen that droplet for micro-scale bump assumes nearly spherical shape for all time instants. This can be understood from the capillary length. Capillary length is defined as $\lambda=(\sigma/\ \rho g\ )^{0.5}$, and gives information about the relative importance of gravitational force. For water the capillary length is about 2.7 mm.

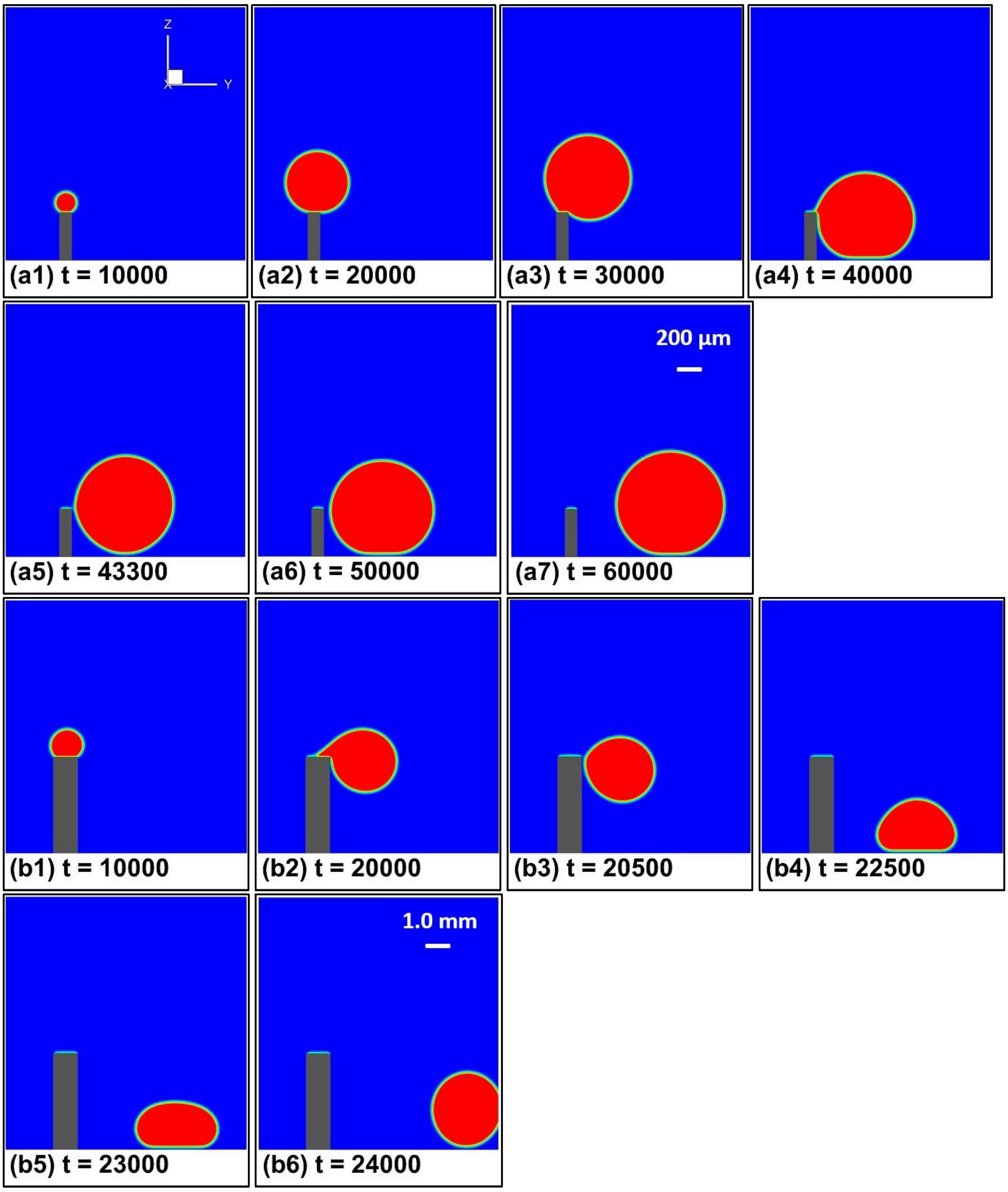

Figure 6.10 Droplet shedding and subsequent gravity assisted removal from surface when α = 45º, θ_{patch} =50º and (a) *d* = 100 µm, *h* = 400 µm, (b) *d* = 1mm, *h* = 4 mm.

If the droplet diameter is larger than capillary length then gravitational effect becomes dominant and that flattens the shape of droplet. However, diameter of the droplet for micro-scale bump remains smaller than the capillary length throughout the condensation process. The droplet shedding occurs at time *t* = 43300 (Fig. 6.10 (a5)) with the diameter of droplet about 0.8mm which is still smaller than the capillary length, hence the gravitational effects will not be significant. Therefore, the droplet after shedding does not immediately roll off the surface and instead remains attached to surface until it grows big enough to experience large gravitational pull to get removed from the surface. As mentioned earlier, efficient water collection requires effective droplet removal from the surface. It can be seen in Fig. 6.10 (a (5-7)) that even from the of droplet shedding time (t = 43300) to later time (t =60000) the droplet is unable to get removed from surface. This inefficient removal may deteriorate water collection performance as well as cause several problems such as water flooding of micro-structures. On the other hand, in case of millimeter scale bump shedding droplet size is comparable to capillary length, and gravity assisted droplet removal is possible (Fig. 6.10(b3)). Besides, droplet removal is much faster for millimeter scale bump as can be seen from Fig. 6.10(b (3-6)). Therefore, in rest of the work droplet shedding from millimeter scale bumps is investigated.

6.4.5 EFFECTS OF BUMP DIAMETER

The effects of diameter of cylindrical bump on the critical bump height are studied. Bump diameter is varied from d=1.0 mm to d=4 mm with a step of 1.0 mm. Surface inclination and contact angle of hydrophilic patch are fixed at $\alpha = 45^o$ and $\theta_{patch} = 50^o$, respectively. Increasing bump diameter increases the solid-liquid contact area perpendicular to direction of droplet shedding. This increases the pinning resistance force and in turn a greater gravitational force would be required to dislodge the droplet. Figure 6.11 shows the variation of critical volume as the bump height increases for four different bump diameters. The critical volume trend is similar for all bump diameters, that is, increasing bump diameter increases critical volume at all bumps heights. Furthermore, the critical bump height also increases with bump diameter.

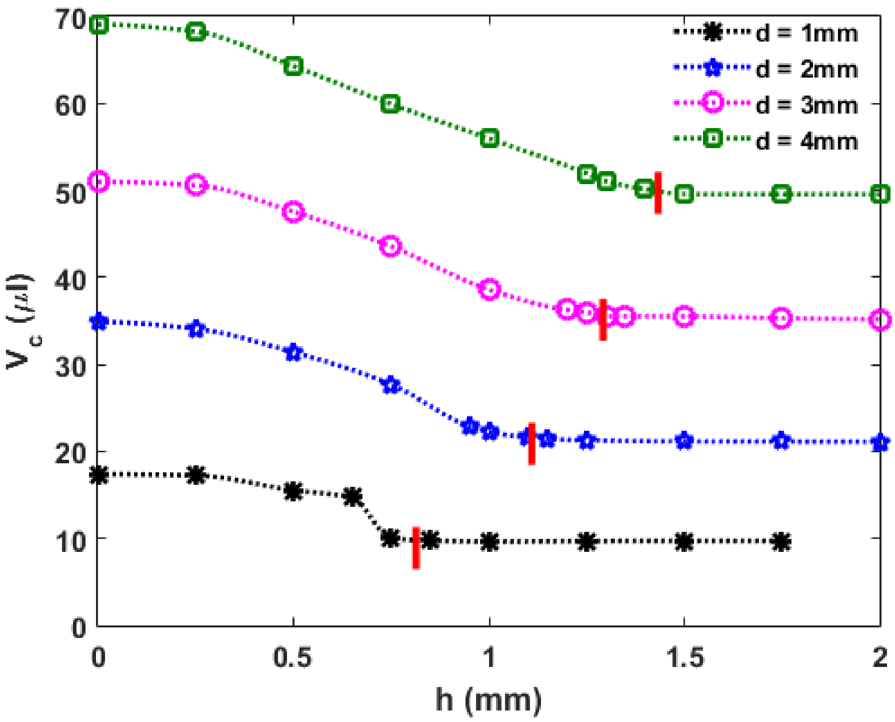

Figure 6.11 Critical volume variation with bump height for different bump diameters. Red bars represent the critical bump height.

6.4.6 EFFECTS OF SURFACE INCLINATION

Surface inclination also affects critical volume of shedding droplet and the critical bump height, as changing inclination alters magnitude of perpendicular and parallel components of force of gravity. The bump diameter and patch contact angle are fixed at d = 2mm and θ_{patch} = 50^o, respectively. The surface inclination is varied from α = 30^o to α = 60^o with a step of 15^o. Small surface inclination (30^o) increases the critical volume at smaller bump heights significantly, which is due to smaller component of force of gravity perpendicular to surface (Fig. 6.12). The critical bump height increases with decreasing surface inclination.

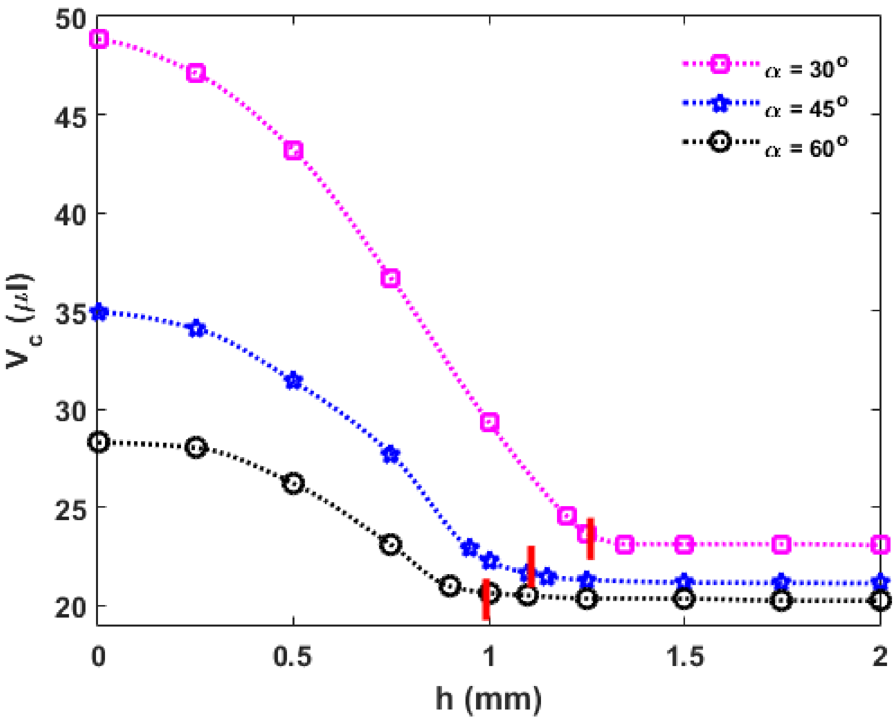

Figure 6.12 Critical volume variation with height for different surface inclinations. Red bars represent the critical bump height.

6.4.7 EFFECTS OF WETTABILITY CONTRAST

To invesitgate the effects of surface wettability, the critical volume is calculated for four diffenent contact angles of patch, i.e., θ_{patch} = 30°, 50°, 81°, and 101°. The contact angle of superhydrophobic surface is fixed at θ =176°. Bump diameter and surface inclination are also fixed at d = 2mm and α = 45°, respectively. It can be seen from Fig.6.13 that critical volume stongly depeneds on wettability contrast of patch and superhydrophobic surface. At all bump heights, the surfaces with larger patch contact angle dislodge the droplets with smaller volumes. Similarly the critical bump height is smallest for θ_{patch} =101° and increases with wettability.

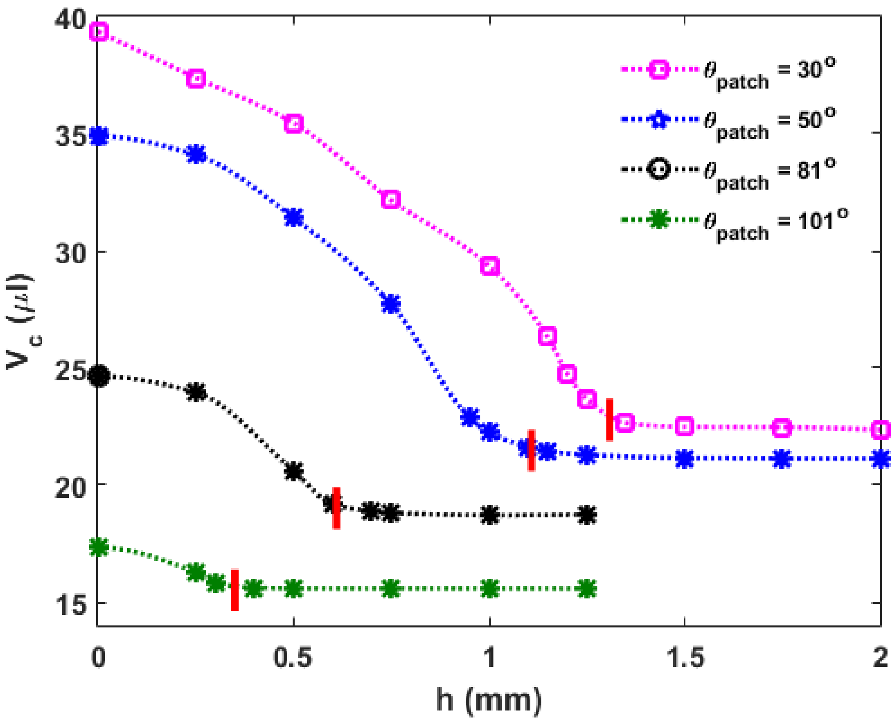

Figure 6.13 Critical volume variation with bump height for different contact angles of hydrophilic patch. Red bars represent the critical bump height.

6.4.8 SCALING LAW

The critical bump height of cylindrical bump is investigated as a function of parameters, including bump diameter *d*, surface slope α and hydrophilic patch wettability θ_{patch}. Bump diameter is varied from *d* = 1mm to *d* = 4mm. Surface slope is changed from α =30° to α =60°. Hydrophilic patch contact angle is changed from θ_{patch} 30° to θ_{patch} 101°. Critical bump height values are plotted in Fig.6.14. A curve fit relation is obtained, which is given as follows.

$$\frac{h}{d} = 0.46\cos\theta_{patch}\cos\alpha\frac{\lambda}{d} + 0.25 \qquad (6.3)$$

where λ is the capillary length, defined as $\lambda=(\sigma/\ \rho g\ )^{0.5}$., and *h/d* and λ/d are dimensionless quantities.

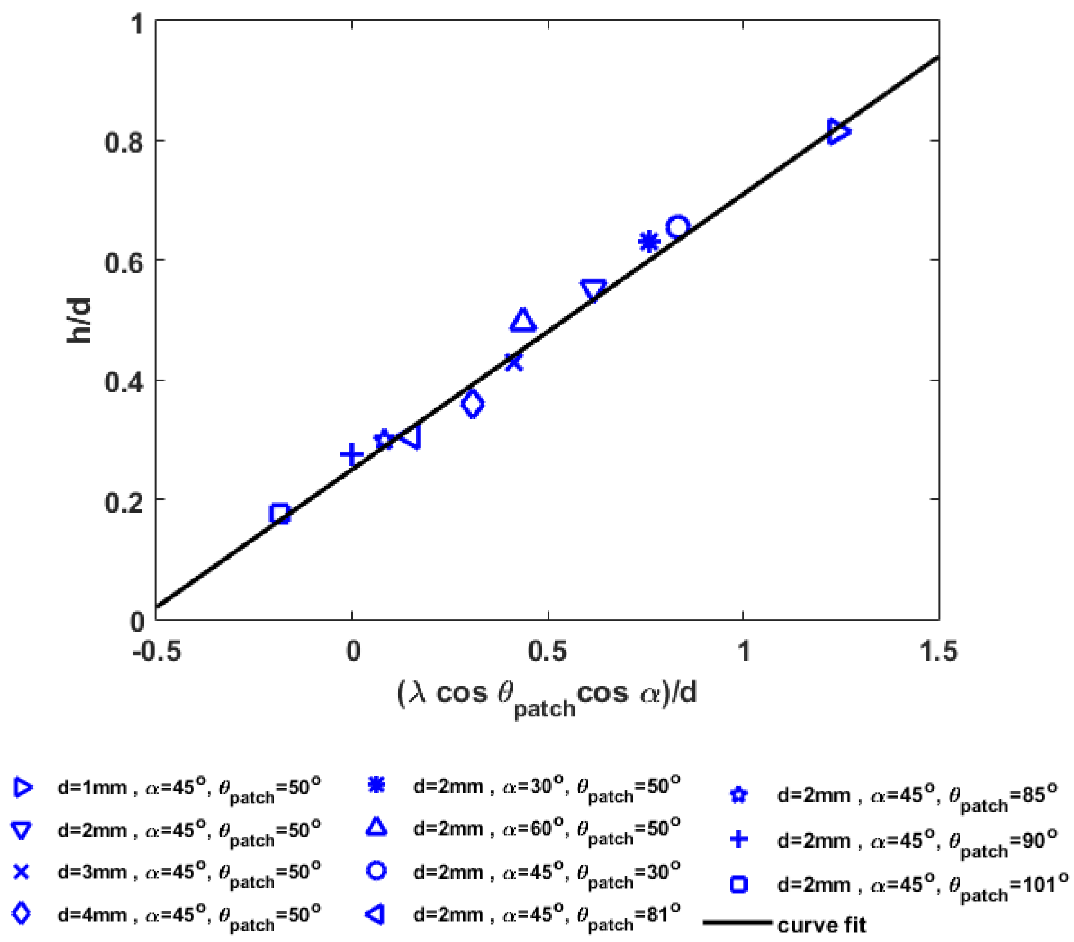

Figure 6.14 Curve fit relationship between critical bump height and other parameters.

6.5 SUMMARY

In this work a three-dimensional lattice Boltzmann method was used to investigate droplet shedding from dessert beetle inspired bumps. It was explained that bump shape and height can significantly influence the critical volume of the shedding droplet. The perpendicular component of gravitational force was observed to plays active role in early droplet shedding for bumps with nonzero-height. The major findings of this work are summarized as follows:

1. The critical volume of shedding droplets is maximum at zero bump height and decreases with increasing bump height till a certain value, called the critical bump height, and does not change significantly with further increase in bump height.

2. For the same hydrophilic patch area, the critical volume is smaller for hemispherical bump compared to cylindrical bump, which can be attributed to surface curvature.
3. Furthermore, it was found that micro-scale bump compared to millimeter scale bump sheds droplet smaller than water capillary length, which makes gravity assisted removal of condensing droplet inefficient.
4. For cylindrical bump, the investigation of parameters, including bump diameter, surface slope and wettability contrast was also conducted. It was found that the critical bump height enhances with increasing bump diameter, wettability of hydrophilic patch and decreasing surface inclination. Similar trends were also found for the critical volume of shedding droplets.

In the present Chapter, only droplet condensation was studied. In the next Chapter, droplet impact process simultaneous with condensation will be investigated.

CHAPTER 7

DROPLET IMPACT IN PRESENCE OF SATURATED VAPOR

7.1 INTRODUCTION

In this work, the impact of droplet at saturated temperature on cold level or slanted surface in the presence of inlet saturated vapor was investigated, using a three-dimensional lattice Boltzmann method. The focus was placed on the Jakob number, the Prandtl number, Weber number and surface slope. The saturation conditions for droplet impact are used, because generally fog harvesting is conducted at higher relative humidity, close to one hundred percent, where vapor pressure of water is equal to saturation pressure at that temperature.

7.2 PROBLEM DEFINITION

Fog droplet size vary from 1 μm to 50 μm. In present study impact of fog droplet of size 1 μm with impact velocities up to 6 m/s on level and inclined surfaces is investigated. The schematics of droplet impact on level and inclined surfaces and computational domain are shown in Fig.7.1. In both cases, droplet and surrounding vapor are initially at saturated temperature. Droplet impact dynamics are investigated by studying the influence of nondimensional numbers, including Weber number We, the Jakob number Ja and the Prandtl number Pr.

$$\mathrm{We} = \rho U^2 D/\sigma,\ \mathrm{Pr} = C_v\mu/\lambda,\ \mathrm{Ja} = C_v(T_s - T_{bw})/h_{fg} \tag{7.1}$$

where D is droplet diameter, μ is viscosity, σ is surface tension, ρ is liquid density, U is droplet impact velocity, C_v is specific heat at constant volume, h_{fg} is specific latent heat of condensation ,T_s is saturation temperature, T_{bw} is temperature of bottom wall and λ is thermal conductivity.

Weber number We is described as the relative importance of the deforming inertial forces compared to the surface tension of the droplets. The Prandlt number Pr is expressed as the ratio of momentum diffusivity to thermal diffusivity and the Jakob number Ja is expressed as ratio of sensible heat to latent heat in phase change heat transfer problems.

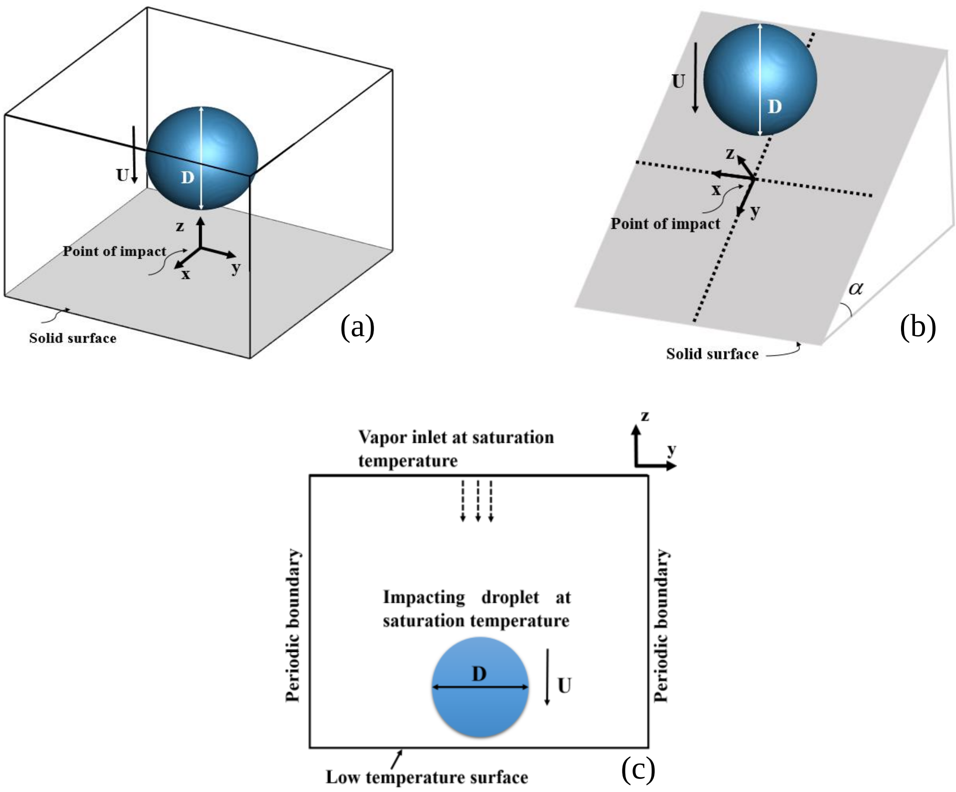

Figure 7.1 Schematics of droplet impact on (a) level surface and (b) inclined surface (c) computational domain.

In the present study, the conversion factor between physical length unit and LB length unit is 1.0 lu = 1/60 μm. Different from previous chapters, droplet liquid to surrounding gas density and viscosity ratios are fixed at ρ/ρ_g=36.5 and μ/μ_g=36.5, respectively, where g represents gas. The small density ratio of 36.5 is used due to limitations of current LBM framework. To simplify the problem, only superhydrophobic surfaces with fixed contact angle of θ=140° for both level and slanted surfaces, are considered. Moreover, contact angle hysteresis is not assumed in this work. Another reason for selection of superhydrophobic surface is its higher water collection rate as compared to hydrophilic surfaces owing effective removal of condensing droplets [217]. Following Phadnis and Rykaczewski [218] convection due to surface tension variation is not considered in this work as it is more important for droplet evaporation case. Specific heat at constant volume C_v and specific latent heat of condensation h_{fg} are also fixed and their values are determined according to procedures described in references [137,138]. The 100% humidity case is considered, that is, the droplet and surrounding vapor are initially set at saturated temperature and also the top wall pressure is fixed at saturated pressure. Therefore, the main focus is placed on the nondimensional numbers, including the Jakob number, the Prandtl number, surface inclination and Weber number. Weber number is mainly determined by impact velocity. The Jakob number is determined by temperature difference between initial saturation temperature of domain (droplet and surrounding vapor) and bottom surface temperature, while the Prandtl number is calculated by method elaborated in reference [137]. The actual Prandtl number of water at standard temperature and pressure is higher. However, Prandtl number is kept lower than one due to limitations of current LBM framework.

Furthermore, two additional nondimensional numbers, namely spreading factor and nondimensional time are used to study the evolution of spreading. In case of perpendicular impact, spreading is radially symmetric (Fig. 7.2 (a)). Therefore, the spreading factor is defined as

$$S^*=S/D \tag{7.2}$$

where S is the spreading length defined as maximum spreading distance (see Fig. 2(a))

However, droplet impact on slanted surface introduces asymmetry, which is investigated by using two spreading factors, one in lateral direction (S_x^*) and the other in longitudinal direction (S_y^*). Therefore, they are called lateral and longitudinal spreading factors, respectively, and are defined as

$$S_x^*=S_x/D,\ S_y^*=S_y/D \tag{7.3}$$

where S_x and S_y are spreading lengths defined as the maximum distance between two contact edges along x and y axis (Fig. 7.2(b-c)), respectively. Besides, nondimensional time is defined to investigate spreading dynamics temporally as

$$t^*=Ut/D \tag{7.4}$$

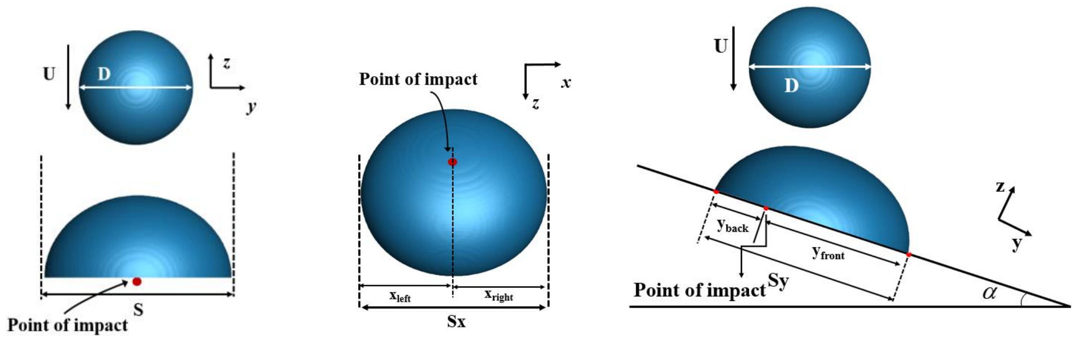

(a) (b) (c)

Figure 7.2 (a) Spreading length of droplet impact on level surface, and (b) lateral and (c) longitudinal spreading lengths and contact edges motion for impact on inclined surface.

7.3 METHODOLOGY

In this work three-dimensional pseudopotential phase-change lattice Boltzmann method based on Gong and Cheng [143] model is used. In pseudopotential LBM, interparticle interactions cause the spontaneous segregation of the fluid into two phases with high and low densities when the temperature is below the critical temperature [131,133]. Furthermore, the interface movement is not needed to be tracked explicitly. In Gong and Cheng [143] model, two particle distribution functions are employed. These are density distribution function and temperature distribution function. Temperature term through equation of state is used to couple these functions. Mathematical formulation of this model is presented in section 3.7. This model has been successfully used for condensation and boiling studies in the previous studies [131,133,143]. The wetting characteristics of the surface are achieved by computing a specific adhesion force between the gas/liquid phase and solid walls as explained in section 3.3.

7.3.1 COMPUTATIONAL DOMAIN AND BOUNDARY CONDITIONS

The computational domain is a three-dimensional rectangular box. The surface inclination is actually realized by changing the impact angle relative to level surface. Periodic boundary conditions are applied on left and right sides, and bounce back boundary condition is applied on lower wall. The constant pressure inlet [187,188] boundary condition is applied on top. Besides, constant temperature boundary conditions [219] are applied on bottom and top.

To carry out grid independence test, a droplet is allowed to impact on a cold flat surface using four sets of grids, and the maximum spreading factor is computed (Table. 7.1). Initial saturated temperature of droplet and surrounding vapor is T_s=0.80T_c, where T_c is critical temperature. Bottom wall temperature is lower than the saturated temperature and can be determined from Jakob number. Here, the Jakob number, the Prandtl number and Weber number are set at Ja = 0.5, Pr = 1.0 and We = 0.36, respectively. It can be seen from table 7.1, the grid with lattice nodes 200x200x160 has the error close to 0.5%, hence adopted in the present study. Furthermore, the same grid size was found to be able to ensure grid independency for droplet impact on inclined surface.

Table 7.1 Grid independence test for droplet spreading factor at Ja = 0.5, Pr = 1.0 and We=0.36

Grid size (lattice units)	140x140x120	200x200x120	200x200x160	220x220x180
S^*(max)	1.1827	1.1823	1.155	1.1495
Relative error	3.31%	3.27%	0.55%	-

7.3.2 VALIDATION

The present LBM model is first validated for the perpendicular impact on a level surface similarly as explained in section 5.3.2.

Next, the validation of phase change process is carried out. This LBM framework has been previously used for condensation as well as boiling studies [131,133,143]. Therefore, in this work validation only for bubble growth and departure diameter from heated surface in pool boiling is conducted. The computational domain is composed of 150 x 500 lattice nodes. Initially the domain is occupied with liquid at saturated temperature T=0.8T_c. Bounce back boundary condition is applied on bottom wall, top boundary is set as outflow, while the left and right boundaries are periodic boundaries. Adiabatic boundary condition is applied on the bottom. As well known, the bubbles are generated at defects at superheated temperature. Therefore, a higher temperature of T=1.54T_c is applied at center of bottom wall. As shown in Fig. 7.3, bubble nucleates and rises under buoyant force. As time passes, more heat is transferred, bubble grows, and bubble neck appears (Fig. 7.3(d)) and finally departs (Fig. 7.3(e)) from the bottom surface. Departing bubble diameter can be analytically determined by a relation proposed by Fritz [220], which is given as

$$D_{bubble}=0.0208\theta[\sigma/g(\rho - \rho_g)]^{0.5} \tag{7.5}$$

where D_{bubble} is bubble diameter and θ is the contact angle. Simulations are conducted for different values of gravity. Bubble departure diameter is compared with relation of Eq. (7.5) in Fig. 7.4, which shows a good agreement.

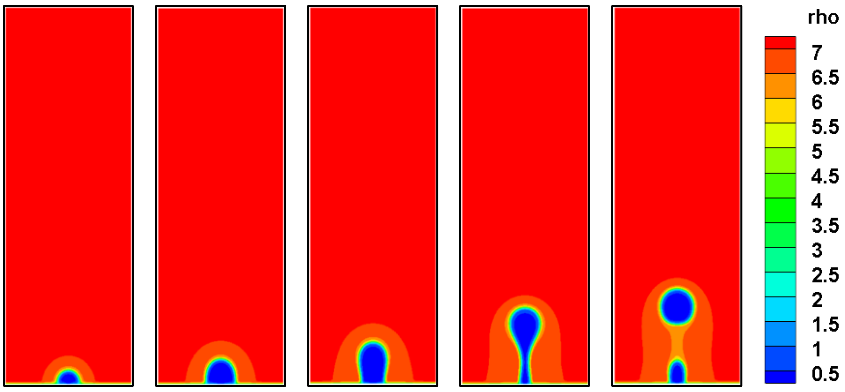

(a) (b) (c) (d) (e)

Figure 7.3 Bubble nucleation and departure at gravitational acceleration g = 5.0x10^{-5}.

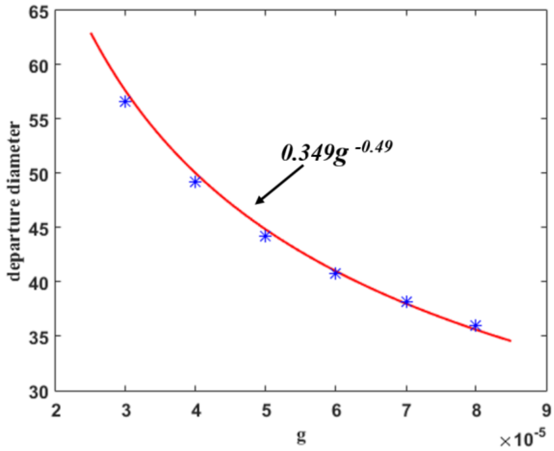

Figure 7.4 Dependence of bubble departure diameter on gravity.

7.4 RESULTS AND DISCUSSION

7.4.1 DROPLET IMPACT ON LEVEL SURFACE

Figure 7.5(a, b) shows the sequences of mid-plane snapshots of droplet normal impact under isothermal and non-isothermal conditions. The velocity fields inside and surroundings of droplet are shown in Fig. 7.6.Weber number is fixed at We=0.36 for both isothermal and non-isothermal impact cases. The Jakob number is fixed at Ja=0.5, which has the temperature of saturated vapor of T=0.8Tc and bottom wall of T=0.656Tc. The Prandtl number is set at Pr=1.0. For the isothermal environment, droplet impacts on the surface, begins to spread as shown in Fig 7.5 (a1). This can also be seen from the velocity field (Fig. 7.6(a1)). The spreading continues until maximum value around t*=0.44 (Fig. 7.5(a2)), called maximum spreading factor, is achieved. Afterwards, surface tension effects appear and droplet starts retraction (t*=0.80, Fig. 7.5(a3)). Then droplet oscillates until the initial kinetic energy is damped. The Fig. 7.5(a4)) shows the spreading during these oscillations that is also observed from upward velocity vectors at t*=1.2 (Fig. 7.6(a4)). To maintain the consistency, same scale is used for all velocity fields in this study. After few oscillations droplet equilibrium stage is achieved at t* > 2.8 as shown in Fig. 7.5(a5). The evolution of spreading factor is shown in Fig. 7.7(a). Peak value around t*=0.44 is the maximum spreading factor. The retraction phase starts after t*=0.44 and ends around t*=0.80. In oscillations (which start after t^*=0.80 and end near t^*=2.8) droplet spreads and retracts with gradually reducing amplitude until the equilibrium phase (at $t^* > 2.8$) is reached.

As for droplet impact under non-isothermal conditions, the droplet size increases with time compared to the isothermal case as shown in Fig. 7.5(b). The temperature contours are shown in Fig. 7.5(c), where the temperature is normalized as Temp = $(T-T_{bw})/(T_s-T_{bw})$. As soon as the droplet and surrounding vapors are exposed to bottom cold surface, the temperature decreases near wall and around the impinging droplet as revealed in Fig. 7.5(c1) (t^*=0.2). Decrease in liquid temperature near wall induces the phase change of vapor into liquid. This draws the surrounding vapor towards adjacent edges of the droplet near bottom surface as shown in Fig. 7.6 (b1). Due to phase change more advection of saturated vapor from top surface occurs (Fig. 7.6(b2)). Furthermore, two vortices appear near edges of droplet. The evolution of droplet is in retraction phase around t^*=0.8. Due to retraction, droplet interface moves upward and advection of vapors on top reduces as can be seen from velocity vectors in Fig. 7.6(b3). Vapor advection starts over soon after the end of retraction phase (Fig. 7.6(b4)). Enhanced size of droplet can be noticed from Fig. 7.5(b5). Fig. 7.7(a) shows evolutions of the spreading factor and normalized volume. Droplet volume is normalized with initial volume V_i before the impact. For consistency sake, largest value of first peak of both isothermal and non-isothermal cases is termed as maximum spreading factor. It can be seen (Fig. 7.7(a)), the maximum spreading factor is larger in non-isothermal case. The retraction rate is also faster compared to isothermal case. Furthermore, it can be seen the droplet volume remains constant all the time in case of isothermal impact, whereas it increases due to condensation in non-isothermal conditions. The increase in spreading factor compared to isothermal case is also evident from Fig. 7.7(a).

Next the average heat flux on a plane in droplet next to bottom surface at Z=1 is studied. The heat flux at a point on plane Z=1 is given as $q=-\lambda(T(x,y,1) - T_{bw})/\delta x$. Then the average heat flux on the plane is given as $\sum q/N+1$, where N is total number of point inside droplet on the plane. Fig. 7.7(b) shows the evolution of average heat flux. As soon as droplet hits the surface, temperature near surface decreases resulting the decreasing heat flux. The heat flux then increases (inset image Fig. 7.7(b)) during spreading and a part of retraction phase from t^*=0.4 to t^*=0.7 due to motion of high temperature fluid from top of droplet towards bottom. Then some small peaks in heat flux curve can be seen during droplet oscillations before reaching equilibrium. In equilibrium phase heat flux also reduces with time due to decrease in temperature contrast near surface.

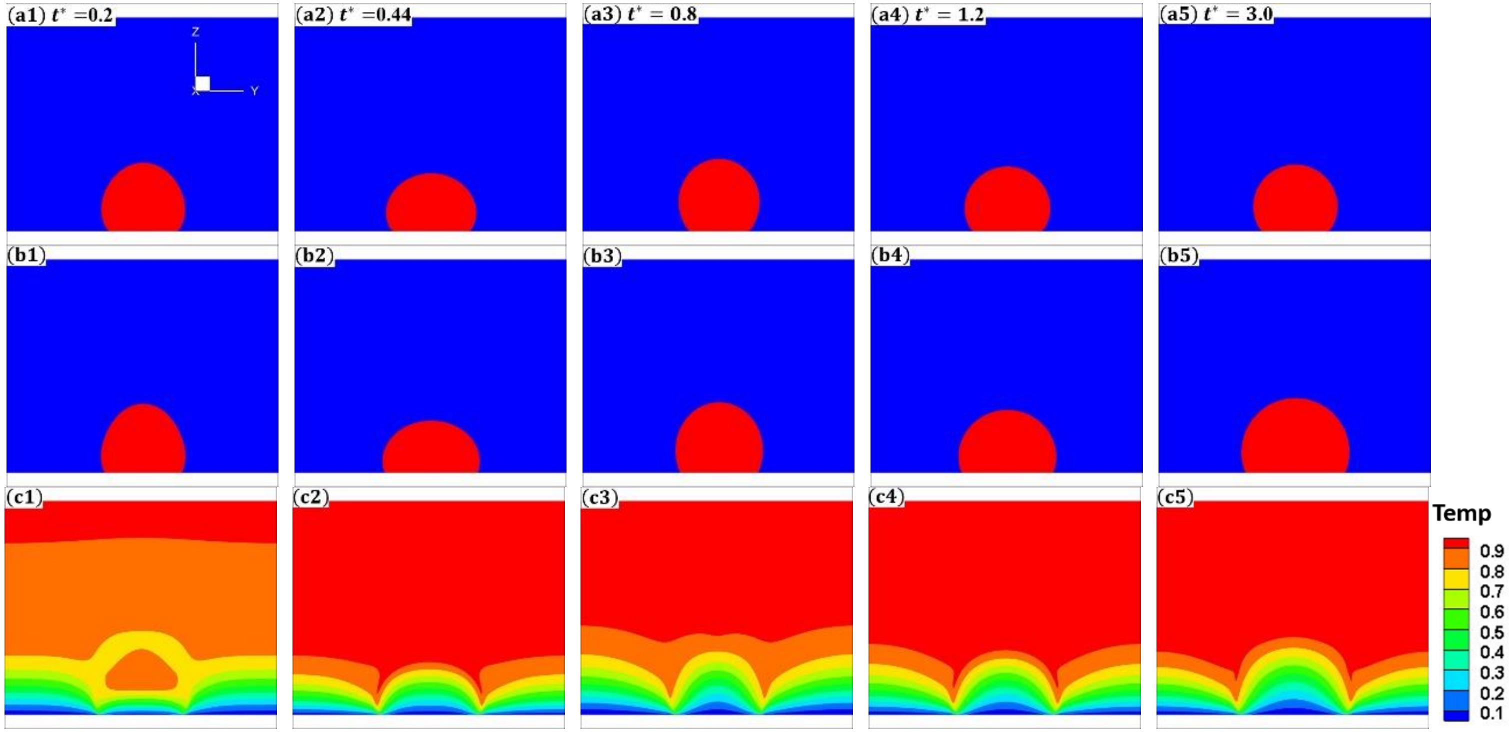

Figure 7.5 Evolutions of droplet impact on level surface under (a) isothermal conditions (b) non-isothermal conditions and (c) temperature field in non-isothermal case. The images show cross sectional view of mid-plane along x-axis.

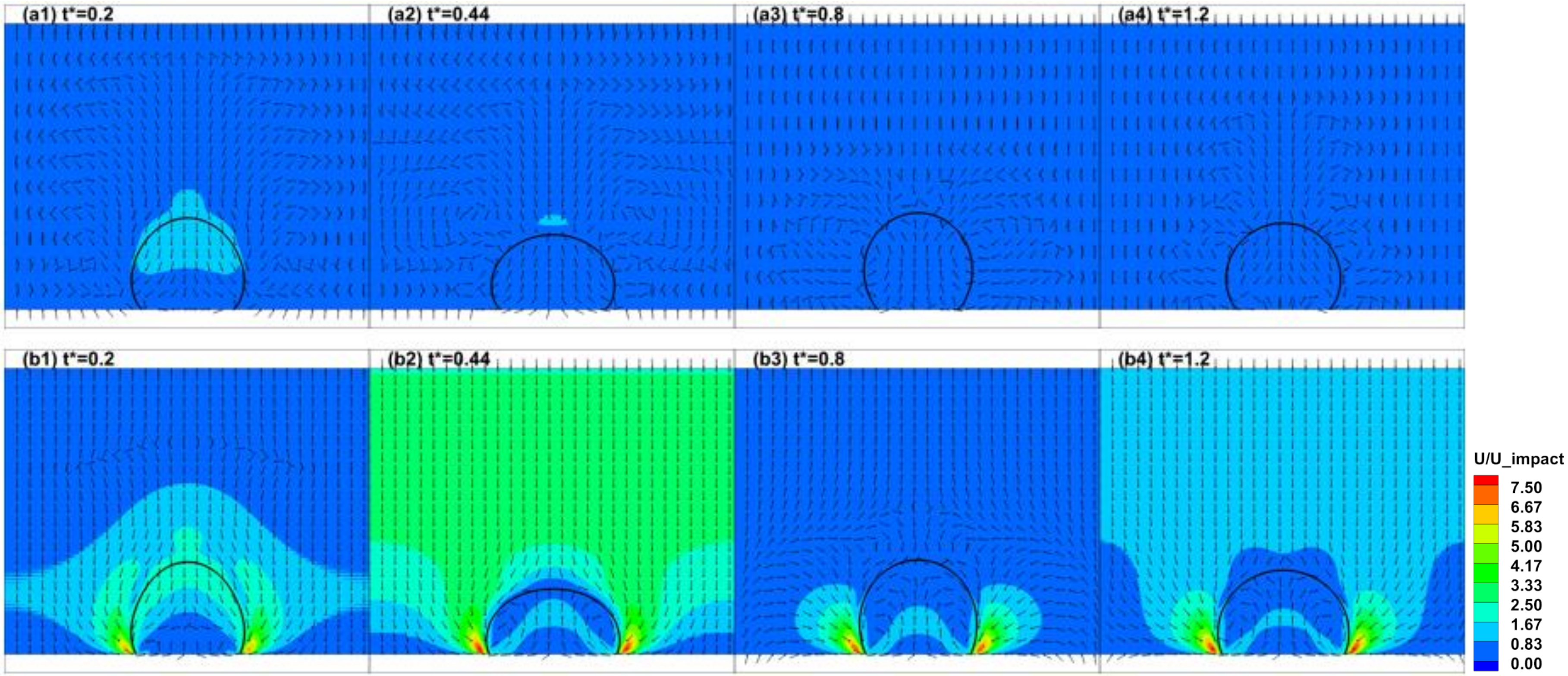

Figure 7.6 Cross sectional view of evolution of velocity field in mid-plane along x-axis in (a) isothermal case and (b) non-isothermal case.

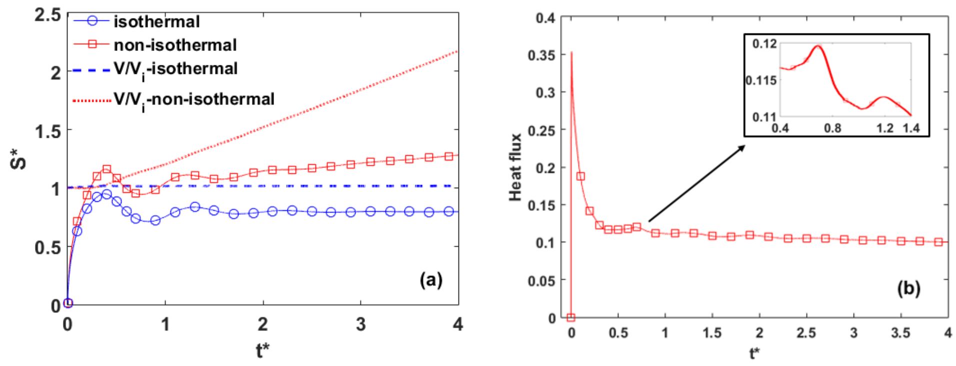

Figure 7.7 Temporal evolution of (a) spreading factor and normalized volume in both isothermal and non-isothermal cases (b) average heat flux.

7.4.1.1 EFFECTS OF JAKOB NUMBER

The evolution of droplet spreading for different Jakob numbers,i.e Ja=0.0 (isothermal case), 0.15, 0.35 and 0.50, is shown in Fig. 7.8. Images of isothermal case (Fig. 8 (a1,b1)) are added to facilitate the comparison. The Prandlt number and Weber number are fixed at Pr=1.0 and We=0.36, respectively. The velocity fields are presented in Fig. 7.9. It can be seen that increasing the Jakob number droplet size increases Fig. 8 (b1,b4). This is due to the reason that increasing Jakob number enhances the temperature contrast between saturated vapor and bottom surface, and as a result more phase change of vapors into liquid occurs. This can also be seen from velocity fields at t*=3.0 in Fig. 7.9, which shows higher velocity of vapors towards droplet near bottom surface at higher Jakob number compared to small Jakob number. The evolution of spreading factors is presented in Fig. 7.10 (a). The maximum spreading factor around t*=0.44 increases with Jakob number. During oscillation and equilibrium phases and spreading factor increases faster for larger Jakob number. Fig. 7.10 (b) shows the evolution of heat flux. The heat flux trend is similar for all Jakob numbers, however magnitude of heat flux increases with the Jakob number.

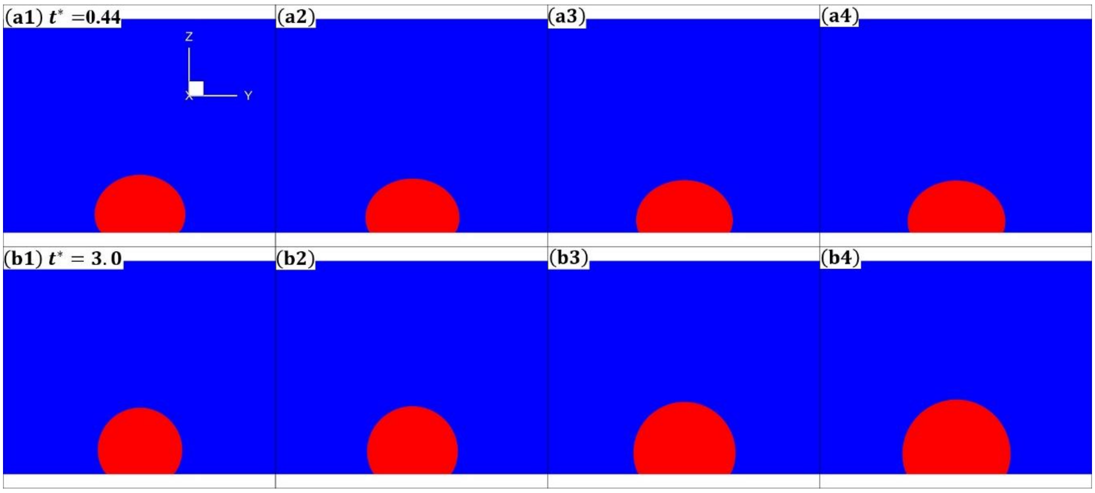

Figure 7.8 Images of droplet impact on level surface at two time instants (a) *t=0.44 (b) *t**=3.0 for different Jakob numbers: Ja= 0.0 (isothermal), 0.15, 0.35 and 0.50 (from left to right), The images show cross sectional view of mid-plane along x-axis.**

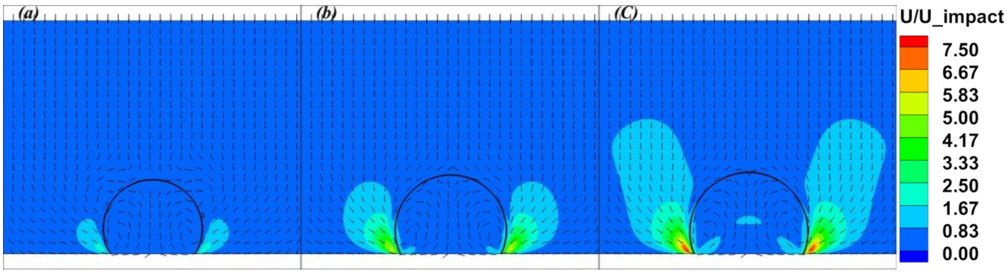

Figure 7.9 Images of velocity field at instant *t=3.0 for different Jakob numbers: 0.15, 0.35 and 0.50 (from left to right), the images show cross sectional view of mid-plane along x-axis.**

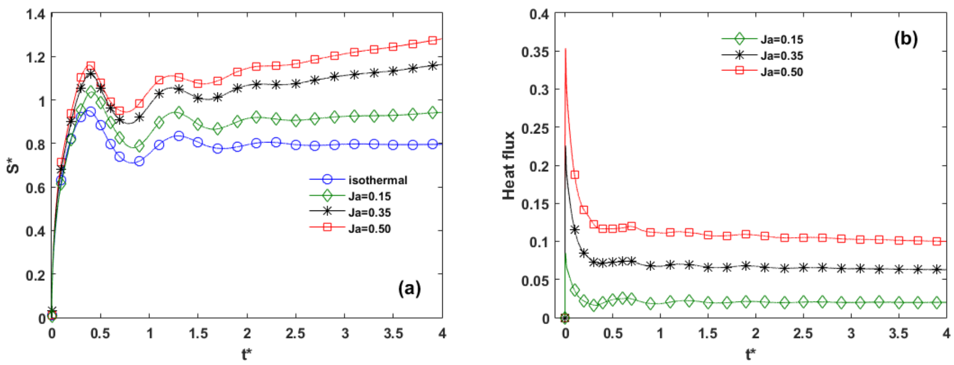

Figure 7.10 Evolutions of, (a) spreading factor and (b) heat flux, for different Jakob numbers: 0.15, 0.35, 0.50.

7.4.1.2 EFFECTS OF PRANDTL NUMBER

The Prandtl number is changed from Pr=0.25 to 1.0 with a step of 0.25 while the Jakob number and Weber are fixed at Ja=0.5 and We=0.36, respectively. Figures 7.11 and

7.12 show images of droplet impact and velocity fields, respectively. It can be seen from Eq. (7.1) that with decreasing the Prandtl number the thermal conductivity increases. As seen from Fig.7.12 (a-c), decreasing Prandtl accumulates more vapor near bottom surface and thus induces more condensation, and as a result droplet size increases faster for small Prandtl number (Fig. 7.11(b,d)). Moreover, the maximum spreading factor is larger for all values of Prandtl number compared to isothermal case (time t^*=0.44); however, change in Prandtl has nearly no effects on maximum spreading factor as shown in Fig. 7.13(a). The evolutions of heat flux are shown in Fig. 7.13(b). It is seen that reducing the Prandtl number enhances heat flux. The peaks (near t^*=0.44) become more prominent at small Prandtl number which is due higher thermal conductivity.

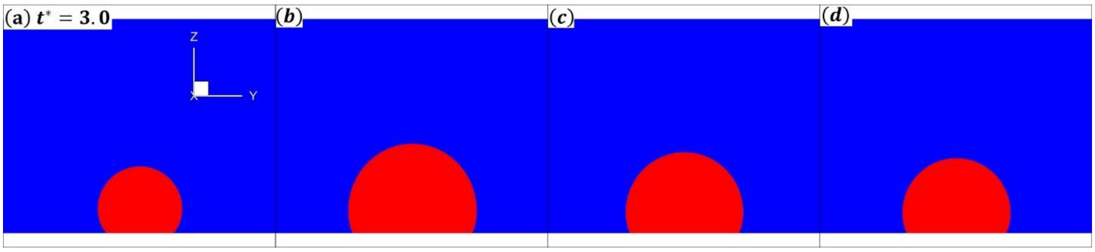

Figure 7.11 Images of droplet impact on level surface at time instant t^*=3.0 for (a) isothermal case and (b-d) for different Prandtl numbers: Pr= 0.25, 0.50 and 1.0 (from (b) to (d), respectively). The images show cross sectional view of mid-plane along x-axis.

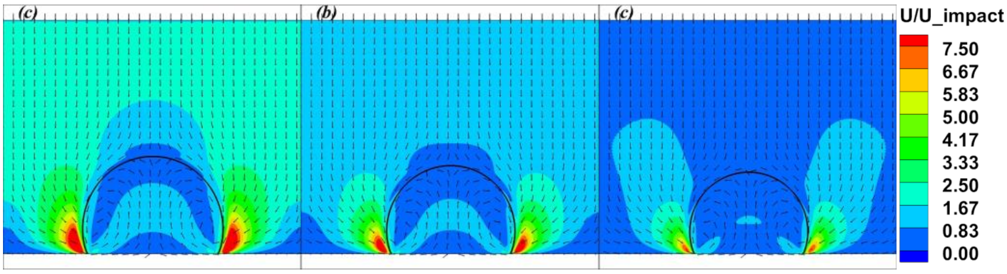

Figure 7.12 Images of velocity field at time instant t^*=3.0 for different Prandtl number: Pr= 0.25, 0.50 and 1.0 (from (a) to (c), respectively). The images show cross sectional view of mid-plane along x-axis.

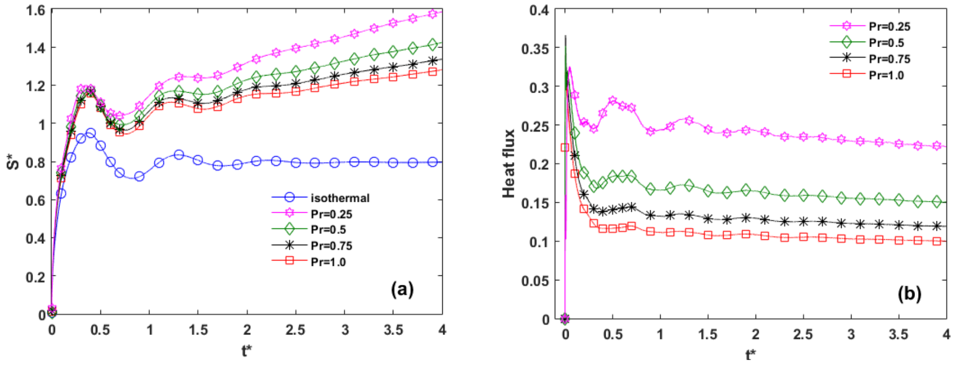

Figure 7.13 Evolutions of (a) spreading factor and (b) heat flux for different Jakob numbers: 0.15, 0.35 and 0.50.

7.4.1.3 EFFECTS OF WEBER NUMBER

Figure 7.14 shows temporal images of droplet impact for different Weber numbers, i.e., We= 0.05, 0.36 and 0.52. The Jakob number and Prandtl number are fixed at Ja=0.5 and Pr=1.0, respectively. For smaller Weber number We=0.05 droplet spreading and retraction is faster as shown by evolution of spreading factor in Fig. 7.15(a). Furthermore, spreading factor increases more rapidly in case of small Weber number after the retraction ,i.e., for time $t^*>0.8$. As seen from Fig. 7.15(b), heat flux is small for smaller Weber number that is due to the reason that during impact with small velocity less hot liquid inside the droplet moves towards bottom wall leading to smaller temperature contrast near surface.

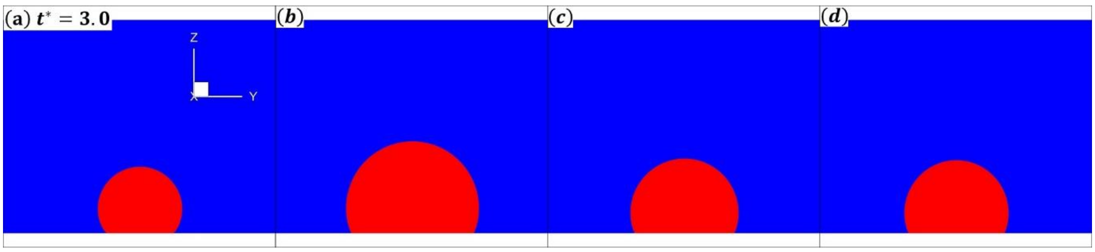

Figure 7.14 Images of droplet impact on level surface at time instant t^*=3.0 for (a) isothermal case and (b-d) for nonisothermal case with different Weber numbers: We= 0.05, 0.36 and 0.52 (from (b) to (d), respectively). The images show cross sectional view of mid-plane along x-axis.

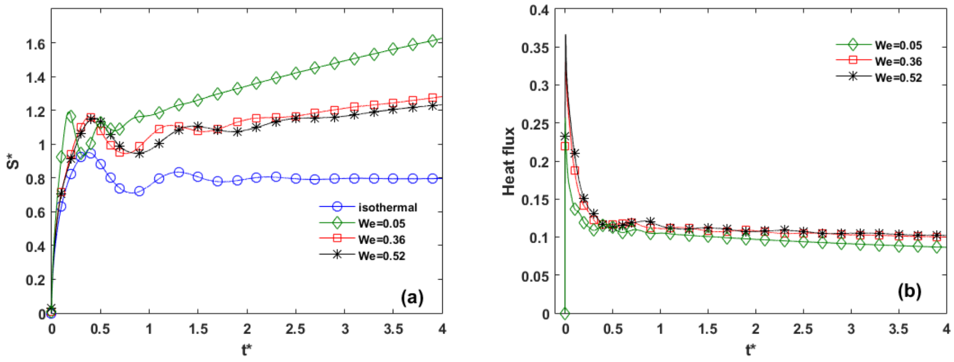

Figure 7.15 Evolutions of (a) spreading factor and (b) heat flux for different Weber numbers: 0.05, 0.36 and 0.52.

7.4.2 DROPLET IMPACT ON SLANTED SURFACE

The evolutions of droplet impact on surface at inclination α=45^{o} under isothermal and non-isothermal conditions are shown Fig. 7.16(a, b). Velocity fields are shown in Fig. 7.17(a, b). The Jakob number, the Prandlt number and Weber number are fixed at Ja=0.5, Pr=1.0 and We=0.36, respectively. In isothermal case, droplet spreads upon impaction (Fig 7.16(a1, a2)), which represents both downward (along positive y-axis) and upward or uphill (along negative y-axis) spreading of droplet lamella relative to point of impact. Note that the point of impact is shown as white dot for reference. Figure 7.17(a2) at t*=0.44 represents the end of spreading phase where liquid starts to move upward to follow the retraction process which ends near t*=0.8 (Fig 7.16(a3)). Then, the droplet moves downward as revealed from velocity vector directions in Fig. 7.17 (a4). On the other hand, droplet show less downward motion in the case of non-isothermal impact (Fig. 16(b)). The difference is more obvious in Figs. 16(a3, a4) and 16(b3, b4), the back edge slides downward only slightly in non-isothermal case compared to isothermal case. As seen from Fig. 17(b2, b3), a big vortex appears near front edge whereas small one near back edge. The liquid velocity vectors as well as the front edge interface have downward direction of motion, which is opposite to condensing vapor drawing towards the front edge Fig. 17(b2-b4). However, the downward motion of interface of back edge and vapor motion directions are nearly in same direction (along positive y-axis) during retraction phase (later than t*=0.44). Therefore, more injection of condensing liquid occurs at back edge or in other words condensation rate is faster at back edge compared to front edge, thus downward motion of back edge appears to be reduced. Fig. 7.16(c) shows the evolution of temperature field. It can be seen that low temperature region inside droplet near the bottom surface grows bigger with increase in size of droplet showing the decrease of temperature contrast near bottom surface with time.

Figure 7.18(a) compares the evolution of spreading factors along lateral and longitudinal directions. It can be noticed that both spreading factors are similar in magnitude at all the time, representing a symmetric spreading along both directions. This is because of the fact that inertial effects are not high enough at small droplet size (1.0 μm) and Weber number (0.36). However, dynamics of back and front contact edges are asymmetric as shown in Fig. 7.18(c). In isothermal case, back contact edge shortly moves upward (along negative y direction, before $t^{*}<0.44$) and then mainly spreads in downward direction. It is seen from Fig. 7.18(c) that in case of non-isothermal impact, downward motion of back contact edge is reduced confirming the observation made earlier, that is, the condensation is faster at the back contact edge.

Next, motion of left and right contact edges along later direction is plotted in Fig. 7.18(d). The spreading and retraction of both left and right contact edges is symmetric. Besides, as discussed earlier, spreading factor evolution along lateral direction is also similar to longitudinal spreading. Therefore, for simplification, in the next sections focus will only be placed on longitudinal spreading and contact lines motion along y axis.

Next the spreading factors evolutions of droplet impact on flat surface are compared to that of inclined surface in Fig. 7.18(b). It is noticeable that the spreading and retraction occurs earlier for both isothermal and non-isothermal cases for droplet impact on flat surface. In the later stage, time greater than 2.0, the spreading rate becomes similar for both level and inclined surfaces. Furthermore, surface inclination has little effect on maximum spreading factor.

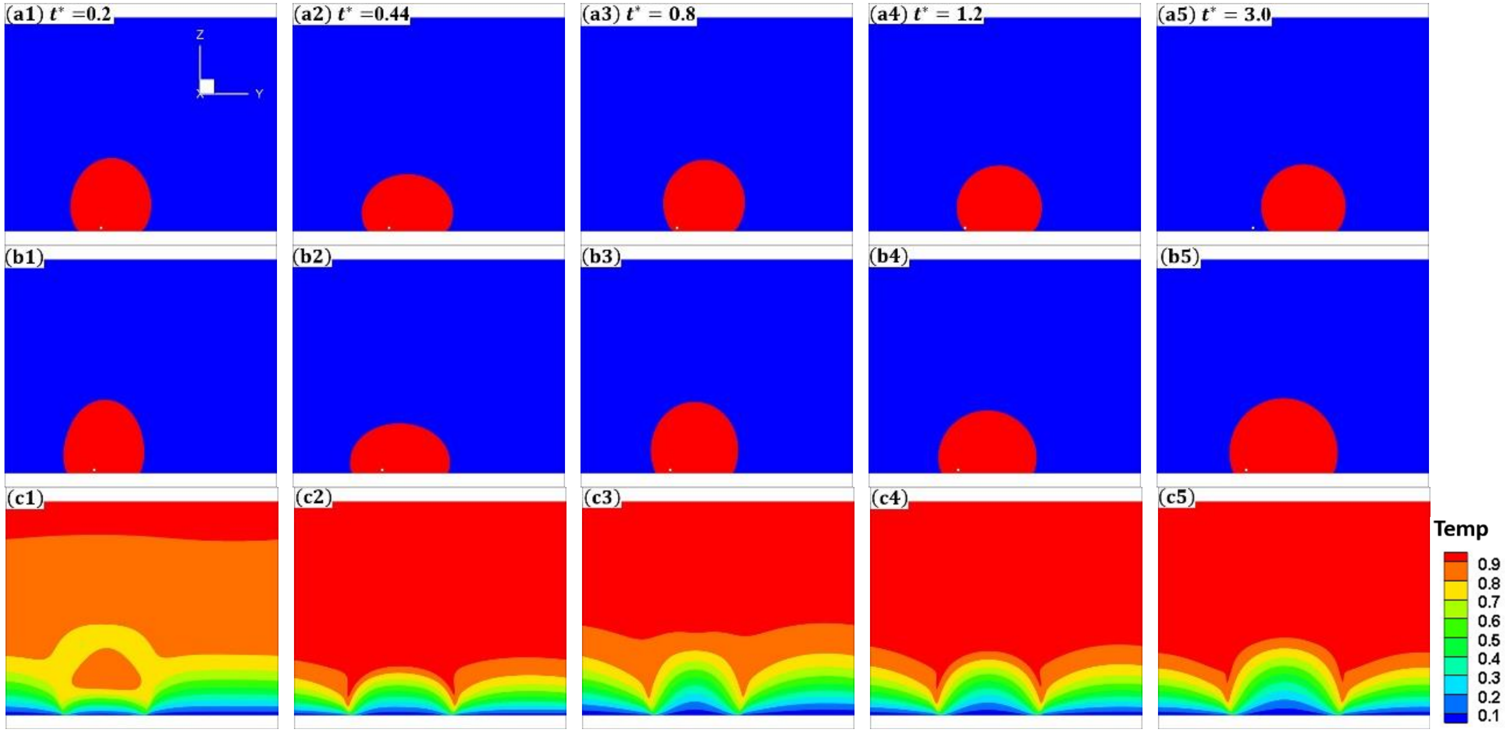

Figure 7.16 Evolutions of droplet impact on inclined surface under (a) isothermal conditions (b) non-isothermal conditions and (c) temperature field in non-isothermal case. The images show cross sectional view of mid-plane along x-axis.

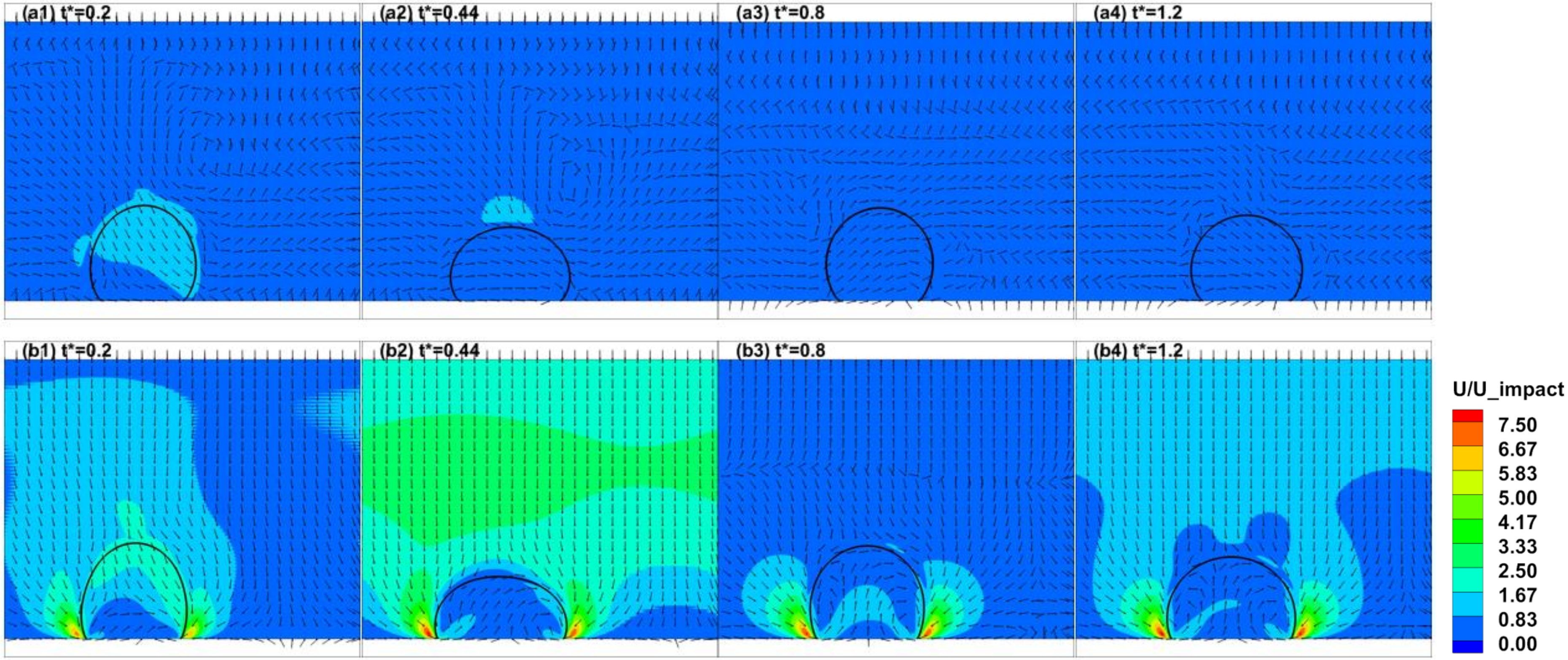

Figure 7.17 Cross sectional view of evolution of velocity field in mid-plane along x-axis in (a) isothermal case and (b) non-isothermal case

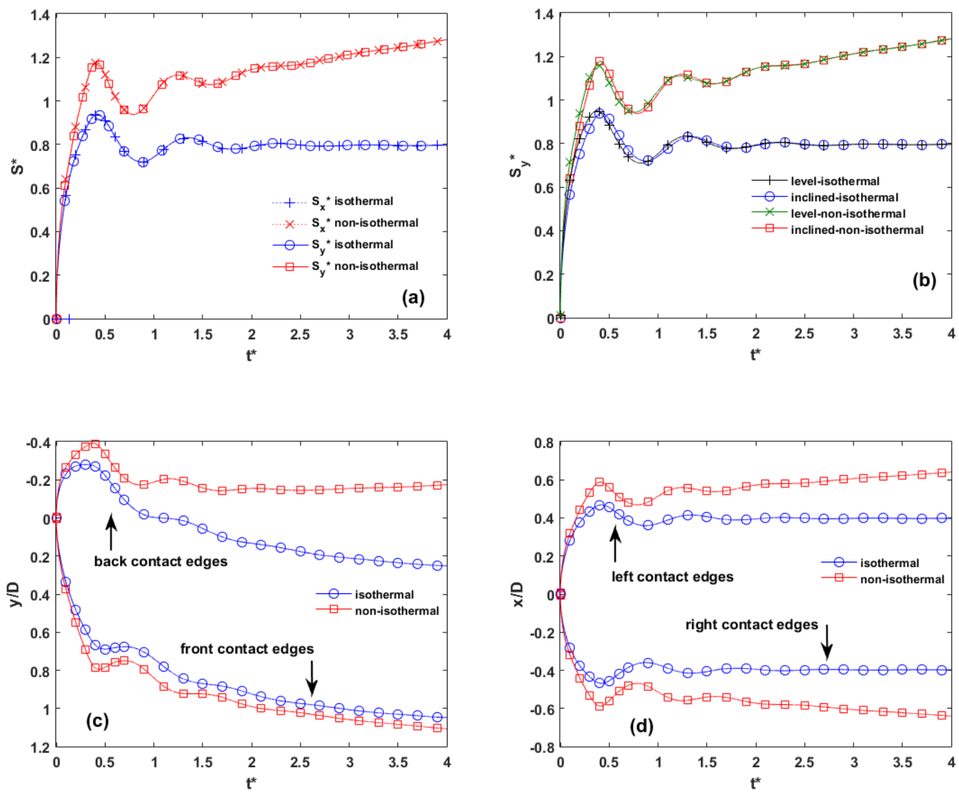

Figure 7.18 Temporal evolutions of (a) lateral and longitudinal spreading factors (b) longitudinal spreading factor (inclined surface) and spreading factor (level surface) (c) motion of back and front edges and (d) motion of left and right edges.

7.4.2.1 EFFECTS OF SURFACE INCLINATION

Figure 7.19 shows temporal evolution of droplet impact on surface with three different inclinations: α=30^{o}, 45^{o} and 60^{o}. The Jakob number, the Prandtl number and Weber are fixed at Ja=0.5, Pr=1.0 and We=0.36, respectively. As revealed from Fig.7.19, increasing surface inclination, droplet travels more distance. This is also confirmed from the motion of back and front contact edges (Fig. 7.20(b)). The spreading factor and heat flux are potted in Figs. 7.20(a) and 7.20(c), which show nearly similar patterns for all the surface inclinations.

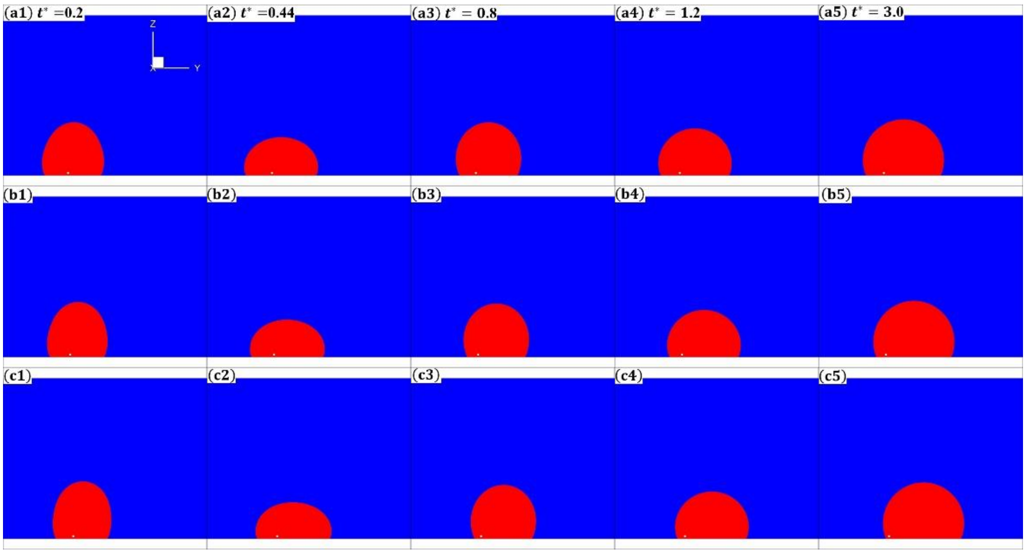

Figure 7.19 Evolutions of droplet impact on inclined surface for three different inclinations (a) α=30° (b) α=45° and (c) α=60°, The images show cross sectional view of mid-plane along x-axis.

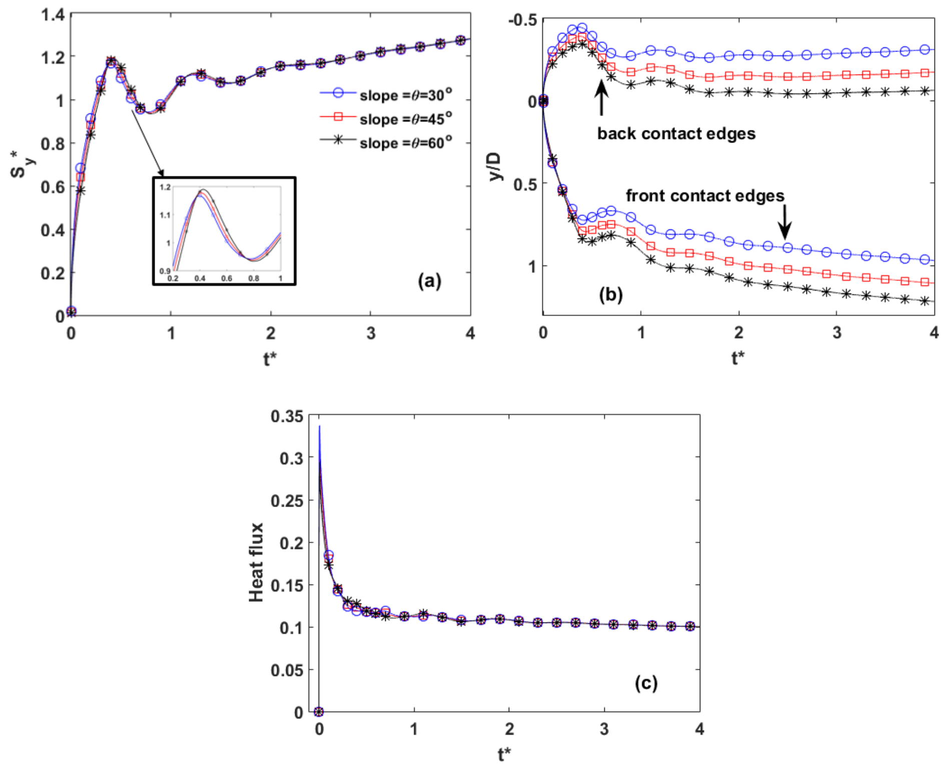

Figure 7.20 Evolutions of (a) spreading factor (b) front and back contact edges and (c) heat flux, for three different slopes: α=30°, α=45° and α=60°.

7.4.2.2 EFFECTS OF JAKOB NUMBER

Time sequences of images of droplet impact on surface of inclination α=45° at three different Jakob numbers, i.e, Ja=0.15, 0.35 and 0.50, are presented in Fig. 7.21. The

Prandtl number and Weber number are set at Pr=1.0 and We=0.36, respectively. Differences in droplet size and back edge motion are quite obvious in Fig. 7.21(a,b,c). The back contact edge moves less in downward direction at lager Jakob number as observed from Fig. 7.21(c5). Figure 7.22(b) shows the spreading evolution of back and front contact edges. The evolution of back contact edge confirms that increasing Jakob number reduces the downward motion of back contact edge. Furthermore, increase of droplet size with the Jakob number can also be observed from lager spreading factor values at time greater than t*=0.4 (Fig. 7.22 (a)), which is due higher heat transfer as seen from Fig. 7.22 (c).

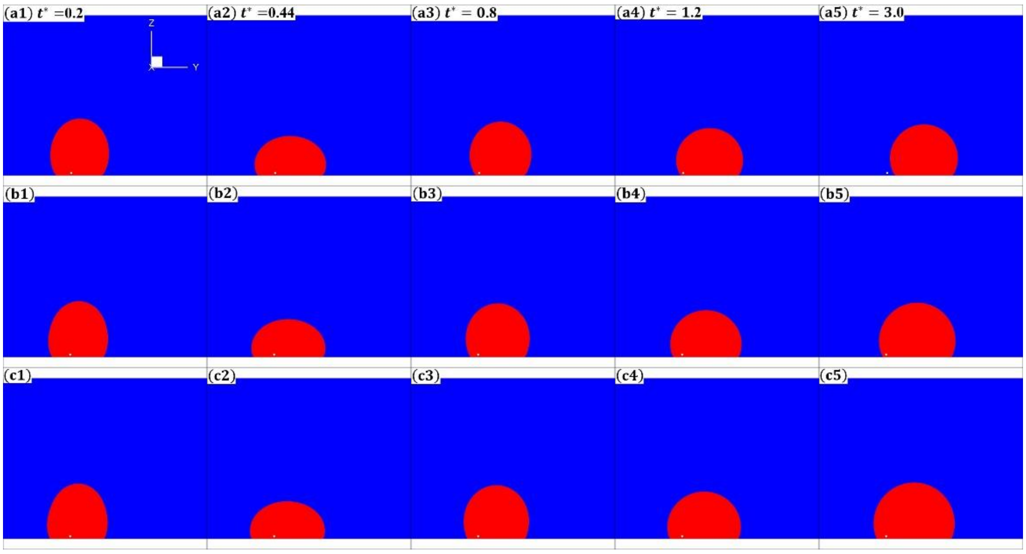

Figure 7.21 Evolution of droplet impact on inclined surface for different Jakob numbers (a) Ja= 0.15 (b) Ja= 0.35 and (c) Ja= 0.5, surface inclination α=45º, The images show cross sectional view of mid-plane along x-axis.

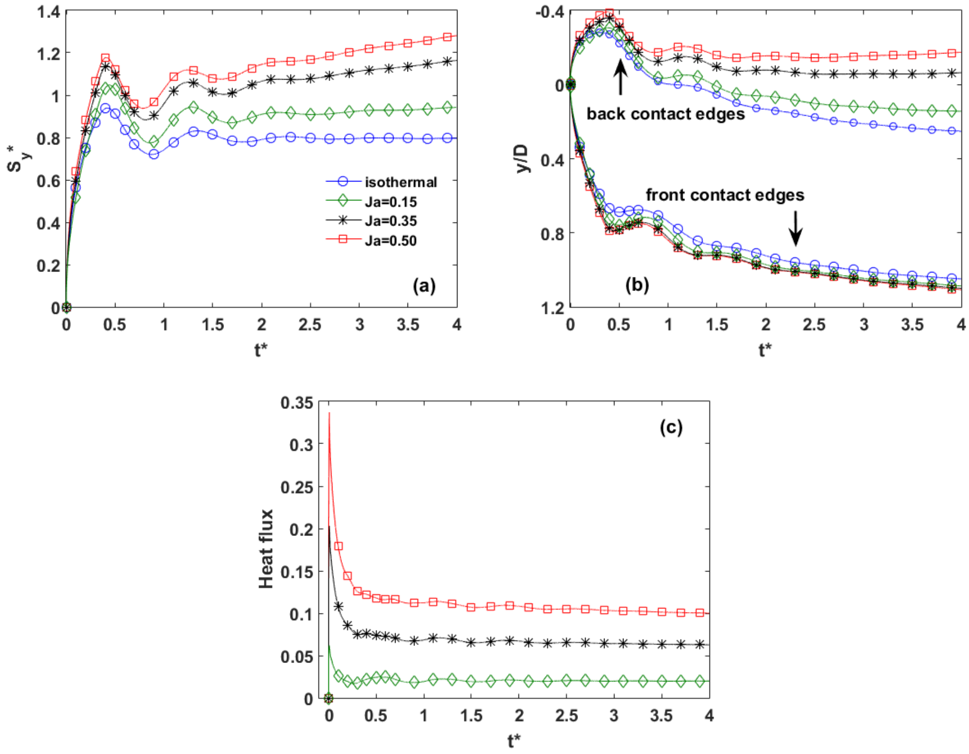

Figure 7.22 The evolutions of (a) spreading factor (b) front and back contact edges and (c) heat flux, for three different Jakob numbers: 0.15, Ja= 0.35 and Ja= 0.5.

7.4.2.3 EFFECTS OF PRANDTL NUMBER

Figure 7.23 represents temporal evolution of droplet impact on surface at inclination α=45^{o} for four different Prandtl numbers, i.e., Pr=0.25, 0.50, 0.75 and1.0. The Jakob number and Weber number are fixed at Ja=0.5 and We=0.36, respectively. Figure 7.23(a5, b5, c5) shows lager droplet size for smaller Prandtl number which is due to higher condensation. The condensation decreases with increasing Prandlt number which can be attributed to decrease of heat flux as seen from Fig.7.24 (c). Figure 7.24 (b) reveals no significant effects of Prandtl number on dynamics of back and front contact edges spreading till time t*=4.4,which corresponds to maximum spreading factor (Fig. 7.24 (a)). However, thereafter the back contact edges moves faster in down direction with increasing Prandtl number.

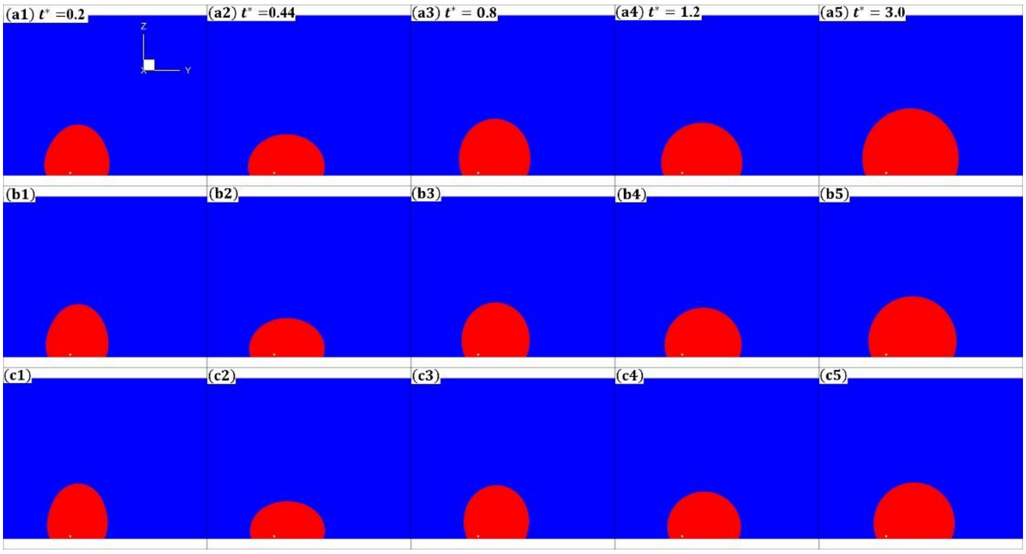

Figure 7.23 Evolution of droplet impact on inclined surface for different Prandtl numbers (a) Pr= 0.25 (b) Pr= 0.50 and (c) Pr= 1.0, surface inclination α=45º, The images show cross sectional view of mid-plane along x-axis.

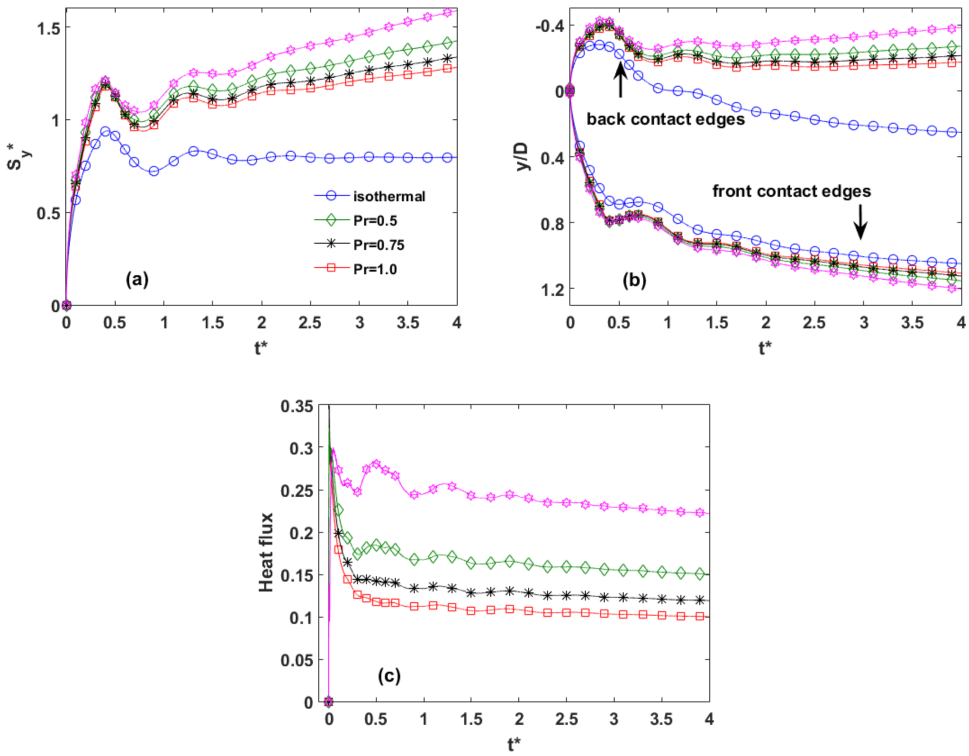

Figure 7.24 The evolutions of (a) spreading factor (b) front and back contact edges and (c) heat flux, for four different Prandtl numbers: Pr=0.25,0.50,0.75 and1.0.

7.4.2.4 EFFECTS OF WEBER NUMBER

Figure 7.25 shows evolution of droplet impact at three different Weber numbers, i.e., We=0.05, 0.36 and 0.52. The Jakob number and Prandtl number are fixed at Ja=0.5 and Pr=1.0, respectively. It can be seen that droplet moves faster in downward direction for larger Weber number. Figure 7.26(b) shows that front contact edge spreads faster in downward direction for larger Weber number. However, back contact edge spreads upward faster for smaller Weber number.

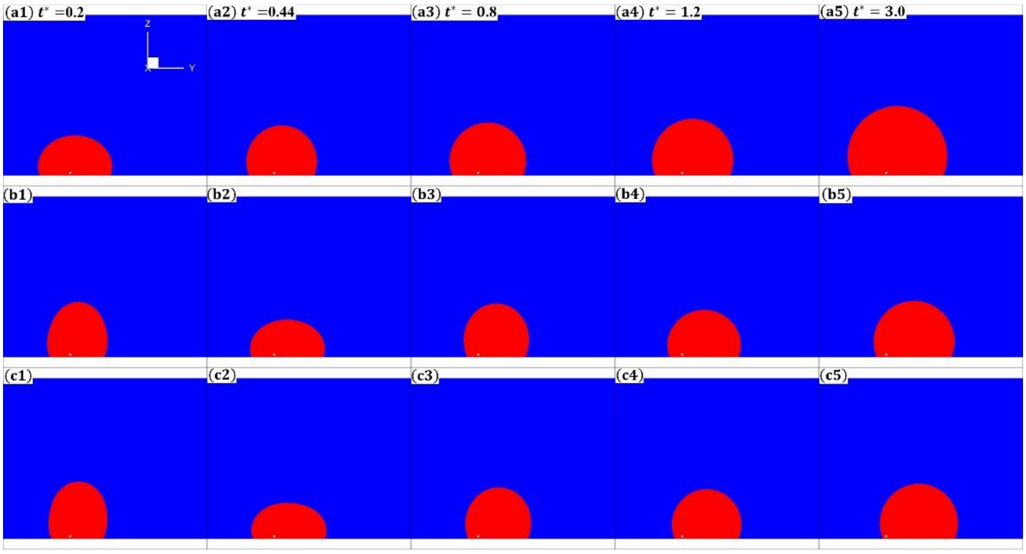

Figure 7.25 Evolution of droplet impact on inclined surface for different Weber numbers (a) We= 0.05 (b) We= 0.36 and (c) We= 0.52, surface inclination α=45º, The images show cross sectional view of mid-plane along x-axis.

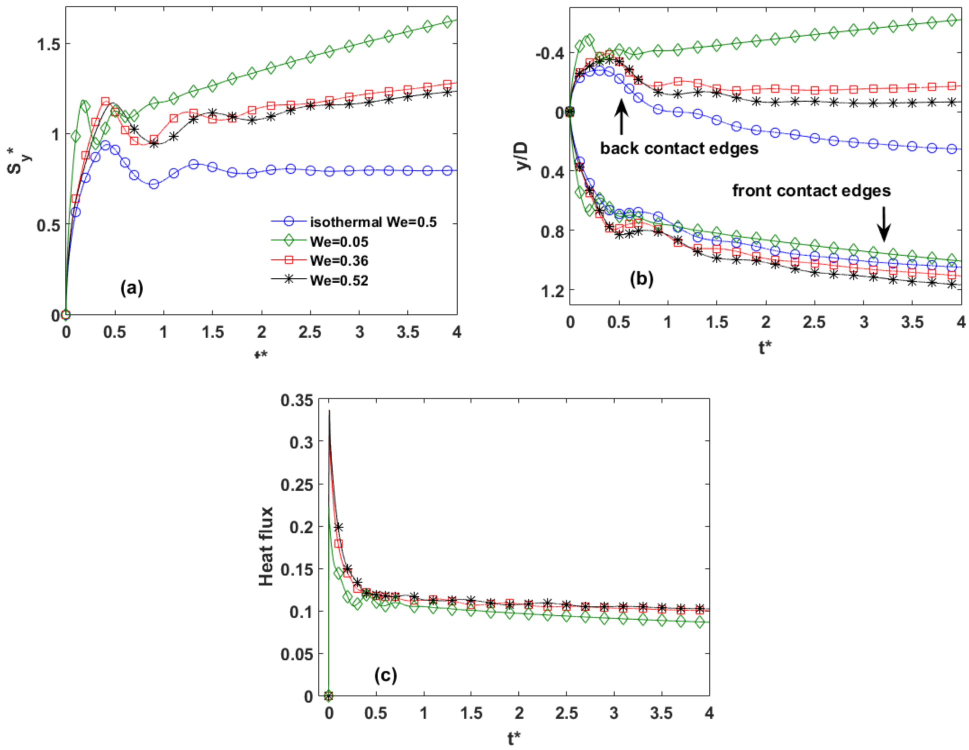

Figure 7.26 The evolutions of (a) spreading factor (b) front and back contact edges and (c) heat flux, for four different Weber numbers: We=0.05,0.36 and0.52.

7.5 SUMMARY

In this work a fog droplet impact on cold surface in presence of saturated vapor was investigated. The temperature difference between bottom surface and inlet vapor induces condensation, which in turn influences the droplet impact dynamics. The effects of parameters, such the Jakob number, the Prandtl number, surface slope and Weber number on dynamics of impacting droplet were investigated. The main finding of this study are summarized as follows:

1. Upon droplet impact on cold surface, the droplet temperature near the surface decreases which causes the phase change of vapor into liquid and thus droplet size increases. The condensation of vapor affects the maximum spreading factor and retraction of droplet, then in equilibrium phase droplet grows steadily. The maximum spreading factor is found be higher and retraction rate faster compared to isothermal case of droplet impact.

2. The spreading factor corresponding to maximum spreading factor and thereafter increases with the Jakob number. The change of the Prandtl number has little effect on maximum spreading factor. The heat flux increases with increasing Jakob number and decreasing Prandtl number. The Weber number affects the rate of spreading and retraction phases. The smaller Weber number has faster spreading and retraction rates, while smaller heat flux.

3. Introduction of slope induces asymmetry in contact lines motion along longitudinal direction. In isothermal case droplet is observed to move faster in downward direction compared to nonisothermal case. The significant difference is found in the dynamics of back contact edge. The back contact edge spreads slowly in downward direction for nonisothermal case. This slower motion of back contact edge is attributed to faster condensation in surrounding region compared to front contact edge. Droplet travels further in downward direction by increasing surface inclination. The increase of the Jakob number and decrease of the Prandtl number slow down the downward spreading.

CHAPTER 8

CONCLUSIONS AND RECOMMENDATIONS

8.1CONCLUSIONS

To understand the underlying physics of fog harvesting on beetle inspired surfaces, two key physical process, namely droplet impact and condensation, are studied using the lattice Boltzmann method. The focus was placed on four sub-problems. Firstly, the droplet impact on beetle inspired nanotextured hemispherical bumps was investigated. Secondly, the influence of surface slope on impact of two successive droplets was investigated. Thirdly, shedding of condensing droplets on hydrophilic/superhydrophobic bumps was studied. Finally, droplet impact on cold surface in presence of saturated vapor was investigated.

The major findings of these four studies are summarized below:

1. **Droplet impact dynamics on nanotextured bumps: topology effects**

In this study, droplet impact process captured three different states, i.e., Cassie state, droplet rebound and Wenzel state, depending on the bump geometry and Weber number. As well known, droplets in the Cassie state remain suspended on the nanostructure, hence are easy to collect compared to in the Wenzel state (droplet wets the nanostructure) and droplet rebound (droplet is lost to atmosphere). It was observed that droplet retraction rate on textured bumps was even faster than on smooth bumps. Wider interpost spacings induced the Wenzel state, whereas narrow interpost spacings induced higher retraction velocities leading to droplet rebound. The droplet rebound was observed on bumps with smaller radius and the Cassie state with larger radius. Importantly, this study highlighted that droplets impacting on nanotextured bumps with higher posts and larger radius were in the Cassie state, which is favorable for water collection. The bumps with taller posts and smaller radius lead to droplet rebound.

2. Oblique impact of two successive droplets on a flat surface

In this study, the dynamics of two identical droplets successively and obliquely impacting on a flat surface have been investigated. Firstly, it was found that the interaction between two successively impinging droplets can result in quite different dynamics compared to that of single droplets. Oblique impact causes asymmetric droplet spreading, with the downward spreading dominant over the lateral spreading. The increase in the surface slope leads to faster downward spreading and reduced lateral spreading. It was highlighted that the coalescence of the two droplets can result in abrupt changes in the evolution of the back and left/right contact edges, which is attributed to the partial landing of the trailing droplet on the leading droplet. The offset between the two droplets further increases the asymmetry of the combined droplet's dynamics. The increase of lateral offset causes the increase of the maximum lateral spread factor and the reduction of the maximum longitudinal spread factor, whereas the increase of longitudinal offset results in the opposite change.

3. Critical volume of a condensing droplet shedding from beetle inspired bumps

In this work, shedding of condensing droplet from dessert beetle inspired bumps was investigated. The perpendicular component of gravitational force was observed to play an active role in early droplet shedding on bumps with nonzero heights. The critical volume of droplet decreases with increasing the bump height until a critical bump height, and thereafter it does not change significantly. For the same hydrophilic patch area, the critical volume was smaller in case of hemispherical bump compared to cylindrical bump, which can be attributed to surface curvature. It was found that micro-scale bumps compared to millimeter scale bumps shed droplets smaller than water capillary length, which lead to inefficient gravity assisted removal of condensing droplet. In case of cylindrical bumps, droplet critical volume enhances with increasing bump diameter and wettability of hydrophilic patch, and decreasing surface inclination. Similar trend was found for the critical bump height.

4. Droplet impact in presence of saturated vapor

In this study, a fog droplet impact on cold surfaces in presence of saturated vapor is investigated. Upon impact on cold surface, the droplet temperature near the surface decreases which causes the phase change of vapor into liquid and thus droplet size increases. The maximum spreading factor increases with the Jakob number. The change of the Prandtl number has little effect on the maximum spreading factor. The heat flux increases with increasing the Jakob number and decreasing the Prandtl number. The Weber number affects the rate of spreading and retracting phases. It was observed that introduction of slope induces asymmetry in contact line motion along longitudinal direction. In the isothermal case, droplet is observed to move faster in the downward direction compared to the non-isothermal case. The significant difference was found in the dynamics of back contact edge, which spreads slowly in the downward direction in the non-isothermal case. This slower motion of back contact was attributed to faster condensation in surrounding region compared to the front contact edge. The increase of the Jakob number and decrease of the Prandtl number further slow down the downward spreading.

Overall, in this work the droplet impact and condensation on beetle inspired bumps and level or slanted surfaces were investigated. It was illustrated that nanotextured bumps of larger radius and higher posts heights are favorable for Cassie state. Surface inclination also influences the water collection, as the increasing inclination can stimulate droplet motion towards downhill collection reservoir. It was highlighted that slanted surfaces with higher inclination can produce faster downward spreading of droplet for both single droplet and two droplets impact cases. Furthermore, it was displayed that increasing the Jakob number and decreasing the Prandtl number reduce downward spreading for single droplet impact case. The lateral and longitudinal offsets reduce downward spreading for two droplet impact case. Moreover, the volume of shedding droplets from hydrophilic/superhydrophobic bumps was dependent on bump height till the critical bump height.

8.2 RECOMMENDATIONS FOR FUTURE RESEARCH

Although this thesis work has addressed the knowledge gaps introduced in Chapter 1, it can be extended in a number directions for further research.

1. **Droplet impact on hemispherical textured bumps: nanostructure shape effects**

In this thesis work, droplet impacting nanotextured bumps only with straight posts was studied. However, the effects post shape, such as tapered posts, can also be taken into account. The outcomes of droplet impacting on bumps with tapered and straight posts can be quite different. The key parameters, including geometrical parameters of posts and droplet impact velocity and droplet impact retraction time can be investigated. The comparison of these two type of posts would be able to reveal the geometrical parameters of posts for best water collection surfaces.

In fog droplets impact case, the effects of gravity can be neglected as they are smaller in size compared to the water capillary length. Nonetheless, if larger droplets, such as rain droplets, impact on these nanotextured bumpy surfaces, then effects of gravity cannot be neglected. In such a scenario, the droplet impact dynamics will be different from the fog droplet impact case. A study can be conducted to investigate the millimeter size rain droplet impact on textured bumpy surfaces.

2. **Maximum spreading factor relation for single and multiple droplets impact on inclined surfaces**

Understanding multiple droplets impact and subsequent coalescence is important for fog harvesting, as lateral/longitudinal offset between the two droplets can be crucial to determine the diameter/width of wire/ribbon of water collecting mesh. In such droplet impact studies the maximum spreading factor is an important parameter. A number of relations of maximum spreading factor are available in literature for droplet impact on level surfaces. On the other hand, only handful reports have discussed maximum spreading factor of single droplet impacting on inclined surfaces. A study can be conducted to thoroughly investigate single and multiple droplets impact on inclined surfaces to develop the relation for maximum spreading factor.

3. Investigation of droplet shedding from hemispherical hydrophilic/superhydrophobic bumps

A detailed study of condensing droplet shedding from hemispherical bumps is required, as it was explained in this work the droplet shed earlier for hemispherical bump compared to cylindrical bump. This quicker shedding of droplet can create space for condensation of new droplet that in turn will increase the condensation rate, leading to larger water collection rates. It would be interesting to investigate the effects of parameters, such as bump radius of curvature, surface slope, shedding time and wettability for hemispherical bumps. The development of relation between droplet shedding time and other parameters can be helpful in designing efficient water collecting surfaces.

REFERENCES

[1] World Economic Forum, Global Risks 2015: Insight Report, (2015). www.weforum.org/risks.

[2] A. Hybel, B. Godskesen, M. Rygaard, Selection of spatial scale for assessing impacts of groundwater-based water supply on freshwater resources., J. Environ. Manage. 160 (2015) 90–7.

[3] N.D. Chaturvedi, S. Bandyopadhyay, Optimization of multiple freshwater resources in a flexible-schedule batch water network, Ind. Eng. Chem. Res. 53 (2014) 5996–6005.

[4] C. Chartres, A. Sood, The Water for Food Paradox, Aquat. Procedia. 1 (2013) 3–19.

[5] I.A. Shiklomanov, Appraisal and Assessment of World Water Resources, Water Int. 25 (2000) 11–32.

[6] B.B.. b Yang, X. Wen, X. Sun, Irrigation depth far exceeds water uptake depth in an oasis cropland in the middle reaches of Heihe River Basin, Sci. Rep. 5 (2015) 15206.

[7] S. Gorjian, B. Ghobadian, T. Tavakkoli Hashjin, A. Banakar, Experimental performance evaluation of a stand-alone point-focus parabolic solar still, Desalination. 352 (2014) 1–17.

[8] N. Buras, Hydrology and Water Supply, in: Manag. Urban Water Supply, Springer Netherlands, Dordrecht, 2003: pp. 11–22.

[9] O. Klemm, R.S. Schemenauer, A. Lummerich, P. Cereceda, V. Marzol, D. Corell, J. Van Heerden, D. Reinhard, T. Gherezghiher, J. Olivier, P. Osses, J. Sarsour, E. Frost, M.J. Estrela, J.A. Valiente, G.M. Fessehaye, Fog as a fresh-water resource: Overview and perspectives, Ambio. 41 (2012) 221–234.

[10] R.S. Schemenauer, P. Cereceda, Fog collection's role in water planning for developing countries, Nat. Resour. Forum. 18 (1994) 91–100.

[11] S.A. Abdul-Wahab, V. Lea, Reviewing fog water collection worldwide and in Oman, Int. J. Environ. Stud. 65 (2008) 485–498.

[12] R.S. Schemenauer, P. Cereceda, A proposed standard fog collector for use in high-elevation regions, J. Appl. Meteorol. 33 (1994) 1313–1322.

[13] R.S. Schemenauer, P.I. Joe, The collection efficiency of a massive fog collector, Atmos. Res. 24 (1989) 53–69.

[14] D. Briassoulis, A. Mistriotis, D. Eleftherakis, Mechanical behaviour and properties of agricultural nets. Part II: Analysis of the performance of the main categories of agricultural nets, Polym. Test. 26 (2007) 970–984.

[15] J. de D. Rivera, Aerodynamic collection efficiency of fog water collectors,

Atmos. Res. 102 (2011) 335–342.

[16] K.C. Park, S.S. Chhatre, S. Srinivasan, R.E. Cohen, G.H. McKinley, Optimal Design of Permeable Fiber Network Structures for Fog Harvesting, Langmuir. 29 (2013) 13269–13277.

[17] J.R. Henschel, M.K. Seely, Ecophysiology of atmospheric moisture in the Namib Desert, Atmos. Res. 87 (2008) 362–368.

[18] A.R. Parker, C.R. Lawrence, Water capture by a desert beetle, Nature. 414 (2001) 33–34.

[19] L. Zhai, M.C. Berg, F.Ç. Cebeci, Y. Kim, J.M. Milwid, M.F. Rubner, R.E. Cohen, Patterned superhydrophobic surfaces: Toward a synthetic mimic of the namib desert beetle, Nano Lett. 6 (2006) 1213–1217.

[20] R.P. Garrod, L.G. Harris, W.C.E. Schofield, J. Mcgettrick, L.J. Ward, D.O.H. Teare, J.P.S. Badyal, Mimicking a Stenocara Beetle ' s Back for Microcondensation Using Plasmachemical Patterned Superhydrophobic - Superhydrophilic Surfaces, Langmuir. 23 (2007) 689–693.

[21] C. Dorrer, J. Rühe, Mimicking the stenocara beetle - Dewetting of drops from a patterned superhydrophobic surface, Langmuir. 24 (2008) 6154–6158.

[22] S.J. Hong, C.C. Chang, T.H. Chou, Y.J. Sheng, H.K. Tsao, A drop pinned by a designed patch on a tilted superhydrophobic surface: Mimicking desert beetle, J. Phys. Chem. C. 116 (2012) 26487–26495.

[23] T. Nørgaard, M. Dacke, Fog-basking behaviour and water collection efficiency in Namib Desert Darkling beetles., Front. Zool. 7 (2010) 23.

[24] L. Zhang, J. Wu, M.N. Hedhili, X. Yang, P. Wang, Inkjet printing for direct micropatterning of a superhydrophobic surface: toward biomimetic fog harvesting surfaces, J. Mater. Chem. A. 3 (2015) 2844–2852.

[25] K. Yin, H. Du, X. Dong, C. Wang, J. Duan, J. He, A simple way to achieve bioinspired hybrid wettability surface with micro/nanopatterns for efficient fog collection, Nanoscale. (2017).

[26] H. Bai, L. Wang, J. Ju, R. Sun, Y. Zheng, L. Jiang, Efficient water collection on integrative bioinspired surfaces with star-shaped wettability patterns, Adv. Mater. 26 (2014) 5025–5030. \

[27] Y. Wang, L. Zhang, J. Wu, M.N. Hedhili, P. Wang, A facile strategy for the fabrication of a bioinspired hydrophilic–superhydrophobic patterned surface for highly efficient fog-harvesting, J. Mater. Chem. A. 3 (2015) 18963–18969.

[28] Y. Wang, X. Wang, C. Lai, H. Hu, Y. Kong, B. Fei, J.H. Xin, Biomimetic Water-Collecting Fabric with Light-Induced Superhydrophilic Bumps, ACS Appl. Mater. Interfaces. 8 (2016) 2950–2960.

[29] H. Zhu, Z. Guo, Hybrid engineered materials with high water-collecting efficiency inspired by Namib Desert beetles, Chem. Commun. 52 (2016) 6809–6812.

[30] W. Hu, W. Liu, F. Zhu, X. Zhang, H. Zhang, The fabrication of PDMS-based functional surface mimicking the namib desert beetle back for collecting water vapor in the air, in: 9th IEEE Int. Conf. Nano/Micro Eng. Mol. Syst. IEEE-NEMS 2014, 2014: pp. 417–421.

[31] A. Ritter, C.M. Regalado, G. Aschan, Fog water collection in a subtropical Elfin Laurel Forest of the Garajonay National Park (Canary Islands): A combined approach using artificial fog catchers and a physically based impaction model, J. Hydrometeorol. 9 (2008) 920–935.

[32] Y. Hou, M. Yu, X. Chen, Z. Wang, S. Yao, Recurrent filmwise and dropwise condensation on a beetle mimetic, 9 (2014) 71–81.

[33] R. Rioboo, C. Tropea, M. Marengo, Outcomes from a drop impact on solid surfaces, At. Sprays. 11 (2001) 155–165.

[34] R. Rioboo, M. Marengo, C. Tropea, Time evolution of liquid drop impact onto solid, dry surfaces, Exp. Fluids. 33 (2002) 112–124.

[35] S. Chandra, C.. T. Avedisian, On the Collision of a Droplet with a Solid Surface, in: Proc. R. Soc. London A, 1991: p. 13.

[36] T. Mao, D. Kuhn, H. Tran, Spread and rebound of liquid droplets upon impact on flat surfaces, AIChE J. 43 (1997) 2169–2179.

[37] M. Pasandideh-Fard, Y.M. Qiao, S. Chandra, J. Mostaghimi, Capillary effects during droplet impact on a solid surface, Phys. Fluids. 8 (1996) 650.

[38] C. Clanet, C. Béguin, D. Richard, D. Quéré, Maximal deformation of an impacting drop, J. Fluid Mech. 517 (2004) 199–208.

[39] Y.H. Yeong, J. Burton, E. Loth, I.S. Bayer, Drop impact and rebound dynamics on an inclined superhydrophobic surface, Langmuir. 30 (2014) 12027–12038.

[40] A. Asai, M. Shioya, S. Hirasawa, T. Okazaki, Impact of an ink drop on paper, J. Imaging Sci. Technol. 37 (1993) 205–207.

[41] B. L. Scheller, D.W. Bousfield, Newtonian drop impact with a solid surface, AIChE Journal, 41(6). 41 (1995) 1357–1367.

[42] C. Ukiwe, D.Y. Kwok, On the maximum spreading diameter of impacting droplets on well-prepared solid surfaces, Langmuir. 21 (2005) 666–673.

[43] I. V. Roisman, Inertia dominated drop collisions. II. An analytical solution of the Navier-Stokes equations for a spreading viscous film, Phys. Fluids. 21 (2009).

[44] C. Stow, M. Hadfield, An experimental investigation of fluid flow resulting from the impact of a water drop with an unyielding dry surface, in: Proc. R. Soc. A 373:419–41 (1981).

[45] C. Mundo, M. Sommerfeld, C. Tropea, Droplet-wall collisions: Experimental studies of the deformation and breakup process, Int. J. Multiph. Flow. 21 (1995) 151–173. doi:10.1016/0301-9322(94)00069-V.

[46] L. Xu, W.W. Zhang, S.R. Nagel, Drop splashing on a dry smooth surface, Phys. Rev. Lett. 94 (2005). doi:10.1103/PhysRevLett.94.184505.

[47] L. Xu, L. Barcos, S.R. Nagel, Splashing of liquids: Interplay of surface roughness with surrounding gas, Phys. Rev. E. 76 (2007) 66311.

[48] S.T. Thoroddsen, K. Takehara, T.G. Etoh, Micro-splashing by drop impacts, J. Fluid Mech. 706 (2012) 560–570.

[49] A.L. Yarin, Drop Impact Dynamics: Splashing, Spreading, Receding, Bouncing…, Annu. Rev. Fluid Mech. 38 (2006) 159–192.

[50] C. Josserand, S.T. Thoroddsen, Drop impact on a solid surface, Annu. Rev. Fluid Mech. 48 (2016) 365–391.

[51] I. V. Roisman, K. Horvat, C. Tropea, Spray impact: Rim transverse instability initiating fingering and splash, and description of a secondary spray, Phys. Fluids. 18 (2006).

[52] G. Agbaglah, C. Josserand, S. Zaleski, Longitudinal instability of a liquid rim, Phys. Fluids. 25 (2013).

[53] S.T. Thoroddsen, J. Sakakibara, Evolution of the fingering pattern of an impacting drop, Phys. Fluids. 10 (1998) 1359–1374.

[54] H. Marmanis, S.T. Thoroddsen, Scaling of the fingering pattern of an impacting drop, 8 (1996) 1344–1346.

[55] S.D. Aziz, S. Chandra, Impact, recoil and splashing of molten metal droplets, Int. J. Heat Mass Transf. 43 (2000) 2841–2857.

[56] N.Z. Mehdizadeh, S. Chandra, J. Mostaghimi, Formation of fingers around the edges of a drop hitting a metal plate with high velocity, J. Fluid Mech. (2004) 353–373.

[57] B.W. Faßmann, S.E. Bansmer, T.J. Möller, R. Radespiel, M. Hartmann, High velocity impingement of single droplets on a dry smooth surface, Exp. Fluids. 54 (2013) 1516.

[58] S. Choo, H.J. Choi, H. Lee, Water-collecting behavior of nanostructured surfaces with special wettability, Appl. Surf. Sci. 324 (2015) 563–568.

[59] J. Guadarrama-Cetina, A. Mongruel, M.G. Medici, E. Baquero, A.R. Parker, I. Milimouk-Melnytchuk, W. González-Viñas, D. Beysens, Dew condensation on desert beetle skin, Eur. Phys. J. E. 37 (2014).

[60] B. White, A. Sarkar, A.M. Kietzig, Fog-harvesting inspired by the Stenocara beetle - An analysis of drop collection and removal from biomimetic samples with wetting contrast, Appl. Surf. Sci. 284 (2013) 826–836.

[61] J.K. Domen, W.T. Stringfellow, M. Kay, C. Shelly, Fog water as an alternative and sustainable water resource, Clean Techn Env. Policy. 16 (2014) 235–249.

[62] Š. Šikalo, C. Tropea, E.N. Ganić, Impact of droplets onto inclined surfaces, J.

Colloid Interface Sci. 286 (2005) 661–669.

[63] S.F. Lunkad, V. V. Buwa, K.D.P. Nigam, Numerical simulations of drop impact and spreading on horizontal and inclined surfaces, Chem. Eng. Sci. 62 (2007) 7214–7224.

[64] C. Shen, C. Yu, Y. Chen, Spreading dynamics of droplet on an inclined surface, Theor. Comput. Fluid Dyn. 30 (2016) 237–252.

[65] Y. Shen, S. Liu, C. Zhu, J. Tao, Z. Chen, H. Tao, L. Pan, G. Wang, T. Wang, Bouncing dynamics of impact droplets on the convex superhydrophobic surfaces, 221601 (2017).

[66] S. Chen, V. Bertola, S. Chen, V. Bertola, Drop impact on spherical soft surfaces, 82106 (2017).

[67] Y. Liu, M. Andrew, J. Li, J.M. Yeomans, Z. Wang, Symmetry-breaking in drop bouncing on curved surfaces, Nat. Commun. 6 (2015) 1–8.

[68] D. Khojasteh, A. Bordbar, R. Kamali, M. Marengo, Curvature effect on droplet impacting onto hydrophobic and superhydrophobic spheres, Int. J. Comut. Fluid Dyn. 31 (2017) 310–323.

[69] S. Chen, V. Bertola, Drop impact on spherical soft surfaces, Phys. Fluids. 29 (2017).

[70] Y.C. Jung, B. Bhushan, Dynamic effects of bouncing water droplets on superhydrophobic surfaces, Langmuir. 24 (2008) 6262–6269.

[71] P. Hao, C. Lv, F. Niu, Y. Yu, Water droplet impact on superhydrophobic surfaces with microstructures and hierarchical roughness, Sci. China Physics, Mech. Astron. 57 (2014) 1376–1381.

[72] Z. Wang, C. Lopez, A. Hirsa, N. Koratkar, Impact dynamics and rebound of water droplets on superhydrophobic carbon nanotube arrays, Appl. Phys. Lett. 91 (2007).

[73] A.I. Aria, M. Gharib, Physicochemical characteristics and droplet impact dynamics of superhydrophobic carbon nanotube arrays, Langmuir. 30 (2014) 6780–6790.

[74] G. Kwak, D.W. Lee, I.S. Kang, K. Yong, G. Kwak, D.W. Lee, I.S. Kang, K. Yong, A study on the dynamic behaviors of water droplets impacting nanostructured surfaces, 42139 (2012).

[75] P. Tsai, S. Pacheco, C. Pirat, L. Lefferts, D. Lohse, Drop impact upon micro- and nanostructured superhydrophobic surfaces, 25 (2009) 12293–12298.

[76] D.J. Lee, H.M. Kim, Y.S. Song, J.R. Youn, Water droplet bouncing and superhydrophobicity induced by multiscale hierarchical nanostructures, ACS Nano. 6 (2012) 7656–7664.

[77] M. McCarthy, K. Gerasopoulos, R. Enright, J.N. Culver, R. Ghodssi, E.N. Wang, Biotemplated hierarchical surfaces and the role of dual length scales on

the repellency of impacting droplets, Appl. Phys. Lett. 100 (2012).

[78] H. Kim, C. Lee, M.H. Kim, J. Kim, Drop impact characteristics and structure effects of hydrophobic surfaces with micro- and/or nanoscaled structures, Langmuir. 28 (2012) 11250–11257.

[79] D. Soltman, V. Subramanian, and V. Subramanian, Inkjet-printed Line morphologies and temperature control of the coffee ring effect, Langmuir. 24 (2008) 2224–2231.

[80] R.E. Saunders, J.E. Gough, B. Derby, Delivery of human fibroblast cells by piezoelectric drop-on-demand inkjet printing, Biomaterials. 29 (2008) 193–203.

[81] W.M. Grissom, F.A. Wierum, Liquid spray cooling of a heated surface, Int. J. Heat Mass Transf. 24 (1981) 261–271.

[82] T.M. Squires, S.R. Quake, Microfluidics: Fluid physics at the nanoliter scale, Rev. Mod. Phys. 77 (2005) 977–1026.

[83] A. Gupta, R. Kumar, Droplet impingement and breakup on a dry surface, Comput. Fluids. 39 (2010) 1696–1703.

[84] A. Gupta, R. Kumar, Two-dimensional lattice Boltzmann model for droplet impingement and breakup in low density ratio liquids, Commun. Comput. Phys. 10 (2011) 767–784.

[85] D. Zhang, K. Papadikis, S. Gu, Application of a high density ratio lattice-Boltzmann model for the droplet impingement on flat and spherical surfaces, Int. J. Therm. Sci. 84 (2014) 75–85.

[86] K.A. Raman, R.K. Jaiman, T. Lee, H. Low, A numerical study on electrowetting-induced jumping and transport of droplet, Int. J. Heat Mass Transf. 99 (2016) 805–821.

[87] R. Li, N. Ashgriz, S. Chandra, J.R. Andrews, S. Drappel, Coalescence of two droplets impacting a solid surface, Exp. Fluids. 48 (2010) 1025–1035.

[88] P.J. Graham, M.M. Farhangi, A. Dolatabadi, Dynamics of droplet coalescence in response to increasing hydrophobicity, Phys. Fluids. 24 (2012).

[89] J.R. Castrejón-Pita, K.J. Kubiak, A.A. Castrejón-Pita, M.C.T. Wilson, I.M. Hutchings, Mixing and internal dynamics of droplets impacting and coalescing on a solid surface, Phys. Rev. E - Stat. Nonlinear, Soft Matter Phys. 88 (2013).

[90] I. V Roisman, B. Prunet-Foch, C. Tropea, M. Vignes-Adler, Multiple Drop Impact onto a Dry Solid Substrate, J. Colloid Interface Sci. 256 (2002) 396–410.

[91] K.A. Raman, R.K. Jaiman, T.S. Lee, H.T. Low, On the dynamics of crown structure in simultaneous two droplets impact onto stationary and moving liquid film, Comput. Fluids. 107 (2015) 285–300.

[92] J. Wu, J.J. Huang, W.W. Yan, Lattice Boltzmann investigation of droplets impact behaviors onto a solid substrate, Colloids Surfaces A Physicochem. Eng. Asp. 484 (2015) 318–328.

[93] W. Zhou, D. Loney, A.G. Fedorov, F.L. Degertekin, D.W. Rosen, Lattice Boltzmann simulations of multiple-droplet interaction dynamics, Phys. Rev. E. 89 (2014) 33311.

[94] H. Fujimoto, S. Ito, I. Takezaki, Experimental study of successive collision of two water droplets with a solid, Exp. Fluids. 33 (2002) 500–502.

[95] A.Y. Tong, S. Kasliwal, H. Fujimoto, On the successive impingement of droplets onto a substrate, Numer. Heat Transf. Part A Appl. 52 (2007) 531–548.

[96] K. Ashoke Raman, R.K. Jaiman, T.S. Lee, H.T. Low, Lattice Boltzmann study on the dynamics of successive droplets impact on a solid surface, Chem. Eng. Sci. 145 (2016) 181–195.

[97] K. Ashoke Raman, R.K. Jaiman, T.-S. Lee, H.-T. Low, Dynamics of simultaneously impinging drops on a dry surface: Role of impact velocity and air inertia, J. Colloid Interface Sci. 486 (2017) 265–276.

[98] M. Massinon, H. Boukhalfa, F. Lebeau, The effect of surface orientation on spray retention, Precis. Agric. 15 (2014) 241–254.

[99] W. Nusselt, Die oberflachenkondesationdes wasserdamffes, Zetrschr.Ver.Deutch.Ing. 60 (1916) 541–546.

[100] E. Sparrow, J. Gregg, A boundary layer treatment of laminar film condensation, J. Heat Transf. 81 (1) (1959) 13–18.

[101] M.M. Chen, An analytical study of laminar film condensation: part 1 - flat plates, J. Heat Transf. 83 (1) (1961) 48–55.

[102] J.F. Welch, J.W. Westwater, Microscopic Study of Dropwise Condensation, in: International Heat Transfer Conference, Colorado , USA , p. 302, 1961, n.d.

[103] A. Lee, M.W. Moon, H. Lim, W.D. Kim, H.Y. Kim, Water harvest via dewing, Langmuir. 28 (2012) 10183–10191.

[104] X. Chen, J. Wu, R. Ma, M. Hua, N. Koratkar, S. Yao, Z. Wang, Nanograssed Micropyramidal Architectures for Continuous Dropwise Condensation, (2011) 4617–4623.

[105] Y. Shang, Y. Hou, M. Yu, S. Yao, Modeling and optimization of condensation heat transfer at biphilic interface, Int. J. Heat Mass Transf. 122 (2018) 117–127.

[106] E.S.R. Negeed, S. Hidaka, M. Kohno, Y. Takata, High speed camera investigation of the impingement of single water droplets on oxidized high temperature surfaces, Int. J. Therm. Sci. 63 (2013) 1–14.

[107] G. Strotos, N. Nikolopoulos, K.S. Nikas, K. Moustris, Cooling effectiveness of droplets at low Weber numbers: Effect of temperature, Int. J. Therm. Sci. 72 (2013) 60–72.

[108] E. Kompinsky, G. Dolan, E. Sher, Experimental study on the dynamics of binary fuel droplet impacts on a heated surface, Chem. Eng. Sci. 98 (2013) 186–194.

[109] G. Liang, I. Mudawar, Review of drop impact on heated walls, Int. J. Heat Mass Transf. 106 (2017) 103–126.

[110] J. Lv, Y. Song, L. Jiang, J. Wang, Bio-inspired strategies for anti-icing, ACS Nano. 8 (2014) 3152–3169.

[111] L. Huang, Z. Liu, Y. Liu, Y. Gou, L. Wang, Effect of contact angle on water droplet freezing process on a cold flat surface, Exp. Therm. Fluid Sci. 40 (2012) 74–80.

[112] Z. Jin, H. Zhang, Z. Yang, Experimental investigation of the impact and freezing processes of a water droplet on an ice surface, Int. J. Heat Mass Transf. 109 (2017) 716–724.

[113] S.S. Siavoshani, Effect of substrate properties on molten metal droplet impact, University of Toronto, National Library of Canada, 2001.

[114] S. Shiri, J.C. Bird, Heat exchange between a bouncing drop and a superhydrophobic substrate, Proc. Natl. Acad. Sci. 114 (2017) 6930–6935.

[115] A. Alizadeh, V. Bahadur, S. Zhong, W. Shang, R. Li, J. Ruud, M. Yamada, L. Ge, A. Dhinojwala, M. Sohal, Temperature dependent droplet impact dynamics on flat and textured surfaces, Appl. Phys. Lett. 100 (2012).

[116] G. Tryggvason, B. Bunner, A. Esmaeeli, D. Juric, N. Al-Rawahi, W. Tauber, J. Han, S. Nas, Y.J. Jan, A Front-Tracking Method for the computations of multiphase flow, J. Comput. Phys. 169 (2001) 708–759.

[117] C.W. Hirt, B.D. Nichols, Volume of fluid (VOF) method for the dynamics of free boundaries, J. Comput. Phys. 39 (1981) 201–225.

[118] M. Sussman, E. Fatemi, P. Smereka, S. Osher, An improved level set method for incompressible two-phase flows, Comput. Fluids. 27 (1998) 663–680.

[119] H. Liu, A.J. Valocchi, Q. Kang, Three-dimensional lattice Boltzmann model for immiscible two-phase flow simulations, Phys. Rev. E. 85 (2012) 46309.

[120] R. Scardovelli, S. Zaleski, Direct numerical simulation of free-surface and interfacial flow, Annu. Rev. Fluid Mech. 31 (1999) 567–603.

[121] M. Bussmann, J. Mostaghimi, S. Chandra, On a three-dimensional volume tracking model of droplet impact, Phys. Fluids. 11 (1999) 1406–1417.

[122] Z. Jian, C. Josserand, S. Popinet, P. Ray, S. Zaleski, Two mechanisms of droplet splashing on a solid substrate, J. Fluid Mech. 835 (2018) 1065–1086.

[123] J.C. Yang, T.Y. Qi, T.Y. Han, J. Zhang, M.J. Ni, Elliptical spreading characteristics of a liquid metal droplet impact on a glass surface under a horizontal magnetic field, Phys. Fluids. 30 (2018).

[124] F. Gibou, L. Chen, D. Nguyen, S. Banerjee, A level set based sharp interface method for the multiphase incompressible Navier-Stokes equations with phase change, J. Comput. Phys. 222 (2007) 536–555.

[125] N. Samkhaniani, M.R. Ansari, Numerical simulation of bubble condensation using CF-VOF, Prog. Nucl. Energy. 89 (2016) 120–131.

[126] S. Osher, J.A. Sethian, Fronts propagating with curvature-dependent speed: Algorithms based on Hamilton-Jacobi formulations, J. Comput. Phys. 79 (1988) 12–49.

[127] S. Chen, G.D. Doolen, Lattice Boltzmann Method for fluid flows, 30 (1998) 329–364. doi:10.1007/978-3-540-27982-2.

[128] M.R. Swift, W.R. Osborn, J.M. Yeomans, Lattice Boltzmann simulation of nonideal fluids, Phys. Rev. Lett. 75 (1995) 830–833.

[129] X. He, S. Chen, R. Zhang, A Lattice Boltzmann scheme for incompressible multiphase flow and its application in simulation of Rayleigh – Taylor Instability, J. Comput. Phys. 663 (1999) 642–663.

[130] T. Lee, C.L. Lin, A stable discretization of the lattice Boltzmann equation for simulation of incompressible two-phase flows at high density ratio, J. Comput. Phys. 206 (2005) 16–47.

[131] X. Shan, H. Chen, Simulation of nonideal gases and liquid-gas phase transitions by the lattice Boltzmann equation, Phys. Rev. E. 49 (1994) 2941–2948. doi:10.1103/PhysRevE.49.2941.

[132] H.W. Zheng, C. Shu, Y.T. Chew, Lattice Boltzmann interface capturing method for incompressible flows, Phys. Rev. E. 72 (2005) 56705. doi:10.1103/PhysRevE.72.056705.

[133] X. Shan, H. Chen, Lattice Boltzmann model for simulating flows with multi phases and components, Phys. Rev. E. 47 (1993) 1815–1819.

[134] C. Zhang, P. Cheng, W.J. Minkowycz, Lattice Boltzmann simulation of forced condensation flow on a horizontal cold surface in the presence of a non-condensable gas, Int. J. Heat Mass Transf. 115 (2017) 500–512.

[135] M.A. Hygum, I. V. Karlin, V.N. Popok, Free surface entropic lattice Boltzmann simulations of film condensation on vertical hydrophilic plates, Int. J. Heat Mass Transf. 87 (2015) 576–582.

[136] M.A. Hatani, H. Amirshaghaghi, M.H. Rahimian, A. Begmohammadi, Lattice Boltzmann simulation of condensation over different cross sections and tube banks, J. Mech. Sci. Technol. 31 (2017) 4943–4955.

[137] X. Liu, P. Cheng, Lattice Boltzmann simulation of steady laminar film condensation on a vertical hydrophilic subcooled flat plate, Int. J. Heat Mass Transf. 62 (2013) 507–514.

[138] X. Liu, P. Cheng, Lattice Boltzmann simulation for dropwise condensation of vapor along vertical hydrophobic flat plates, Int. J. Heat Mass Transf. 64 (2013) 1041–1052.

[139] M. Li, C. Huber, Y. Mu, W. Tao, Lattice Boltzmann simulation of condensation in the presence of noncondensable gas, Int. J. Heat Mass Transf. 109 (2017)

1004–1013.

[140] A. Ashrafi, A. Moosavi, Droplet condensation on chemically homogeneous and heterogeneous surfaces, J. Appl. Phys. 120 (2016). doi:10.1063/1.4962645.

[141] T. Sun, W. Li, S. Yang, Numerical simulation of bubble growth and departure during flow boiling period by lattice Boltzmann method, Int. J. Heat Fluid Flow. 44 (2013) 120–129.

[142] Z. Dong, W. Li, Y. Song, A numerical investigation of bubble growth on and departure from a superheated wall by lattice Boltzmann method, Int. J. Heat Mass Transf. 53 (2010) 4908–4916.

[143] S. Gong, P. Cheng, A lattice Boltzmann method for simulation of liquid-vapor phase-change heat transfer, Int. J. Heat Mass Transf. 55 (2012) 4923–4927.

[144] S. Gong, P. Cheng, Lattice Boltzmann simulation of periodic bubble nucleation, growth and departure from a heated surface in pool boiling, Int. J. Heat Mass Transf. 64 (2013) 122–132.

[145] S. Gong, P. Cheng, Numerical investigation of saturated flow boiling in microchannels by the lattice boltzmann method, Numer. Heat Transf. Part A Appl. 65 (2014) 644–661.

[146] S. Gong, P. Cheng, Lattice Boltzmann simulations for surface wettability effects in saturated pool boiling heat transfer, Int. J. Heat Mass Transf. 85 (2015) 635–646.

[147] Q. Li, Q.J. Kang, M.M. Francois, Y.L. He, K.H. Luo, Lattice Boltzmann modeling of boiling heat transfer: The boiling curve and the effects of wettability, Int. J. Heat Mass Transf. 85 (2015) 787–796.

[148] T. Sun, W. Li, Three-dimensional numerical simulation of nucleate boiling bubble by lattice Boltzmann method, Comput. Fluids. 88 (2013) 400–409.

[149] R. Zhang, H. Chen, Lattice Boltzmann method for simulations of liquid-vapor thermal flows, Phys. Rev. E. 67 (2003) 6.

[150] Q. Li, P. Zhou, H.J. Yan, Improved thermal lattice Boltzmann model for simulation of liquid-vapor phase change, Phys. Rev. E. 96 (2017).

[151] L. Biferale, P. Perlekar, M. Sbragaglia, F. Toschi, Convection in multiphase fluid flows using lattice boltzmann methods, Phys. Rev. Lett. 108 (2012).

[152] Q. Li, K.H. Luo, Q.J. Kang, Y.L. He, Q. Chen, Q. Liu, Lattice Boltzmann methods for multiphase flow and phase-change heat transfer, Prog. Energy Combust. Sci. 52 (2016) 62–105.

[153] Q. Chang, J.I.D. Alexander, Analysis of single droplet dynamics on striped surface domains using a lattice Boltzmann method, Microfluid. Nanofluidics. 2 (2006) 309–326. doi:10.1007/s10404-005-0075-2.

[154] X. Cheng, Y. Zhu, L. Zhang, C. Wang, S. Li, Lattice Boltzmann simulation of multiple droplets impingement and coalescence in an inkjet-printed line

patterning process, Int. J. Comut. Fluid Dyn. 31 (2017) 450–462.

[155] M. Ebrahim, A. Ortega, N. Delbosc, M.C.T. Wilson, J.L. Summers, Simulation of the spreading of a gas-propelled micro-droplet upon impact on a dry surface using a lattice-Boltzmann approach, Phys. Fluids. 29 (2017).

[156] T. Lee, L. Liu, Lattice Boltzmann simulations of micron-scale drop impact on dry surfaces, J. Comput. Phys. 229 (2010) 8045–8063.

[157] K.A. Raman, R.K. Jaiman, T.S. Lee, H.T. Low, Lattice Boltzmann simulations of droplet impact onto surfaces with varying wettabilities, Int. J. Heat Mass Transf. 95 (2016) 336–354.

[158] S. Shen, F. Bi, Y. Guo, Simulation of droplets impact on curved surfaces with lattice Boltzmann method, Int. J. Heat Mass Transf. 55 (2012) 6938–6943.

[159] Y. Tanaka, Y. Washio, M. Yoshino, T. Hirata, Numerical simulation of dynamic behavior of droplet on solid surface by the two-phase lattice Boltzmann method, Comput. Fluids. 40 (2011) 68–78.

[160] M. Taghilou, M.H. Rahimian, Lattice Boltzmann model for thermal behavior of a droplet on the solid surface, Int. J. Therm. Sci. 86 (2014) 1–11.

[161] W.Z. Yuan, L.Z. Zhang, Lattice Boltzmann simulation of droplets impacting on superhydrophobic surfaces with randomly distributed rough structures, Langmuir. 33 (2017) 820–829.

[162] D. Zhang, K. Papadikis, S. Gu, Investigations on the droplet impact onto a spherical surface with a high density ratio multi-relaxation time lattice-Boltzmann model, Commun. Comput. Phys. 16 (2014) 892–912.

[163] D. Zhang, K. Papadikis, S. Gu, Three-dimensional multi-relaxation time lattice-Boltzmann model for the drop impact on a dry surface at large density ratio, Int. J. Multiph. Flow. 64 (2014) 11–18.

[164] Y.Q. Zu, Y.Y. Yan, Lattice Boltzmann method for modelling droplets on chemically heterogeneous and microstructured surfaces with large liquid-gas density ratio, IMA J. Appl. Math. 76 (2011) 743–760.

[165] F.H. Harlow, J.E. Welch, Numerical calculation of time-dependent viscous incompressible flow of fluid with free surface, Phys. Fluids. 8 (1965) 2182–2189.

[166] T.R. Vijaybabu, K. Anirudh, S. Dhinakaran, LBM simulation of unsteady flow and heat transfer from a diamond-shaped porous cylinder, Int. J. Heat Mass Transf. 120 (2018) 267–283.

[167] Z. Wang, H. Shang, J. Zhang, Lattice Boltzmann simulations of heat transfer in fully developed periodic incompressible flows, Phys. Rev. E. 95 (2017).

[168] S. Gong, P. Cheng, A lattice Boltzmann method for simulation of liquid-vapor phase-change heat transfer, Int. J. Heat Mass Transf. 55 (2012) 4923–4927.

[169] X. He, G.D. Doolen, Thermodynamic foundations of kinetic theory and Lattice

Boltzmann models for multiphase flows, in: J. Stat. Phys., 2002: pp. 309–328.

[170] X. He, L.-S. Luo, Lattice Boltzmann Model for the Incompressible Navier--Stokes Equation, J. Stat. Phys. 88 (1997) 927–944.

[171] N. Martys, H. Chen, Simulation of multicomponent fluids in complex three-dimensional geometries by the lattice Boltzmann method, Phys. Rev. E. 53 (1996) 743–750.

[172] R. Benzi, L. Biferale, M. Sbragaglia, S. Succi, F. Toschi, Mesoscopic modeling of a two-phase flow in the presence of boundaries: The contact angle, Phys. Rev. E - Stat. Nonlinear, Soft Matter Phys. 74 (2006) 1–14.

[173] A. A. Mohammed, Lattice Boltzmann method: fundamentals and engineering applications with computer codes, 2012.

[174] R. Benzi, S. Succi, M. Vergassola, The lattice Boltzmann equation: theory and applications, Phys. Rep. 222 (1992) 145–197.

[175] D. Raabe, Overview of the lattice Boltzmann method for nano- and microscale fluid dynamics in materials science and engineering, Model. Simul. Mater. Sci. Eng. 12 (2004) R13–R46.

[176] D.H. Rothman, J.M. Keller, Immiscible cellular-automaton fluids, J. Stat. Phys. 52 (1988) 1119–1127.

[177] A.K. Gunstensen, D.H. Rothman, S. Zaleski, G. Zanetti, Lattice Boltzmann model of immiscible fluids, Phys. Rev. A. 43 (1991) 4320–4327.

[178] T. Inamuro, T. Ogata, S. Tajima, N. Konishi, An improved lattice Boltzmann method for incompressible two-phase flows with large density differences, J. Comput. Phys. 198 (2004) 628–644.

[179] Y.H. Qian, D. D'Humières, P. Lallemand, Lattice BGK Models for Navier-Stokes Equation, Europhys. Lett. 17 (1992) 479–484.

[180] D. a. Wolf-Gladrow, Lattice Gas Cellular Automata and Lattice Boltzmann Models, 2000.

[181] H. Huang, M.C. Sukop, X.-Y. Lu, Introduction, in: Multiph. Lattice Boltzmann Methods Theory Appl., John Wiley & Sons, Ltd, 2015: pp. 1–17.

[182] P. Yuan, L. Schaefer, Equations of state in a lattice Boltzmann model, Phys. Fluids. 18 (2006).

[183] S. Gong, P. Cheng, Numerical investigation of droplet motion and coalescence by an improved lattice Boltzmann model for phase transitions and multiphase flows, Comput. Fluids. 53 (2012) 93–104.

[184] M.C. Sukop, D.T. Thorne, Lattice boltzmann modeling: An introduction for geoscientists and engineers, 2006.

[185] A.J. Ladd, Numerical simulations of particulate suspensions via a discretized Boltzmann Equation. Part 1. theoretical foundation, J. Fluid Mech. 271 (1994)

285–309.

[186] T. Krüger, H. Kusumaatmaja, A. Kuzmin, O. Shardt, G. Silva, E. Viggen, The lattice Boltzmann method: principles and practice, Springer, Switzerland, 2017.

[187] Q. Zou, X. He, On pressure and velocity boundary conditions for the lattice Boltzmann BGK model, Phys. Fluids. 9 (1997) 1591–1598.

[188] H. Huang, M. Sukop, X. Lu, Multiphase Lattice Boltzmann Methods: Theory and Application, Wiley, 2015.

[189] Q. Li, K.H. Luo, X.J. Li, Lattice Boltzmann modeling of multiphase flows at large density ratio with an improved pseudopotential model, Phys. Rev. E - Stat. Nonlinear, Soft Matter Phys. 87 (2013).

[190] Q. Li, K.H. Luo, X.J. Li, Forcing scheme in pseudopotential lattice Boltzmann model for multiphase flows, Phys. Rev. E - Stat. Nonlinear, Soft Matter Phys. 86 (2012) 1–9.

[191] P. Lallemand, L.-S. Luo, Theory of the lattice Boltzmann method: Dispersion, dissipation, isotropy, Galilean invariance, and stability, Phys. Rev. E. 61 (2000) 6546–6562.

[192] Z. Yu, L.-S. Fan, Multirelaxation-time interaction-potential-based lattice Boltzmann model for two-phase flow, Phys. Rev. E. (2010) 1–14.

[193] M.E. McCracken, J. Abraham, Multiple-relaxation-time lattice-Boltzmann model for multiphase flow, Phys. Rev. E. 71 (2005).

[194] Q. Li, Y.L. He, G.H. Tang, W.Q. Tao, Improved axisymmetric lattice Boltzmann scheme, Phys. Rev. E. 81 (2010) 1–10.

[195] J. Chao, R. Mei, R. Singh, W. Shyy, A filter-based, mass-conserving lattice Boltzmann method for immiscible multiphase flows, Int. J. Numer. Methods Fluids. 66 (2011) 622–647.

[196] N.F. Carnahan, K.E. Starling, Intermolecular repulsions and the equation of state for fluids, AlChE J. 18 (1972) 1184–1189. doi:10.1002/aic.690180615.

[197] N.F. Carnahan, Equation of state for nonattracting rigid spheres, J. Chem. Phys. 51 (1969) 635.

[198] G. Hazi, A. Markus, On the bubble departure diameter and release frequency based on numerical simulation results, Int. J. Heat Mass Transf. 52 (2009) 1472–1480.

[199] A.L. Kupershtokh, D.A. Medvedev, Lattice Boltzmann equation method in electrohydrodynamic problems, J. Electrostat. 64 (2006) 581–585.

[200] D.M. Fernandez, A. Torregrosa, P.S. Weiss-Penzias, B.J. Zhang, D. Sorensen, R.E. Cohen, G.H. McKinley, J. Kleingartner, A. Oliphant, M. Bowman, Fog water collection effectiveness: mesh intercomparisons, Aerosol Air Qual. Res. 18 (2018) 270–283.

[201] X. Chen, R. Ma, H. Zhou, X. Zhou, L. Che, S. Yao, Z. Wang, Activating the microscale edge effect in a hierarchical surface for frosting suppression and defrosting promotion, (2013) 1–8.

[202] N. Miljkovic, R. Enright, E.N. Wang, Growth dynamics during dropwise condensation on nanostructured superhydrophobic surfaces, in: MNHMT2012, Atlanta, Georgia, USA, 2012.

[203] A.B.D. Cassie, S. Baxter, Wettability of porous surfaces, Trans. Faraday Soc. 40 (1944) 546–551.

[204] T. Bobinski, G. Sobieraj, M. Psarski, G. Celichowski, J. Rokicki, Droplet bouncing on the surface with micro-structure, Arch. Mech. 69 (2017) 177–193.

[205] M. Psarski, J. Marczak, G. Celichowski, G.B. Sobieraj, K. Gumowski, F. Zhou, W. Liu, Hydrophobization of epoxy nanocomposite surface with 1H,1H,2H,2H-perfluorooctyltrichlorosilane for superhydrophobic properties, Cent. Eur. J. Phys. 10 (2012) 1197–1201.

[206] Y. Shen, S. Liu, C. Zhu, J. Tao, Z. Chen, H. Tao, L. Pan, G. Wang, T. Wang, Bouncing dynamics of impact droplets on the convex superhydrophobic surfaces, Appl. Phys. Lett. 110 (2017).

[207] R. Zhang, X. He, S. Chen, Interface and surface tension in incompressible lattice Boltzmann multiphase model, Comput. Phys. Commun. 129 (2000) 121–130.

[208] Š. Šikalo, H.D. Wilhelm, I. V. Roisman, S. Jakirlić, C. Tropea, Dynamic contact angle of spreading droplets: Experiments and simulations, Phys. Fluids. 17 (2005) 1–13.

[209] L. Wang, H. Huang, X.-Y. Lu, Scheme for contact angle and its hysteresis in a multiphase lattice Boltzmann method, Phys. Rev. E. 87 (2013) 13301.

[210] X. Gu, A. Gupta, R. Kumar, Lattice Boltzmann simulation of drop collision and surface impingement at high density ratio, (2009) 1–24.

[211] A. Dupuis, J.M. Yeomans, Droplets on patterned substrates: Water off a beetle's back, Int. J. Numer. Methods Fluids. 50 (2006) 255–261.

[212] Q. Zhang, D. Sun, Y. Zhang, M. Zhu, Lattice Boltzmann modeling of droplet condensation on superhydrophobic nanoarrays, Langmuir. 30 (2014) 12559–12569.

[213] X. Fu, Z. Yao, P. Hao, Numerical simulation of condensation on structured surfaces, Langmuir. 30 (2014) 14048–14055. doi:10.1021/la503504r.

[214] M.E. Kutay, A.H. Aydilek, E. Masad, Laboratory validation of lattice Boltzmann method for modeling pore-scale flow in granular materials, Comput. Geotech. 33 (2006) 381–395.

[215] C.G.L. Furmidge, Studies at phase interfaces. I. The sliding of liquid drops on solid surfaces and a theory for spray retention, J. Colloid Sci. 17 (1962) 309–324.

[216] M. Miwa, A. Nakajima, A. Fujishima, K. Hashimoto, T. Watanabe, Effects of the Surface Roughness on Sliding Angles of Water Droplets on Superhydrophobic Surfaces, Langmuir. 16 (2000) 5754–5760.

[217] K.S. Yang, K.H. Lin, C.W. Tu, Y.Z. He, C.C. Wang, Experimental investigation of moist air condensation on hydrophilic, hydrophobic, superhydrophilic, and hybrid hydrophobic-hydrophilic surfaces, Int. J. Heat Mass Transf. 115 (2017) 1032–1041.

[218] A. Phadnis, K. Rykaczewski, The effect of Marangoni convection on heat transfer during dropwise condensation on hydrophobic and omniphobic surfaces, Int. J. Heat Mass Transf. 115 (2017) 148–158.

[219] T. Inamuro, M. Yoshino, H. Inoue, R. Mizuno, F. Ogino, A lattice Boltzmann method for a binary miscible fluid mixture and its application to a heat-transfer problem, J. Comput. Phys. 179 (2002) 201–215.

[220] W. Fritz, Berechnung des maximal volumes von Dampfblasen, Phys. Zeitschrift. 36 (1935) 379–384.